

Ninevah University

College of Electronics Engineering

Electronic Engineering Department



Advanced Antenna Design for RF-Based Energy Harvesting Systems

Mohammed Muataz Hasan

A Thesis in

Electronic Engineering

Supervised by

Assistant Professor Dr. Ahmed Mohamed Ahmed Sabaawi

1446 AH

2024 AD

Advanced Antenna Design for RF-Based Energy Harvesting Systems

A thesis introduced by

Mohammed Muataz Hasan

To

The Council of the College of Electronics Engineering

Ninevah University

as a Partial Fulfillment of the Requirements

for the Degree of Master of Science

in

Electronic Engineering

Supervised by

Assistant Professor Dr. Ahmed Mohamed Ahmed Sabaawi

Supervisor Certification

I certify that the dissertation entitled (**Advanced Antenna Design for RF-Based Energy Harvesting Systems**) was prepared by **Mohammed Muataz Hasan** under my supervision at the Department of Electronic Engineering, Ninevah University, as a partial requirement for the Master of Science Degree in Electronic Engineering.

Signature:

Name: Assist. Prof. Dr. Ahmed Mohammed Ahmed

Date: / /2024

Report of Linguistic Reviewer

I certify that the linguistic reviewing of this dissertation was carried out by me and it is accepted linguistically and in expression.

Signature:

Name: Lect. Dr. Lateef Ahmed Mohammed

Date: / /2024

Report of the Head of Department

I certify that this dissertation was carried out in the Department of Electronic Engineering. I nominate it to be forwarded to discussion.

Signature:

Name: Assist. Prof. Dr. Harith Ahmed Mohammed

Date: / /2024

Report of the Head of Postgraduate Studies Committee

According to the recommendations presented by the supervisors of this dissertation and the linguistic reviewer, I nominate this dissertation to be forwarded to discussion.

Signature:

Name: Assist. Prof. Dr. Harith Ahmed Mohammed

Date: / /2024

Committee Certification

We the examining committee, certify that we have read this dissertation entitled (**Advanced Antenna Design for RF-Based Energy Harvesting Systems**) and have examined the postgraduate student (**Mohammed Muataz Hasan**) in its contents and that in our opinion; it meets the standards of a dissertation for the degree of Master of Science in Electronic Engineering.

Signature:

Name: Prof. Dr. Jaafar Ramadan Mohammed
Head of committee

Date: / /2024

Signature:

Name: Assist. Prof. Dr. Mohammed
Abdulrahman Ahmed

Member

Date: / /2024

Signature:

Name: Assist. Prof. Dr. Saad Wasmi Osman
Member

Date: / /2024

Signature:

Name: Assist. Prof. Dr. Ahmed Mohammed
Ahmed

Member and Supervisor

Date: / /2024

The college council, in its meeting on / / 2024, has decided to award the degree of Master of Science in Electronic Engineering to the candidate.

Signature:

Name: Prof. Khaled Khalil Muhammad
Dean of the College

Date: / /2024

Signature:

Name: Assist. Prof. Dr. Bilal A. jebur
Council registrar

Date: / /2024

بِسْمِ اللّٰهِ الرَّحْمٰنِ الرَّحِیْمِ

﴿ وَقُلِ اَعْمَلُوا فَسَيَرَى اللّٰهُ عَمَلَكُمْ وَرَسُولُهُ وَالْمُؤْمِنُونَ وَسَتُرَدُّونَ اِلَى
عَالِمِ الْغَيْبِ وَالشَّهَادَةِ فَيُنَبِّئُكُمْ بِمَا كُنْتُمْ تَعْمَلُونَ ﴾

صدق الله العظيم

[سورة التوبة: 105]

ACKNOWLEDGEMENTS

Praise be to Allah, who has assisted me and made my paths correct, helping me to complete this project to obtain a master degree in electronic engineering.

With great pleasure, I would like to express my gratitude to my supervisor, Assistant. Prof. Ahmed Mohammed Ahmed, for his insightful advice, precise guidance, and wealth of knowledge.

I would like to express my appreciation to the dean of the College of Electronics Engineering and the president of the University of Ninevah for their contributions to preserving science and the educational process.

I would like to express my gratitude to the head of the department of electronics engineering as well as to all of my instructors at the College of Electronics Engineering for their efforts during my study journey.

I would like to extend my sincere thanks to Eng. Qusai H. Sultan from the Communication Engineering Department for his support.

A special thanks to my family. Words cannot express my gratitude to my father and my mother for all of the sacrifices that you have made for me. Your prayers for me have sustained me thus far.

I would like to thank my beloved wife for supporting me, and my dear daughter Dina for being such a nice girl and for always making me feel happier.

I would like to extend my sincere thanks to my brother and my sister for their significant support.

Lastly, I am also thankful to my classmates for their cooperation and teamwork.

Abstract

The receiving antenna is one of the main components of both the Radio Frequency Energy Harvesting (RFEH) system and the Wireless Power Transfer (WPT) system, since it is responsible for capturing the electromagnetic waves from free space. The thesis demonstrates the ideal design specifications of the receiving antennas used by RFEH systems and how multiband and wideband antennas are preferred for RFEH systems.

This thesis introduces a variety of three novel multiband patch antennas as well as three novel wideband patch antennas designed and optimized for RFEH systems. All of the introduced antennas are fabricated using Printed Circuit Board Technology (PCB) technology using Flame Retardant (FR-4) substrate, and their performance is tested in the lab. The measurement results showed acceptable tolerance errors compared with the simulated results. Several techniques are employed during the implementation of the introduced antennas in order to increase the bandwidth and improve the performance, including combining fractal geometry and using the Defected Ground Structure (DGS).

The first proposed antenna (a drone-shaped fractal antenna) supports six resonating frequencies and achieved a peak gain of (2.83 dBi) at a frequency of 2.45 GHz. The second proposed antenna (microstrip patch antenna based on a half-wave dipole) supports eleven resonating frequencies and achieved a peak gain of (6.349 dBi) at the frequency of 3.95 GHz. The third proposed antenna (modified hexagonal slot antenna) supports four resonating frequencies and achieved a peak gain of (3.203 dBi) at the frequency of 2.4045 GHz. The fourth proposed antenna (a compact patch antenna with a modified structure) has a maximum bandwidth of (1.0813 GHz) and achieved a peak gain of (4 dBi) at the frequency (5.4 GHz). The fifth proposed antenna (a modified square monopole patch antenna with Coplanar Waveguide

(CPW)-Feeding technique), the CPW feeding technique implemented in order to achieve wideband frequency characteristics, the antenna has a maximum bandwidth of (2.963 GHz) and achieved a peak gain of (4.31 dBi) at the frequency (2.6 GHz). The sixth proposed antenna (a modified hexagonal monopole patch antenna with (CPW) feeding technique) has a maximum bandwidth of (3.9723 GHz) and achieved a peak gain of (4.481 dBi) at the frequency (3 GHz). All of the proposed antennas achieved high performance, which makes them suitable receiving antennas for RFEH systems.

Contents

Chapter One

Introduction and literature review

1.1	Introduction.....	1
1.2	Literature Review	5
1.3	Aims of the Thesis	12
1.4	Thesis Layout.....	13

Chapter Two

Theoretical background

2.1	Introduction.....	14
2.2	RFEH Versus WPT	14
2.3	Antenna Design Specifications in RFEH Systems.....	17
2.4	RFEH Antenna Technologies	24
2.5	Antenna Types	27

Chapter Three

Design, Simulation, and Implementation of Multiband Antennas for Radio Frequency Energy Harvesting Applications

3.1	Introduction.....	31
3.2	Drone Shaped Fractal Antenna with Defected Ground Structure for RFEH Applications	32
3.2.1	Design Fractal Shape 1.....	32
3.2.2	The Design of the First Proposed Multiband Antenna (Antenna-1) 33	
3.2.3	Impact of the number of stages on Antenna-1	37

3.2.4	Parametric analysis for the proposed selected (Antenna-1-c)	39
3.2.5	(Antenna-1-c) Optimization	45
3.2.6	Comparison between (Antenna-1-d) and (Antenna-1-c)	46
3.3	Microstrip Multiband Patch Antenna Based on a Half-Wave Dipole Antenna for RFEH Applications	50
3.3.1	A Brief Review of the Half-Wave Dipole Antenna.....	50
3.3.2	Design and Construction of the Second Proposed Multiband Antenna (Antenna-2).....	51
3.3.3	Simulated Results for the Proposed Antenna-2	53
3.3.4	Parametric analysis for the proposed (Antenna-2).....	56
3.3.5	Antenna-2 Optimization.....	65
3.3.6	Comparison between (Antenna-2-a), (Antenna-2-b) and (Antenna-2-c)	69
3.4	Modified Hexagonal Slot Antenna with a Defected Ground Structure for RFEH Applications	74
3.4.1	Design and Construction of the First Stage of the Proposed Multiband Antenna (Antenna-3-a)	74
3.4.2	Simulated Results for the Proposed (Antenna-3-a)	76
3.4.3	Design and Construction of the Second Stage of the Proposed Multiband Antenna (Antenna-3-b).....	77
3.4.4	Simulated Results for the Proposed (Antenna-3-b)	79
3.4.5	Comparison between the simulated results of the two proposed antennas (Antenna-3-a) and (Antenna-3-b)	80
3.4.6	Parametric analysis for the proposed (Antenna-3-b).....	81
3.4.7	(Antenna-3-b) Optimization.....	87
3.5	Fabrication and Experimental Results.....	92
3.5.1	The experimental results for the optimized Antenna-1.....	93
3.5.2	The experimental results for the optimized Antenna-2.....	95
3.5.3	The experimental results for the optimized Antenna-3	97

Chapter Four

Design, Simulation, and Implementation of Wideband Antennas for Radio Frequency Energy Harvesting Applications

4.1	Introduction.....	99
4.2	(Antenna-4) a compact patch antenna with a modified structure.....	100
4.2.1	Design Fractal Shape 2.....	100
4.2.2	Design and Construction.....	101
4.2.3	Simulated Results for the Proposed Antenna-4	103
4.2.4	Parametric Analysis for the Proposed Antenna-4	105
4.2.5	Simulated Radiation Pattern for the Proposed (Antenna-4)	110
4.3	(Antenna-5) a Modified Square Monopole Patch Antenna with (CPW) Feeding Technique	112
4.3.1	Design and Construction.....	112
4.3.2	Simulated Results for the Proposed (Antenna-5).....	113
4.3.3	Parametric Analysis for the Proposed (Antenna-5)	115
4.3.4	Simulated Radiation Pattern for the Proposed (Antenna-5)	121
4.4	(Antenna-6) a Modified Hexagonal Monopole Patch Antenna with (CPW) Feeding Technique	123
4.4.1	Design and Construction.....	123
4.4.2	Simulated Results for the Proposed (Antenna-6).....	125
4.4.3	Parametric Analysis for the Proposed (Antenna-6)	127
4.4.4	Simulated Radiation Pattern for the Proposed (Antenna-6)	133
4.5	Fabrication and Experimental Results.....	135
4.5.1	The experimental results for the proposed wideband Antenna-4	135
4.5.2	The experimental results for the proposed wideband antenna-5	138
4.5.3	The experimental results for the proposed wideband antenna-6	140

Chapter Five

Conclusions and Future works

5.1	Conclusions.....	143
5.2	Future Works.....	146
5.3	Publications Arising from This Research	147

List of Tables

Table No.	Title	Page No.
1-1	Comparison between different ambient energy sources	4
2-1	Comparison between WPT and RFEH technologies	15
2-2	Overview of the major advantages and disadvantages of various antenna design techniques	26
3-1	The simulated results of reflection coefficient $ S_{11} $ magnitude in [dB] for each stage of the drone shaped antenna	39
3-2	Simulated results for the final design of the proposed drone shaped antenna (Antenna-1-d) after optimization.	47
3-3	Simulated results of the proposed Antenna-2	55
3-4	Simulated results of the proposed optimized (Antenna-2-c)	70
3-5	Simulated results of the proposed (Antenna-3-b) after optimization	88
4-1	Simulated results for the proposed (Antenna-4)	105
4-2	Simulated results for the proposed (Antenna-5)	113
4-3	Simulated results for the proposed (Antenna-6)	125

List of Figures

Figure No.	Title	Page No.
1.1	Overview of the various sources of ambient energy	3
1.2	Block diagram of RFEH System.	3
2.1	Block diagram of WPT (Wireless Power Transfer) system.	15
2.2	The variation in received power at various frequencies with the receiving antenna's gain ($G_r = 2$ dBi) at a distance of 100 meters from the transmitting antenna ($G_t = 16$ dBi), the transmitting power is 20 dBm.	19
2.3	Dipole Antenna.	27
2.4	Rectangular Patch Antenna.	28
2.5	Yagi Antenna.	28
2.6	Parabolic Dish Antenna.	29
2.7	Horn Antenna.	29
2.8	Helical Antenna.	30
3.1	Fractal shape design 1: (a) The initiator line; (b) The first iteration; (c) mirror shape (b) on y-axis; (d) mirror shape (c) on x-axis; (e) The final shape design.	33
3.2	Combine the novel fractal shape with different geometrical shapes.	34
3.3	Antenna construction; (a) standard square patch; (b) modified square patch.	34
3.4	Construction stages of the proposed Antenna-1	36
3.5	Two substrate ground types of the proposed Antenna-1	36
3.6	The dimensions for each stage of the drone-shaped antenna	37
3.7	The simulated results of the reflection coefficient $ S_{11} $ for each stage of the drone shaped antenna.	38
3.8	The simulated results of the reflection coefficient $ S_{11} $ for different scale up factors of (Antenna-1-c).	40
3.9	The simulated results of the reflection coefficient $ S_{11} $ for different scale down factors of (Antenna-1-c).	41
3.10	The simulated results of the reflection coefficient $ S_{11} $ for different ground plane lengths of (Antenna-1-c).	42
3.11	The simulated results of the reflection coefficient $ S_{11} $ for different ground plane widths of (Antenna-1-c).	43
3.12	The simulated results of reflection coefficient $ S_{11} $ for different feeding inset widths of (Antenna-1-c).	44
3.13	The front patch with slot cut and the defected ground structure of the proposed (Antenna-1-d).	45

3.14	The Dimensions for the optimized (Antenna-1-d).	46
3.15	The simulated results of the reflection coefficient $ S_{11} $ for the optimized (Antenna-1-d) and (Antenna-1-c).	47
3.16	Simulated 3D radiation pattern of the directivity magnitude in [dBi] for some of (Antenna-1-d) supported frequencies.	48
3.17	Simulated 2D radiation pattern of the directivity magnitude in [dBi] for some of (Antenna-1-d) supported frequencies.	49
3.18	Illustration of a conventional half-wave dipole antenna.	50
3.19	The basic design of the proposed antenna (Antenna-2); the upper fins highlighted by red; the middle fins highlighted by blue; the lower fins highlighted by green.	51
3.20	The dimensions of the proposed Antenna-2.	54
3.21	The simulated results of the reflection coefficient $ S_{11} $ for the proposed Antenna-2.	55
3.22	The simulated results of the reflection coefficient $ S_{11} $ for the proposed (Antenna-2) compare the full back ground plane with the back ground structure.	56
3.23	The simulated results of the reflection coefficient $ S_{11} $ for the proposed (Antenna-2) when increasing the length of the lower fins.	57
3.24	The simulated results of the reflection coefficient $ S_{11} $ for the proposed (Antenna-2) when decreasing the length of the lower fins.	58
3.25	The simulated results of the reflection coefficient $ S_{11} $ for the proposed (Antenna-2) when decreasing the length of the middle fins.	60
3.26	The simulated results of the reflection coefficient $ S_{11} $ for the proposed (Antenna-2) when decreasing the length of the upper fins.	61
3.27	The simulated results of the reflection coefficient $ S_{11} $ when changing all of the fin's width for the proposed (Antenna-2).	62
3.28	The simulated results of the reflection coefficient $ S_{11} $ when changing the scale of the proposed (Antenna-2).	63
3.29	The simulated results of the reflection coefficient $ S_{11} $ when changing the width of the microstrip vertical feed line of Antenna 2.	64
3.30	The first optimization stage (Antenna-2-a).	65
3.31	The second optimization stage (Antenna-2-b).	66
3.32	The third optimization stage (Antenna-2-c).	66
3.33	The dimensions of the first optimization stage (Antenna-2-a).	66
3.34	The dimensions of the second optimization stage (Antenna-2-b).	67
3.35	The dimensions of the third optimization stage (Antenna-2-c).	68
3.36	The simulated results of the reflection coefficient $ S_{11} $ for each optimization stage (Antenna-2-a), (Antenna-2-b), and (Antenna-2-c).	69
3.37	Simulated 3D radiation pattern of the directivity magnitude in [dBi] for some of (Antenna-2-c) supported frequencies.	72

3.38	Simulated 2D radiation pattern of the directivity magnitude in [dBi] for some of (Antenna-2-c) supported frequencies.	73
3.39	The first stage of the proposed antenna (Antenna-3-a) with dimensions.	75
3.40	The simulated results of the reflection coefficient $ S_{11} $ for the proposed (Antenna-3-a).	76
3.41	The construction steps for creating the front patch of the proposed antenna (Antenna-3-b).	77
3.42	The second stage of the proposed antenna (Antenna-3-b) with dimensions.	78
3.43	The simulated results of the reflection coefficient $ S_{11} $ for the proposed (Antenna-3-b).	79
3.44	The simulated results of reflection coefficient $ S_{11} $ for different width values of the feed line of (Antenna-3-b).	81
3.45	The simulated results of reflection coefficient $ S_{11} $ for different length values of the feed line of (Antenna-3-b).	82
3.46	Simulated results of the reflection coefficient $ S_{11} $ for different length values of (Antenna-3-b) ground plane.	83
3.47	Simulated results of the reflection coefficient $ S_{11} $ for different width values of (Antenna-3-b) ground plane.	84
3.48	The simulated results of the reflection coefficient $ S_{11} $ for different scale down factors of (Antenna-3-b).	85
3.49	The simulated results of the reflection coefficient $ S_{11} $ for different scale up factors of (Antenna-3-b).	86
3.50	The dimensions of the proposed (Antenna-3-b) after optimization: (a) The front patch; (b) The defected ground structure (DGS)	88
3.51	The simulated results of the reflection coefficient $ S_{11} $ for the proposed (Antenna-3-b) before and after optimization.	89
3.52	The simulated 3D radiation pattern of the directivity magnitude in [dBi] for the optimized (Antenna-3-b) operating frequencies.	90
3.53	The simulated 2D radiation pattern of the directivity magnitude in [dBi] for the optimized (Antenna-3-b) operating frequencies.	91
3.54	The reflection coefficient $ S_{11} $ for both the simulated and the practical fabricated (Antenna-1).	93
3.55	The normalized 2D radiational pattern of the directivity for the proposed (Antenna-1) showed the simulated and measured results.	94
3.56	The physical structure of the proposed (Antenna-1).	94
3.57	The testing environment for the proposed (Antenna-1).	94
3.58	The reflection coefficient $ S_{11} $ for both the simulated and the practical fabricated (Antenna-2).	95
3.59	The normalized 2D radiational pattern of the directivity for the proposed (Antenna-2) showed the simulated and measured results.	96

3.60	The physical structure of the proposed (Antenna-2).	96
3.61	The testing environment used to measure the normalized 2D radiation pattern for the proposed (Antenna-2).	96
3.62	The reflection coefficient $ S_{11} $ for both the simulated and the practical fabricated (Antenna-3).	97
3.63	The normalized 2D radiational pattern of the directivity for the proposed (Antenna-3) showed the simulated and measured results.	98
3.64	The physical structure of the proposed (Antenna-3).	98
3.65	The testing environment used to measure the normalized 2D radiation pattern for the proposed (Antenna-3).	98
4.1	Fractal shape design 2: (a) initiator line; (b) first iteration; (c) mirror shape (b) on y-axis; (d) mirror shape (c) on x-axis; (e) final shape design.	100
4.2	Construction steps for creating the two modified radiation tapered structures of the proposed (Antenna-4).	102
4.3	Dimensions of the proposed (Antenna-4): (a) the two opposite modified radiation tapered structures; (b) the microstrip feed line.	103
4.5	Simulated result of the reflection coefficient $ S_{11} $ for the proposed (Antenna-4).	104
4.6	Simulated result of the reflection coefficient $ S_{11} $ for the proposed (Antenna-4) for different width values of the antenna feedline.	105
4.7	Simulated result of the reflection coefficient $ S_{11} $ for the proposed (Antenna-4) for different length values of the antenna feedline.	106
4.8	Simulated result of reflection coefficient $ S_{11} $ for the proposed (Antenna-4) for different number of modified shapes.	107
4.9	Simulated result of reflection coefficient $ S_{11} $ for the proposed (Antenna-4) for different scale-up factors.	108
4.10	Simulated result of reflection coefficient $ S_{11} $ for the proposed (Antenna-4) for different scale-down factors.	109
4.11	Simulated 3D radiation pattern of the directivity magnitude in [dBi] for the proposed (Antenna-4).	110
4.12	Simulated 2D radiation pattern of the directivity magnitude in [dBi] for the proposed (Antenna-4).	111
4.13	The dimensions for the proposed (Antenna-5).	113
4.14	Simulated result of the reflection coefficient $ S_{11} $ for the proposed (Antenna-5).	114
4.15	The simulated results of the reflection coefficient $ S_{11} $ for different width values of the (Antenna-5) feed line.	115
4.16	The simulated results of the reflection coefficient $ S_{11} $ for different length values of the (Antenna-5) feed line.	116
4.17	The simulated result of the reflection coefficient $ S_{11} $ for different length values of the two-ground plane of the proposed (Antenna-5).	117

4.18	The simulated result of the reflection coefficient $ S_{11} $ for different width values of the two-ground plane of the proposed (Antenna-5).	118
4.19	The simulated result of the reflection coefficient $ S_{11} $ for different scale-up factors of the proposed (Antenna-5).	119
4.20	The simulated result of the reflection coefficient $ S_{11} $ for different scale-down factors of the proposed (Antenna-5).	120
4.21	The simulated 3D radiation pattern of the directivity magnitude in [dBi] for the proposed (Antenna-5).	121
4.22	The simulated 2D radiation pattern of the directivity magnitude in [dBi] for the proposed (Antenna-5).	122
4.23	Construction steps for creating the modified hexagonal monopole patch of the proposed (Antenna-6).	124
4.24	The dimensions for the proposed (Antenna-6).	125
4.25	The simulated result of the reflection coefficient $ S_{11} $ for the proposed (Antenna-6).	126
4.26	The simulated results of the reflection coefficient $ S_{11} $ for different width values of the (Antenna-6) feed line	127
4.27	The simulated results of the reflection coefficient $ S_{11} $ for different length values of the (Antenna-6) feed line.	128
4.28	The simulated result of the reflection coefficient $ S_{11} $ for different length values of the two-ground plane of the proposed (Antenna-6).	129
4.29	The simulated result of the reflection coefficient $ S_{11} $ for different width values of the two-ground plane of the proposed (Antenna-6).	130
4.30	The simulated result of the reflection coefficient $ S_{11} $ for different scale-up factors of the proposed (Antenna-6).	131
4.31	The simulated result of the reflection coefficient $ S_{11} $ for different scale-down factors of the proposed (Antenna-6).	132
4.32	The simulated 3D radiation pattern of the directivity magnitude in [dBi] for the proposed (Antenna-6).	133
4.33	The simulated 2D radiation pattern of the directivity magnitude in [dBi] for the proposed (Antenna-6).	134
4.34	The reflection coefficient $ S_{11} $ for both the simulated and the practical fabricated (Antenna-4).	136
4.35	The normalized 2D radiational pattern of the directivity for the proposed (Antenna-4) showed the simulated and measured results.	136
4.36	The physical structure of the proposed (Antenna-4).	137
4.37	The testing environment for the proposed (Antenna-4).	137
4.38	The reflection coefficient $ S_{11} $ for both the simulated and the practical fabricated (Antenna-5).	138
4.39	The normalized 2D radiational pattern of the directivity for the proposed (Antenna-5) showed the simulated and measured results.	139
4.40	The physical structure of the proposed (Antenna-5).	139

4.41	The testing environment used to measure the normalized 2D radiation pattern for the proposed (Antenna-5).	140
4.42	The reflection coefficient $ S_{11} $ for both the simulated and the practical fabricated (Antenna-6).	141
4.43	The normalized 2D radiational pattern of the directivity for the proposed (Antenna-6) showed the simulated and measured results.	141
4.44	The physical structure of the proposed (Antenna-6).	142
4.45	The testing environment used to measure the normalized 2D radiation pattern for the proposed (Antenna-6).	142

List of Symbols

Symbol	Explanation	Unit
η	The efficiency of the antenna.	
λ	The wavelength of the radio frequency signal	[meter]
C	The speed of light	[meter / second]
f_r	The resonant frequency of the antenna	[hertz]
Q	The quality factor of the antenna	
ϵ_r	Dielectric constant.	

Abbreviations	
Tx	Transmitter
Rx	Receiver
RF	Radio Frequency
CST	Computer Simulation Technology
DC	Direct Current
RFEH	Radio Frequency Energy Harvesting
WPT	Wireless Power Transfer
WS	Wireless Sensor
IoT	Internet of Things
GSM	Global System for Mobile Communication
DCS	Digital Cellular System
UMTS	Universal Mobile Telecommunications System
LTE	Long Term Evolution
WIMAX	Worldwide Interoperability for Microwave Access
WLAN	Wireless Local Area Network
AM	Amplitude Modulation
FM	Frequency Modulation
Wi-Fi	Wireless Fidelity
FR-4	Flame Retardant - 4
CP	Circularly Polarized
SMA	Sub Miniature version A
FSPL	Free Space Path Loss
ARBW	Axial Ratio Bandwidth
ISM	Industrial Scientific & Medical
UHF	Ultra-High Frequency
PCB	Printed Circuit Board
CPW	Coplanar Waveguide

Chapter One

INTRODUCTION AND LITERATURE REVIEW

1.1 Introduction

The term RFEH (Radio Frequency Energy Harvesting) refers to transducing the ambient electromagnetic energy carried by the radio frequency signals that may be available in free space in a specific geographical area into useful electrical energy. This electrical energy could be used to provide the required power for the operation of low-power electronic devices, eliminating the need for wires, batteries, and energy sources. The Internet of Things (IoT), which continues to grow rapidly, has contributed countless connected devices and sensors to the Internet, and by the year 2025, there will be approximately of 30.9 billion linked devices [1].

Sensor networks, including wired and wireless sensors (WS), are one of the main components of the IOT that provide real-time communication of environmental data, including temperature, brightness, and humidity, and use it to protect the ecosystem and ensure user satisfaction [2]. Wireless sensors (WS) are preferred over wired sensors because they offer more installation flexibility since they may be placed in inaccessible locations, including the ocean's depths, subterranean locations, chemical manufacturing facilities, disaster-prone regions, and agricultural farmland. The drawback of these wireless sensors is that their batteries need to be changed on a regular basis in order to extend their life; therefore, the researchers have been examining several energy harvesting strategies to save maintenance costs and allow low-power devices, including the wireless sensors that are deployed remotely, to be self-sustaining.

There are different available ambient energy sources used by different harvesting systems, like the wind, solar, thermal, and radio frequencies. Each energy harvesting system has its own advantages and disadvantages [3] as shown in Table 1-1. The availability, which is the dominant advantage of the radio frequency ambient source compared to the other ambient sources as shown in Figure 1.1, includes, for example, the radio towers that are designed to be relatively fixed and always available to function as transceivers for cellular mobile wireless communications, including GSM/DCS/UMTS/WIMAX/LTE/5G services, as well as the wireless routers that are available at each building, office, and home and work as transceivers to communicate with multiple different devices through WLAN-2.4G, WLAN-5G, and WLAN-6G services.

The wide variety of wireless services, including Wi-Fi signals, cellular networks, TV digital/analog, and AM/FM radio, make the radio frequencies an excellent ambient energy source. Furthermore, the electromagnetic radio waves can penetrate through the building's walls and enclosed areas, so they can be used for indoor and outdoor applications. The lightweight and small size of the RFEH system make it a suitable system for portable applications, unlike other types of ambient energy harvesting systems, for example, wind turbines or solar cell arrays. The main components of the RFEH system are the receiving antenna, impedance matching network, rectification circuit, and power management unit, as shown in Figure 1.2. The impedance matching network is responsible for the conjugate matching between the receiving antenna impedance and the rectification circuit impedance in order to guarantee maximum power transfer. Lumped elements or microstrip transmission lines are used for constructing impedance matching circuits. The rectification circuit needs to have high power conversion efficiency for converting the AC voltage signal to DC voltage by using either a half-wave

rectifier or a full-wave rectifier. The power management unit is responsible for delivering the required power either to a storage device (battery or capacitor) or to the terminal load.

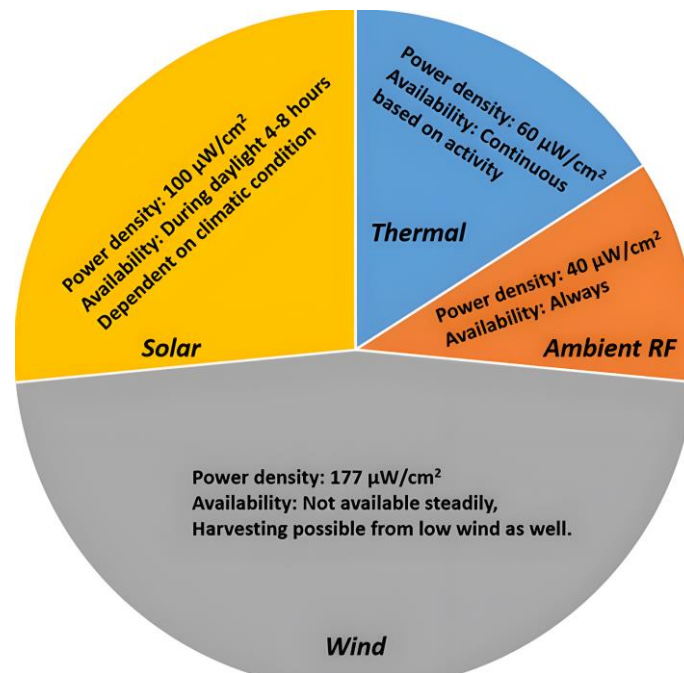


Figure 1.1 Overview of the various sources of ambient energy [3]

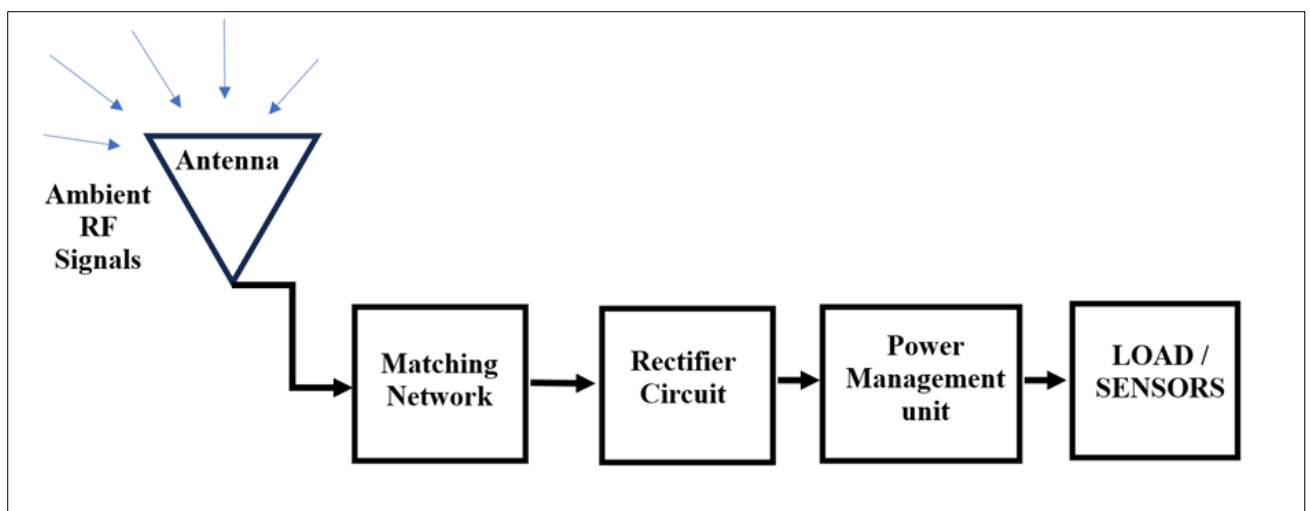


Figure 1.2 Block diagram of RFEH System.

Table 1-1 Comparison between different ambient energy sources [3].

	Solar	Heat/ Thermal	Wind	Ambient RF
Source	Sun	Sun, body, system losses	Wind flow	Wireless networks, radio/TV stations, cell phone & base stations, wireless routers, and radar
Availability	During daylight (4-8 Hours)	Continuous depending on the system's activity or functionality	Rely on climatic condition	Always
Harvesting mechanism	Solar/photovoltaic cell	Thermoelectricity, Seebeck effect	DC motor, turbine, aeroelastic, anemometer	Rectenna
Power density	100 $\mu\text{W}/\text{cm}^2$	60 $\mu\text{W}/\text{cm}^2$	177 $\mu\text{W}/\text{cm}^2$	40 $\mu\text{W}/\text{cm}^2$ or (GSM: 0.1 $\mu\text{W}/\text{cm}^2$, WI-FI: 1 mW/cm^2)[4]
Efficiency	11.7% to 26.7% Depending on different classification	5% to 15%	—	0.4% to over 50% at -40 dBm to -5 dBm input power (Can be increased with more input power)
Advantages	High energy output, low-profile harvester, commercially available, advanced technology	Commercially available, smaller harvester	Possible to harvest with low wind	Certainty of available power, commercially available, low-profile harvester circuitry
Disadvantages	very depending on weather, substantial area needed, and problem with incident light orientation	Thermal matching issue, low power, large area requirement	Availability fluctuates, and the harvesting equipment can be large.	The propagation of electromagnetic waves (EM waves) can be significantly affected by weather conditions (fog, rain, or humid air), propagation medium (multipath effects and attenuation through structures), and wireless signal power availability and distance. low input power results low rectification efficiency.

1.2 Literature Review

- 1- In 2010, A. Georgiadis et al. introduced a paper on a three-layer square aperture-coupled patch antenna with dual linear polarization. The proposed antenna is implemented using two Arlon 25N PCB substrates. The first substrate contains the patch (radiator) with a cross-shaped slot. The second substrate contains the feed networks. Furthermore, a 6 mm foam layer (Rohacell 51) is placed between the two Arlon 25 N substrates in order to obtain the bandwidth to cover the 2.45 GHz band. The proposed antenna supports only a single frequency band with an operating frequency of 2.45 GHz and a bandwidth of 100 MHz. The measured gain of the proposed antenna was (7.7 dBi) with a dimension of (34 mm × 34 mm × 7 mm) however, the area of the foam is unspecified and bigger than the patch [5].

- 2- In 2012, Antwi Nimo et al. introduced a paper on an intermittent meander-line patch antenna fabricated using PCB technology on Duriod 5880 substrate with dimensions of (52 mm × 50 mm × 1.57 mm). The proposed antenna supports six resonating frequencies between (700 MHz and 8 GHz) with a measured gain of (-1 dBi) at the frequency of 1 GHz, (0.5 dBi) at the frequency of 1.6 GHz, (-2.5 dBi) at the frequency of 1.8 GHz, (-0.8 dBi) at the frequency of 2.3 GHz, (-0.2 dBi) at the frequency of 2.7 GHz, and (-3 dBi) at the frequency of 6.4 GHz [6].

- 3- In 2012, G. Monti et al. introduced a paper on a capacitively loaded T-shaped monopole patch with a coplanar waveguide feeding line as the receiving antenna for the (Rectenna) device. The proposed antenna is fabricated using PCB technology on FR-4 substrate with a dimension of (101.8 mm × 46.5 mm × 1.6 mm) and supports only a single frequency

band with a resonance frequency of 866.6 MHz and an input impedance of 50Ω . The proposed antenna has a peak gain of (2 dBi) [7].

- 4- In 2013, Kyriaki Niotaki et al. introduced a paper on a slot-loaded dual-band folded dipole antenna fabricated using PCB technology on an Arlon 25N substrate. The proposed antenna supports two resonating frequencies, 915 MHz and 2.45 GHz, with a measured gain of (1.87 dBi) at the frequency of 915 MHz, (4.18 dBi) at the frequency of 2.45 GHz. The size of the proposed antenna was (60 mm \times 60 mm \times 60 mm) [8].
- 5- In 2013, Shabnam Ladan et al. introduced a paper on a microstrip-fed dipole antenna implemented by folding two poles and fabricated using PCB technology on a Rogers 5880 substrate with a dimension of (62 mm \times 62 mm) and separated by a ground plane. The proposed antenna supports only a single frequency band with an operating frequency of 900 MHz. The measured gain of the antenna was (1.8 dBi) at the frequency of 900 MHz [9].
- 6- In 2015, Md. Kamal Hosain et al. introduced a paper on a Circular-shaped planar inverted-F antenna (PIFA) with two radiating layers fabricated using PCB technology on a 0.765 mm FR4 substrate with a volume of (π mm \times 6² mm \times 1.584 mm). The proposed antenna supports only a single frequency band with a resonance frequency of 915 MHz and a bandwidth of 18 MHz. The maximum simulated antenna gain was (-20.2 dBi) [10].
- 7- In 2015, Seung Tae Khang et al. introduced a paper on a folded dipole antenna implemented using a 0.1 mm thick copper sheet with dimensions of (30 mm \times 30 mm \times 10 mm) and supporting only a single frequency band with an operating frequency of 918 MHz and a bandwidth of 26 MHz.

The peak gain of the proposed dipole antenna was (1 dBi) at the frequency of 918 MHz [11].

- 8- In 2016, Chaoyun Song et al. introduced a paper on a bow-tie-shaped planar cross-dipole patch antenna. The proposed antenna is fabricated using PCB technology on FR-4 substrate with a dimension of (160 mm × 160 mm × 1.6 mm). The proposed antenna supports a frequency range of (550 MHz - 2.5 GHz) with an antenna peak gain of (5 dBi) [12].
- 9- In 2017, Chaoyun Song et al. introduced a paper on a dual-band antenna supporting two frequency ranges (0.9 GHz – 1.1 GHz) and (1.8 GHz – 2.5 GHz). The proposed antenna is fabricated using PCB technology on a Rogers RT6002 substrate and designed with the OCFD (Off-Center-Fed Dipole) technique by combining two pairs of dipole long arms and short arms and a radial stub where the two dipole arms are asymmetrical and have unequal lengths. The dimensions of the proposed antenna were (120 mm × 120 mm × 1.52 mm). The authors unspecified the gain of the antenna and only mentioned the max directivity of (1.8 dBi) at the frequency of 0.9 GHz, (3.5 dBi) at the frequency of 1.8 GHz, and (3.3 dBi) at 2.4 GHz [13].
- 10- In 2017, Shanpu Shen et al. introduced a paper on dual-port L-probe microstrip patch antenna, which consists of two single-port L-probe patch antennas stacked back-to-back with adjacent grounds. The proposed antenna prototype is fabricated using PCB technology on a Rogers 3003 substrate with an overall dimension of (200 mm × 175 mm × 46.6 mm) and supporting three frequency bands with resonating frequencies of 925 MHz, 1.85 GHz, and 2.15 GHz. The proposed antenna prototype has a peak gain of (8.15 dBi) at the frequency of 915 MHz, (7.15 dBi) at the

frequency of 1.850 GHz, and (8.15 dBi) at the frequency of 2.15 GHz [14].

11- In 2018, Ang Jie et al. introduced a paper on a multilayered circularly polarized (CP), dual-band, stacked slit-and slotted-patch antenna. The proposed antenna supports two frequency ranges (0.908 GHz - 0.922 GHz) and (2.35 GHz - 2.5 GHz) with a peak gain of (5.41 dBi) at the frequency of 918 MHz, (7.94 dBi) at the frequency of 2.48 GHz. The size of the proposed antenna was (120 mm x 120 mm x 8.67 mm) [15].

12- In 2018, Sandhya Chandravanshi et al. introduced a paper on a two layer differentially fed slot antenna using two FR-4 substrates and a copper sheet that acts as a reflector. The proposed antenna supports three frequency bands of (2.1 GHz) and (2.4 GHz - 2.48 GHz) and (3.3 GHz - 3.8 GHz) with a peak gain of (7 dBi) at the frequency of 2 GHz, (5.5 dBi) at the frequency of 2.5 GHz and (9.2 dBi) at the frequency of 3.5 GHz respectively. The proposed antenna has an overall dimension of (120 mm × 120 mm × 30 mm) [16].

13- In 2018, Shi Yanyan et al. introduced a paper on a fractal antenna with a double layer of FR-4 substrate. The top substrate contains the main radiator fractal patch of the proposed antenna, whereas the bottom substrate contains a helical patch and the ground plane. The proposed antenna supports a single frequency band of (2.4 GHz to 2.51 GHz) with a dimension of (38 mm × 38 mm × 3.2 mm). The proposed antenna gain varies from (-2.5 dBi to 3.8 dBi) in the range of the frequency band and gradually increases at the center frequency of WiFi, with 2.2 dBi at the resonating frequency of 2.45 GHz [17].

- 14- In 2018, Adel Khemar et al. introduced a paper on a circular-shaped monopole patch antenna with a Coplanar Waveguide (CPW) feeding line. The proposed antenna is fabricated using PCB technology on FR-4 substrate with a dimension of (130 mm × 80 mm × 1.6 mm). Furthermore, the proposed antenna supports a frequency range of (815 MHz - 3000 MHz) with an antenna gain of (2.6 dBi) at the frequency of 900 MHz, (3.6 dBi) at the frequency of 1.8 GHz, (3.8 dBi) at the frequency of 2.1 GHz, and (4.7 dBi) at the frequency of 2.45 GHz [18].
- 15- In 2018, Liu Yang et al. introduced a paper on a corrugated slot line based microstrip patch antenna fabricated using PCB technology on a Rogers RO4350 substrate with a dimension (70 mm × 66 mm × 1.016 mm). The proposed antenna supports four frequency bands with resonating frequencies of 0.9 GHz, 1.575 GHz, 2.025 GHz and 2.36 GHz. The proposed antenna has a peak gain of (1 dBi) at the frequency of 900 MHz, (1.6 dBi) at the frequency of 1.575 GHz, (2.64 dBi) at the frequency of 2.025 GHz, and (-0.19 dBi) at the frequency of 2.36 GHz [19].
- 16- In 2018, Valentina Palazzi et al. introduced a paper on an antenna prototype consisting of two patch antennas with two annular slots, used proximity-coupled-fed technique with two SMA (Sub Miniature version A) connectors, and fabricated on a thin paper substrate. The first antenna supports a frequency range of (0.79 GHz - 0.96 GHz) with a peak gain of (2.3 dBi), whereas the second antenna supports two frequency ranges of (1.71 GHz - 2.17 GHz) and (2.5 GHz - 2.69 GHz) with a varied gain of (4 dBi – 6 dBi), respectively. The proposed antenna prototype has an overall dimension of (110 mm × 110 mm × 1.2 mm) [20].

- 17- In 2018, Miaowang Zeng et al. introduced a paper on a monopole patch antenna that consists of two elements. The first element is a Koch fractal element with a longer bent that supports the GSM900 band, and the second element is a shorter radiation element that supports GSM1800. The proposed antenna is fabricated using PCB technology on an Arion substrate with a substrate dimension of (100 mm × 60 mm × 0.8). The proposed antenna has a peak gain of (0.95 dBi) at the frequency of 880 MHz and a (3.15 dBi) at the frequency of 1.83 GHz [21].
- 18- In 2019, Maizatul Alice Meor Said et al. introduced a paper on a rectangular patch antenna consisting of a double layer FR-4 substrate separated by an airgap. The proposed antenna supports single frequency bands with a resonating frequency of 2.45 GHz and a peak gain of (8.35 dBi). The size of the proposed antenna was (100 mm × 100 mm × 8.2 mm) [22].
- 19- In 2020, Gargi Shukla et al. introduced a paper on a dipole structure antenna implemented using PCB technology on FR-4 substrate with a dimension of (120 mm × 96 mm × 1.6 mm). The proposed antenna supports two frequency bands with resonating frequencies of 1.07 GHz and 2.45 GHz. The proposed antenna has a simulated peak gain of (5.63 dBi) at both of its resonating frequencies [23].
- 20- In 2021, Sunanda Roy et al. introduced a paper on a dual planer structure bow-tie dipole antenna with a triangular shape and fed by the co-axial technique. The proposed antenna was implemented using PCB technology on FR-4 substrate with a dimension of (160 mm × 160 mm × 1.6 mm). The proposed antenna supports four frequency bands with resonating frequencies of 0.85 GHz, 1.81 GHz, 2.18 GHz, and 2.4 GHz.

The proposed antenna has a peak gain of (3.95 dBi) at the frequency of 0.85 GHz, (4.45 dBi) at the frequency of 1.81 GHz, (4.42 dBi) at the frequency of 2.18 GHz, and (4.82 dBi) at the frequency of 2.4 GHz [24].

21- In 2022, Sunanda Roy et al. introduced a paper on a self-complementary antenna with a toothed planar structure and a common center feeding position. The proposed antenna was implemented using PCB technology on FR-4 substrate with a dimension of (160 mm × 160 mm × 1.6 mm). The proposed antenna supports four frequency bands with resonating frequencies of 0.9 GHz, 1.8 GHz, 2.12 GHz, and 2.4 GHz. The proposed antenna has a peak gain of (6 dBi) [25].

22- In 2022, Surajo Muhammad et al. introduced a paper on a wideband antenna consisting of a circular-ring radiator with two circular and rectangular slots. The proposed antenna was implemented using PCB technology on FR-4 substrate with a dimension of (56 mm × 50 mm × 1.6 mm). The proposed antenna supports a frequency range of (1.55 GHz - 3.14 GHz) with a peak measured gain of (1.8 dBi) at the frequency of 1.8 GHz, (2.1 dBi) at the frequency of 2.1 GHz, (2.7 dBi) at the frequency of 2.45 GHz, and (3.1 dBi) at the frequency of 2.65 GHz [26].

1.3 Aims of the Thesis

The aim of this thesis is to carefully design and tune several multiband and wideband patch antennas using theoretical analysis and trial and error techniques in order to target the most required frequency bands used by RFEH systems, including WLAN-2.4G, WLAN-5G, WLAN-6G, WIMAX, and mobile cellular network services. The thesis provides design guidelines and procedures for new researchers in this field. The objectives of this research are the following:

- 1- Investigate the requirements of the receiving antenna used for the RFEH system and the frequencies of interest used by this innovative technology.
- 2- Select the appropriate type of antenna, which is the patch antenna, since it is one of the most practical antenna types due to its compact footprint, light weight, and low cost of production.
- 3- Design novel fractal shapes.
- 4- Use the novel fractal shapes to design several novel multiband and wideband patch antennas.
- 5- Employ the Computer Simulation Technology (CST) microwave studio software for the modeling and simulation of the designed antennas.
- 6- Implement several techniques for the design of the antennas, including employing fractal geometry shapes, using the Defected Ground Structure (DGS), applying slot cuts, and using the Coplanar Waveguide (CPW) feeding technique, in order to achieve the best performance.
- 7- Study and analyze the performance of each of the designed antennas with the help of parametric analyses in order to optimize the antennas and achieve the final design.
- 8- Fabricate the designed antennas, then test their performance in the lab.
- 9- Draw the primary conclusion of this work by comparing the measured and simulated results.

1.4 Thesis Layout

This thesis included various investigations in order to achieve the previously described aims. Five chapters are presented in the following order:

- The first chapter provided an introduction and a literature review of various multiband and wideband antennas that were proposed by the researchers for RF energy harvesting systems. In addition, it discussed the advantages and disadvantages of the most famous ambient energy sources that are available on the surface of the earth.
- The second chapter addressed the differences between the RFEH and WPT systems and the challenges that face designing a suitable receiving antenna for RFEH systems, highlighting the preferred antenna characteristics for this purpose and providing an overview of various types of antennas.
- The third chapter covered the design, simulation, and implementation of three novel multiband antennas optimized for RFEH systems and demonstrated a comparison between the simulated and experimental results.
- The fourth chapter covered the design, simulation, and implementation of three novel wideband antennas optimized for RFEH systems and demonstrated a comparison between the simulated and experimental results.
- The fifth chapter addressed the conclusion of this research and included suggestions for further work as well as the publications arising from this research.

Chapter Two

THEORETICAL BACKGROUND

2.1 Introduction

This chapter will discuss the differences between the RFEH and WPT systems and the challenges of designing a suitable receiving antenna for RFEH systems. Furthermore, emphasize the preferred antenna characteristics for this purpose and provide an overview of various types of antennas.

2.2 RFEH Versus WPT

WPT and RFEH are two innovative alternative energy technologies that can potentially provide wireless energy distribution. WPT technologies can be classified into three categories based on how they are coupled: inductive coupling, electromagnetic (EM) radiation, and magnetic resonance coupling [27]. By utilizing WPT, an automatic power transfer to the device that demands it can be a practical way to offer a cordless experience [28], [29]. WPT is suitable for short-range situations where the transmitter and receiver are close to one another, such as a few meters. The general frequencies of interest for WPT are 2.4 GHz, 5.8 GHz, and 900 MHz [30]. However, studies on WPT schemes are still in their early stages.

The receiving side of the WPT system contains the same components as the RFEH system, which are the receiving antenna, impedance matching network, rectification circuit, and power management unit, except that the location of the source for electromagnetic energy (the transmitter) for the

WPT system is known and already identified, as shown in Figure 2.1 unlike the source of ambient RF energy for the RFEH system, which is unknown. Table 2-1 shows a comparison between the two emerging technologies.

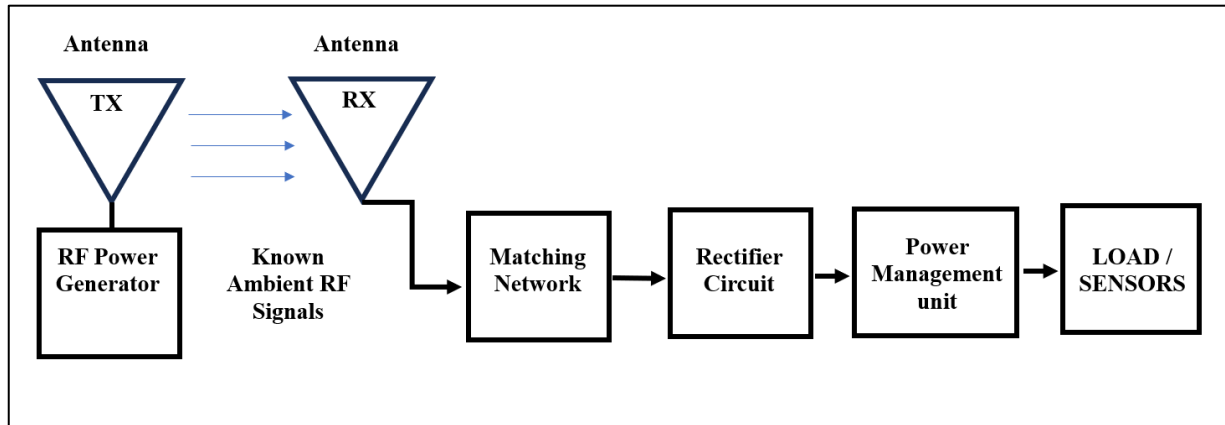


Figure 2.1 Block diagram of WPT system.

Table 2-1 Comparison between WPT and RFEH technologies [3].

	WPT	RFEH
Energy supply	Dedicated antenna for transmitting RF power	Collection of ambient sources, including wireless networks, radios and televisions, cell towers, wireless routers, etc.
Recognized RF ambient source (polarization, direction, transmit power)	Yes	No
Receiving antenna characteristics (for ideal scenario)	High gain, multiband/wideband	Omnidirectional, wideband/multiband, RF energy harvesting from unknown polarization
Availability	Potentially available upon demand	Reduces because of a lack of resources, often in rural areas
Efficiency	high since a dedicated source is available	Low efficiency in most situations (may be lower in areas with low power density)

Furthermore, the Friis transmission equation [31] can be used to estimate the received power by an antenna at the receiving end of both WPT and RFEH systems in the Far-field region, as shown in equation (2-1). With a particular antenna transmitted power, equation (2-1) may result in an accurate approximation of the antenna received power. Considering it ignores environmental attenuation.

$$P_R = P_t G_t G_r \left(\frac{\lambda}{4\pi R} \right)^2 \quad (2 - 1)$$

where:

P_R = The received power in [watt].

P_t = The transmitted power in [watt].

G_t = The transmitting antenna gain.

G_r = The receiving antenna gain.

λ = The wavelength of RF signal in [meter].

R = The far-field distance from the transmitting antenna in [meter].

The Far-field region is the region of the field of an antenna where the angular field distribution is independent of the distance from the antenna, unlike the near-field region, which is dependent on the distance from the antenna. The Far-field region is commonly existed at distance greater than $(2D^2/\lambda)$ from the antenna, whereas the near-field region is commonly existed at distance greater than $0.62(D^3/\lambda)^{0.5}$, where D is the maximum overall dimension of the antenna [37].

Furthermore, the path loss equation can be used to estimate the power loss in RFEH systems in the far field region, as shown in equation (2-2) [4]. Considering that not all of the factors that impact the propagation process, including reflection, diffraction, and absorption, are considered in this equation.

$$P_l = \frac{P_t}{P_r} = \frac{(4\pi R)^2}{G_t G_r \lambda^2} = \frac{(4\pi FR)^2}{G_t G_r C^2} \quad (2 - 2)$$

where:

P_l = The path loss during the signal propagation.

C = The speed of light in [meter / second].

F = The Frequency of the signal in [hertz].

2.3 Antenna Design Specifications in RFEH Systems.

The receiving antennas are essential for capturing the electromagnetic waves from free space; choosing the right one is critical for RFEH systems. The wide availability of radio frequency ambient sources, including GSM900, GSM1800, UMTS2100, LTE2600, WLAN-2.4G, WLAN-5G, and WIMAX bands, is an advantage for RFEH systems. In order to increase the scavenging power, it is recommended to combine all the available sources from different frequency bands. The receiving antenna has a major impact on the system performance since it is responsible for collecting ambient RF energy from the free space in order to transduce it to a useful DC voltage by interfacing the antenna with an appropriate rectification circuit to create a prototype device known as a (Rectenna).

There are different designs for the receiving antennas of the RFEH systems that were introduced by the researchers [5]-[26]. From the RFEH perspective, the system is designed to work in uncertain electromagnetic environments, so in order to collect more RF ambient energy from different electromagnetic transmitting sources, the wideband (broadband) antennas and the multiband antennas are more suitable for this purpose since they are simultaneously resonating with multiple frequency bands, which allow collecting RF ambient energy from different wireless services [32], [33].

It's important to consider the radiation characteristics of the antenna for an RFEH system, such as its operating frequency, bandwidth, polarization, directivity, gain, and power flux density. Another important factor to consider is the telecommunication traffic densities and antenna orientation. The ideal receiving antenna for the RFEH system should resonate with a large variety of frequency bands that are supported by various wireless services and have omnidirectional radiation characteristics with a moderate gain. The goal of the receiving antenna is to deliver sufficient power to turn on the rectifier circuit of the RFEH system, which is challenging in a real-world scenario. Below are the basic selection properties of receiving antennas for the RFEH system.

1- Operating Frequency

The RFEH receiving antenna should support operating frequencies that exist and are available in a specific geographical area for a specific targeted application. Multiband antennas are preferred over single-band antennas in order to obtain more power. The significant free space path loss (FSPL) over long distances affects the total amount of received RF power, especially with higher operating frequencies, as explained in equation (2-2). Furthermore, multiband antennas with reasonably low frequency designs can be employed. However, wideband antennas can also be used to capture power across

multiple frequency ranges. Wideband antennas can be utilized in many countries with a variety of frequency assignments [34]. Figure 2.2 shows the received power with the same transmitting power at various frequencies.

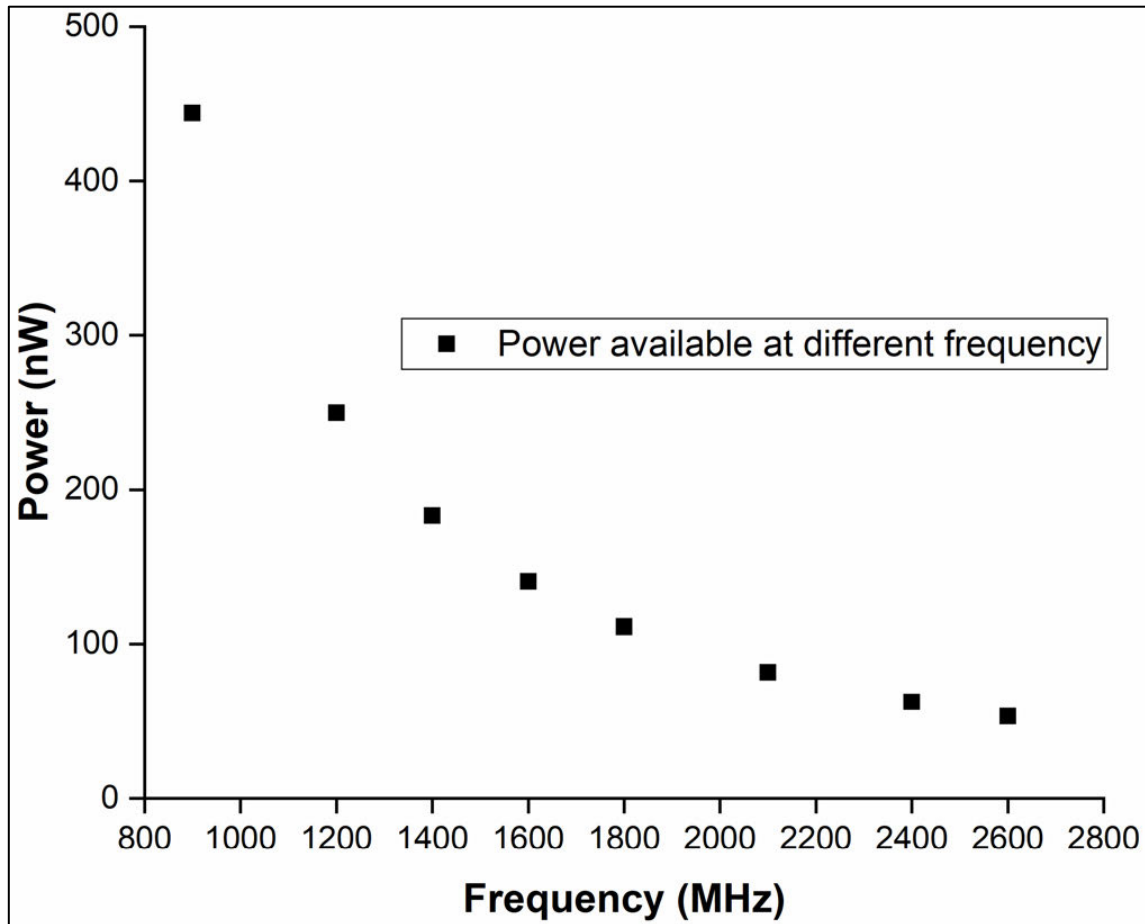


Figure 2.2 The variation in received power at various frequencies with the receiving antenna's gain ($G_r = 2$ dBi) at a distance of 100 meters from the transmitting antenna ($G_t = 16$ dBi), the transmitting power is 20 dBm [3].

2- Radiation Pattern

The antenna radiation pattern is a mathematical function or graphical representation of the radiation characteristics of the antenna as a function of spatial coordinates. The directional coordinates are typically used to illustrate the radiation pattern, which is typically determined in the far-field region. The properties of a radiation pattern include directivity, phase or polarization,

radiation intensity, radiation flux density, and field strength. The antenna field pattern plots the electric or magnetic field magnitude as a function of angular space, while the power pattern plots the electric or magnetic field magnitude squared as a function of angular space. The radiation lobes are distinct parts of a radiation pattern that are categorized by their radiation intensity as main or major lobes, minor lobes, side lobes, and back lobes. The major lobe, also known as the main beam, is the radiation lobe having the direction of peak radiation, and any other lobes are considered minor lobes. Also, the back lobe has approximately 180° with respect to the major lobe.

3- Polarization

Antenna polarization is the direction of the electromagnetic waves when they are radiated by the antenna. A mismatch in the polarization between the transmitting and receiving antennas causes the received power to drop. The ability of a circularly polarized (CP) antenna to receive electromagnetic energy from various polarizations makes it valuable. Therefore, it may be useful to use a wideband CP antenna in order to capture energy from random polarization. At the same time, the design and implementation of CP antennas that support multiband and wideband frequencies that cover Wi-Fi, LTE, WiMAX, ISM, and 5G bands is challenging since generating CP radiation with a low-profile antenna and wide ARBW (Axial Ratio Bandwidth) is difficult to accomplish [35].

4- Gain of the Receiving Antenna

The gain of the antenna $\mathbf{G}(\theta, \phi)$ is a directional function and is defined as the ratio between the maximum power density of an antenna at a given distance $\mathbf{S}(\theta, \phi)$ to the power density of an ideal omnidirectional or isotropic antenna $\mathbf{S}(\text{isotropic})$ at the same distance, radiating the same power [31], as

stated in equation (2-4). The requirement for a high-gain antenna is contingent upon the demands of the intended application. In RFEH applications, a moderate-gain antenna is desired since the antenna gain and directivity are proportional to each other, as illustrated in equation (2-3), and according to [36], the harvested power in RFEH systems is not improved by increasing the directivity of the receiving antennas. Whereas WPT systems require a high-directivity receiving antenna since the ambient electromagnetic source (the transmitted antenna) is known and already identified.

$$G(\theta, \phi) = D(\theta, \phi) * \eta \quad (2 - 3)$$

where:

$G(\theta, \phi)$ = The gain of the antenna magnitude in dBi.

$D(\theta, \phi)$ = The directivity of the antenna magnitude in dBi.

η = The efficiency of the antenna.

$$G(\theta, \phi) = \frac{S(\theta, \phi)}{S_{\text{isotropic}}} = \frac{4\pi R^2 S(\theta, \phi)}{P_t} \quad (2 - 4)$$

where:

$G(\theta, \phi)$ = The gain of the antenna magnitude in dBi.

$S(\theta, \phi)$ = maximum power density of an antenna at a given distance in [watt/m²].

$S(\text{isotropic})$ = power density of isotropic antenna in [watt/m²]

P_t = The transmitted power by the antenna in [watt]

R = Distance between the transmitting and the receiving antenna in [meter]

As a result, the power density (S) at a specific distance (R) from an antenna is illustrated with the below equation.

$$S = \frac{P_t G_t}{4\pi R^2} \quad (2 - 5)$$

where:

S = The maximum power density of the transmitted antenna at a given distance in [watt/m²].

G_t = The gain of the transmitted antenna magnitude in dBi.

P_t = The transmitted power by the antenna in [watt].

R = Distance between the transmitting and the receiving antenna. [meter].

An ideal isotropic antenna is known to have a zero gain (G = 0 dBi). It is also possible to use the previously indicated equations with the receiving antennas as well.

5- Bandwidth

The bandwidth of the antenna describes the range of frequencies over which the antenna can properly radiate or receive energy. One or more frequencies can be implemented in the design of the receiving antennas. To simultaneously harvest RF power from many RF sources, a wide bandwidth is preferred. The following formula relates the antenna's bandwidth to its Q-factor:

$$Q = \frac{F_r}{BW} \quad (2 - 6)$$

where:

Q = The quality factor of the antenna.

BW = The bandwidth of the antenna.

Fr = The resonant frequency of the antenna in [hertz].

A high Q-factor antenna leads to a narrower bandwidth. When antenna size is reduced, the unloaded Q-factor decreases and the antenna's bandwidth widens. Furthermore, the Bode-Fano criterion [31] demonstrates that only a limited number of frequencies might end up in desirable impedance matching, and a wider bandwidth can be obtained at the expense of a higher reflection coefficient. In general, wideband antennas have bigger dimensions than narrowband antennas. Given the limitations of antenna performance, designing an ultra-wideband antenna will be highly inefficient. On the other hand, it is difficult to build multiband antennas with stable radiation patterns, polarization, and efficiency throughout a large frequency range.

6- Efficiency and Size of The Antenna

The shape, size, material, frequency, and impedance of the antenna all impact its efficiency. Efficiency drops when the antenna's physical size decreases as well [37]. In RFEH, a trade-off between size and antenna efficiency is anticipated. The relationship between radiated power and radiation efficiency (η) is calculated using this formula ($\eta = P_{rad} / P_{in}$), where (P_{in}) refers to the input power in watt and (P_{rad}) refers to the radiated power in watt.

7- Sensitivity

Rectifying antennas (Rectennas) have several design limitations, one of them is that they are unable to capture low power in ambient environments. Therefore, in order to increase the sensitivity of the rectenna and enable operation in ultra-low-power circumstances, the losses from the matching network, rectification device, and dielectric substrate should be kept to a minimum [38].

2.4 RFEH Antenna Technologies

The efficiency of the RFEH system is directly impacted by the performance of the antenna, which is the front-end part of every RF power-receiving equipment. As a result, choosing the right antenna and designing it properly require careful consideration. Critical operating circumstances for RFEH antennas include ultra-low power density, varying incident power levels, and randomly changing incoming waves with different polarizations. Different antenna types will be discussed in this section.

The development of modern, smaller-scale electronic devices encouraged antenna engineers to construct small antennas as a low-profile option for RFEH. Patch antennas are one of the most practical antenna types due to their small size, low weight, and low cost of manufacture; therefore, they are very suitable for wireless devices. Using fractal geometry in the patch antenna structure is one of the most widely utilized methods in small antennas for RFEH applications [17], [39]-[43]. One possible way to create a small rectenna is to incorporate fractal geometry into the antenna structure because of the self-similarity feature. In a fractal structure, the effective length increases as the iteration order is raised. Furthermore, fractal geometry may be restricted to a small number of iteration orders. The complexity of the

design geometry rises with the number of iterations, which makes fabrication more challenging. Making slots on a patch is another common method of miniaturizing antennas [20], [39], [44]. Fractal geometry can be generated through the implementation of the iterative function system (IFS) algorithm.

This is a useful technique for creating fractal structures through various transformation methods, such as translation, scaling, and rotation. The goal of miniaturizing antennas is to squeeze a large radiating component into a small one by making efficient use of the available space.

There are several reduction techniques for miniaturizing antennas, including meander-line, fractal geometry, ground plane engineering, and use of capacitive or reactive loading [45]. The meandering technique has potential uses in implantable devices and UHF [46]. However, as the close radiating arms tend to cancel each other out in the far field, meander-line antennas cannot be expected to provide significant gain. Fractal antennas can be effectively employed for miniaturization and multiband operation. Different fractal antenna geometries were illustrated in [47], including Sierpinski carpet, Sierpinski gasket, Koch curve, Hilbert curve, snowflake, and Minkowski fractal. The narrow bandwidth characteristics and complex geometry are some of the limitations of fractal antennas. Table 2-2 demonstrates the major advantages and disadvantages of various antenna design techniques [3].

Table 2-2 Overview of the major advantages and disadvantages of various antenna design techniques

Antenna design technique	Advantages	Disadvantages
Meander-line antenna	Decrease in antenna dimension by incorporating meandering microstrip line including of 90-degree twists, straightforward structure, Capability for low UHF.	High gain is not possible, and radiation efficiency is low.
Fractal Antenna	A smaller area is required than with antennas based on Euclidean geometry; it can produce radiation patterns and input impedance similar to big antennas; and because of its space-filling geometry, it uses volume more efficiently.	Miniaturization reduces radiation efficiency, which can result in difficult manufacturing and design procedures, numerical design constraints.
Antenna with Defected Ground Structure (DGS)	Increased slow wave factor allows for smaller design, Decreased in size.	Hard to fabricate and design, Unwanted coupling could be produced by embedded slots, unintentional radiation could cause directivity to decrease, only suitable for planer antennas.

When multiple radio frequency sources operate at different frequency bands, simultaneous power reception from those bands can be beneficial. Furthermore, the sources could have different power budgets and be positioned randomly away from the receiving antenna [33]. In ambient conditions, the available radio frequencies have low power levels, usually between -5 and -30 dBm [12]. In these situations, multiband antennas help improve RFEH. Furthermore, the non-linear fluctuation in rectifier input impedance with input power level, frequency, and load impedance makes multiband antenna/rectenna for RFEH challenging to implement. The multiband antenna's input power is the sum of its input power at each of its supported frequency bands [32]; this can be illustrated with equation (2–7).

$$P_T = \sum_{i=1}^n P_{fi} \quad (2 - 7)$$

Where:

P_T = The total available power due to multiband operation in [watt].

P_{fi} = The power received at i'th frequency in [watt].

n = The number of supported operating frequencies by multiband antenna.

2.5 Antenna Types

Antennas exist in a wide variety, each with distinctive characteristics and applications. The following are some of the most popular types of antennas:

- 1- Dipole Antenna: is the simplest and most widely used type of antenna. A dipole antenna is a type of RF (radio frequency) antenna that is made up of two conductive components, such as rods or wires. It is also referred to as a doublet or dipole aerial. Figure 2.3 illustrates the dipole antenna. The length of the conductive wires (L) is represented by about half of the maximal wavelength in free space at the operating frequency [48].

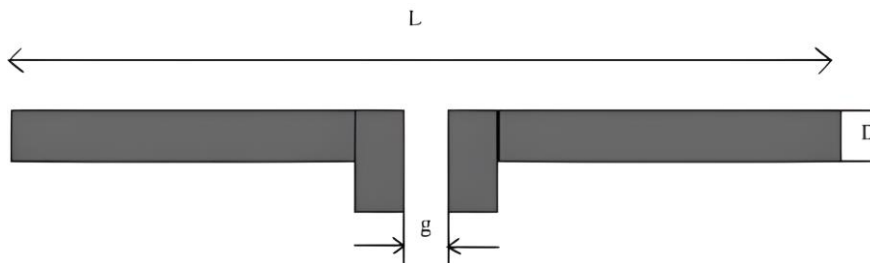


Figure 2.3 Dipole Antenna.

2- Patch Antenna: a low-profile radio antenna utilized indoors in single-floor buildings, houses, and offices. It is made up of two metallic plates stacked on top of one another and put on a small, flat, rectangular, or circular surface. With a dielectric layer in the middle, one plate is referred to as the ground plane, and it is larger than the other. A microstrip, flat panel, or panel antenna are other names for a patch antenna. Figure 2.4 shows illustrate a rectangular patch antenna [49].

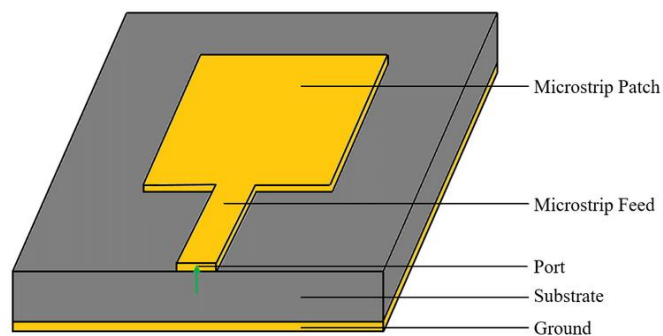


Figure 2.4 Rectangular Patch Antenna.

3- Yagi Antenna: is a directional antenna made up of a driving element, either a dipole or folded dipole, and extra parasitic elements, usually a reflector and one or more directors. It is most frequently utilized in point-to-point communications and employed for communications between two places across a three-to-five-mile medium range and radiates in a single direction. Figure 2.5 illustrates a Yagi antenna [50].

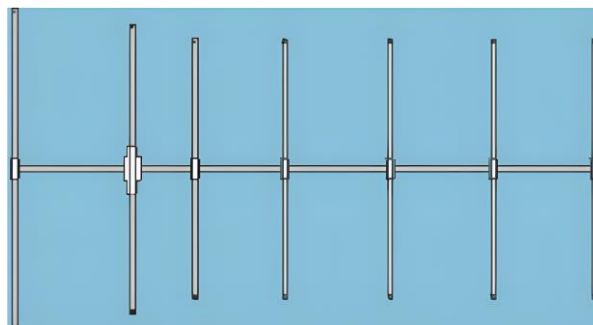


Figure 2.5 Yagi Antenna.

4- Parabolic Dish Antenna: is a high-gain point-to-point antenna and is employed in a variety of applications, including wireless WAN/LAN links for data transmission, satellite communications, spacecraft communication, satellite television, radio astronomy, and radar. It has a parabolic reflector to direct the radio waves, which is a curved surface with a parabola-shaped cross-section. The most popular name is known as a dish antenna. Figure 2.6 shows an example of a parabolic dish antenna [51].



Figure 2.6 Parabolic Dish Antenna.

5- Horn Antenna: is a directional antenna made of a flaring metal waveguide known as a microwave horn, usually utilized at UHF and microwave frequencies above 300 MHz. They are employed as standard calibration antennas to evaluate the gain of other antennas; their broad bandwidth, low losses, high directivity, and ease of construction and adjustment are some of their advantages. Figure 2.7 shows an example of a horn antenna [37].



Figure 2.7 Horn Antenna.

6- Helical Antenna: is a directional antenna with a broadband characteristic. It is made of a helix-shaped conducting wire looped around itself, with a feedline connecting with the helix's bottom and the ground plane. Typically, helical antennas are positioned above a ground plane. The helical antenna is used for satellite communication due to its high directivity and circular polarization of the transmitted electromagnetic waves. Figure 2.8 illustrates of a helical antenna [48].

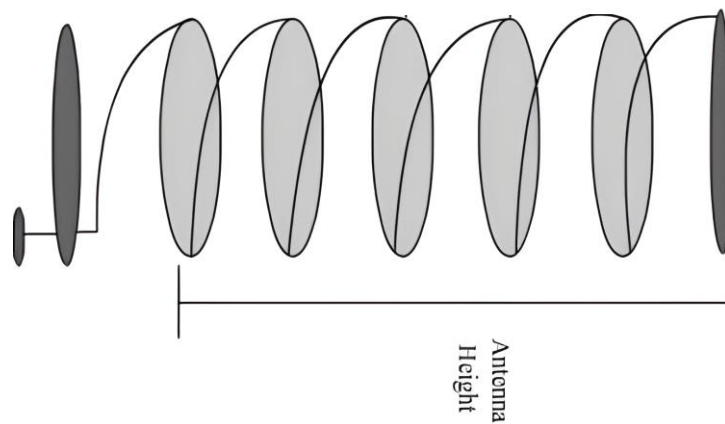


Figure 2.8 Helical Antenna.

Chapter Three

Design, Simulation, and Implementation of Multiband Antennas for Radio Frequency Energy Harvesting Applications

3.1 Introduction

This chapter is focused on multiband antennas since they are preferred antennas for RFEH systems. The receiving antenna is the most crucial component of the RFEH systems since it determines the amount of radio frequency ambient energy that can be collected by the RFEH system, which is converted to a useful DC voltage by special rectification circuits. Three multiband antennas are introduced in this chapter to target the most required frequencies for RFEH systems, including WLAN-2.4G, WLAN-5G, WLAN-6G, Mobile DCS1700, Mobile LTE, Mobile 5G and WIMAX services.

The first proposed antenna (Antenna-1) is a drone-shaped fractal antenna with a defected ground structure (DGS). The second antenna (Antenna-2) is a microstrip patch antenna with multi-Fins. The third antenna (Antenna-3) is a modified hexagonal slot antenna with a defected ground structure (DGS). All three multiband antennas in this chapter are simulated using the CST Studio Suite software, then fabricated using PCB technology on FR-4 substrate due to its light weight, low cost, and low profile, with a dielectric constant $\epsilon_r = 4.3$, a thickness of 1.6 mm, and a loss tangent (δ) of 0.025.

3.2 Drone Shaped Fractal Antenna with Defected Ground Structure for RFEH Applications

A proposed multiband drone shaped fractal antenna (Antenna-1) is introduced in this section that targets the most required frequencies used for radio frequency energy harvesting applications, including WLAN-2.4G, WLAN-5G, WLAN-6G, Mobile DCS1700, Mobile LTE, Mobile 5G, and WIMAX services. A novel fractal shape is designed and combined with a standard square geometrical shape in order to implement the front patch of the antenna. The antenna is simulated with CST Studio Suite software and fabricated on FR-4 substrate due to its light weight, low cost, and low profile, with a dielectric constant $\epsilon_r = 4.3$, a thickness of 1.6 mm, and a loss tangent (δ) of 0.025. Different antenna stages with parametric study, and optimization were implemented to get the best performance from the drone shape fractal antenna.

3.2.1 Design Fractal Shape 1

The design of a novel fractal shape starts with an initiator line with a length of (L), as shown in Figure 3.1 (a). The first iteration translates the initiator line into eight equal lines with a length of ($L/8$) for each of them to form the shape shown in Figure 3.1 (b). The next steps are to expand the shape of the first iteration by two operations; the first is to mirror it on the y-axis, as shown in Figure 3.1 (c). Then mirror it on the x-axis to form the shape shown in Figure 3.1 (d). The final shape is shown in Figure 3.1 (e).

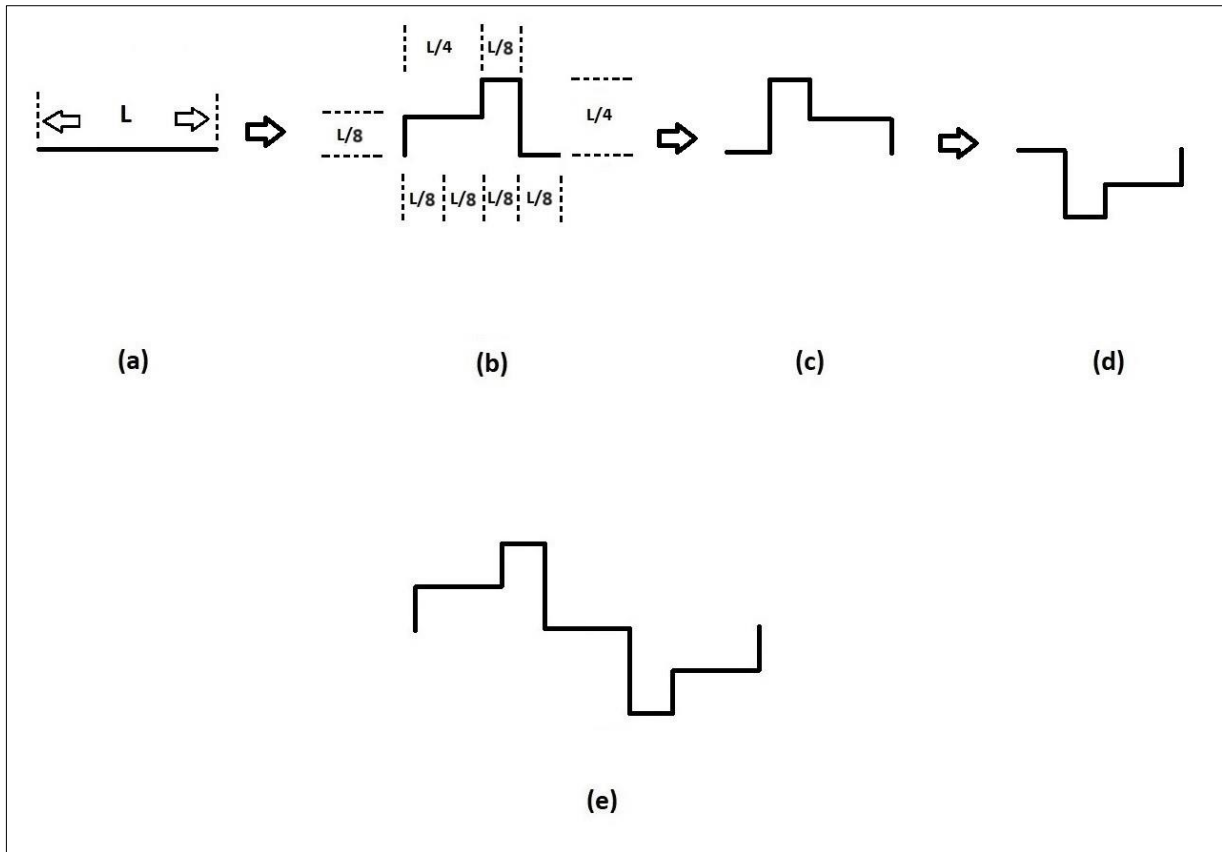


Figure 3.1 Fractal shape design 1: (a) The initiator line; (b) The first iteration; (c) mirror shape (b) on y-axis; (d) mirror shape (c) on x-axis; (e) The final shape design.

3.2.2 The Design of the First Proposed Multiband Antenna (Antenna-1)

Multiband antennas can be constructed by combining the novel fractal shape with one of the different geometrical shapes, like triangle, square, pentagonal, hexagonal, etc. [47], [52], as shown in Figure 3.2. The first stage of the proposed drone-shaped antenna is implemented first by modifying the standard square patch sides in Figure 3.3 (a) with the novel fractal shape that was designed previously in Figure 3.1 (e). This will create the modified square patch shown in Figure 3.3 (b), and this patch will be the cornerstone for implementing the proposed drone-shaped multiband antenna.

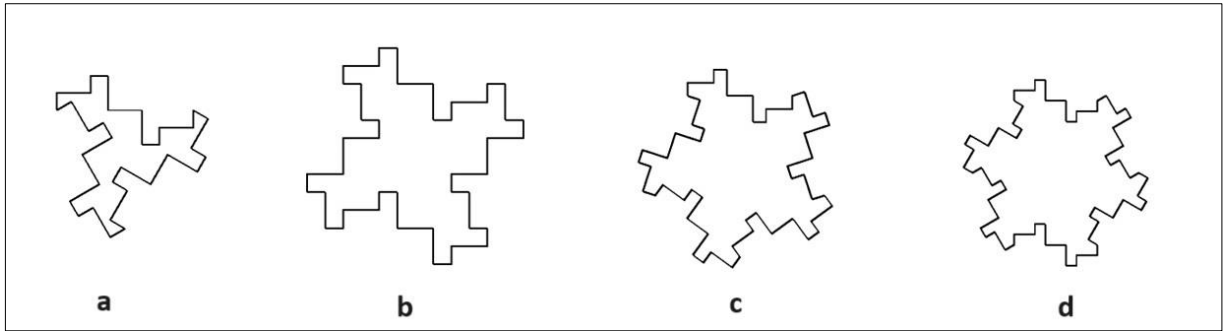


Figure 3.2 Combine the novel fractal shape with different geometrical shapes.

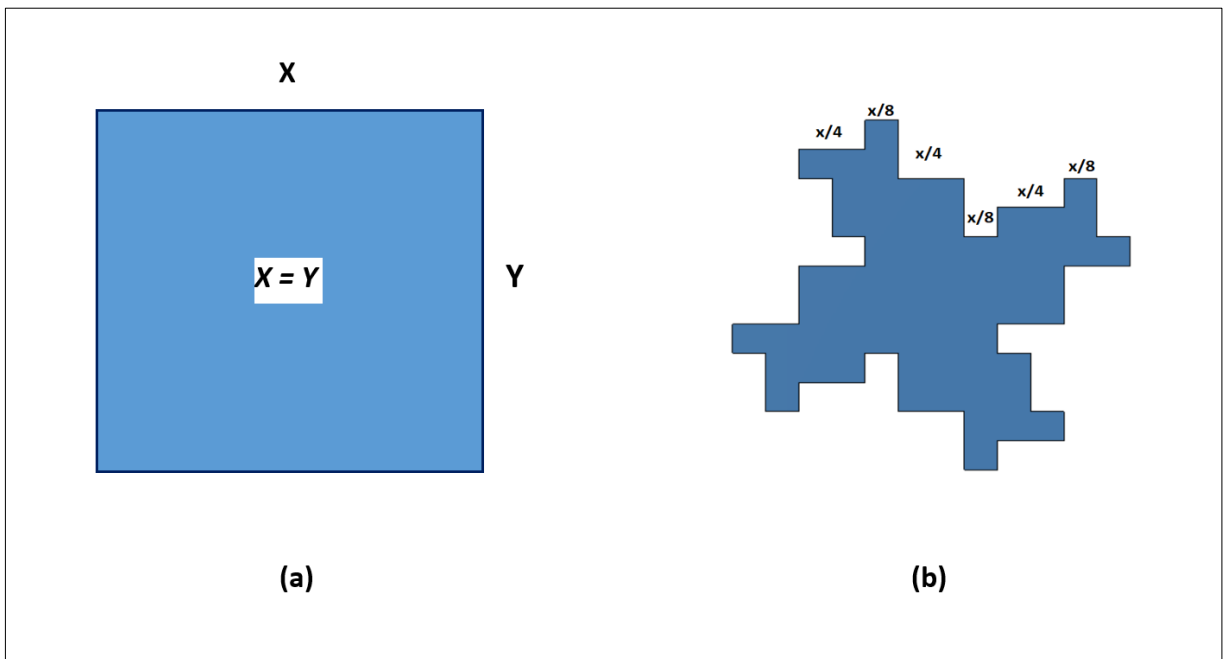


Figure 3.3 Antenna construction; (a) standard square patch; (b) modified square patch.

The total length (L_t) for each side of the modified square patch can be calculated with equation (3-1).

$$L_t = (x/4) + (x/8) + (x/8) + (x/4) + (x/4) + (x/4) + (x/8) + (x/8) + (x/4) + (x/8) + (x/8) = 2x. \quad (3-1)$$

The perimeter of the modified square patch = $4 * 2x = 8x$

Since ($X=Y$) the perimeter of the standard square patch = $4x$

The perimeter ratio between the modified square patch and the standard square patch = $8x / 4x = 2$.

It's clear from the previous calculations that the electrical length for each side of the standard square patch will be doubled by a factor of 2 after the modifications. This is the main advantage of the fractal antenna, which creates longer electrical lengths, increases the perimeter length of the geometrical shape, and also generates more frequencies by using different electrical lengths that correspond to the wavelength (λ) for each operating frequency [47]. Perfect Electrical Conductor (PEC) material is selected for creating the front patch and the back ground plane with [0.035 mm] of thickness.

The first stage of the proposed antenna (Antenna-1-a) is constructed from the modified square patch that is shown in Figure 3.3 (b). Whereas the second stage of antenna (Antenna-1-b) is implemented by copying and scaling down the modified square patch of the first stage using a scale factor of $S = 0.5$, then putting four of the scaled-down modified square patches at each corner of the modified patch at stage 1.

The third stage was implemented by copying and scaling down the modified square patch of the first stage using a scale factor of $S = 0.25$, then putting three of them at each corner of the modified square patches that were created on the second stage. This will create the third stage of antenna (Antenna-1-c) design, as shown in Figure 3.4. Full ground substrate and feeding line width of [1 mm] are implemented in the beginning of designing Antenna-1; later, at the advanced design stage, a Defected Ground Substrate (DGS) with slots cuts in the front patch is implemented in order to get optimal results from Antenna-1. Figure 3.5 shows the two different substrate ground types that are implemented on Antenna-1. The dimensions for each stage of Antenna-1 are shown in Figure 3.6.

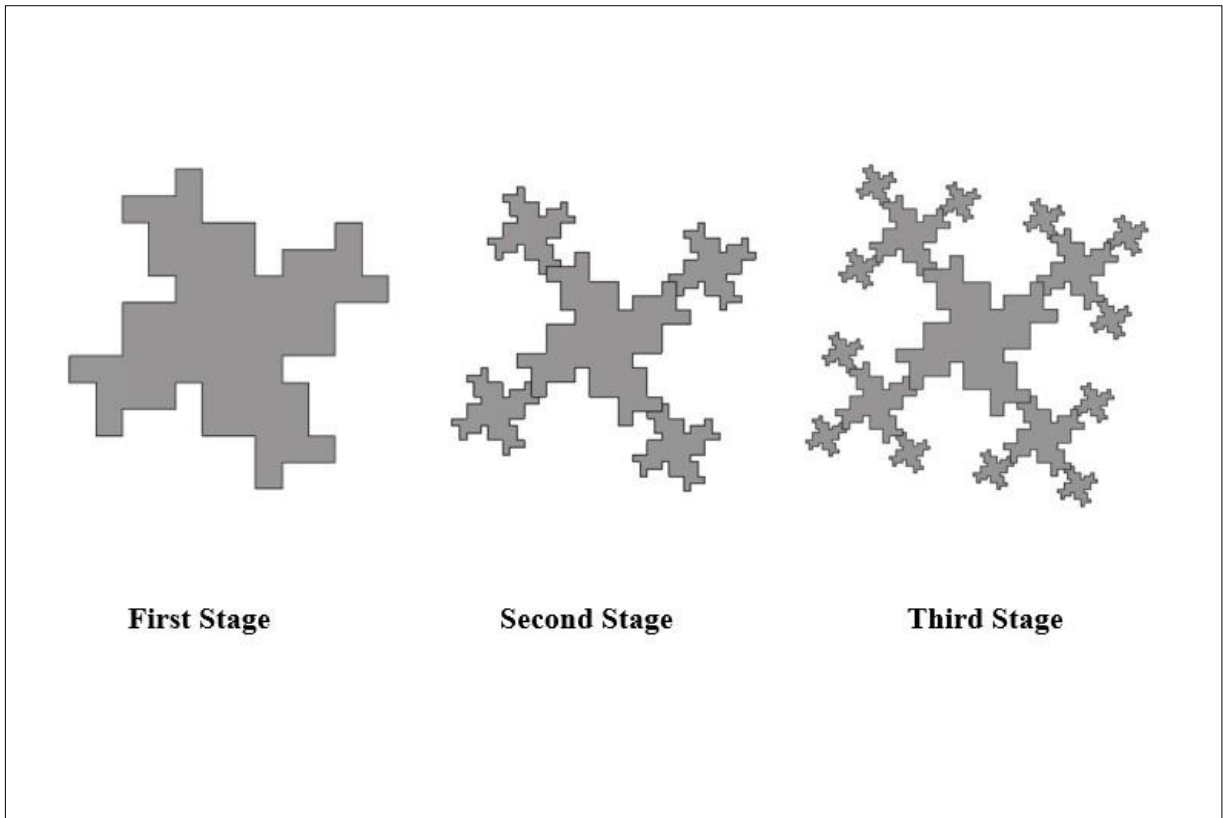


Figure 3.4 Construction stages of the proposed Antenna-1

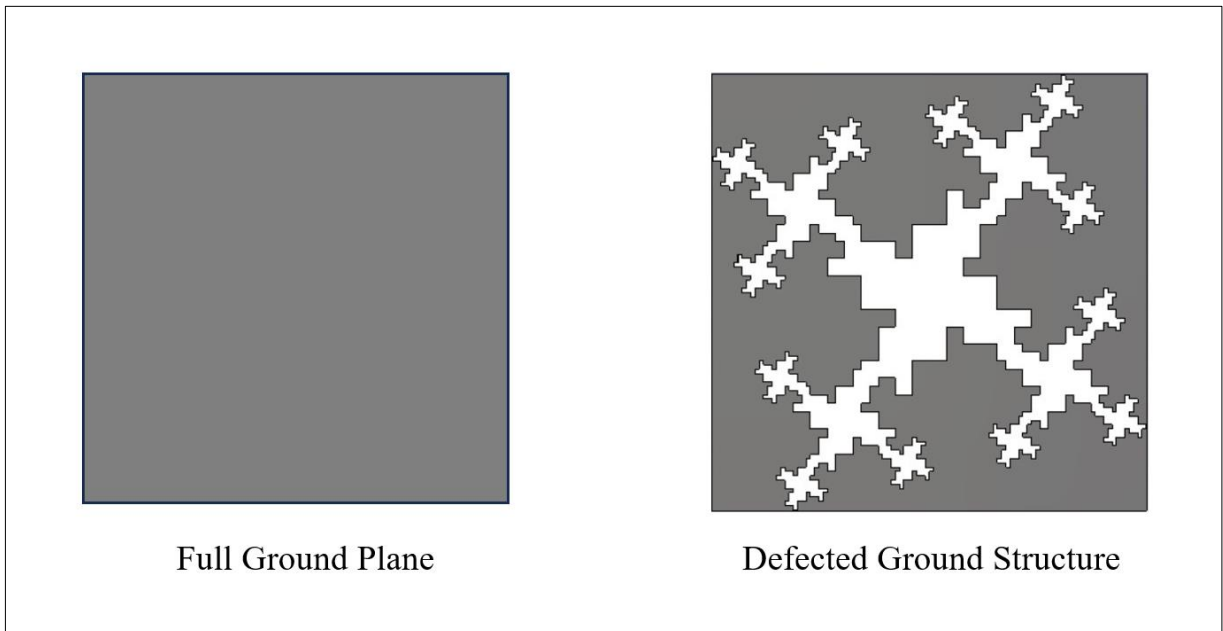


Figure 3.5 Two substrate ground types of the proposed Antenna-1

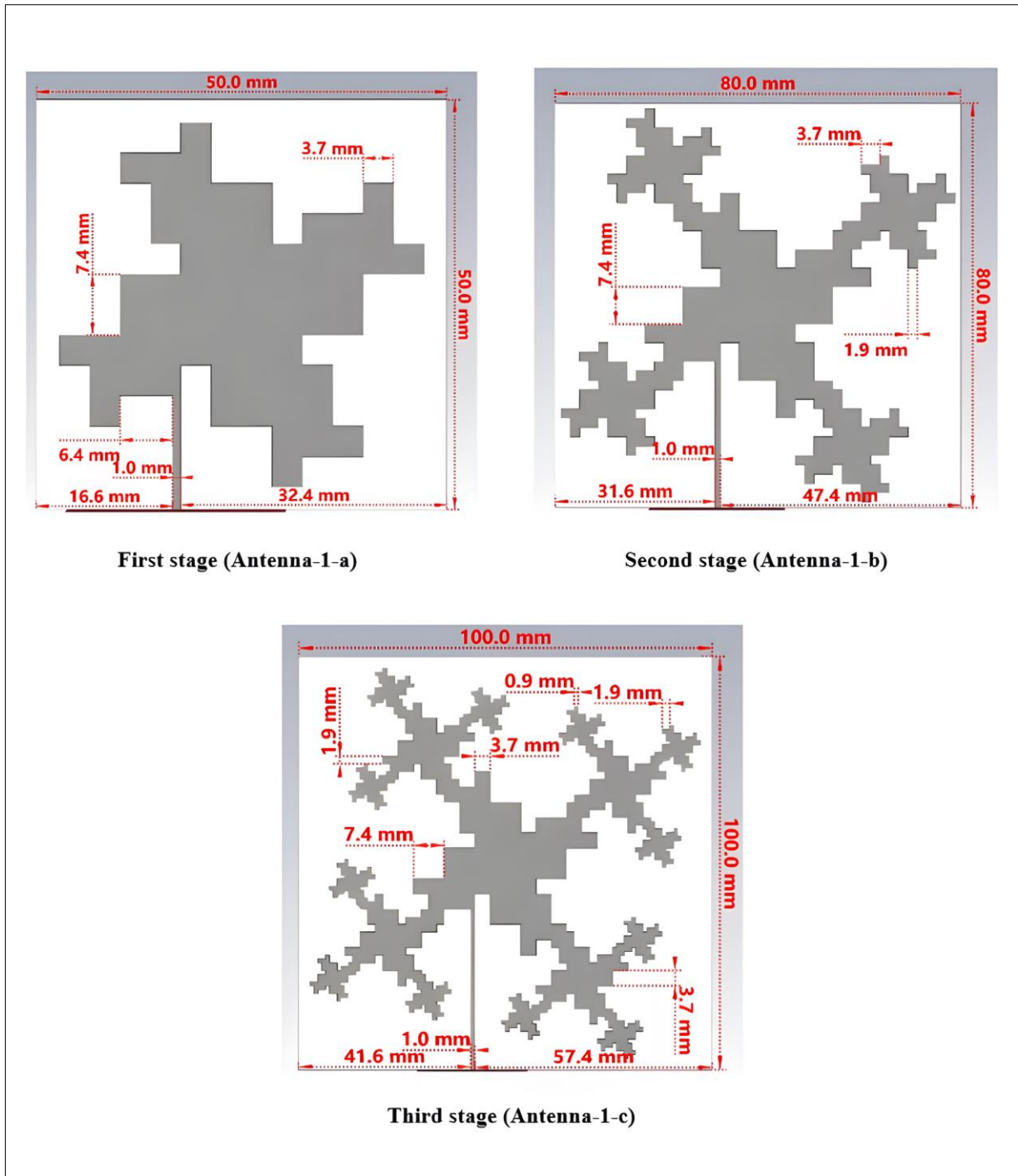


Figure 3.6 The dimensions for each stage of the drone-shaped antenna

3.2.3 Impact of the number of stages on Antenna-1

For multiband antennas, the reflection coefficient $|S_{11}|$ is the main antenna parameter that shows the antenna characteristics and performance at each

frequency. Figure 3.7 shows the simulated results of the reflection coefficient $|S_{11}|$ for each implemented stage of Antenna-1.

The simulated results of the reflection coefficient $|S_{11}|$ showed that the first stage (Antenna-1-a) is resonating at four frequencies (6.7 GHz, 5.86 GHz, 2.1 GHz, and 1.8 GHz). The second stage (Antenna-1-b) resonates at two frequencies (6.4 GHz and 2.6 GHz), and the third stage (Antenna-1-c) resonates at four frequencies (6.7 GHz, 5.8 GHz, 2.4 GHz, and 1.1 GHz). The third stage has been selected and studied since it showed the best results that meet the needs for RF energy harvesting applications since it supports the frequencies of interest (2.4 GHz and 5.8 GHz) that are utilized by WLAN services. As shown in Table 3-1.

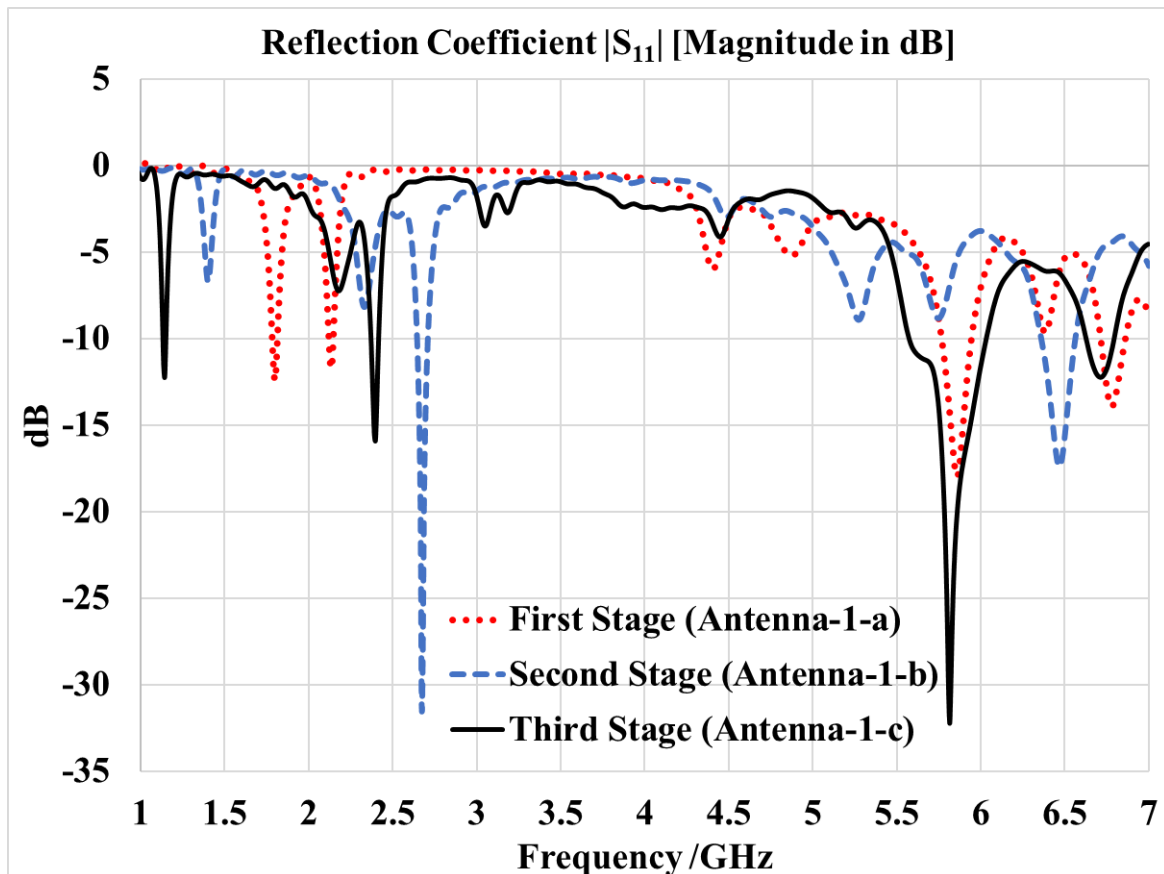


Figure 3.7 The simulated results of the reflection coefficient $|S_{11}|$ for each stage of the drone shaped antenna.

Table 3-1 The simulated results of reflection coefficient $|S_{11}|$ magnitude in [dB] for each stage of the drone shaped antenna

Antenna stage	Resonating frequencies	Simulated results of the reflection coefficient $ S_{11} $ [dB]
First Stage (Antenna-1-a)	(6.7 GHz), (5.86 GHz), (2.1 GHz), (1.8 GHz)	(-13.95 dB), (-17.99 dB), (-11.74 dB), (-12.44 dB)
Second Stage (Antenna-1-b)	(6.4 GHz), (2.6 GHz)	(-17.44 dB), (-31.34 dB)
Third Stage (Antenna-1-c)	(6.7 GHz), (5.8 GHz), (2.4 GHz), (1.1 GHz)	(-12.22 dB), (-32.23 dB), (-15.92 dB), (-12.21 dB)

3.2.4 Parametric analysis for the proposed selected (Antenna-1-c)

As mentioned previously, (Antenna-1-c) will be carefully studied in this section.

A. Impact of scale-up on (Antenna 1-c)

The scaling process on the antenna (Antenna-1-c) has a major impact on its performance since the dimension of the patch antenna will be changed, resulting in a change in the electrical length of the radiator (Front Metal Patch) that corresponds to the wavelengths of the signal (λ) that are inversely proportional to the operating frequency and will result in shifting the resonating frequencies left or right of the frequency spectrum that depend on scaling up or down the antenna. Figure 3.8 shows the effect of scaling up (Antenna-1-c) on the reflection coefficient $|S_{11}|$ for different scale up factors

(1.2), (1.5), and (1.7). It's clear from Figure 3.8 that when the scale of the (Antenna-1-c) increases, all the frequencies will be shifted to the left of the frequency spectrum, and the value of the reflection coefficient $|S_{11}|$ for each frequency will increase. This will cause the lower frequencies to vanish.

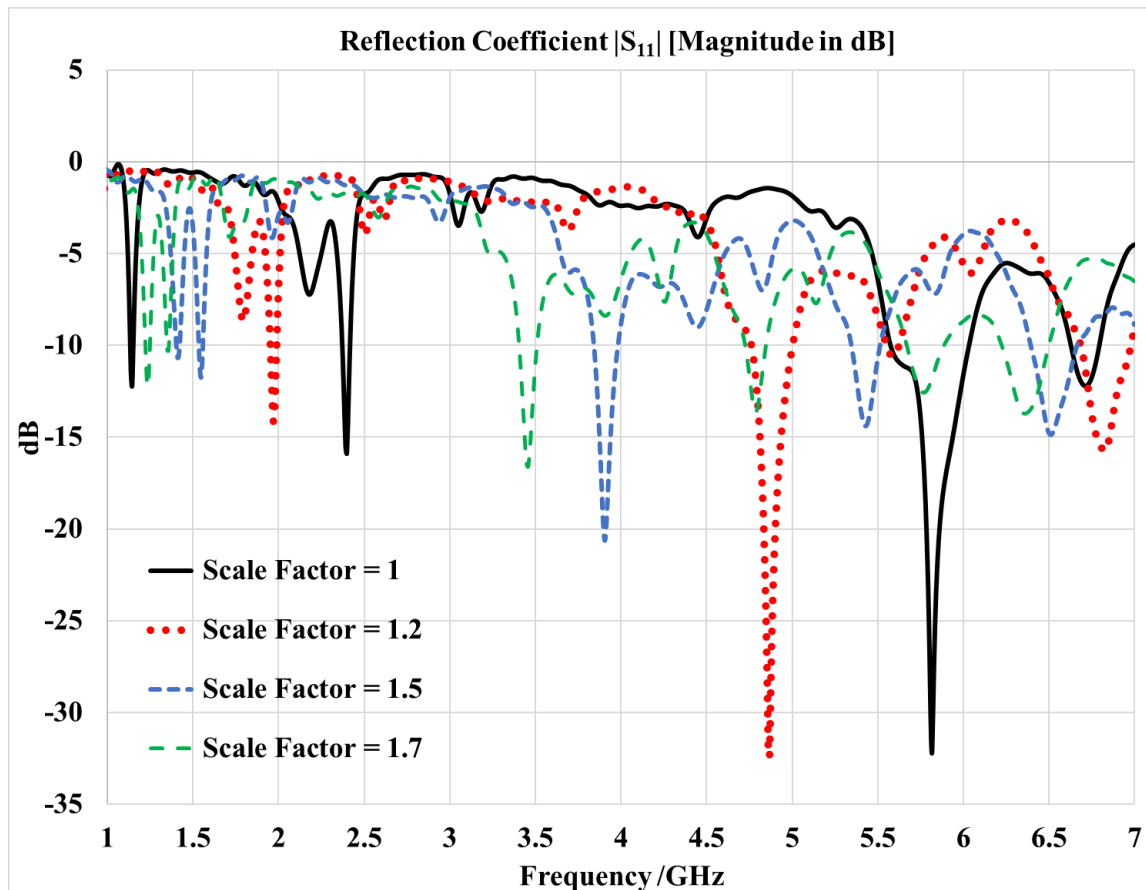


Figure 3.8 The simulated results of the reflection coefficient $|S_{11}|$ for different scale up factors of (Antenna-1-c).

B. Impact of scale-down on (Antenna 1-c)

Figure 3.9 shows the reflection coefficient $|S_{11}|$ simulated results for different scale-down factors (0.8), (0.6), and (0.3) applied to (Antenna-1-c). It's clear from Figure 3.9 that when the scale of the (Antenna-1-c) decreases,

all the frequencies will be shifted to the right of the frequency spectrum. Also, the simulated results show the frequencies (2.4 GHz) and (1.1 GHz) shifted to the right of the frequency spectrum, and the frequencies (6.7 GHz) and (5.8 GHz) disappeared since the frequency spectrum range studied is from (1 GHz to 7 GHz). Also, the magnitude of the reflection coefficient $|S_{11}|$ decreased for the scale factors (0.8) and (0.5) for the frequencies (2.4 GHz) and (1.1 GHz). The simulated results confirmed that the resonating frequencies are dependent on the electrical lengths of the (Antenna-1-c) radiator patch, which directly impacts the wavelength (λ) for each operating frequency.

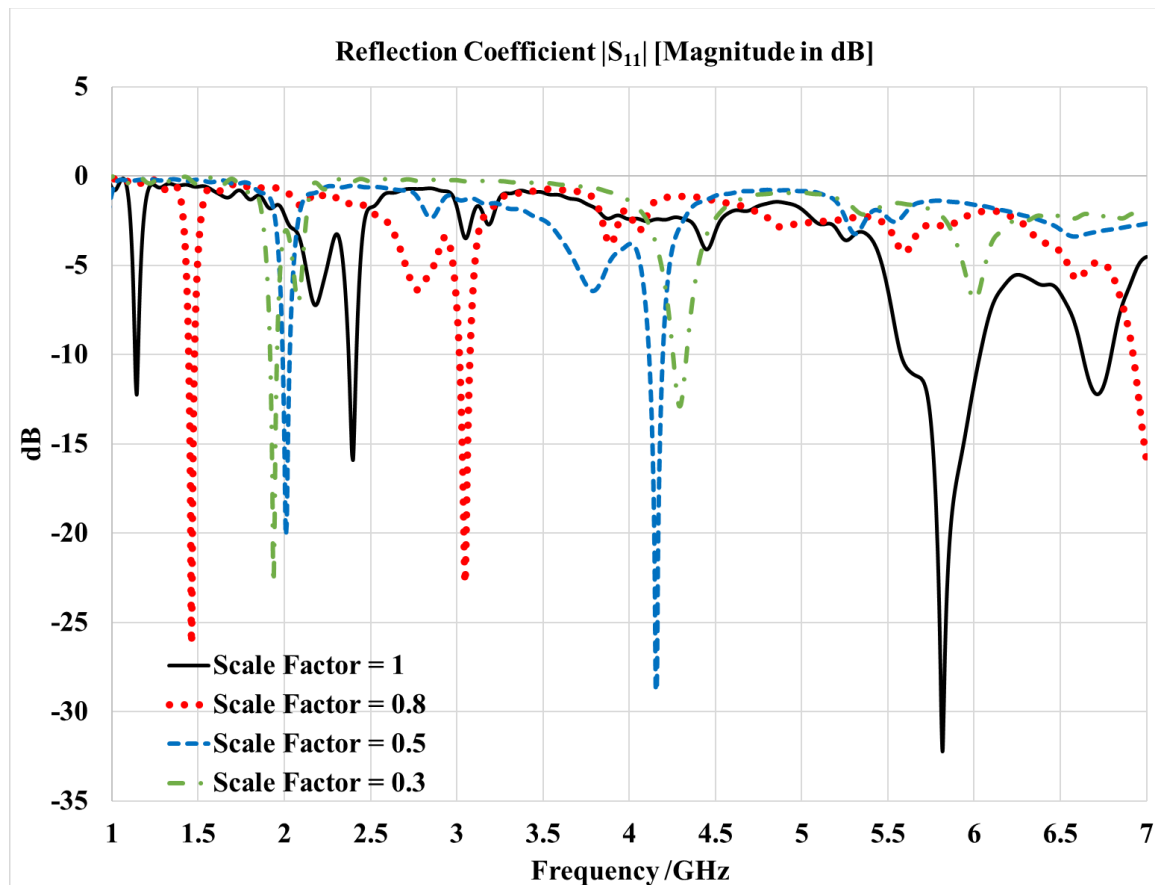


Figure 3.9 The simulated results of the reflection coefficient $|S_{11}|$ for different scale down factors of (Antenna-1-c).

C. Impact of changing the ground plane length for (Antenna 1-c)

A lot of research was made to study the effects of changing the dimensions or shape of the ground plane of the microstrip patch antenna. It's confirmed that there is an impact on the performance of the antenna bandwidth, radiation pattern, gain, and shifting the resonating frequency [53]. Figure 3.10 shows the simulated results for the reflection coefficient $|S_{11}|$ after changing the ground plane length for (Antenna 1-c) for the values [25 mm, 50 mm, 75 mm, 100 mm] and keeping the ground plane width constant at [100 mm]. The best and optimal simulated results from Figure 3.10 are obtained by keeping the ground plane length for (Antenna 1-c) at 100 mm i.e. (full ground plane).

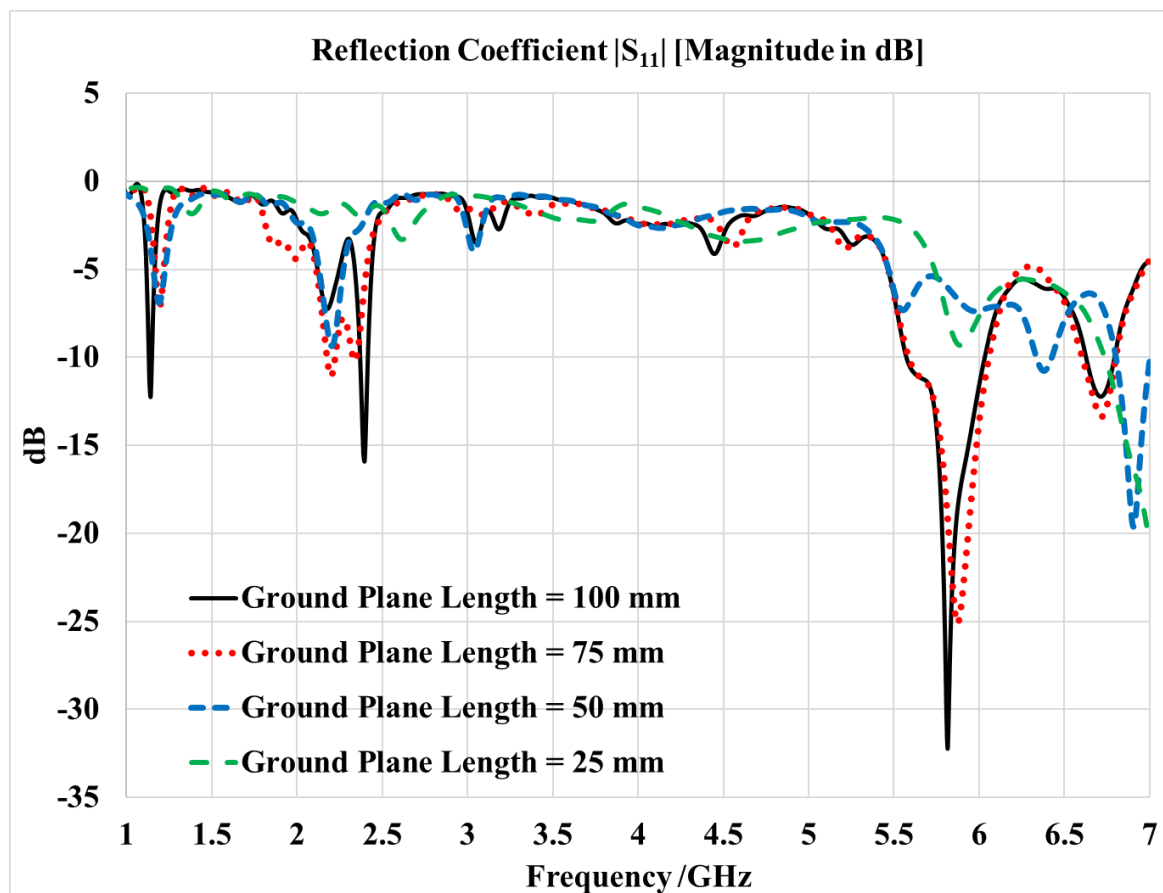


Figure 3.10 The simulated results of the reflection coefficient $|S_{11}|$ for different ground plane lengths of (Antenna-1-c).

D. Impact of changing the ground plane width for (Antenna 1-c)

Figure 3.11 shows the simulated results for the reflection coefficient $|S_{11}|$ after changing the ground plane width for (Antenna 1-c) for the values [25 mm, 50 mm, 75 mm, 100 mm] while keeping the ground plane length constant at [100 mm]. The simulated results showed a major impact on the reflection coefficient $|S_{11}|$ when changing the ground plane width from [100 mm] to [75 mm]. This will generate a new frequency band from (2.13 GHz to 2.32) with a reflection coefficient $|S_{11}|$ magnitude of [-39.6 dB], and the reflection coefficient $|S_{11}|$ magnitude increased for the frequency bands (5.8 GHz), (2.4 GHz), and (1.1 GHz). Also, the simulated results showed that changing the ground plane width from [100 mm] to [50 mm] will shift the frequency band (2.4 GHz) to the left and the frequency band (5.8 GHz) to the right of the frequency spectrum.

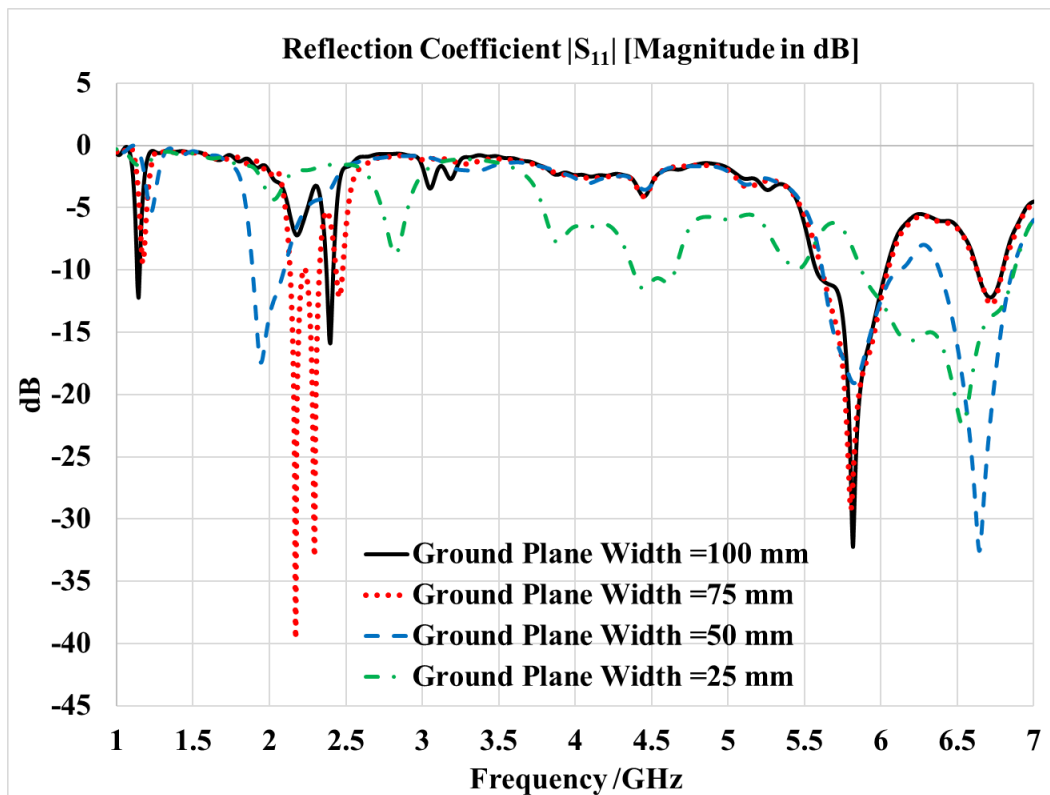


Figure 3.11 The simulated results of the reflection coefficient $|S_{11}|$ for different ground plane widths of (Antenna-1-c).

E. Impact of changing feeding line width for (Antenna 1-c)

Different feeding inset width values [1 mm, 2 mm, 3 mm, 4 mm] for (Antenna-1-c) were applied and simulated. Figure 3.12 shows the simulated results for the reflection coefficient $|S_{11}|$. The simulated results show that increasing the feeding line width for (Antenna-1-c) will increase the magnitude of the reflection coefficient $|S_{11}|$ for some frequencies while decreasing it for others without any frequency shifting. Also, the frequency band (6.7 GHz) was disappeared. This is the major impact of increasing the feeding line width, since it's directly affecting the matching impedance of the antenna.

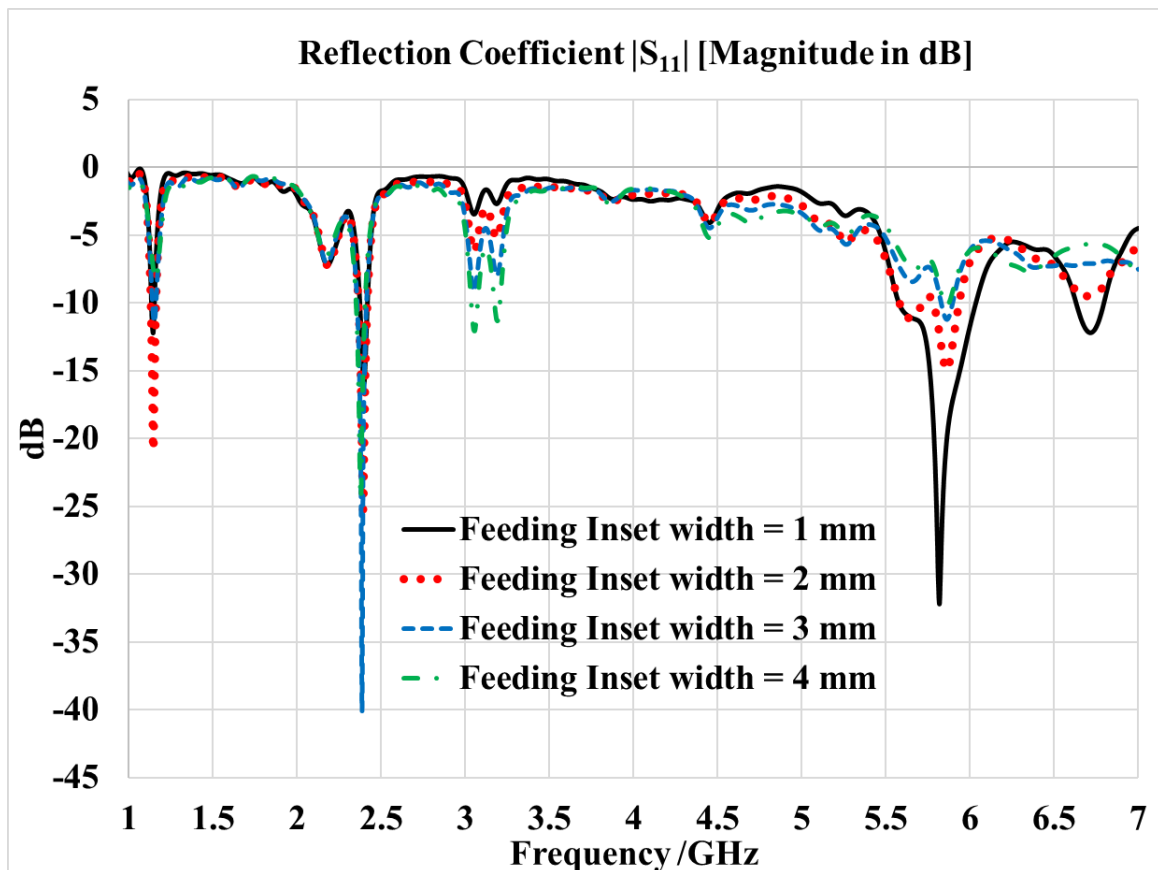


Figure 3.12 The simulated results of reflection coefficient $|S_{11}|$ for different feeding inset widths of (Antenna-1-c).

3.2.5 (Antenna-1-c) Optimization

To get the optimum results and make the (Antenna-1-c) support more resonating frequencies, new modifications were introduced, a slot cuts were applied to the front patch (Radiator) of (Antenna-1-c), and defected ground structure (DGS) was applied to the antenna ground plane [53]. Firstly, the slots were implemented by scaling down the modified square patches that were previously created on different antenna stages shown in Figure 3.4 with a scale factor of $S = 0.25$, then subtracting them from the center of all modified square patches for each stage to implement the new optimized antenna (Antenna-1-d) that is shown in Figure 3.13. Also, the new defected ground structure is implemented by scaling up the front patch with a scale factor of $S = 1.1$, then subtracting the front patch (Radiator) from the full square ground plane on the back of the substrate to create the new defected ground structure shown in Figure 3.13. Also, the feeding inset shifted by [0.82 mm] to the left, as shown in the dimensions of the optimized antenna (Antenna 1-d) in Figure 3.14.

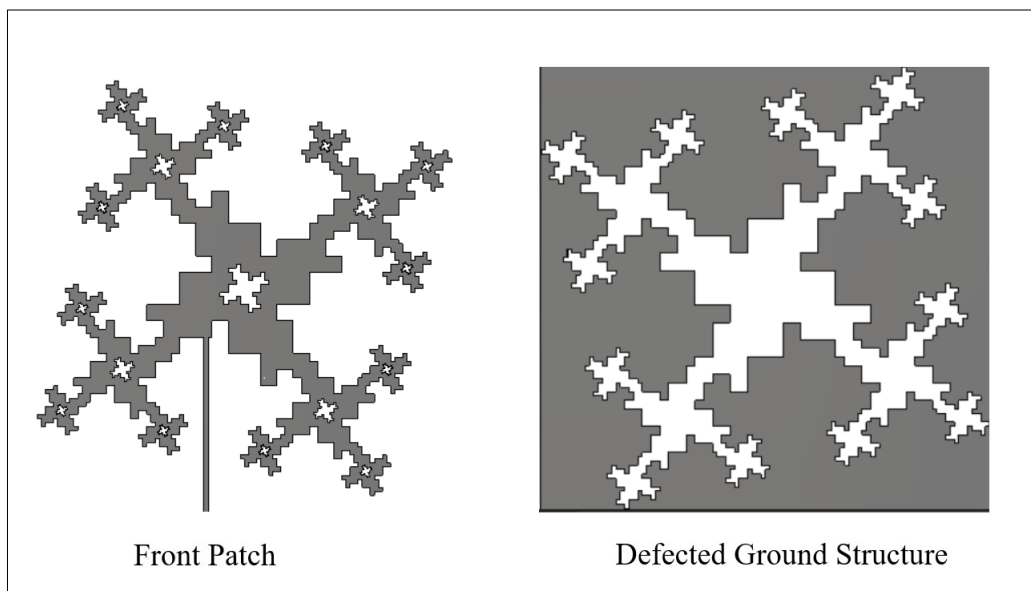


Figure 3.13 The front patch with slot cut and the defected ground structure of the proposed (Antenna-1-d).

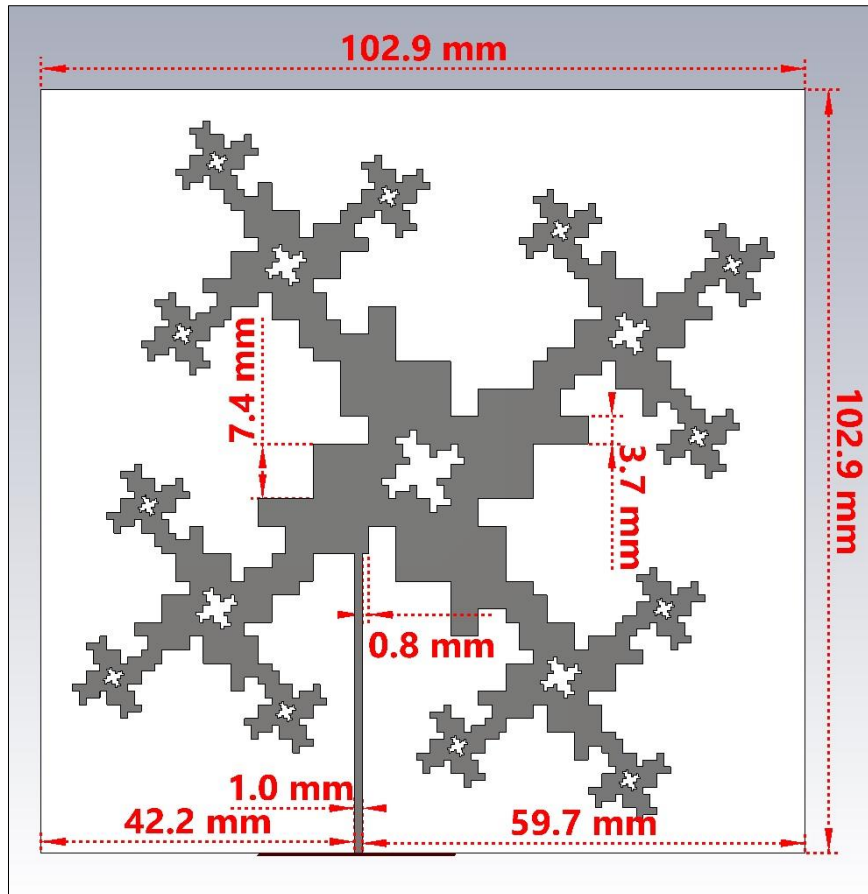


Figure 3.14 The Dimensions for the optimized (Antenna-1-d).

3.2.6 Comparison between (Antenna-1-d) and (Antenna-1-c)

The simulated results of the reflection coefficient $|S_{11}|$ for the optimized (Antenna-1-d) show major performance improvements compared to the results of (Antenna-1-c) as shown in Figure 3.15, More resonating frequencies appeared in the frequency spectrum (3.789 GHz, 3.36 GHz, and 1.7155 GHz), and the bandwidth increased significantly for the resonating frequencies (2.4 GHz) and (5.7 GHz). Table 3-2 shows more details for the optimized (Antenna-1-d) bandwidth, gain, and directivity in [dBi], as well as the wireless RF applications for each resonating frequency supported by optimized (Antenna-1-d).

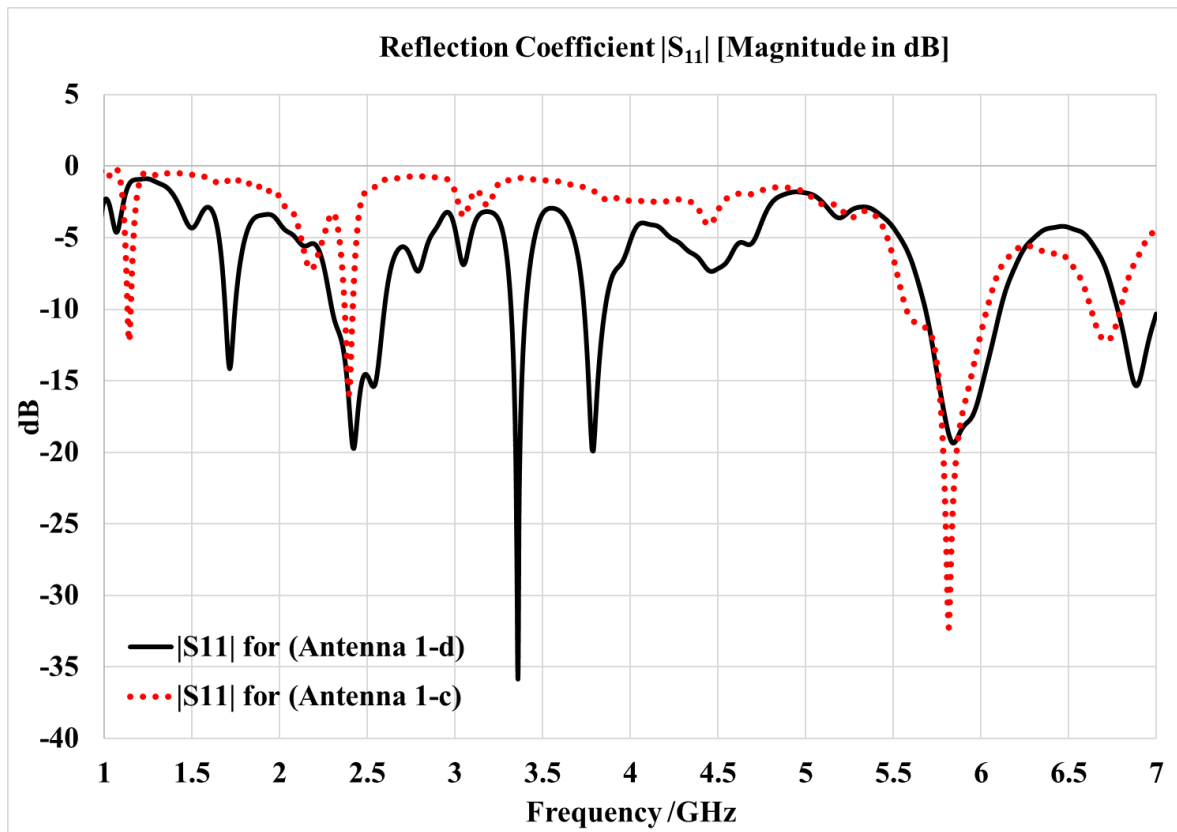


Figure 3.15 The simulated results of the reflection coefficient $|S_{11}|$ for the optimized (Antenna-1-d) and (Antenna-1-c).

Table 3-2 Simulated results for the final design of the proposed drone shaped antenna (Antenna-1-d) after optimization.

Resonating Frequency (GHz)	Return Loss (S_{11}) (dB)	Minimum Frequency (GHz)	Maximum Frequency (GHz)	Band width (GHz)	Directivity (dBi)	Peak Gain (dBi)	Applications	Reference
1.7155	-14.15	1.6901	1.7463	0.056216	4.603	2.785 dBi @ 1.7458 GHz	Mobile DCS 1700, Mobile LTE, Mobile 5G	[54], [55]
2.424	-19.73	2.299	2.5978	0.29883	5.196	2.83 dBi @ 2.45 GHz	WLAN, WIMAX, Mobile LTE	[54], [55]
3.36	-35.83	3.3206	3.4036	0.083023	5.504	-0.79 dBi @ 3.36 GHz	WIMAX, Mobile LTE, Mobile 5G	[54], [55]
3.789	-19.9	3.7373	3.8561	0.11883	4.017	-1 dBi @ 3.856 GHz	WIMAX, Mobile LTE, Mobile 5G	[54], [55]
5.843	-19.36	5.6835	6.1116	0.4281	6.404	2.51 dBi @ 5.8512 GHz	WLAN, WIMAX, Mobile LTE, Mobile 5G	[54], [55]
6.886	-15.33	6.7797	7.007	0.2273	6.895	2.165 dBi @ 6.886 GHz	WLAN, Mobile LTE, Mobile 5G	[54], [55]

Figure 3.16 shows the simulated 3D radiation pattern of the directivity magnitude in [dBi] for some of the (Antenna-1-d) supported frequencies. Also, Figure 3.17 shows the simulated 2D radiation pattern.

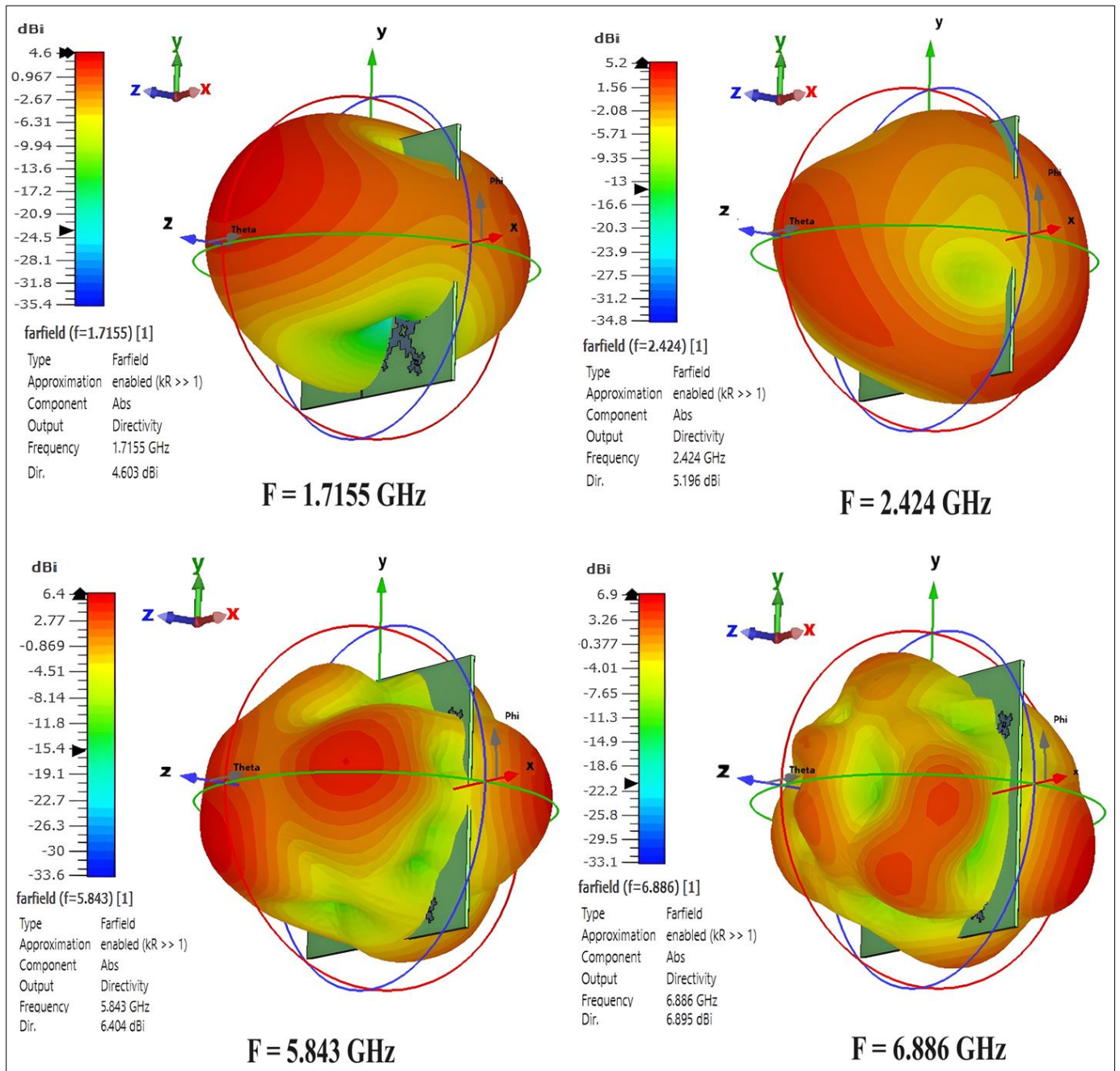


Figure 3.16 Simulated 3D radiation pattern of the directivity magnitude in [dBi] for some of (Antenna-1-d) supported frequencies.

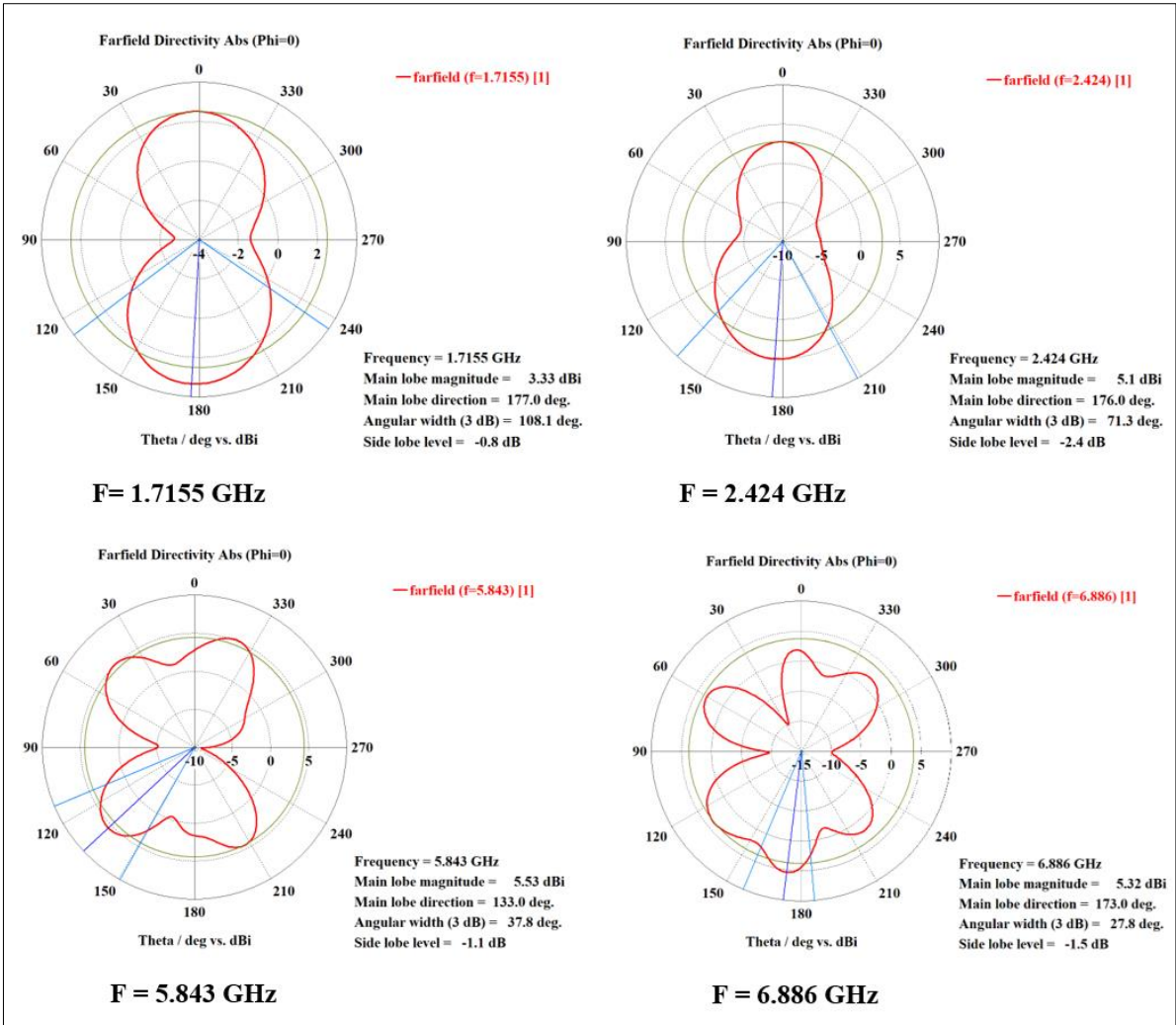


Figure 3.17 Simulated 2D radiation pattern of the directivity magnitude in [dBi] for some of (Antenna-1-d) supported frequencies.

Furthermore, the results showed that the proposed antenna has performance improvements compared to other proposed works, since the proposed optimized antenna achieved a good gain for most of its operating frequencies with respect to its size and thickness, given that it has a much smaller substrate area than [13], [14], [16] and is much thinner than [8], [14], [16], and [17], and, also supports more resonating frequencies required for RFEH applications. It should be mentioned as well that the FR-4 substrate is less expensive than the (Rogers RT6002), (Arlon 25N), and (Rogers 3003) substrates, and the gain of any antenna is directly proportional to its physical size and thickness.

3.3 Microstrip Multiband Patch Antenna Based on a Half-Wave Dipole Antenna for RFEH Applications

3.3.1 A Brief Review of the Half-Wave Dipole Antenna

The conventional half-wave dipole antenna consists of a linear conductive element usually formed from a thin wire and has a total length of $L = \lambda/2$ of the target frequency of operation, where (λ) is the wave length of the signal. This antenna is typically fed by means of a voltage signal applied across a gap that is introduced halfway along its length.

This gap will split the antenna into two poles, and alternating opposite electrical charges will exist at the ends of these two poles, so when the left end is positively charged, the right end is negatively charged, as shown in Figure 3.18 . Then 180 degrees later in the cycle, the right end is positively charged and the left end is negatively charged. This is where the antenna gets the name dipole, meaning "two poles" because of the two electrical charge concentrations existing at either end of the conductor [48].

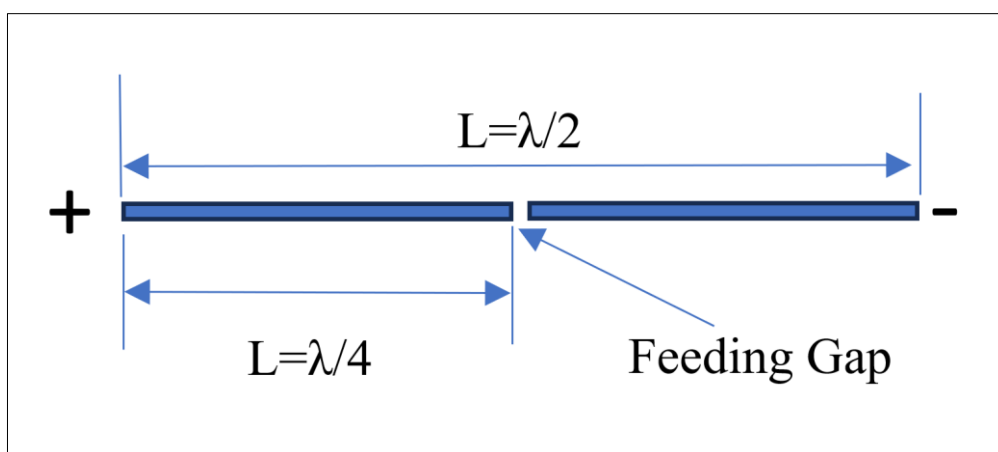


Figure 3.18 Illustration of a conventional half-wave dipole antenna.

3.3.2 Design and Construction of the Second Proposed Multiband Antenna (Antenna-2)

The microstrip patch antenna is constructed based on the concepts of the half-wave dipole antenna. Since the frequency is inversely proportional to the wavelength of the signal, The first step in designing the proposed multiband antenna (Antenna-2) was to select three different operating frequencies (0.5 GHz, 0.9 GHz, and 1.8 GHz). Those are the lower ranges of frequencies that may meet the needs for RFEH applications. The (1.8 GHz) frequency is utilized by mobile LTE and mobile DCS services; the (0.9 GHz) frequency is utilized by mobile LTE and mobile GSM; and the (0.5 GHz) frequency is utilized by WiMAX and TV/Radio Broadcasting services.

These three frequencies were selected to approximately calculate the maximum lengths of the fins that are required for constructing the proposed antenna (Antenna-2). Later on, in the advanced design stages, the proposed antenna-2 will be copied and scaled down by a specific scale factor, then cascaded to implement the optimization stages of the proposed antenna (Antenna-2). The scale-down process will shorten the length of each of the fins, which may correspond to the quarter wavelength ($\lambda/4$) and result in higher resonating frequencies. Figure 3.19 illustrates the basic design of the proposed multiband (Antenna-2).

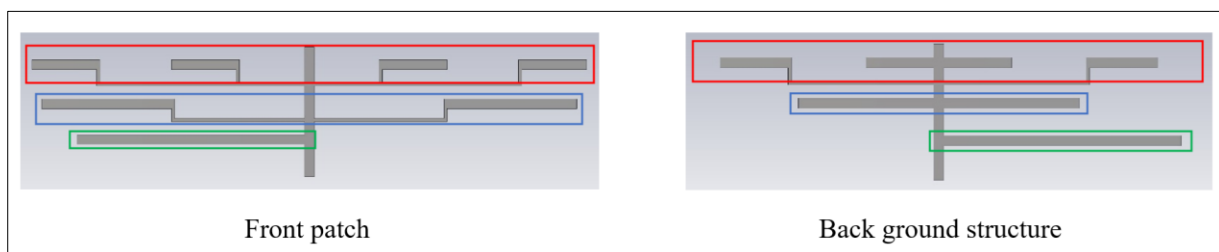


Figure 3.19 The basic design of the proposed antenna (Antenna-2); the upper fins highlighted by red; the middle fins highlighted by blue; the lower fins highlighted by green.

Since the proposed antenna (Antenna-2) is designed to be constructed using PCB technology on FR-4 substrate with a dielectric constant [$\epsilon_r = 4.3$], equation (3-2) is used to approximately calculate the values for the maximum lengths of the (Antenna-2) fins [56]. By putting numbers on equation (3-2), the operating frequency (0.5 GHz) results in a wavelength (λ) equal to [289 mm] and the quarter wavelength ($\lambda/4$) equal to [72 mm]. Further, the operating frequency (0.9 GHz) results in a wavelength (λ) equal to [160 mm] and the quarter wavelength ($\lambda/4$) equal to [40 mm], and the operating frequency (1.8 GHz) results in a wavelength (λ) equal to [80 mm] and the quarter wavelength ($\lambda/4$) equal to [20 mm].

$$\lambda = \frac{C}{\sqrt{\epsilon_r} F} \quad (3 - 2)$$

Were

C = The speed of the light. [meter / second]

λ = The wavelength of the operating frequency. [meter]

F = The operating frequency. [hertz]

ϵ_r = Dielectric constant.

Antenna-2 is constructed based on the concepts of half-wave dipole antennas. The front patch of the proposed antenna (Antenna-2) is implemented by creating a total of seven (7) fins that are connected with a single vertical microstrip feed line centered on the front patch. The microstrip feed line dimensions were [40 mm] of length, [3 mm] of width, and [0.035] of thickness, respectively. The antenna's lower fins, middle fins, and upper fins were distributed along each side of the vertical microstrip feed line by

using four (4) thin horizontal feeding inset lines having the same width of [1 mm] and different lengths, as shown in Figure 3.20, All of the seven (7) fins have the same widths of [3 mm] and lengths of [70 mm] for the single lower fin, [40 mm] for the two middle fins, and [20 mm] for the four upper fins, respectively.

The back ground structure also has a total of seven (7) fins, and it is constructed similarly to the front patch instead of using only two horizontal feeding lines for the two outer upper fins since the other two upper fins, the two middle fins, and the one lower fin were directly connected to the centered vertical microstrip feed line of the back ground structure. The widths of all the fins are equal to [3 mm]. The width of the vertical microstrip feed line is the same for the front patch and the back ground structure, which is equal to [3 mm], as shown in Figure 3.20.

The lengths of the antenna lower fins, middle fins, and upper fins should approximately correspond to the quarter wavelength ($\lambda/4$) of the three operating frequencies as shown in Figure 3.18; therefore, from the previous calculation, three different lengths for the proposed antenna 2 were selected: [70mm] length for the lower fins, [40mm] length for the middle fins, and [20mm] length for the upper fins. Figure 3.20 shows the dimensions of the proposed antenna 2.

3.3.3 Simulated Results for the Proposed Antenna-2

The reflection coefficient $|S_{11}|$ is the main antenna parameter that shows the antenna characteristics and performance for each operating frequency. Figure 3.21 shows the simulated results of the reflection coefficient $|S_{11}|$ for the proposed antenna (Antenna-2). The results show ten (10) resonating frequencies: (0.747 GHz), (1.300 GHz), (1.910 GHz), (2.027 GHz), (2.287 GHz), (3.022 GHz), (3.46 GHz), (3.789 GHz), (5.771 GHz), and (6.623 GHz).

As mentioned previously, equation (3-2) was used only to approximately select reasonable lengths for the lower fins, middle fins, and upper fins. The (0.9 GHz) frequency appeared in the frequency spectrum with a reflection coefficient $|S_{11}|$ of [-8.8 dB], so it will be neglected since it has not reached [-10 dB] in order to be considered a valid operating frequency. For the (1.8 GHz) frequency shifted to (1.9 GHz) and for the (0.5 GHz) frequency shifted to (0.7 GHz), Table 3-3 shows all the resonating frequencies for the proposed antenna (Antenna-2). Most of the resonating frequencies that appear in the frequency spectrum are very important for RFEH applications.

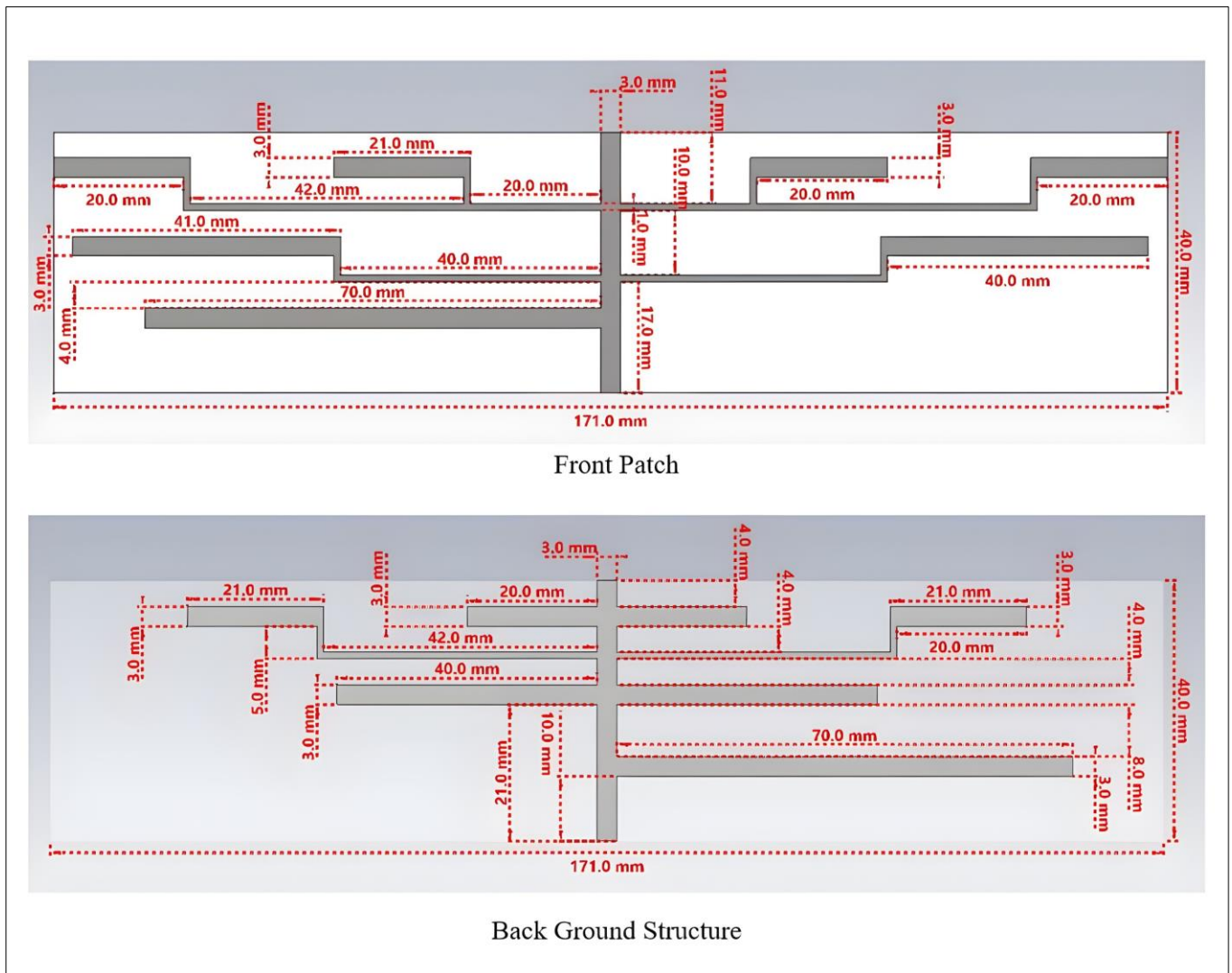


Figure 3.20 The dimensions of the proposed Antenna-2.

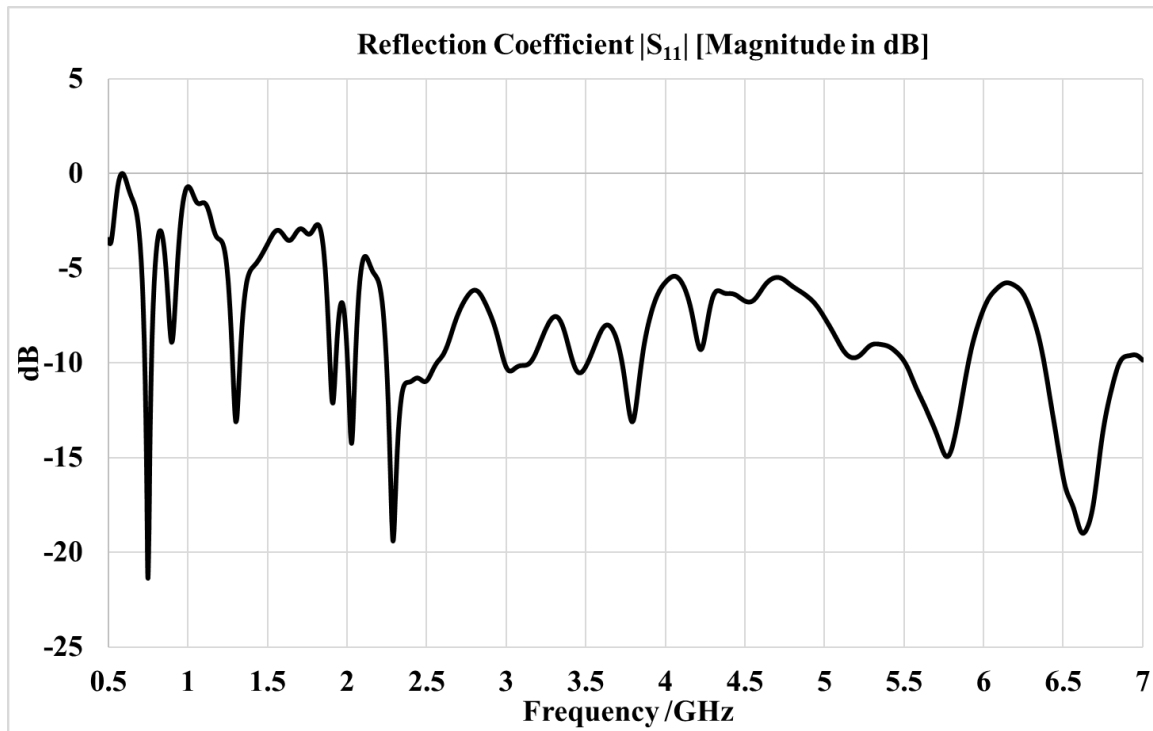


Figure 3.21 The simulated results of the reflection coefficient $|S_{11}|$ for the proposed Antenna-2.

Table 3-3 Simulated results of the proposed Antenna-2

Resonating Frequency [GHz]	Minimum Frequency [GHz]	Maximum Frequency [GHz]	Bandwidth [GHz]	Reflection Coefficient $ S_{11} $ [dB]
0.747	0.728	0.770	0.042	-21.30
1.300	1.279	1.325	0.046	-13.10
1.910	1.891	1.927	0.036	-12.14
2.027	2.002	2.050	0.048	-14.23
2.287	2.246	2.562	0.316	-19.38
3.022	2.988	3.146	0.158	-10.42
3.46	3.420	3.510	0.090	-10.52
3.789	3.727	3.848	0.121	-13.09
5.771	5.506	5.903	0.397	-14.94
6.623	6.379	6.852	0.473	-19.00

3.3.4 Parametric analysis for the proposed (Antenna-2)

A. Impact of Using a Full Back Ground Plane Instead of a Back Ground Structure.

Figure 3.22 shows the simulated results of the reflection coefficient $|S_{11}|$ for the proposed antenna (Antenna-2) when applying a full back ground plane instead of the back ground structure. The simulated results show a significant decrease in the frequency bandwidth using the full ground plane compared to the back ground structure. New frequencies (6.96 GHz), (6.135 GHz), and (1.6 GHz) appeared on the frequency spectrum while many others disappeared. So, the background structure is more suitable for (Antenna-2).

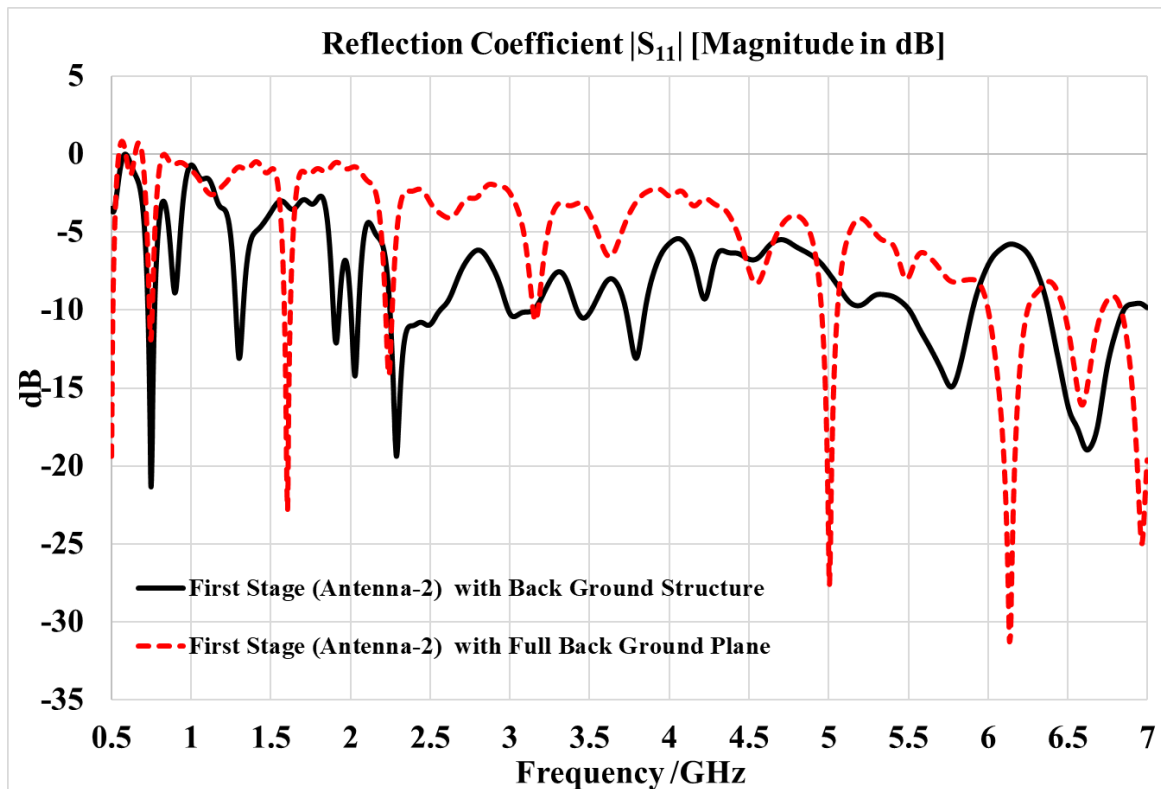


Figure 3.22 The simulated results of the reflection coefficient $|S_{11}|$ for the proposed (Antenna-2) compare the full back ground plane with the back ground structure.

B. Impact of Increasing the Length of the Lower Fins

Figure 3.23 shows the simulated results of the reflection coefficient $|S_{11}|$ when increasing the length of the Antenna-2 lower fins. The simulated results show that when increasing the length of the lower fins from [70 mm] to [75 mm], the frequency (5.771 GHz) shifted left to be (5.55 GHz), the frequency (3.789 GHz) shifted left to be (3.45 GHz), and the frequency (2.287 GHz) shifted left to be (2.22 GHz) on the frequency spectrum. Furthermore, increasing the length of the lower fins from [70 mm] to [80 mm] results in the frequency (5.771 GHz) shifted left to be (5.22 GHz), the frequency (3.789 GHz) shifted left to be (3.49 GHz), and the frequency (2.287 GHz) vanished. The decrease in the resonating frequencies was expected since the frequency is inversely proportional to the wavelength of the signal (λ).

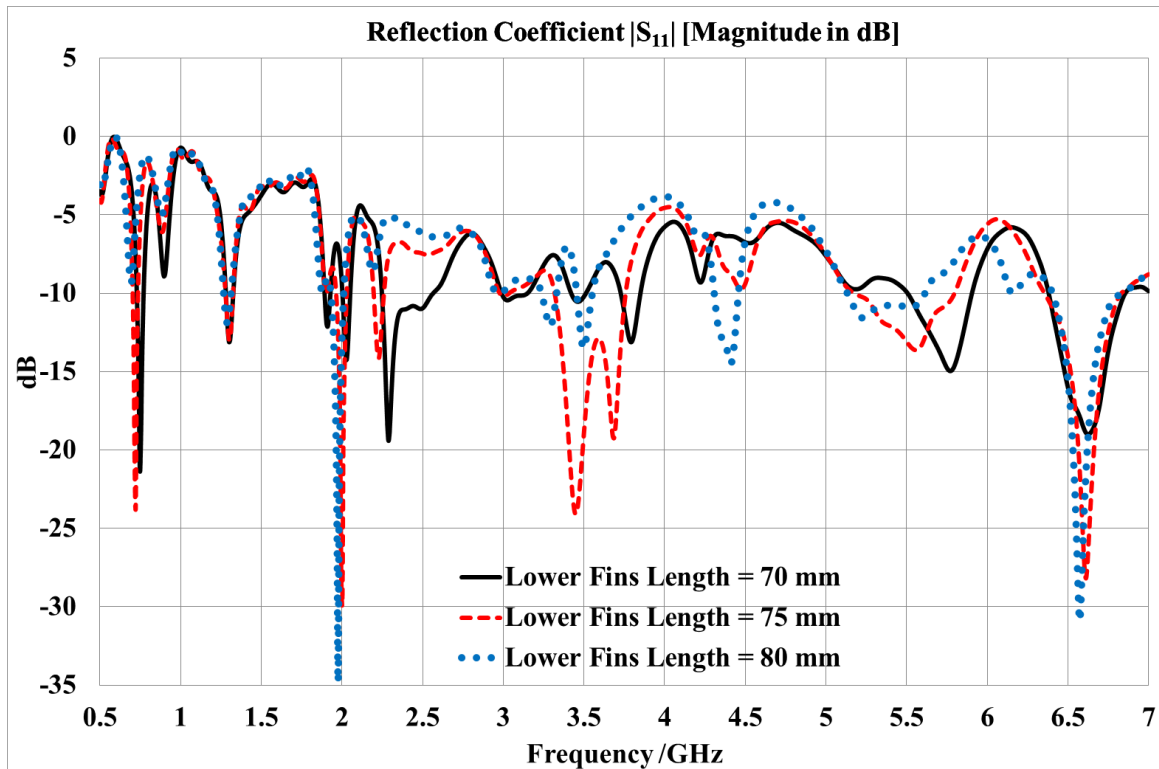


Figure 3.23 The simulated results of the reflection coefficient $|S_{11}|$ for the proposed (Antenna-2) when increasing the length of the lower fins.

C. Impact of Decreasing the Length of the Lower Fins

Figure 3.24 shows the simulated results of the reflection coefficient $|S_{11}|$ when decreasing the length of the Antenna-2 lower fins. The simulated results show that when decreasing the length of the lower fins from [70 mm] to [65 mm], the frequency (0.747 GHz) shifted right to be (0.9095 GHz), the frequency (2.287 GHz) shifted right to be (2.5402), and the frequency (5.771 GHz) shifted right to be (5.9665 GHz) on the frequency spectrum. The increase in the resonating frequencies was expected since the frequency is inversely proportional to the wavelength of the signal.

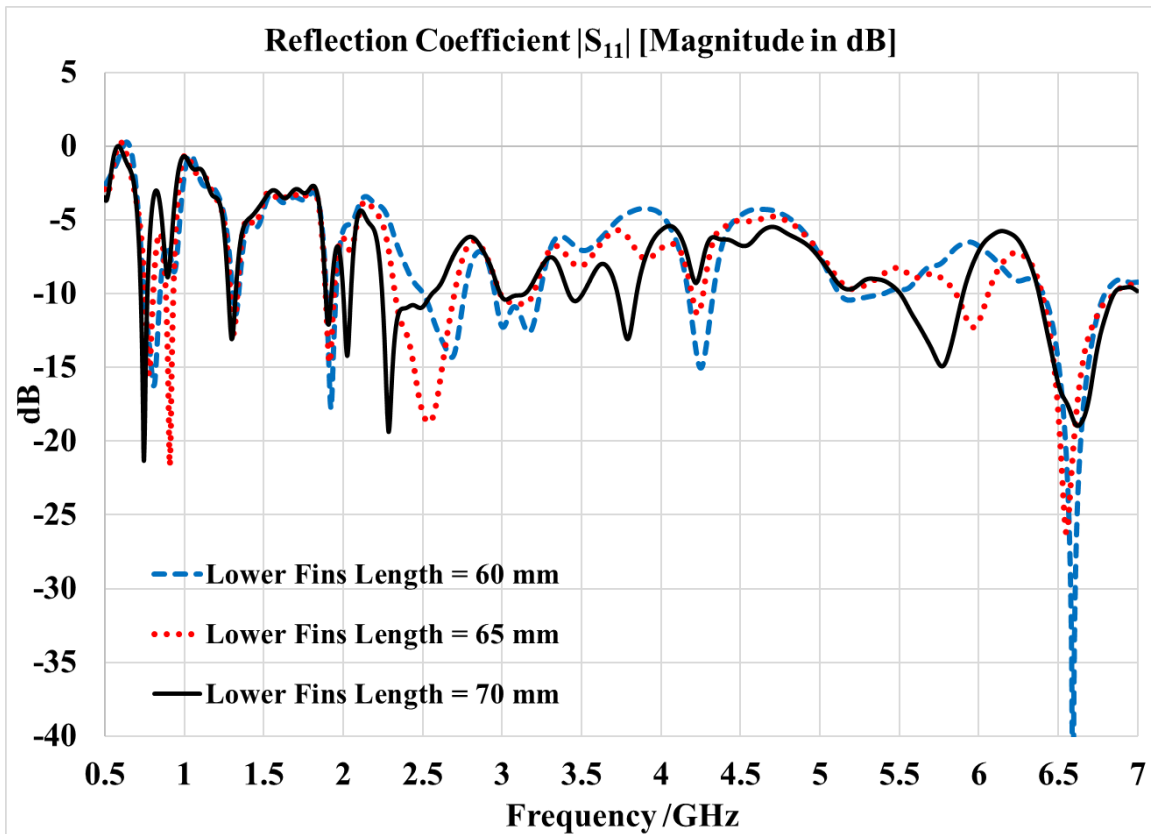


Figure 3.24 The simulated results of the reflection coefficient $|S_{11}|$ for the proposed (Antenna-2) when decreasing the length of the lower fins.

D. Impact of Decreasing the Length of the Middle Fins

Figure 3.25 shows the simulated results of the reflection coefficient $|S_{11}|$ when decreasing the length of the antenna-2 middle fins. Since increasing the length of the middle fins of Antenna-2 will result in overlap between the middle fins of the front patch and the middle fins of the back ground structure, only decreasing the length of the middle fins of Antenna-2 was studied.

The simulated results show that when decreasing the length of the middle fins from [40 mm] to [35 mm], the frequency (1.300 GHz) vanished, the frequency (2.287 GHz) shifted right to be (2.333 GHz), and the frequency (3.789 GHz) shifted right to (4.03 GHz) of the frequency spectrum, while a special case appeared for the frequencies (5.771 GHz) and (6.623 GHz) that were shifted to the left of the frequency spectrum to be (5.66 GHz) and (6.37 GHz), respectively.

Also, the reflection coefficient $|S_{11}|$ improved for some of the resonating frequencies with the introduction of a new resonating frequency (3.2 GHz). Furthermore, by decreasing the length of the middle fins from [40 mm] to [30 mm], the frequency (1.300 GHz) shifted right to (1.527 GHz) and the frequency (2.287 GHz) shifted right to (2.39 GHz) of the frequency spectrum, while a special case appeared for the frequencies (3.789 GHz) and (6.623 GHz), which were shifted to the left of the frequency spectrum to be (3.49 GHz) and (6.49 GHz), respectively, with significant improvements in the bandwidth and the reflection coefficient $|S_{11}|$ for the frequency (5.771 GHz).

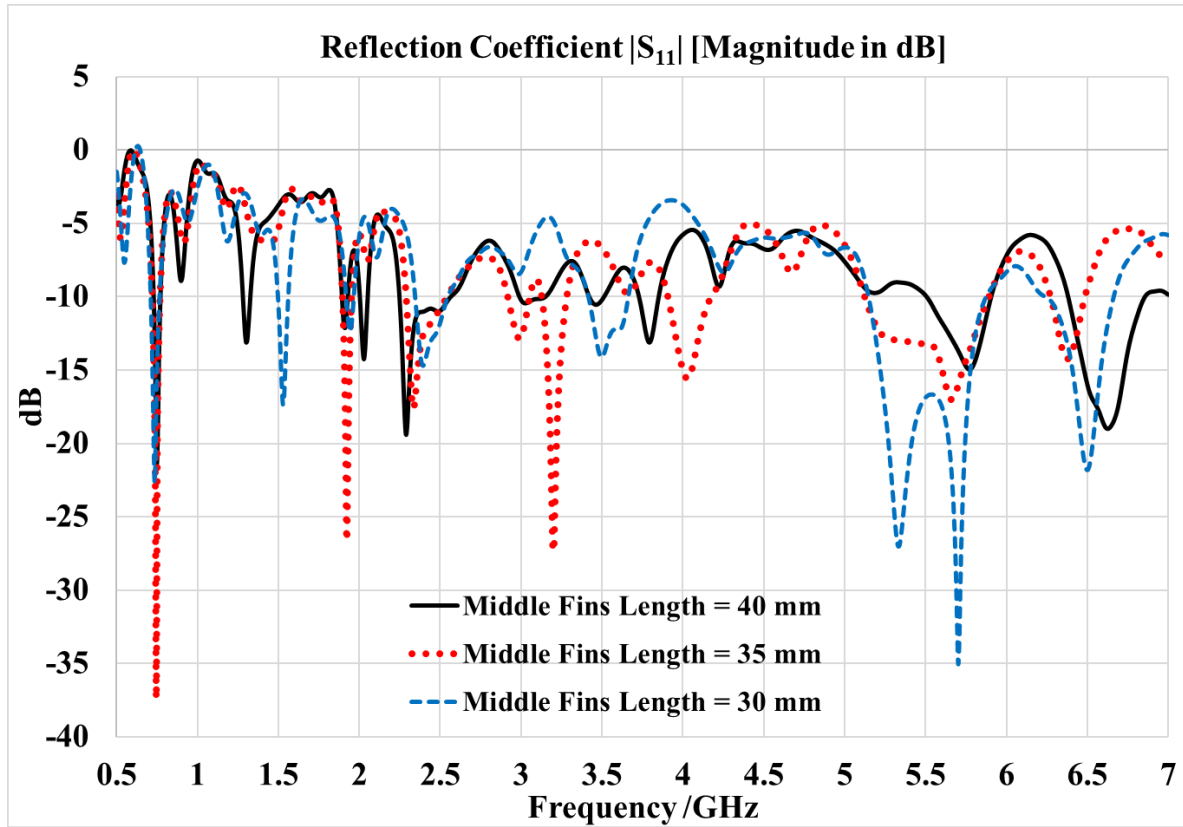


Figure 3.25 The simulated results of the reflection coefficient $|S_{11}|$ for the proposed (Antenna-2) when decreasing the length of the middle fins.

E. Impact of Decreasing the Length of the Upper Fins

Figure 3.26 shows the simulated results of the reflection coefficient $|S_{11}|$ when decreasing the length of the antenna-2 upper fins. Since increasing the length of the upper fins of antenna-2 will result in overlap between the upper fins of the front patch and the upper fins of the back ground structure, only decreasing the length of the upper fins of antenna-2 was studied.

The simulated results show that when decreasing the length of the upper fins from [20 mm] to [10 mm], the frequency (0.747 GHz) vanished, and the frequency (1.300 GHz) shifted right to be (2.26 GHz), and the frequency (1.910 GHz) shifted right to (2.62 GHz), and the frequency (2.027 GHz) shifted right to (2.81 GHz), and the frequency (2.287 GHz) shifted right to

(3.21 GHz), and the frequency (3.789 GHz) shifted right to (3.88 GHz) of the frequency spectrum, while a special case appeared for the frequencies (5.771 GHz) and (6.623 GHz), which were shifted to the left of the frequency spectrum to be (4.89 GHz) and (5.49 GHz), respectively, with significant improvements in the bandwidth for the frequency (3.21 GHz) and improvements in the reflection coefficient $|S_{11}|$ for the frequency (4.89 GHz).

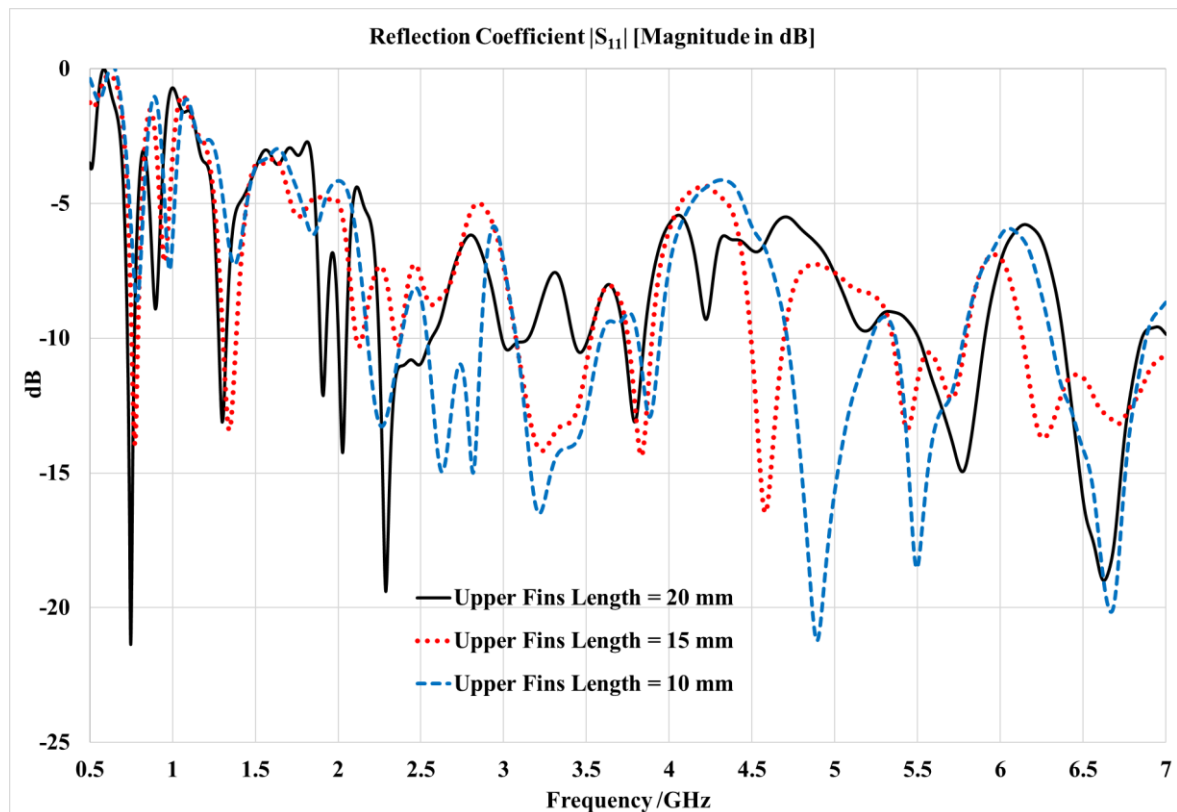


Figure 3.26 The simulated results of the reflection coefficient $|S_{11}|$ for the proposed (Antenna-2) when decreasing the length of the upper fins.

F. Impact of Changing the Fin Width

Figure 3.27 shows the simulated results of the reflection coefficient $|S_{11}|$ when changing all of the fin's width for Antenna-2. The simulated results show that when decreasing the width of all Antenna-2 fins from [3 mm] to [2 mm], the reflection coefficient $|S_{11}|$ improved for the frequencies (0.747 GHz), (1.300 GHz), (2.027 GHz), and (2.287 GHz), while diminishing for the frequencies (1.910 GHz) and (5.771 GHz). Furthermore, the impact of increasing the width of all Antenna-2 fins from [3 mm] to [4 mm] results in an improvement in the reflection coefficient $|S_{11}|$ for the frequencies (0.9 GHz), (1.910 GHz), and (6.623 GHz), respectively. The best results for the reflection coefficient $|S_{11}|$ were obtained when setting the value of all Antenna-2 fins width to [2 mm].

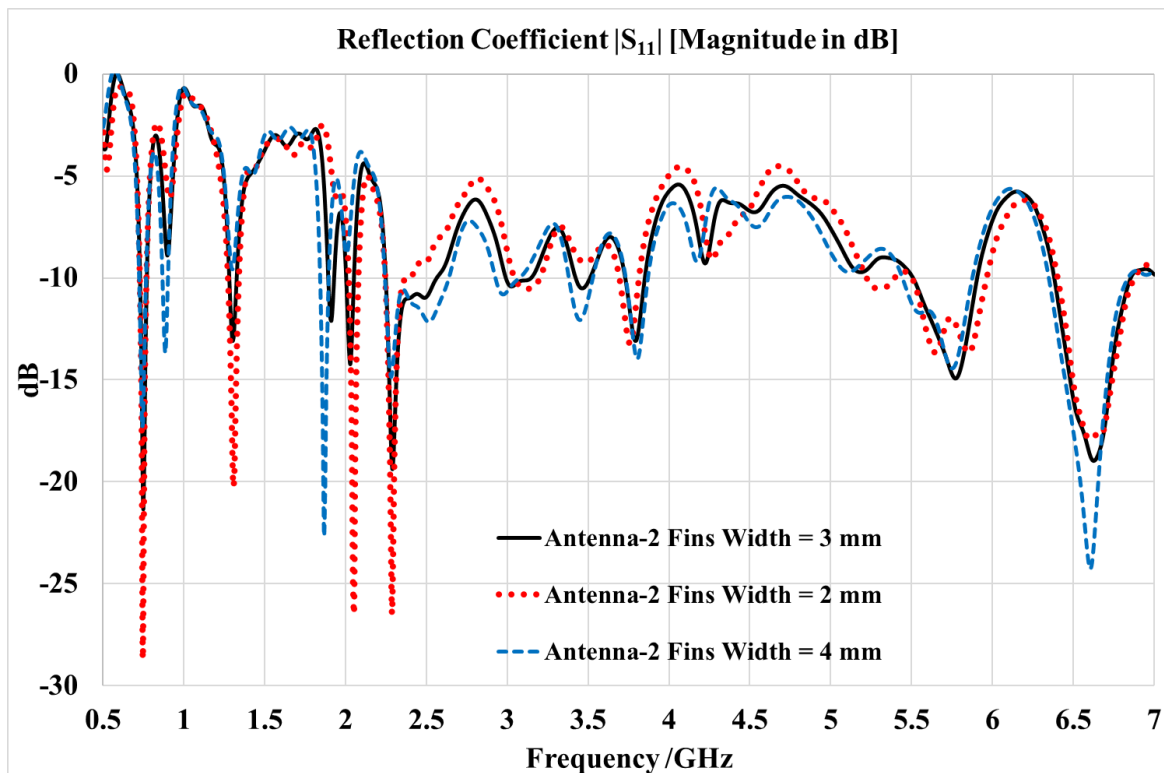


Figure 3.27 The simulated results of the reflection coefficient $|S_{11}|$ when changing all of the fin's width for the proposed (Antenna-2).

G. Impact of Changing the Scale of Antenna-2

Figure 3.28 shows the simulated results of the reflection coefficient $|S_{11}|$ when changing the scale of the antenna. The simulated results show that scaling down the antenna with a scale factor of (0.8) results in shifting all the resonating frequencies to the right of the frequency spectrum. Also, the two resonating frequencies (5.771 GHz) and (6.623 GHz) disappeared since the frequency spectrum studied was between (0.5 GHz) and (7 GHz). Whereas the impact of scaling up the antenna with a scale factor of (1.2) results in shifting all the resonating frequencies to the left of the frequency spectrum. This was expected since the fin lengths will be changed during the scaling process, which results in frequency shifting due to the inverse proportionality between the operating frequencies and the wavelength of the signal (λ).

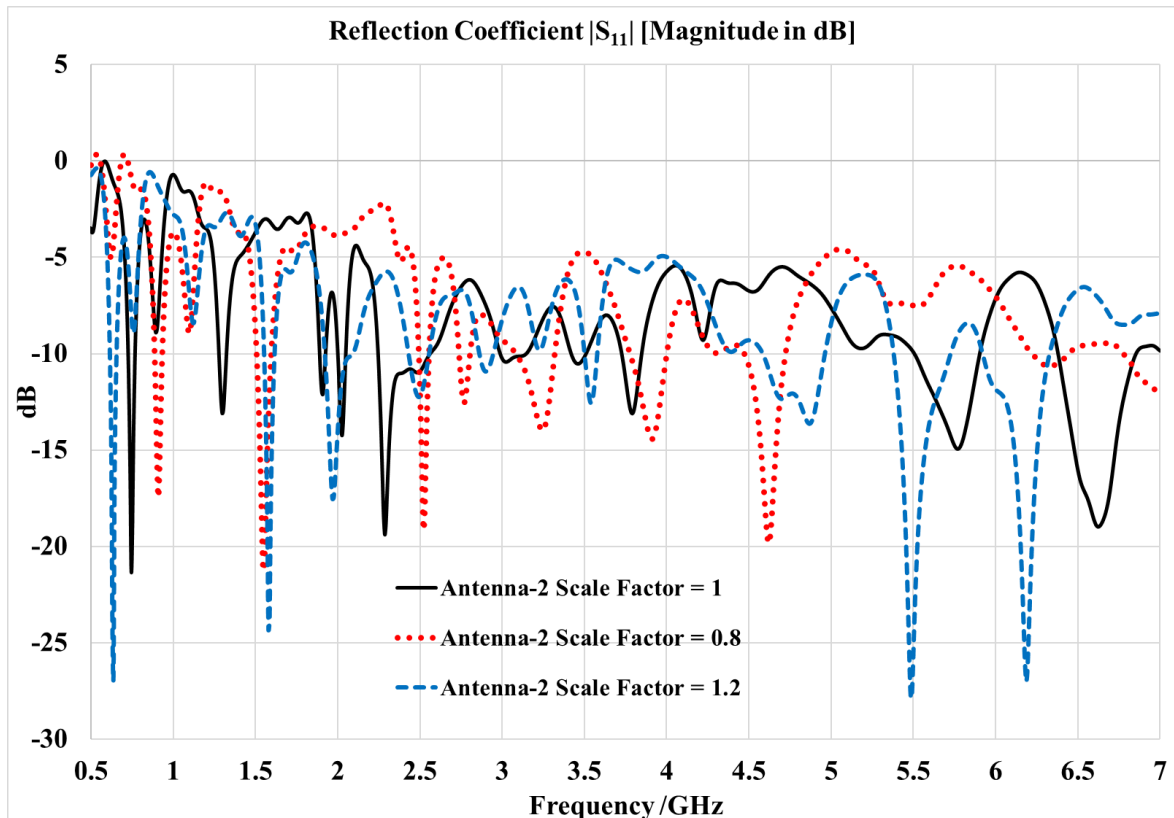


Figure 3.28 The simulated results of the reflection coefficient $|S_{11}|$ when changing the scale of the proposed (Antenna-2).

H. Impact of Changing the Width of the Microstrip Vertical Feed Line

Figure 3.29 shows the simulated results of the reflection coefficient $|S_{11}|$ when changing the microstrip vertical feed line width for Antenna-2. The simulated results show that when increasing the width of the Antenna-2 microstrip vertical feeding line from [3 mm] to [4 mm], the reflection coefficient $|S_{11}|$ improved for the frequencies (1.300 GHz) and (5.771 GHz) while it was decreased for the frequencies (2.027 GHz) and (6.623 GHz). Whereas, when decreasing the width of the Antenna-2 microstrip vertical feed line from [3 mm] to [2 mm], four new frequencies appeared in the frequency spectrum. (2.6 GHz), (3.14 GHz), (3.49 GHz), and (5 GHz), respectively. The optimal results for the reflection coefficient $|S_{11}|$ were obtained when setting the width value of the antenna-2 microstrip vertical feed line to [2 mm].

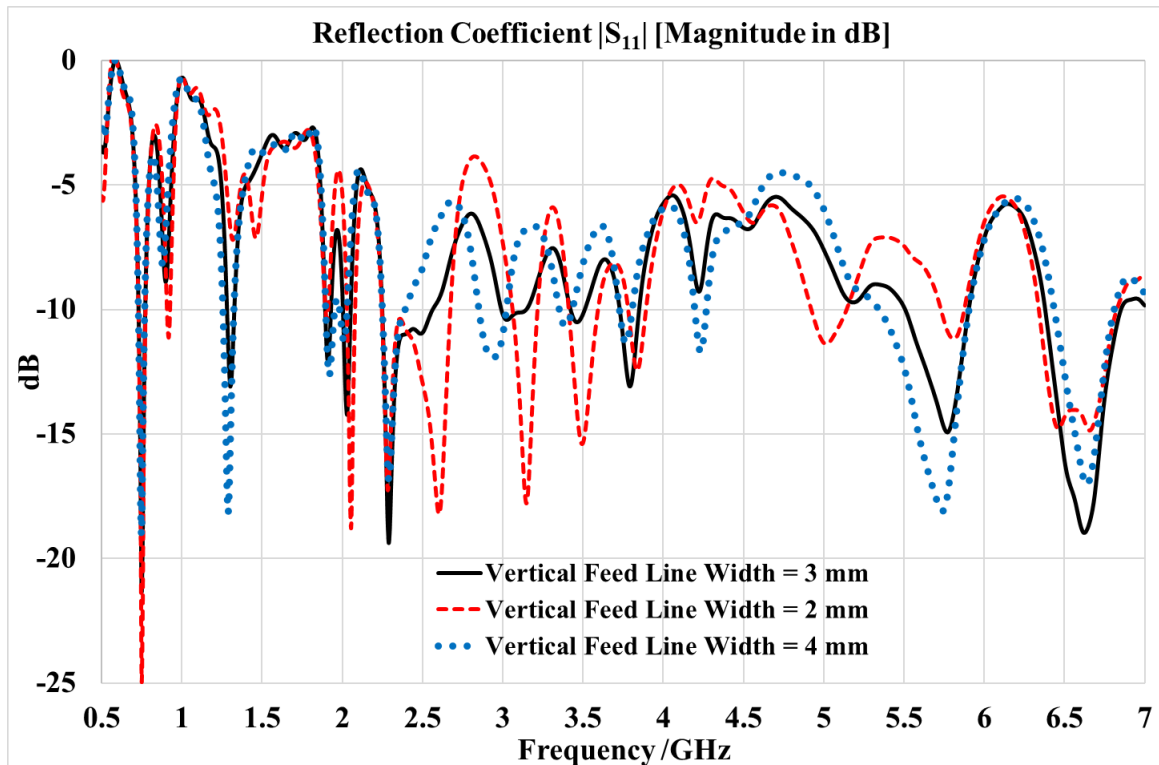


Figure 3.29 The simulated results of the reflection coefficient $|S_{11}|$ when changing the width of the microstrip vertical feed line of Antenna 2.

3.3.5 Antenna-2 Optimization

In order to get the best performance from the multiband antenna (Antenna-2) and target the frequencies of interest for RFEH applications, many modifications were made to the antenna. The first stage of optimization is obtained by: Firstly, set the microstrip vertical feed line width to [2 mm]. Secondly, set the width of all Antenna-2 fins to [2 mm]. Thirdly, set the Antenna-2 lower fins length to [68 mm], the middle fins length to [38 mm], and the upper fins length to [19.5 mm], respectively. After doing the previous modifications, the antenna is named (Antenna-2-a), as shown in Figure 3.30. The second stage of optimizing Antenna-2 is implemented by copying and scaling down (Antenna-2-a) using a scale factor of (0.9) and attaching it to the top of (Antenna-2-a). This will create (Antenna-2-b), which is the second stage of optimizing the antenna, as shown in Figure 3.31. The third stage of optimizing Antenna-2 was implemented by scaling down (Antenna-1-a) using a scale factor of (0.8) and attaching it on top of (Antenna-2-b) then scaling up the resultant antenna using a scale factor of (1.01). This will create the final design (Antenna-2-c), as shown in Figure 3.32. The previous cascaded design procedure was implemented in order to get a wide variety of lengths for the antenna fins that target many frequencies required for RFEH applications. Figure 3.33 shows the dimensions of the first optimization stage (Antenna-2-a), Figure 3.34 shows the dimensions of the second optimization stage (Antenna-2-b), and Figure 3.35 shows the dimensions of the third optimization stage (Antenna-2-c), respectively.



Figure 3.30 The first optimization stage (Antenna-2-a).

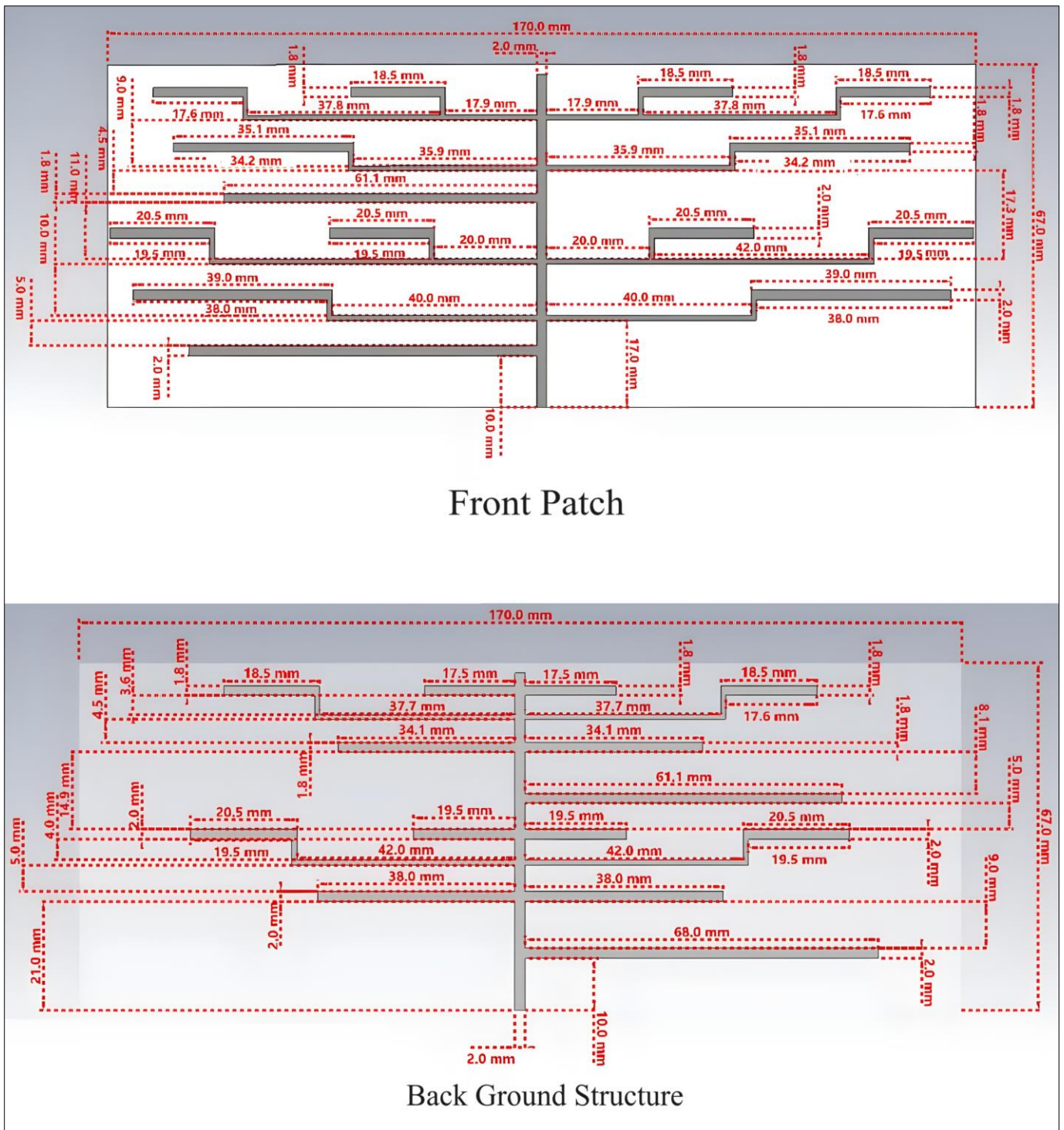
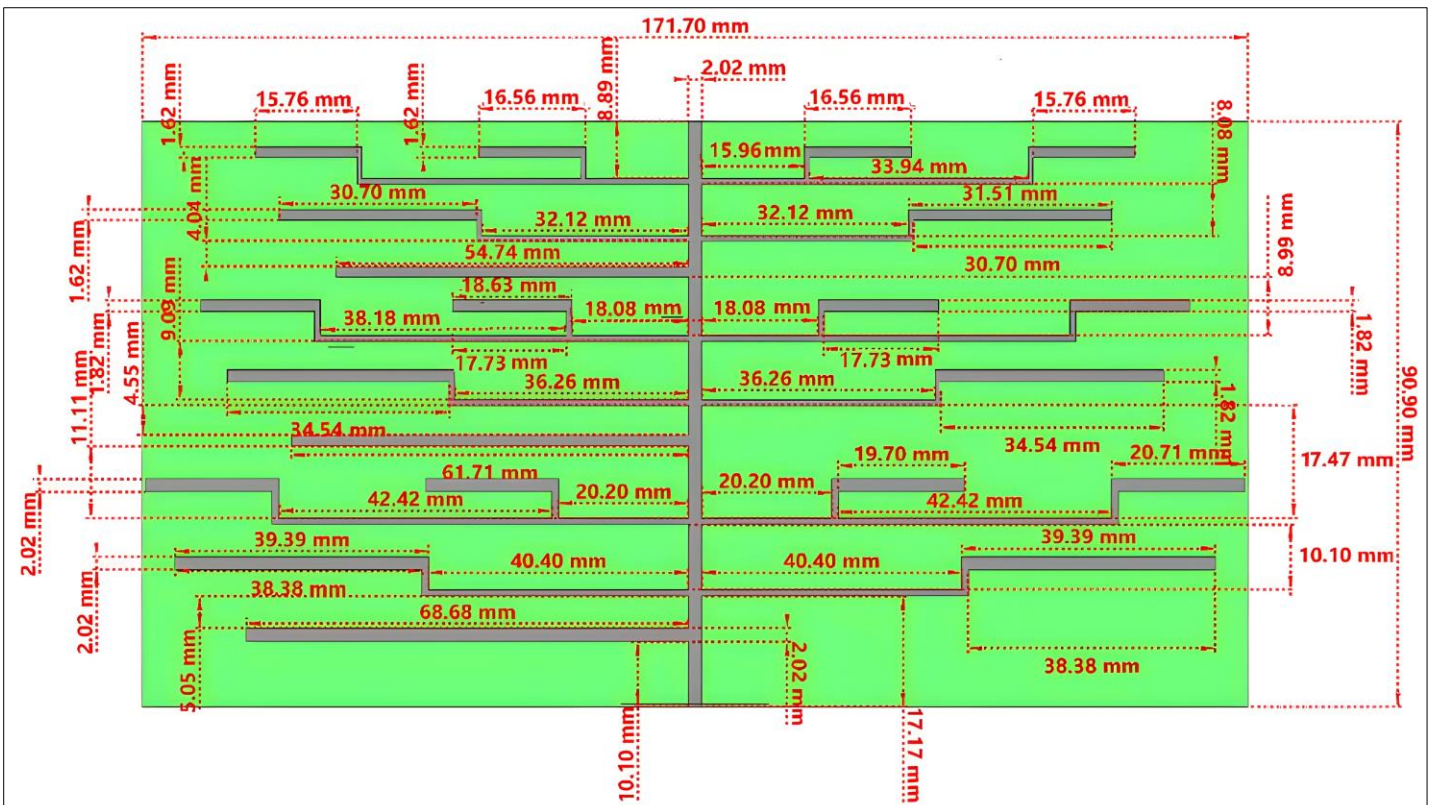
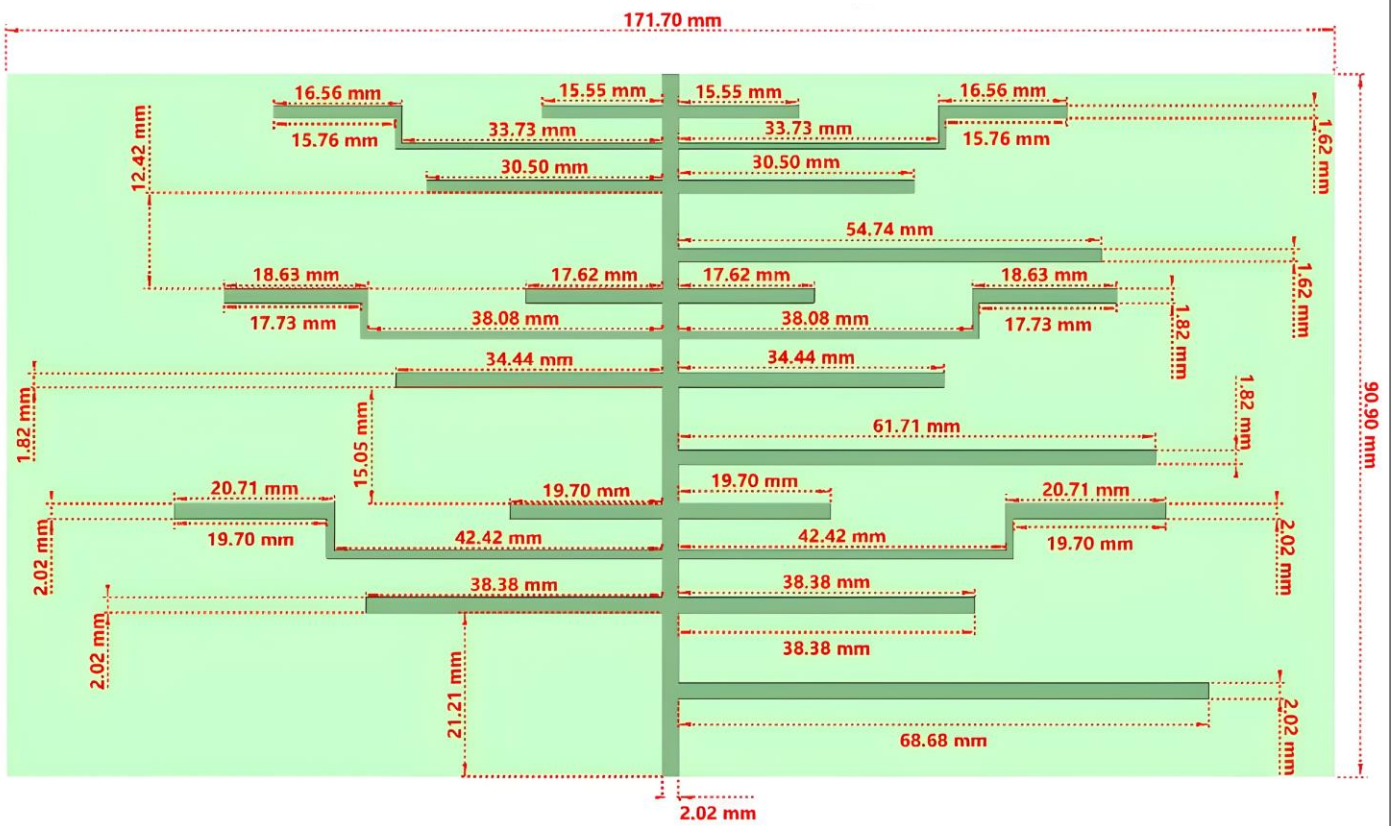


Figure 3.34 The dimensions of the second optimization stage (Antenna-2-b).



Front Patch



Back Ground Structure

Figure 3.35 The dimensions of the third optimization stage (Antenna-2-c).

3.3.6 Comparison between (Antenna-2-a), (Antenna-2-b) and (Antenna-2-c)

Figure 3.36 shows the simulated results of the reflection coefficient $|S_{11}|$ for each optimization stage (Antenna-2-a), (Antenna-2-b), and (Antenna-2-c). The simulated results show major improvements in performance for the third optimization stage (Antenna-2-c). Whereas, the simulated results for the first stage optimization (Antenna-2-a) show low performance for the frequency band of 5 GHz. Furthermore, the simulated results for the second stage optimization (Antenna-2-b) show low performance for the frequency bands (2.4 GHz and 1.8 GHz). Therefore, the third stage of optimization (Antenna-2-c) is the optimal stage for Antenna-2, and it is the final design for antenna-2. Table 3-4 shows the simulated results for the proposed antenna (Antenna 2-c).

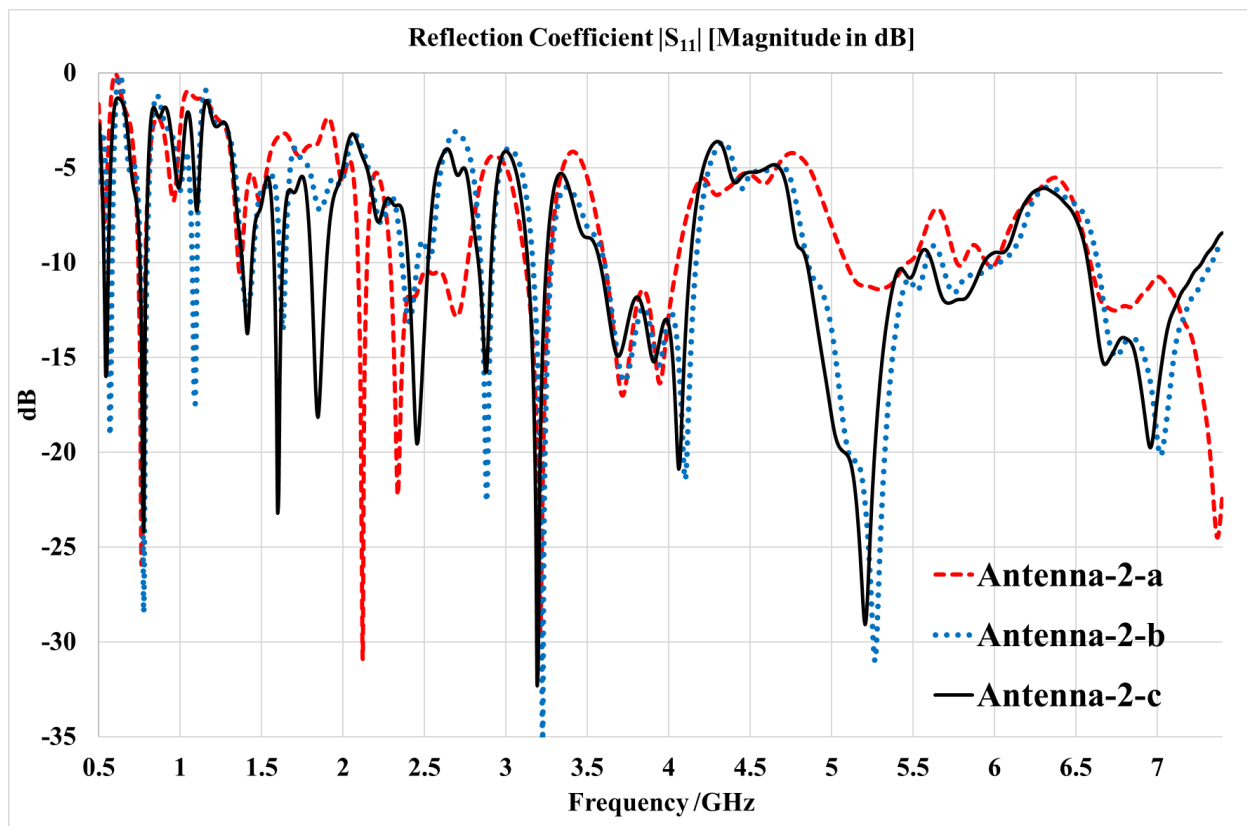


Figure 3.36 The simulated results of the reflection coefficient $|S_{11}|$ for each optimization stage (Antenna-2-a), (Antenna-2-b), and (Antenna-2-c).

Table 3-4 Simulated results of the proposed optimized (Antenna-2-c).

Resonating Frequency (GHz)	Return Loss S ₁₁ (dB)	Minimum Frequency (GHz)	Maximum Frequency (GHz)	Band width (GHz)	Directivity (dBi)	Peak Gain	Applications	Reference
0.776	-24	0.75109	0.7892	0.03811	5.064	2.919 dBi @ 0.7892 GHz	WIMAX, Mobile LTE, Mobile 5G	[54], [55]
1.4108	-13.73	1.38	1.4382	0.0582	2.367	0.7028 dBi @ 1.4382 GHz	WIMAX, Mobile LTE, Mobile 5G	[54], [55]
1.5971	-23.1	1.5757	1.6269	0.0512	4.151	1.572 dBi @ 1.6269 GHz	Mobile LTE, Mobile 5G	[54], [55]
1.8455	-18.13	1.8014	1.8973	0.0959	4.734	1.433 dBi @ 1.8455 GHz	Mobile 5G, Mobile LTE, Mobile DCS 1800	[54], [55]
2.4527	-19.53	2.3989	2.521	0.1221	6.267	4.49 dBi @ 2.4527 GHz	WLAN, WIMAX, Mobile LTE, Mobile 5G	[54], [55]
2.8736	-15.75	2.8305	2.9087	0.0782	6.106	2.989 dBi @ 2.8305 GHz	WIMAX	[54], [55]
3.191	-32.18	3.133	3.24813	0.11513	4.889	3.371 dBi @ 3.133 GHz	RADIOLOCATION, Active sensors (satellite)	[54], [55]
4.06	-20.86	3.57795	4.13119	0.55324	8.371	6.349 dBi @ 3.95 GHz	Mobile LTE, WLAN, WIMAX, Mobile 5G	[54], [55]
5.2058	-29.05	4.8481	5.5255	0.6774	7.571	5.486 dBi @ 5.33 GHz	WLAN, WIMAX, Mobile LTE, Mobile 5G	[54], [55]
5.7164	-12.12	5.615	5.9333	0.3183	6.236	4.921 dBi @ 5.615 GHz	WLAN, WIMAX, Mobile LTE, Mobile 5G	[54], [55]
6.9584	-19.74	6.5738	7.2734	0.6996	8.495	5.386 dBi @ 6.9584 GHz	WLAN, Mobile LTE, Mobile 5G	[54], [55]

The multiband antenna (Antenna-2) was designed carefully and studied step-by-step in order to target the most required frequencies for RFEH applications. The simulated results for the final design of the proposed antenna (Antenna-2-c) showed outstanding performance. Since the antenna supports a high number of total (11) eleven resonating frequencies, as shown in Table 3-4, all of them are required for RFEH applications. Furthermore, the proposed antenna (Antenna-2-c) covered all of the frequencies utilized by the 2.4 GHz (IEEE 802.11) band, which is the most popular and widely used by WLAN services, as well as all of the downlink frequencies utilized by the mobile DCS 1800 frequency band (1,805 MHz – 1,880 MHz) and all of the downlink frequencies for the (band 68) (753 MHz – 783 MHz) that are utilized by the mobile LTE/5G in Europe, the Middle East, and Africa. Furthermore, the final design of the proposed antenna (Antenna-2-c) has achieved a high gain for most of its resonating frequencies. For example, the antenna achieved a high gain of (4.49 dBi) at the frequency of (2.4527 GHz), and a peak gain of (6.349 dBi) at the frequency of (3.95 GHz). Also, the simulated results of the proposed multiband antenna (Antenna-2-c) showed a high bandwidth capacity for most of its resonating frequencies, making it a perfect antenna for RFEH applications. For example, the antennas have a bandwidth capacity of (677 MHz) at the resonating frequency of (5.2 GHz), which covers a lot of frequencies utilized by WLAN, WIMAX, and mobile LTE services. Figure 3.37 shows the simulated 3D radiation pattern of the directivity magnitude in [dBi] for some of the proposed multiband (Antenna-2-c) supported frequencies. Also, Figure 3.38 shows the simulated 2D radiation pattern. The simulated results for the 3D radiation pattern of the directivity showed that the proposed antenna has omnidirectional radiation characteristics for the resonating frequency (1.4108 GHz), which is utilized by WIMAX, Mobile LTE, and Mobile 5G services.

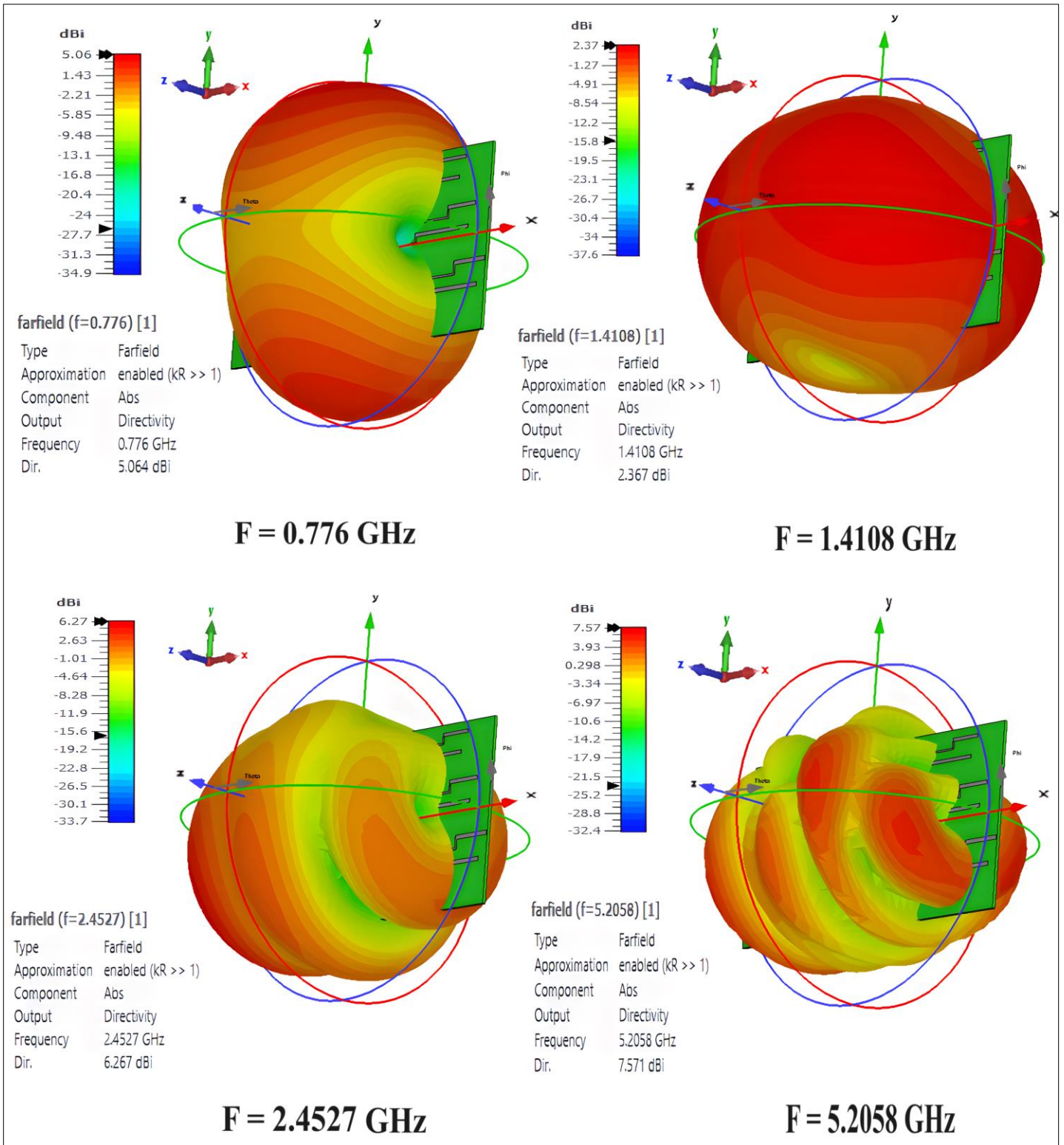


Figure 3.37 Simulated 3D radiation pattern of the directivity magnitude in [dBi] for some of (Antenna-2-c) supported frequencies.

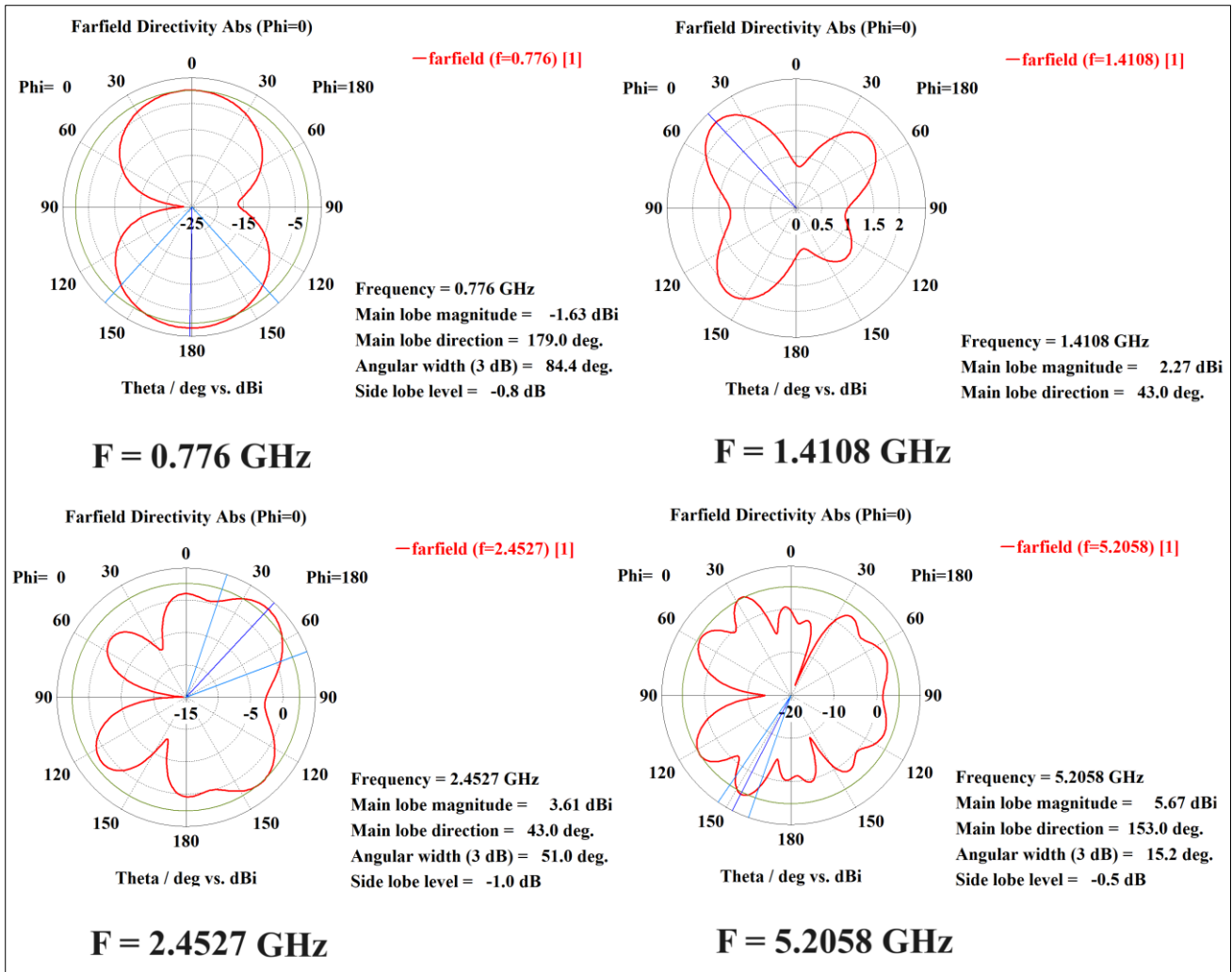


Figure 3.38 Simulated 2D radiation pattern of the directivity magnitude in [dBi] for some of (Antenna-2-c) supported frequencies.

Furthermore, the results showed that the proposed antenna has performance improvements compared to other proposed works, since the proposed optimized antenna achieved a good gain for most of its operating frequencies with respect to its size and thickness, given that it has a much thinner than [8], [14], [16], and [17], and also supports more resonating frequencies required for RFEH applications. It also needs to be mentioned that the FR-4 substrate is less expensive than the (Arlon 25N), and (Rogers 3003) substrates, and the gain of any antenna is directly proportional to its physical size and thickness.

3.4 Modified Hexagonal Slot Antenna with a Defected Ground Structure for RFEH Applications

A novel monopole multiband antenna (Antenna-3) is introduced in this section that targets some of the required frequencies for RFEH applications, including WLAN-2.4G, WLAN-5G, WLAN-6G, WIMAX, Mobile LTE, and Mobile 5G services. A novel fractal shape is designed at the beginning of this chapter and then combined with a conventional hexagonal geometrical shape in order to implement the proposed multiband antenna-3. The antenna is simulated with CST Studio Suite software and fabricated on FR-4 substrate due to its light weight, low cost, and low profile, with a dielectric constant $\epsilon_r = 4.3$, a thickness of 1.6 mm, and a loss tangent (δ) of 0.025. In this section, two antenna stages (Antenna-3-a) and (Antenna-3-b) are proposed.

3.4.1 Design and Construction of the First Stage of the Proposed Multiband Antenna (Antenna-3-a)

The first step for implementing the first stage of the proposed multiband Antenna-3 started by creating the front patch (Radiator) using the modified hexagonal geometrical shape shown in Figure 3.2 (d). The modified hexagonal geometric shape created by replacing all the conventional hexagonal polygon straight side lines with the new fractal shape shown in Figure 3.1 (e), a full ground plane with a thickness of [0.035 mm] and substrate dimensions of [100 mm] of width, [115 mm] of length, and [1.6 mm] of thickness, respectively, was implemented to create the first stage of antenna-3 and named (Antenna-3-a). Furthermore, a microstrip feed line for the proposed antenna is created with a length of [40 mm] and a width of [2 mm], as shown in Figure 3.39.



Figure 3.39 The first stage of the proposed antenna (Antenna-3-a) with dimensions.

3.4.2 Simulated Results for the Proposed (Antenna-3-a)

Figure 3.40 shows the simulated results of the reflection coefficient $|S_{11}|$ magnitude in [dB] for the first stage of the proposed antenna (Antenna-3-a). The simulated results show that (Antenna-3-a) is resonating with nine (9) frequencies (0.98 GHz), (1.4 GHz), (2.98 GHz), (3.23 GHz), (4.036 GHz), (4.87 GHz), (5.12 GHz), (6.064 GHz), and (6.56 GHz). Whereas, the frequency (2.4 GHz) is missed for (Antenna-3-a); therefore, (Antenna-3-b) is introduced by applying some modifications to (Antenna-3-a). Most of these frequencies are required by energy harvesting applications, excluding the frequencies utilized by WLAN-2.4G services.

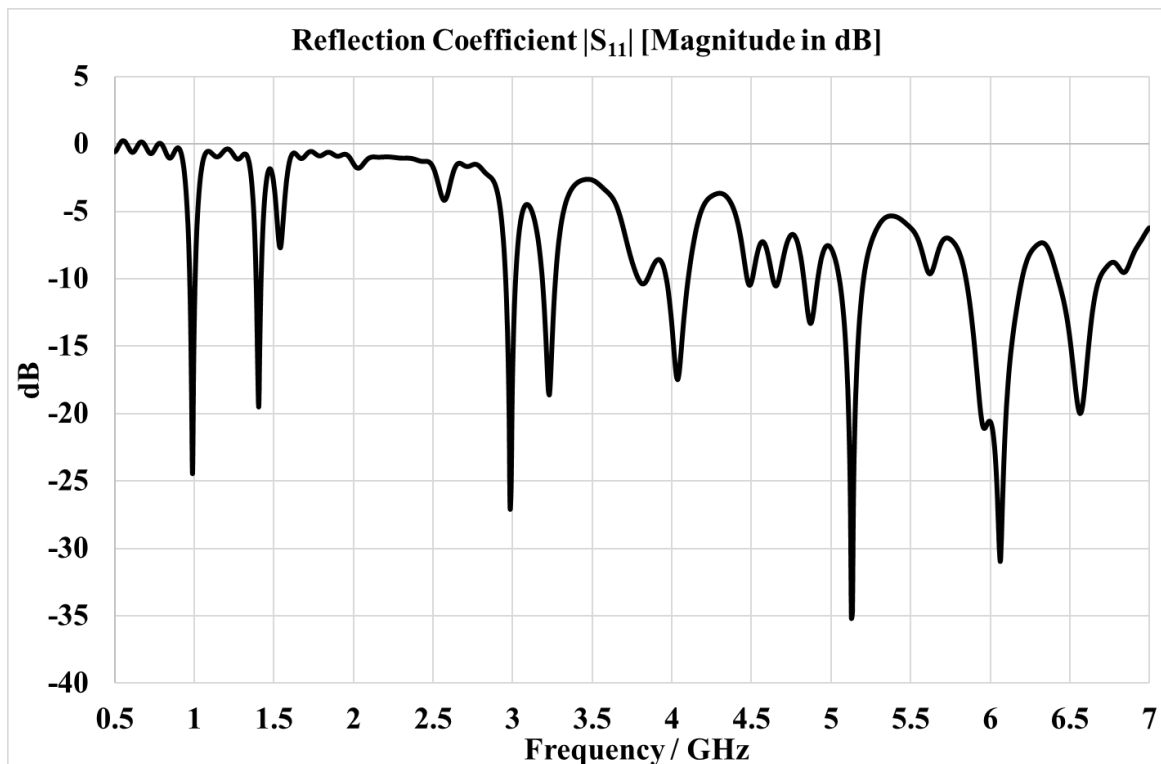


Figure 3.40 The simulated results of the reflection coefficient $|S_{11}|$ for the proposed (Antenna-3-a).

3.4.3 Design and Construction of the Second Stage of the Proposed Multiband Antenna (Antenna-3-b)

The second stage of the proposed antenna (Antenna-3-b) is constructed first by making a slot in the center of the front patch of (Antenna-3-a) by copying and scaling down the modified hexagonal front patch of the first stage of the antenna (Antenna-3-a) with a scale factor of (0.5) as shown in Figure 3.41(a), then subtracting it from the modified hexagonal front patch of the first stage (Antenna-3-a) as shown in Figure 3.41(b) to create the new front patch (Radiator) of the second stage of (Antenna-3) as shown in Figure 3.42. The same substrate dimensions of the first stage (Antenna-3-a) with a full ground plane and feeding line were applied similarly to the first stage of antenna-3, as shown in Figure 3.42.

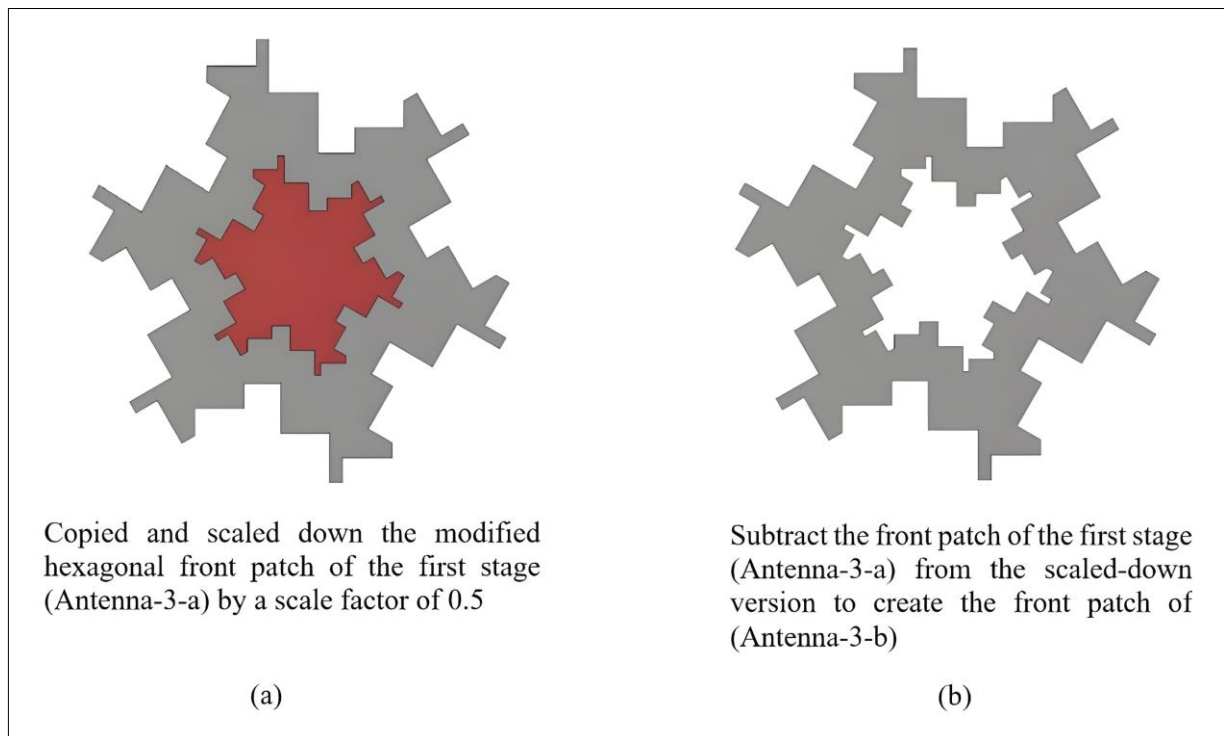


Figure 3.41 The construction steps for creating the front patch of the proposed antenna (Antenna-3-b).

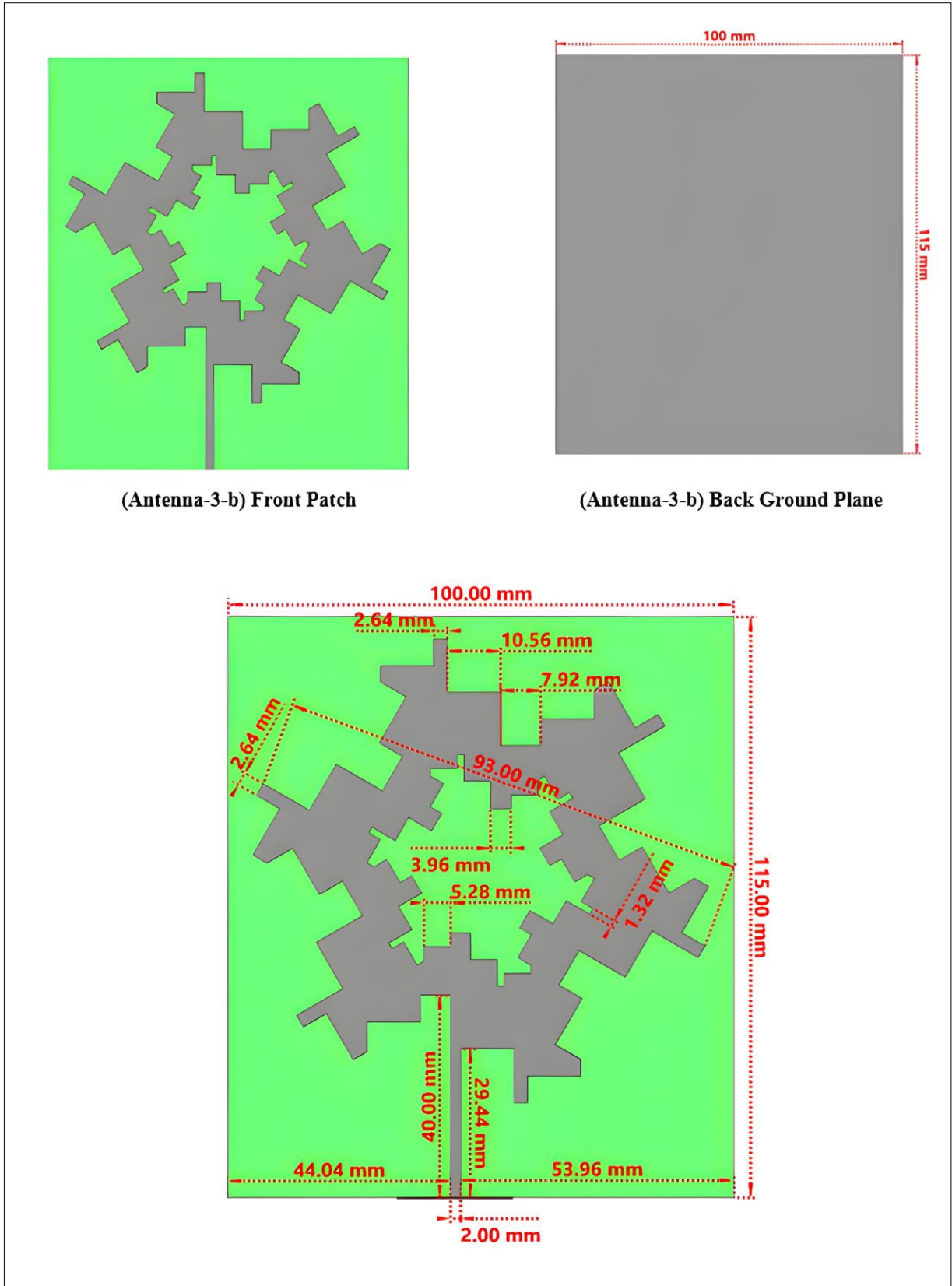


Figure 3.42 The second stage of the proposed antenna (Antenna-3-b) with dimensions.

3.4.4 Simulated Results for the Proposed (Antenna-3-b)

Figure 3.43 shows the simulated results of the reflection coefficient $|S_{11}|$ for the second stage (Antenna-3-b). The simulated results show that (Antenna-3-b) is resonating at six frequencies (1.24 GHz), (2.5 GHz), (4.11 GHz), (4.84 GHz), (5.96 GHz), and (6.78 GHz). Those frequencies could be tuned to target the frequencies required by RFEH applications, including WLAN-2.4G, WLAN-5G, WLAN-6G, mobile LTE, and WiMAX services.

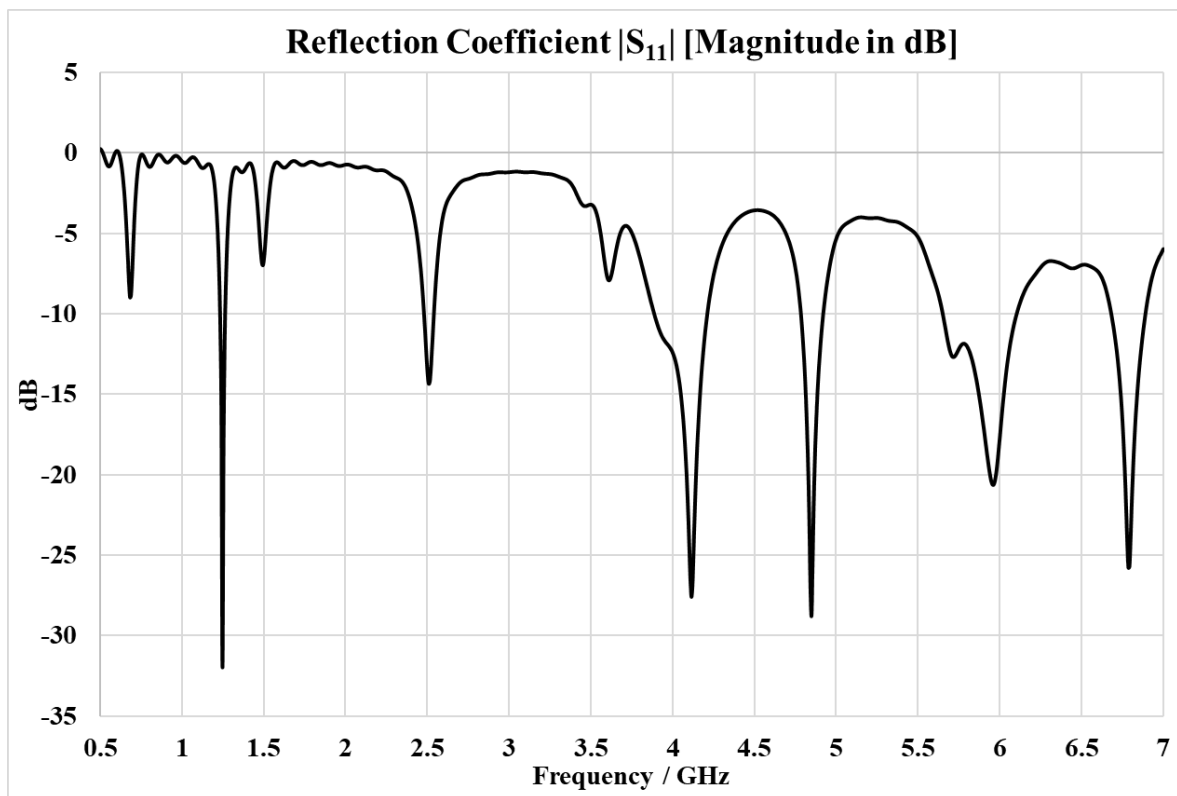


Figure 3.43 The simulated results of the reflection coefficient $|S_{11}|$ for the proposed (Antenna-3-b).

3.4.5 Comparison between the simulated results of the two proposed antennas (Antenna-3-a) and (Antenna-3-b)

The simulated results of the reflection coefficient $|S_{11}|$ show that the first-stage multiband antenna (Antenna-3-a) is resonating at nine (9) frequencies (0.98 GHz), (1.4 GHz), (2.98 GHz), (3.23 GHz), (4.036 GHz), (4.87 GHz), (5.12 GHz), (6.064 GHz), and (6.56 GHz). These frequencies are required for RFEH applications since they support WIMAX, mobile LTE, WLAN-5G, and WLAN-6G services. Unfortunately, the multiband antenna (Antenna-3-a) is missing the frequency band (2.4 GHz) that supports WLAN-2.4G services.

The multiband antenna (Antenna-3-a) could be used in a specific circumstance that doesn't require RFEH for the frequency band (2.4 GHz). Furthermore, the simulated results of the reflection coefficient $|S_{11}|$ show that the second-stage of the multiband antenna (Antenna-3-b) is resonating with six frequencies (1.24 GHz), (2.5 GHz), (4.11 GHz), (4.84 GHz), (5.96 GHz), and (6.78 GHz), and it supports WLAN-2.4G, WLAN-5G, WLAN-6G, mobile LTE, and WiMAX services. From the RFEH perspective, the simulation results showed that both the multiband antennas (Antenna-3-a) and (Antenna-3-b) have good performance.

The second-stage multiband (Antenna-3-b) was selected to be carefully studied since it supports the frequency of 2.5 GHz and could be easily shifted to target WLAN-2.4G services. Also, the multiband antenna (Antenna-3-b) already supports WLAN-5G and WLAN-6G. Mobile LTE and WIMAX services.

3.4.6 Parametric analysis for the proposed (Antenna-3-b)

A. Impact of Changing the Width of the Microstrip Feed Line

Figure 3.44 shows the simulated results of the reflection coefficient $|S_{11}|$ for different width values of the antenna-3-b feed line. The results show that changing the feed line width from [2 mm] to [4 mm] results in improving the reflection coefficient for the frequencies (4.84 GHz) and (1.5 GHz) while diminishing the reflection coefficient for all other resonating frequencies. Furthermore, the simulated results show that changing the feed line width from [2 mm] to [1 mm] results in improving the reflection coefficient for the frequency (5.96 GHz) while diminishing the reflection coefficient for the frequencies (4.84 GHz) and (6.78 GHz). Therefore, the optimal value for the feed line width was to keep it at the value of [2 mm].

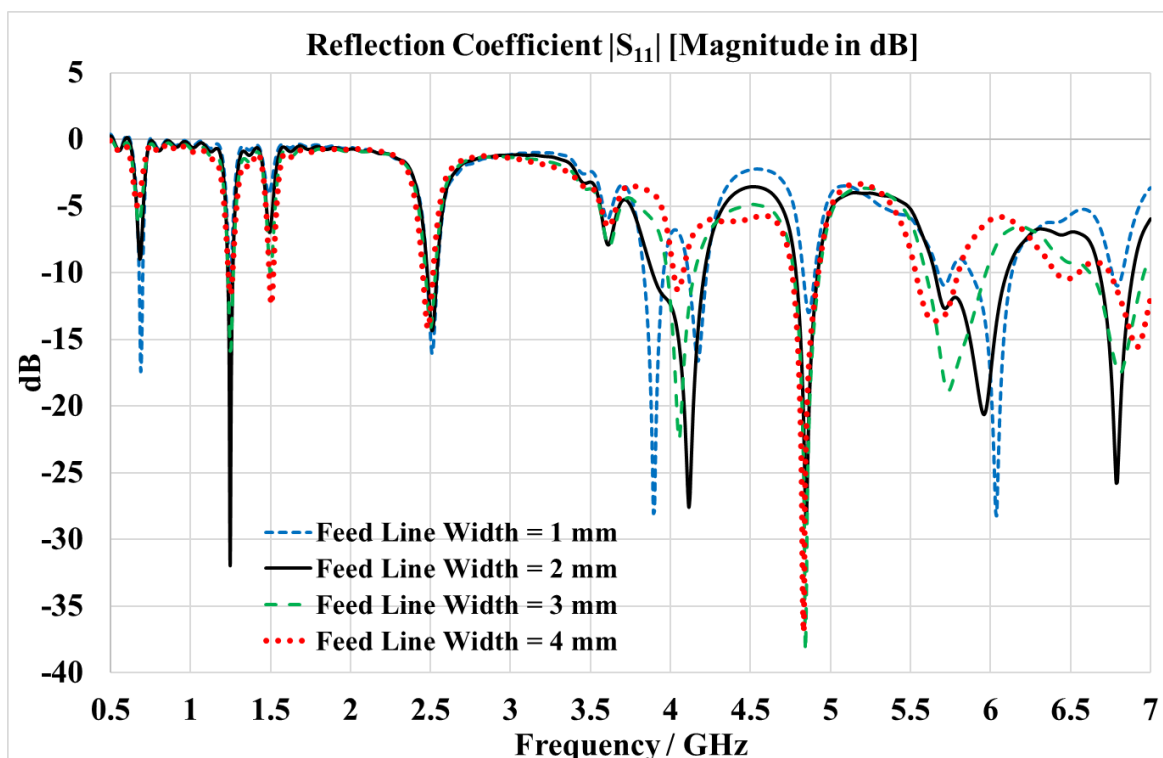


Figure 3.44 The simulated results of reflection coefficient $|S_{11}|$ for different width values of the feed line of (Antenna-3-b).

B. Impact of Changing the Length of the Microstrip Feed Line

Figure 3.45 shows the simulated results of the reflection coefficient $|S_{11}|$ for different length values of the Antenna-3-b feed line. The simulated results show that changing the feed line length from [40 mm] to [30 mm] results in improving the reflection coefficient $|S_{11}|$ for the frequencies (1.24 GHz), (2.5 GHz), (4.11 GHz), (5.96 GHz), and (6.78 GHz), while diminishing the reflection coefficient $|S_{11}|$ for the frequency (4.84 GHz). Also, the results show that changing the feed line length from [40 mm] to [25 mm] results in improving the reflection coefficient $|S_{11}|$ for the frequencies (2.5 GHz), (4.11 GHz), and (4.84 GHz), while diminishing for the frequencies (1.24 GHz), (5.96 GHz), and (6.78 GHz). The optimal value for the feed line length is [30 mm].

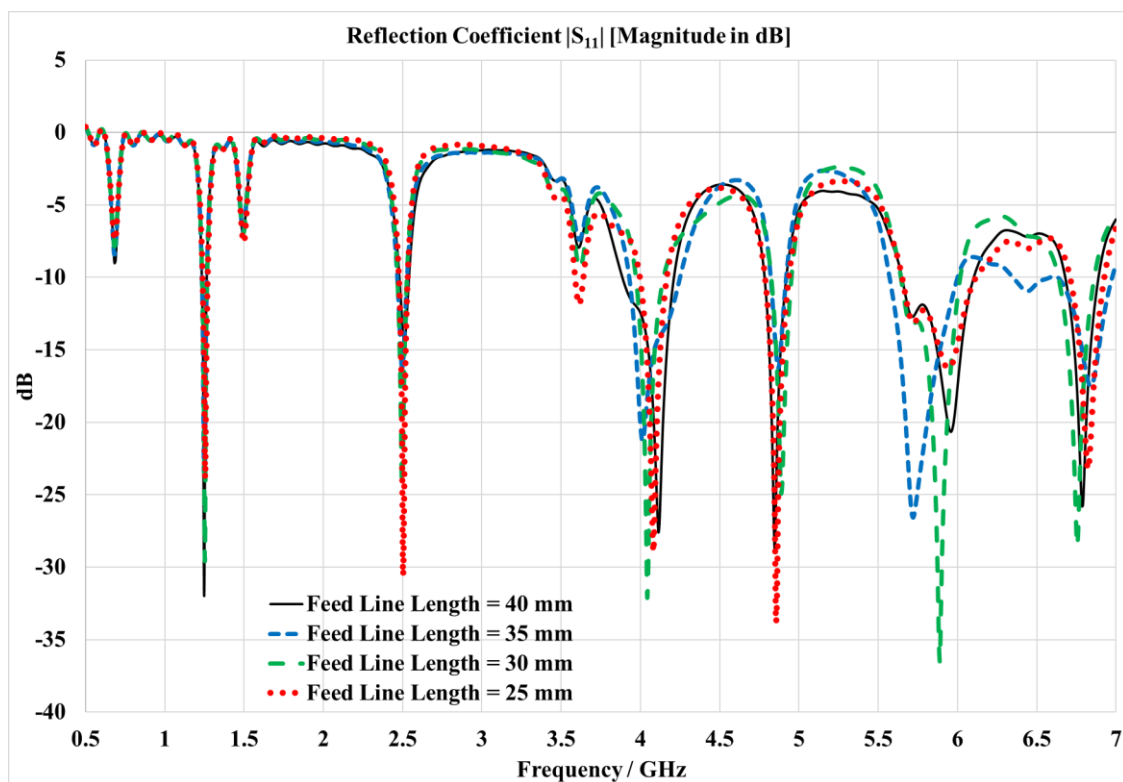


Figure 3.45 The simulated results of reflection coefficient $|S_{11}|$ for different length values of the feed line of (Antenna-3-b).

C. Impact of Changing the Ground Plane Length

Figure 3.46 shows the simulated results for the reflection coefficient $|S_{11}|$ after changing the ground plane length for the proposed antenna (Antenna-3-b) for the values [115 mm, 100 mm, 90 mm, 80 mm] while keeping the ground plane width constant for [100 mm].

The results show that there were no major changes to the reflection coefficient $|S_{11}|$ except shifting the frequency (1.24 GHz) to the right of the frequency spectrum and introducing a new frequency of 0.9 GHz.

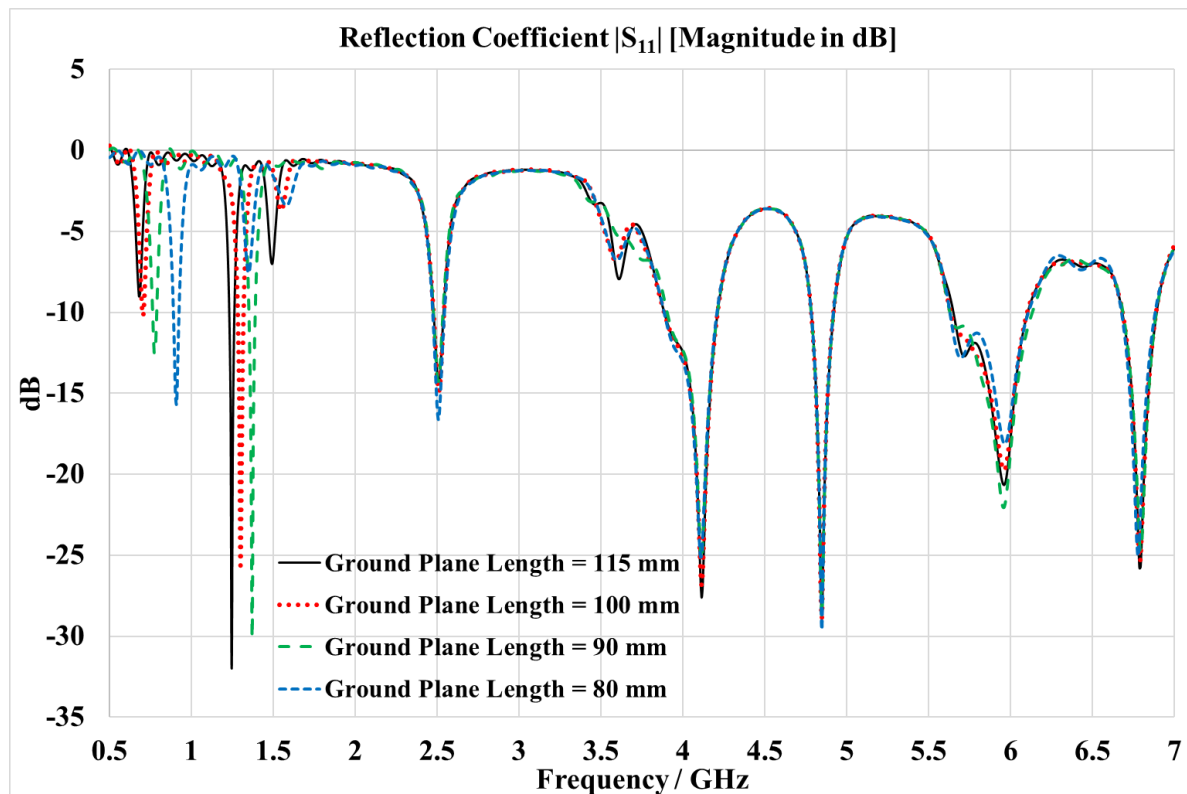


Figure 3.46 Simulated results of the reflection coefficient $|S_{11}|$ for different length values of (Antenna-3-b) ground plane.

D. Impact of Changing the Ground Plane Width

Figure 3.47 shows the simulated results for the reflection coefficient $|S_{11}|$ after changing the ground plane width for the proposed antenna (Antenna-3-b) for the values [70 mm, 80 mm, 90 mm, 100 mm] while keeping the ground plane length constant at [115 mm].

The simulated results show improvement in the bandwidth for the frequency (4.11 GHz) and improvement in the reflection coefficient $|S_{11}|$ for the frequencies (2.5 GHz, 4.84 GHz, and 5.96 GHz) when changing the ground plane width from [100 mm] to [70 mm], whereas diminishing for the frequencies (1.24 GHz, 4.11 GHz), The optimal simulated results were achieved with a ground plane width value of [70 mm].

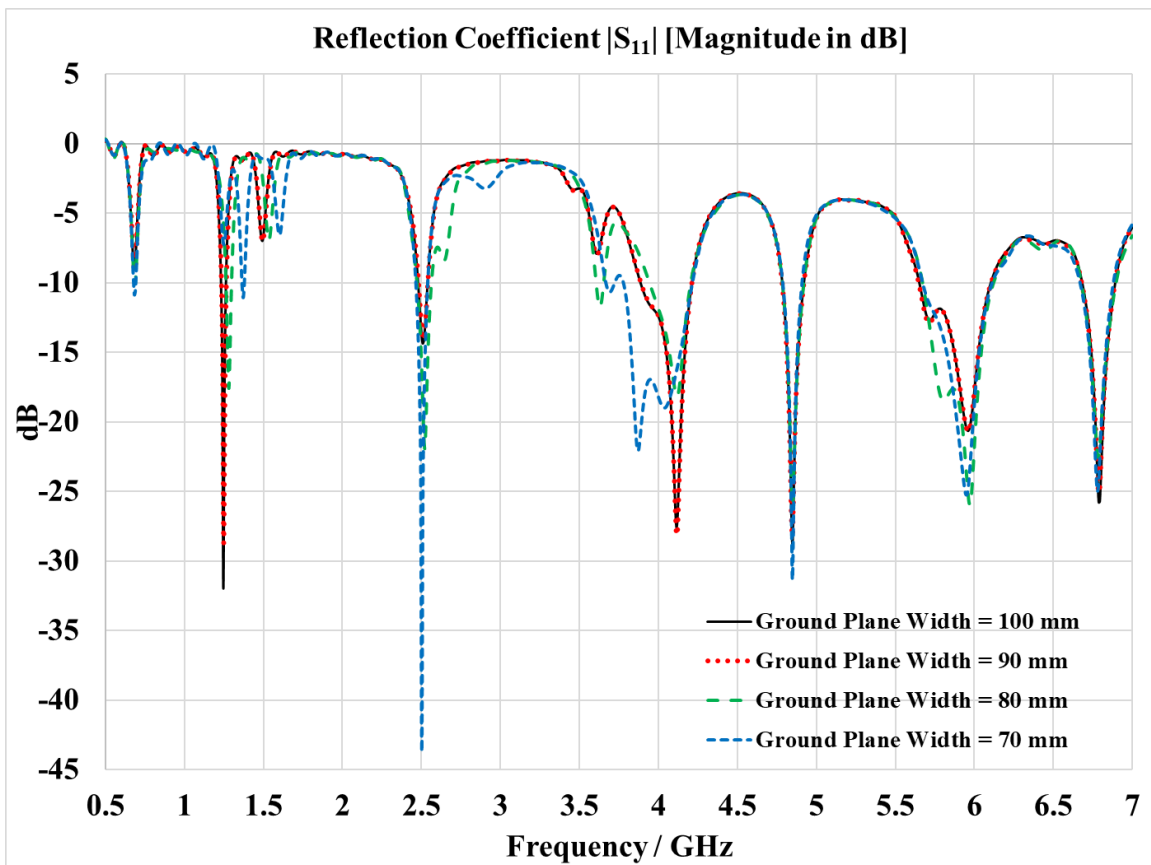


Figure 3.47 Simulated results of the reflection coefficient $|S_{11}|$ for different width values of (Antenna-3-b) ground plane.

E. Impact of Scale Down on Antenna-3-b

Figure 3.48 shows the reflection coefficient $|S_{11}|$ simulated results for different scale-down factors (0.8) and (0.6) applied to (Antenna-3-b). It's clear from Figure 3.48 that when the scale of the (Antenna-3-b) decreases, all the resonating frequencies will be shifted to the right of the frequency spectrum. Also, the simulated results show the higher resonating frequencies have vanished since the frequency spectrum range studied is from (0.5 GHz to 7 GHz).

The simulated results confirmed that the resonating frequencies are dependent on the electrical lengths of the (Antenna-3-b) radiator patch, which directly impacts the wavelength (λ) for each operating frequency.

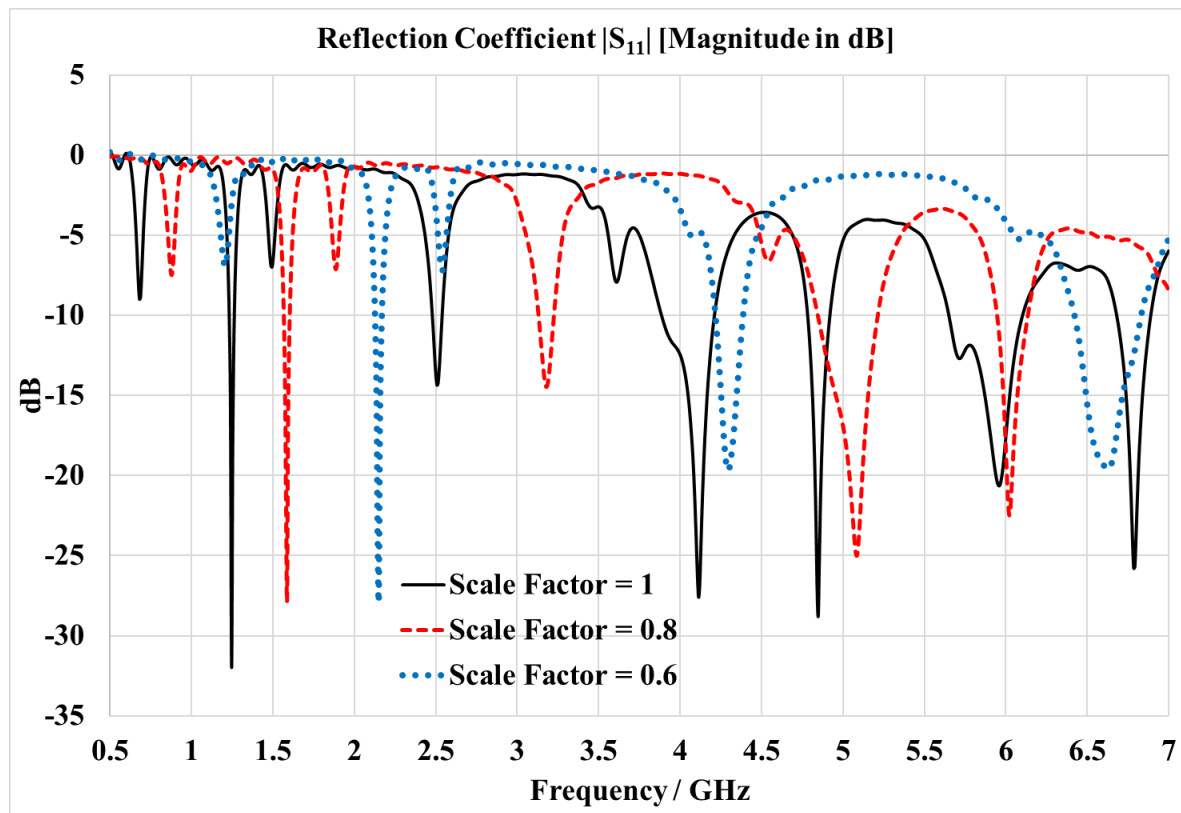


Figure 3.48 The simulated results of the reflection coefficient $|S_{11}|$ for different scale down factors of (Antenna-3-b).

F. Impact of Scale Up on Antenna-3-b

Figure 3.49 shows the reflection coefficient $|S_{11}|$ simulated results for different scale-up factors (1.2) and (1.4) applied to (Antenna-3-b). It's clear from Figure 3.49 that when the scale of the (Antenna-3-b) increases, all the resonating frequencies will be shifted to the left of the frequency spectrum.

The simulated results confirmed that the resonating frequencies are dependent on the electrical lengths of the (Antenna-3-b) radiator patch, which directly impacts the wavelength (λ) for each operating frequency.

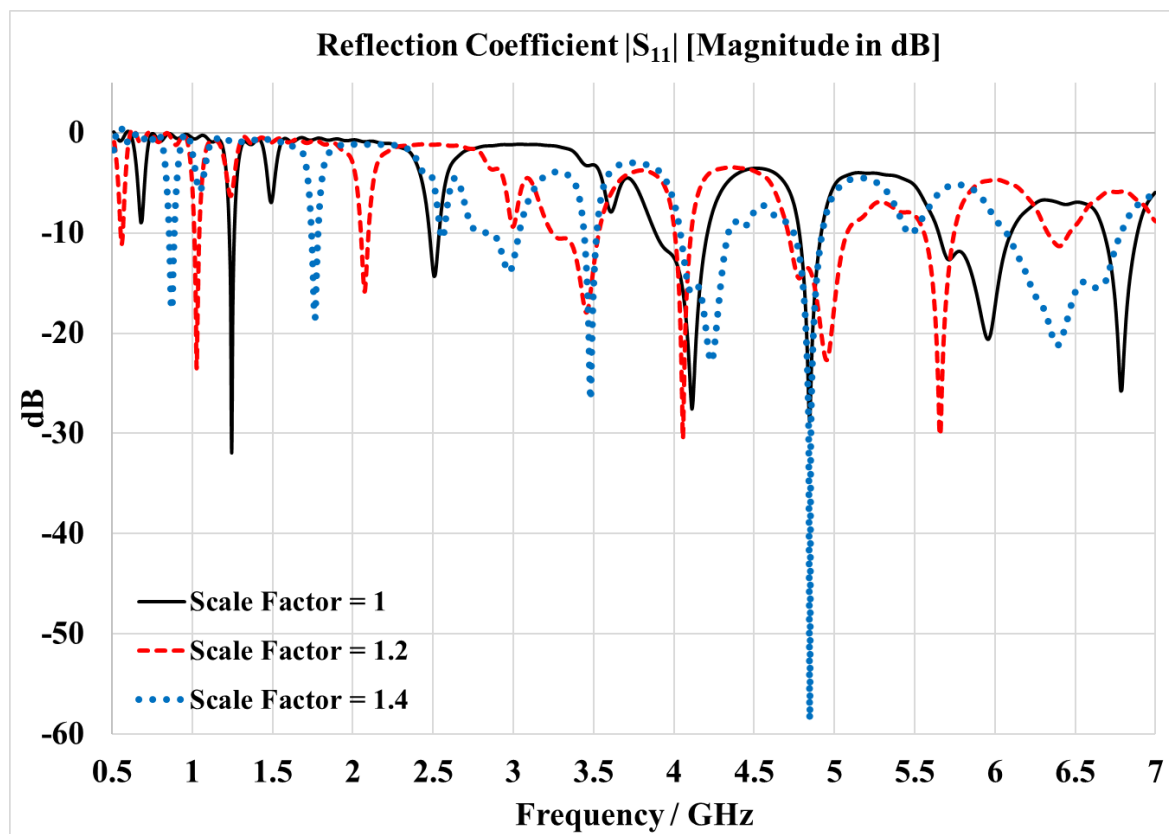


Figure 3.49 The simulated results of the reflection coefficient $|S_{11}|$ for different scale up factors of (Antenna-3-b).

3.4.7 (Antenna-3-b) Optimization

The optimization process for the proposed antenna (Antenna-3-b) was done by employing the simulated results that were collected previously by applying different modifications, including the scaling process and changing the length and width of the antenna feed line, and studying the impacts of each modification on the reflection coefficient $|S_{11}|$. The proposed antenna (Antenna-3-b) is optimized and tuned to target the frequencies of interest that are required for RFEH applications. The resonating frequency of (2.5 GHz) is shifted to the left to be (2.4045 GHz), with significant improvement on the reflection coefficient $|S_{11}|$ value of [-39.77 dB] and an increase in the bandwidth that supports and covers the WLAN-2.4G frequency band, as shown in Table 3-5. Furthermore, the resonating frequency of (5.96 GHz) is shifted to the left to be (5.869 GHz), with significant improvement on the reflection coefficient $|S_{11}|$ value of [-38.05 dB] and wide bandwidth of (510 MHz) that supports and covers a lot of WLAN-5G, WIMAX, and mobile LTE, mobile 5G frequencies. Also, the frequency (4.11 GHz) shifted to the left to be (3.568 GHz), which supports a lot of WIMAX, mobile LTE, and mobile 5G frequencies. The final design of the optimized antenna (Antenna-3-b) was implemented by scaling up the front patch using a scale factor of (1.08) and applying the DGS technique, as shown in Figure 3.50 (b). The feed line length was set to the value of [44.73 mm], and the feed line width was set to the value of [1.14 mm], as shown in Figure 3.50 (a). The simulated results show that the optimized (Antenna-3-b) has major performance improvements compared to the antenna before optimization, as shown in Figure 3.51. Also, Table 3-5 shows more details about the simulated results for the optimized (Antenna 3-b), including resonating frequencies, bandwidth, gain, directivity, and applications for each frequency band.

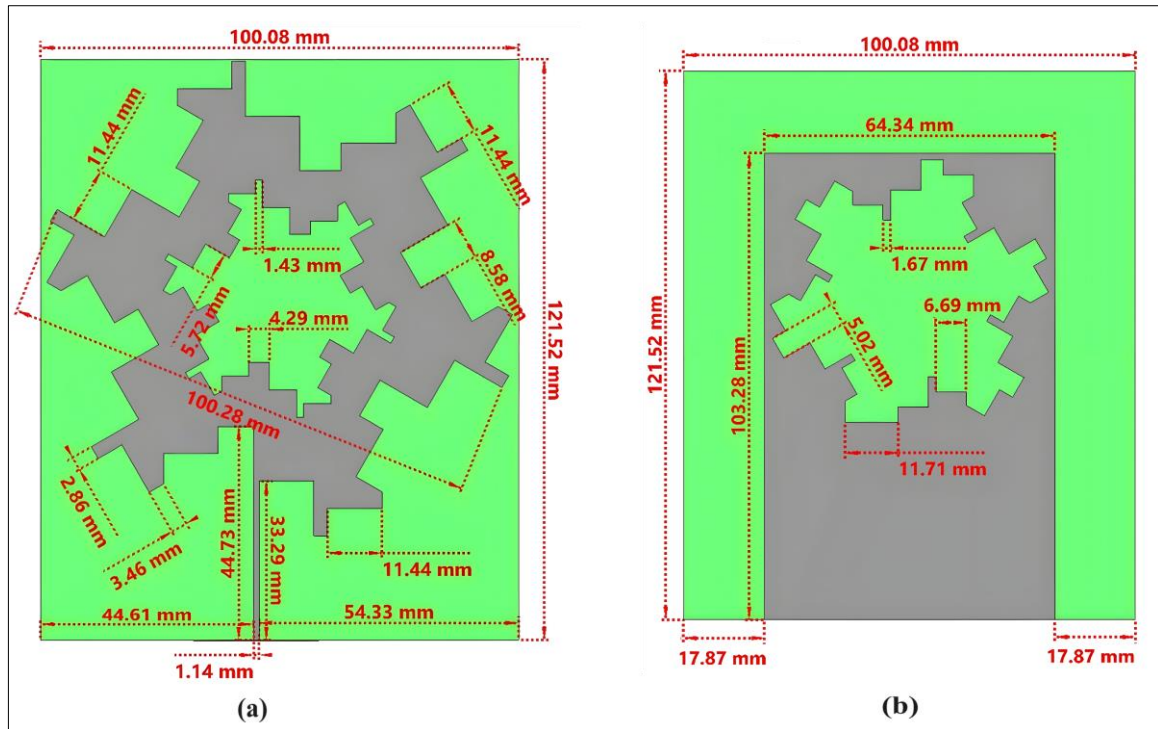


Figure 3.50 The dimensions of the proposed (Antenna-3-b) after optimization: (a) The front patch; (b) The defected ground structure (DGS)

Table 3-5 Simulated results of the proposed (Antenna-3-b) after optimization

Resonating Frequency (GHz)	Return Loss $ S_{11} $ (dB)	Minimum Frequency (GHz)	Maximum Frequency (GHz)	Band width (GHz)	Directivity (dBi)	Peak Gain (dBi)	Applications	Reference
2.4045	-39.77	2.3311	2.4859	0.1548	6.033	3.203 dBi @ 2.4045 GHz	WLAN, mobile LTE, WIMAX, mobile 5G	[54], [55]
3.568	-17.61	3.4892	3.6352	0.146	5.03	1.519 dBi @ 3.568 GHz	mobile LTE, WIMAX, mobile 5G	[54], [55]
4.6405	-12.67	4.5355	4.8874	0.3519	5.909	0.08713 dBi @ 4.6405 GHz	mobile LTE, WIMAX, mobile 5G	[54], [55]
5.869	-38.05	5.7583	6.2684	0.5101	6.434	2.461 dBi @ 5.7583 GHz	WLAN, mobile LTE, WIMAX, mobile 5G	[54], [55]

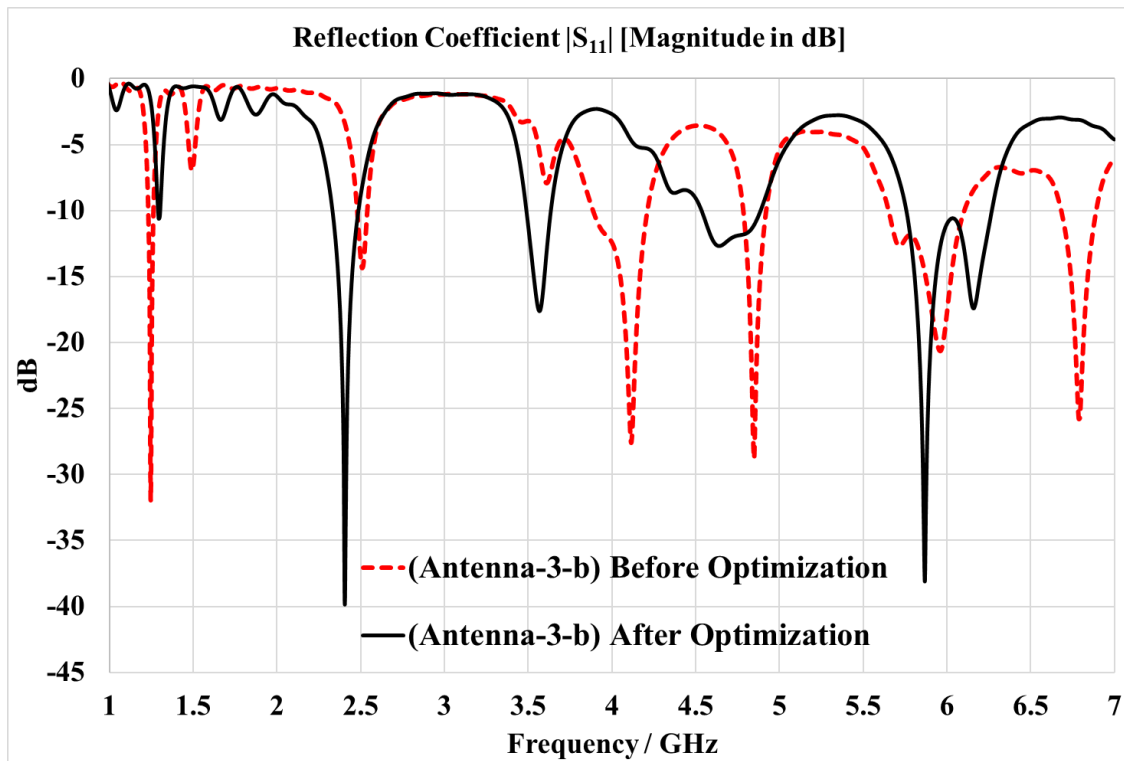


Figure 3.51 The simulated results of the reflection coefficient $|S_{11}|$ for the proposed (Antenna-3-b) before and after optimization.

Furthermore, the simulated results of the optimized antenna (Antenna-3-b) showed that the antenna has achieved a moderate gain for most of the resonating frequencies, with a peak gain of (3.2 dBi) at the frequency of (2.4045 GHz), which is preferable for RFEH applications.

Figure 3.52 shows the simulated 3D radiation pattern of the directivity magnitude in [dBi] for some of the proposed optimized (Antenna-3-b) supported frequencies. Also, Figure 3.53 shows the simulated 2D radiation pattern.

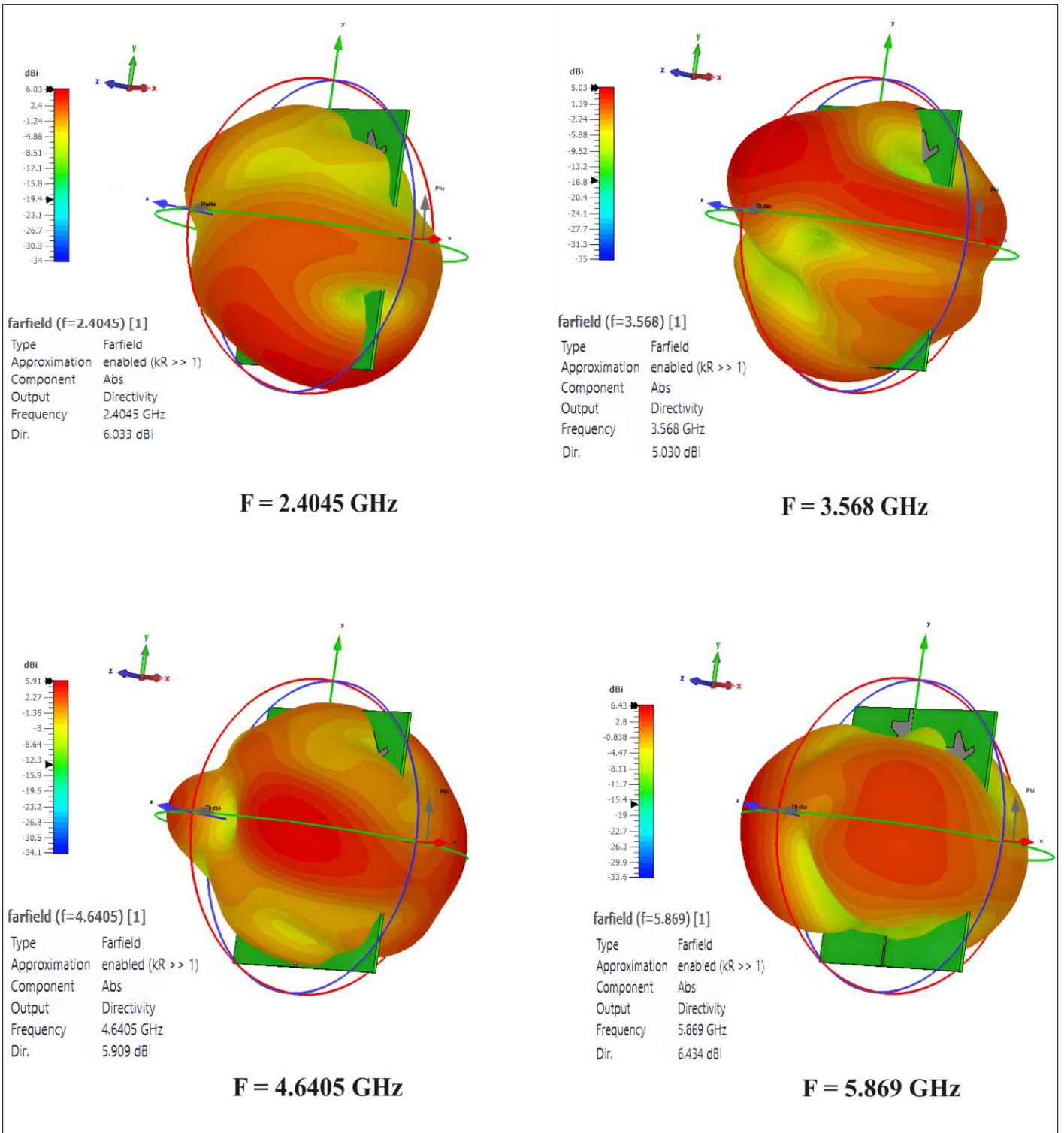


Figure 3.52 The simulated 3D radiation pattern of the directivity magnitude in [dBi] for the optimized (Antenna-3-b) operating frequencies.

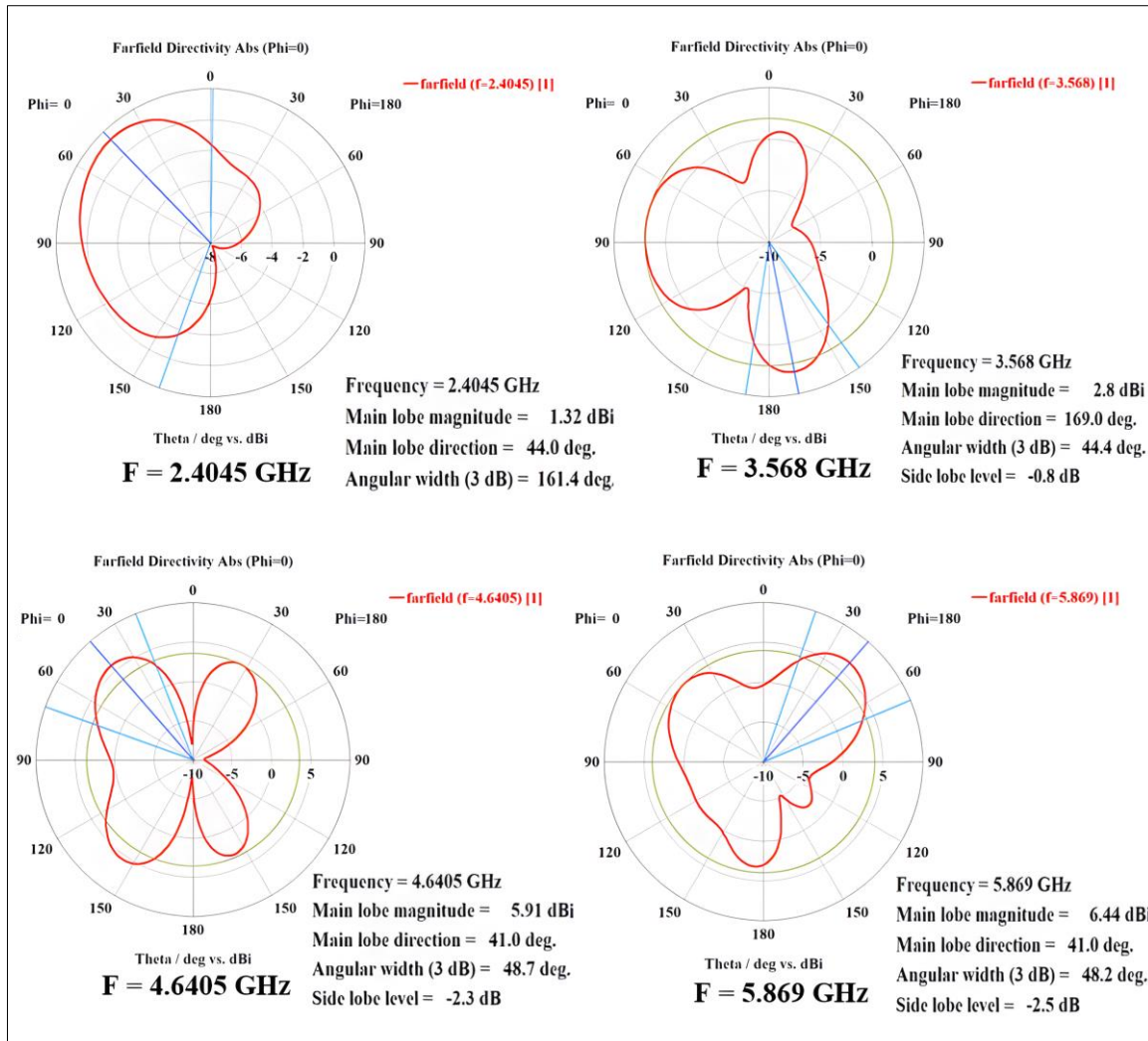


Figure 3.53 The simulated 2D radiation pattern of the directivity magnitude in [dBi] for the optimized (Antenna-3-b) operating frequencies.

Furthermore, the results showed that the proposed antenna has performance improvements compared to other proposed works, since the proposed optimized antenna achieved a good gain for most of its operating frequencies with respect to its size and thickness, given that it has a much smaller substrate area than [13], [14], [16] and is much thinner than [8], [14], [16], and [17], and, also supports more resonating frequencies required for RFEH applications. It should be mentioned as well that the FR-4 substrate is less expensive than the (Rogers RT6002), (Arlon 25N), and (Rogers 3003) substrates, and the gain of any antenna is directly proportional to its physical size and thickness.

3.5 Fabrication and Experimental Results

This section provides a comparison between the simulated results and the experimentally measured results for the optimized final design of each of the multiband antennas that were proposed in this chapter. The measurement results of the reflection coefficient $|S_{11}|$ and the normalized 2D radiation pattern showed acceptable tolerance errors with the simulated results, taking into account the fabrication difficulties due to the fine detail of the geometries that were implemented on all of the proposed antennas, the small slot cuts, soldering effects, and the imperfect testing environment since no fully anechoic chamber was available in the university where the measurement was recorded.

The experimental results of the normalized 2D radiation pattern of each of the fabricated antennas are obtained using a similar antenna that acts as a transmitted antenna supplied with an input power of [7 dBm] and is fixed on a line of sight from the proposed receiving antenna at a distance of [83 cm] to make sure all of the proposed fabricated receiving antennas are located in the far field region. The distance has been calculated using the far-field formula ($R > 2D^2/\lambda$), where (λ) represents the wavelength of the specific measured frequency, (D) is the maximum overall dimension of the fabricated receiving antenna, and (R) is the distance between the transmitted antenna and the receiving antenna.

Furthermore, the device (R&S ZVL vector network analyzer) has been used to measure the reflection coefficient $|S_{11}|$, and the device (Anritsu MS2665C Spectrum Analyzer) has been used to measure the 2D radiation pattern of each of the fabricated receiving antennas.

3.5.1 The experimental results for the optimized Antenna-1.

The measurement results showed good matching with the simulated results in terms of the magnitude of the reflection coefficient $|S_{11}|$ for each resonating frequency, whereas there was shifting for the resonating frequencies 2.424 GHz by 136 MHz, 3.36 GHz by 65 MHz, 3.789 GHz by 169 MHz to the left of the frequency spectrum, and the frequency 5.843 GHz shifted by 510 MHz to the right of the frequency spectrum as shown in Figure 3.54

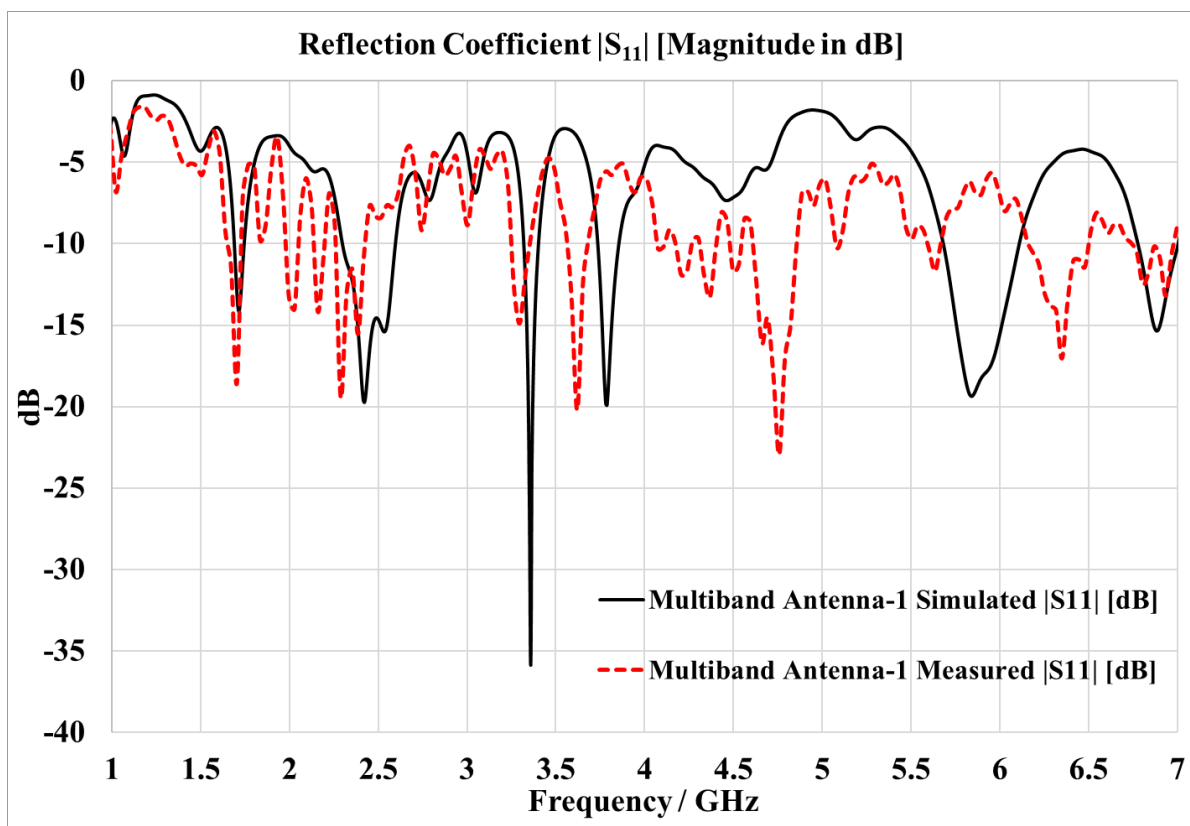


Figure 3.54 The reflection coefficient $|S_{11}|$ for both the simulated and the practical fabricated (Antenna-1).

Furthermore, the measurement results of the normalized 2D radiational pattern showed better matching with the simulated results for the frequency of 3.6 GHz compared to the frequency of 4.7 GHz as shown in Figure 3.55. The physical structure and the testing environment of the proposed (Antenna-1) are shown in Figure 3.56 and Figure 3.57 respectively.

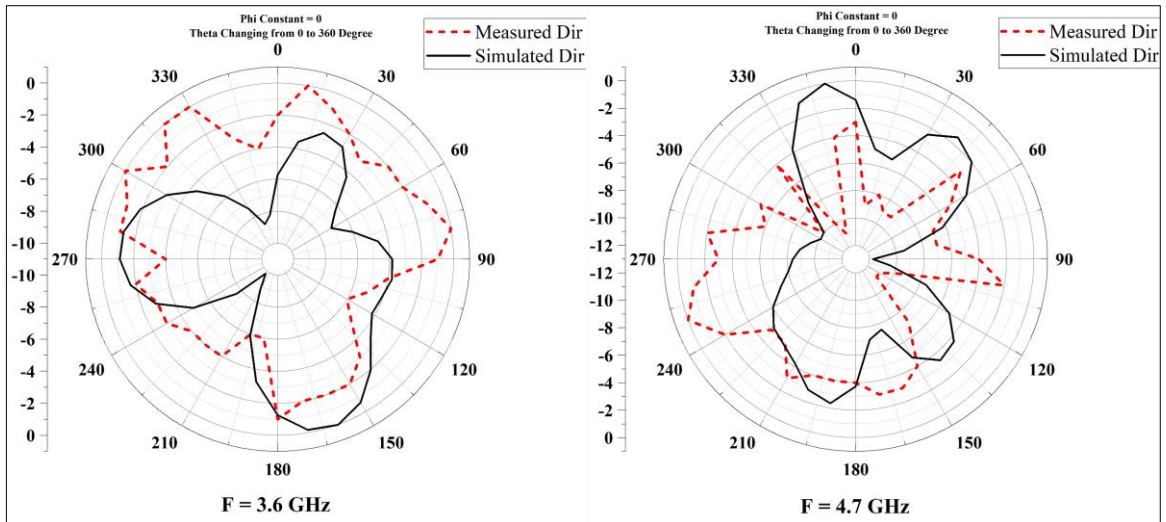


Figure 3.55 The normalized 2D radiational pattern of the directivity for the proposed (Antenna-1) showed the simulated and measured results.

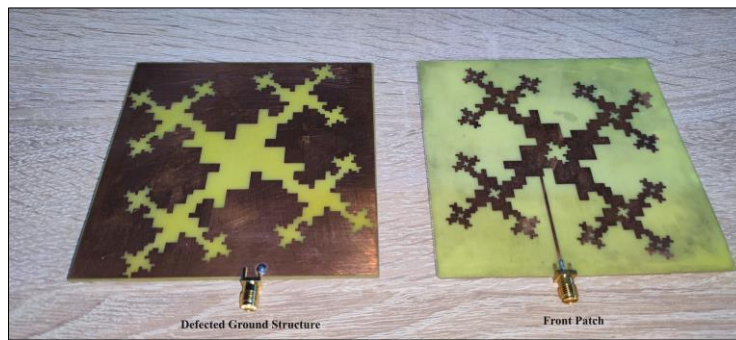


Figure 3.56 The physical structure of the proposed (Antenna-1).

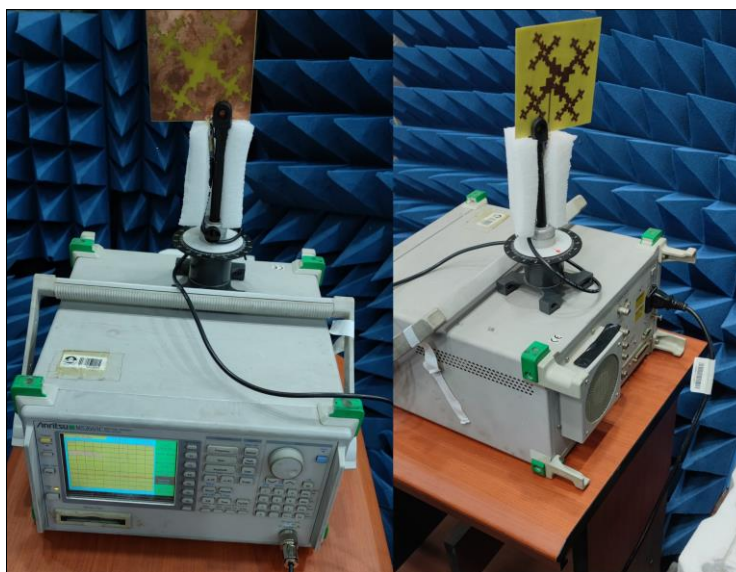


Figure 3.57 The testing environment for the proposed (Antenna-1).

3.5.2 The experimental results for the optimized Antenna-2

The measurement results of the reflection coefficient $|S_{11}|$ showed perfect matching with the simulated results for the resonating frequencies 0.776 GHz, 1.5971 GHz, 1.8455 GHz, 2.4527 GHz, 2.8736 GHz, and 3.191 GHz, whereas there was shifting for the resonating frequencies 5.2058 GHz by 280 MHz and 6.9584 GHz by 490 MHz to the left of the frequency spectrum as shown in Figure 3.58

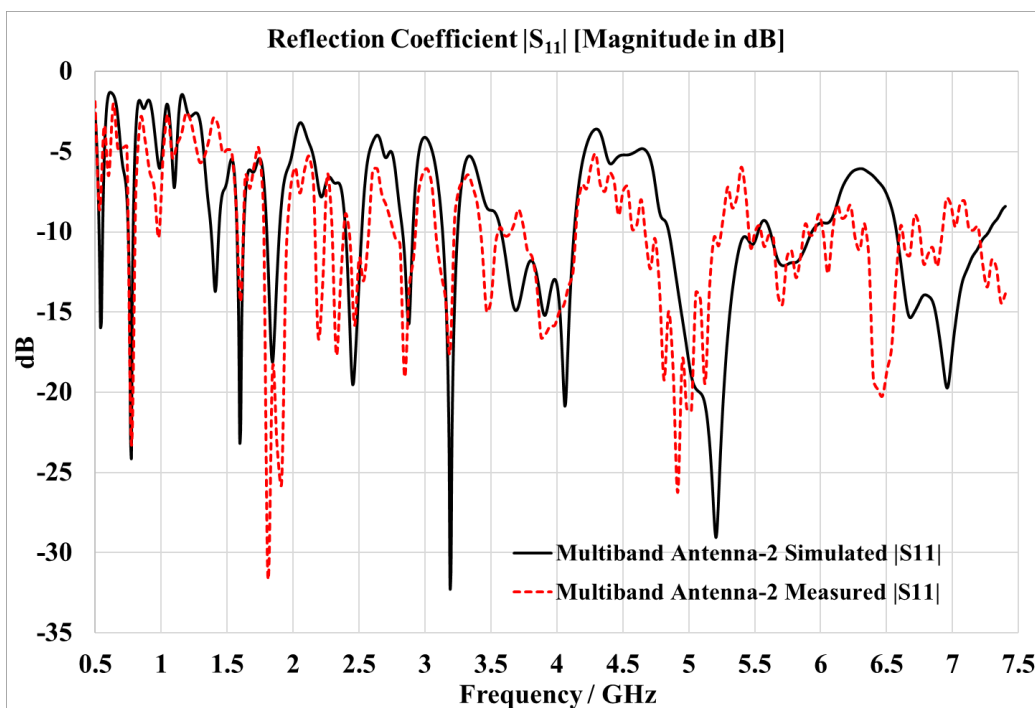


Figure 3.58 The reflection coefficient $|S_{11}|$ for both the simulated and the practical fabricated (Antenna-2).

Furthermore, the measurement results of the normalized 2D radiational pattern showed good matching for the frequency of 2.4 GHz since there was only a shift of 30-degree clockwise compared with the simulated results, The measurement results showed better matching with the simulated results for the frequency of 2.4 GHz compared to the frequency of 5 GHz as shown in Figure 3.59. The physical structure and the testing environment of the proposed (Antenna-2) are shown in Figure 3.60 and Figure 3.61 respectively.

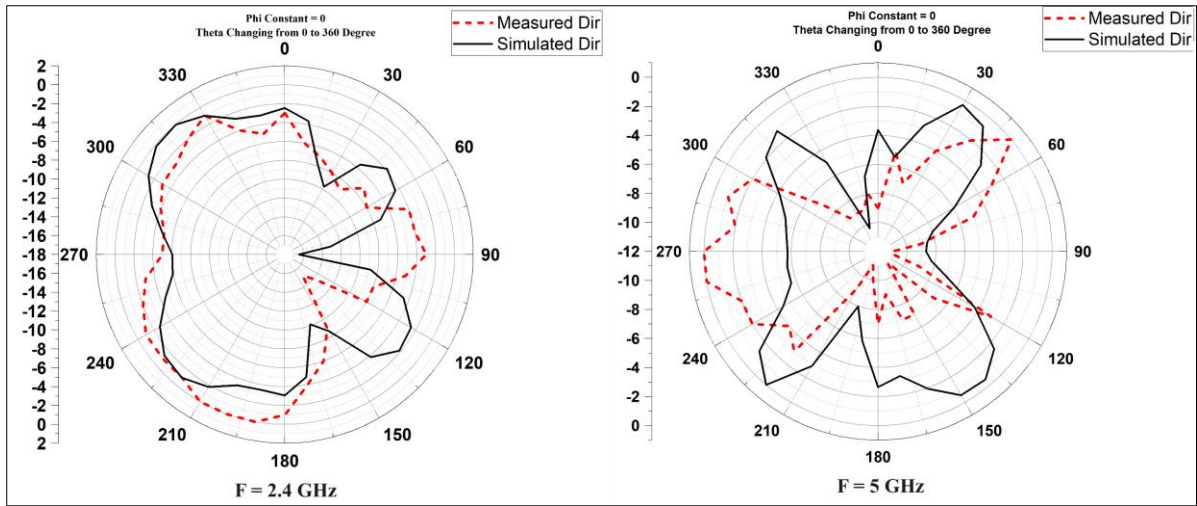


Figure 3.59 The normalized 2D radiational pattern of the directivity for the proposed (Antenna-2) showed the simulated and measured results.

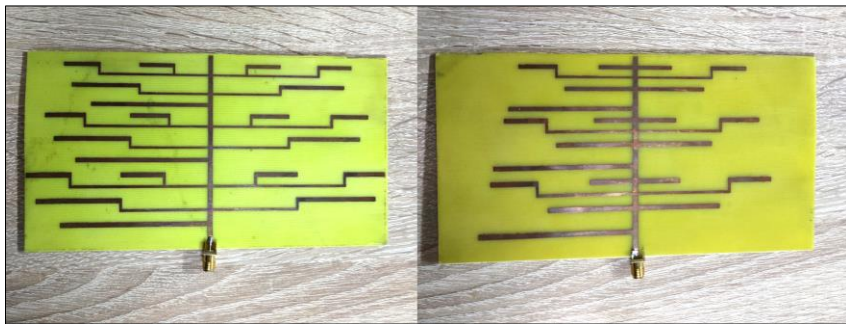


Figure 3.60 The physical structure of the proposed (Antenna-2).

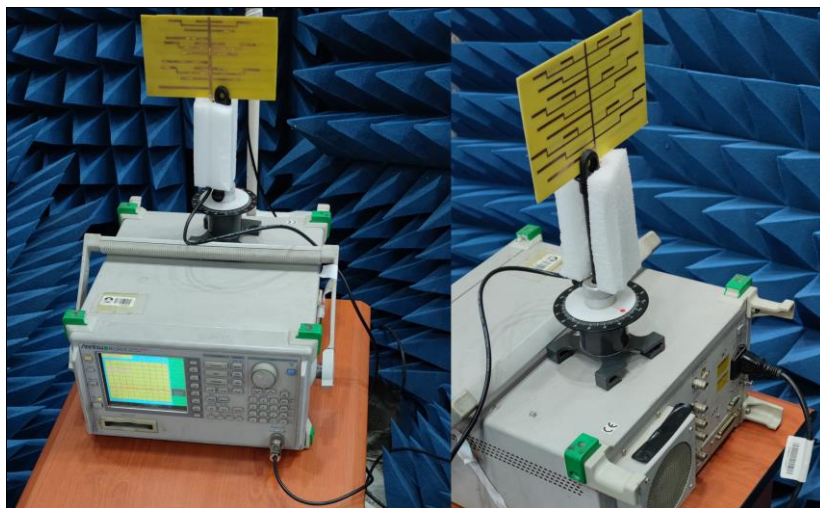


Figure 3.61 The testing environment used to measure the normalized 2D radiation pattern for the proposed (Antenna-2).

3.5.3 The experimental results for the optimized Antenna-3

The measurement results of the reflection coefficient $|S_{11}|$ showed shifting the resonating frequencies of 2.4045 GHz by 200 MHz and 5.869 GHz by 500 MHz to the right of the frequency spectrum. whereas shifting the resonating frequency of 4.6405 GHz by 78 MHz to the left of the frequency spectrum as shown in Figure 3.62.

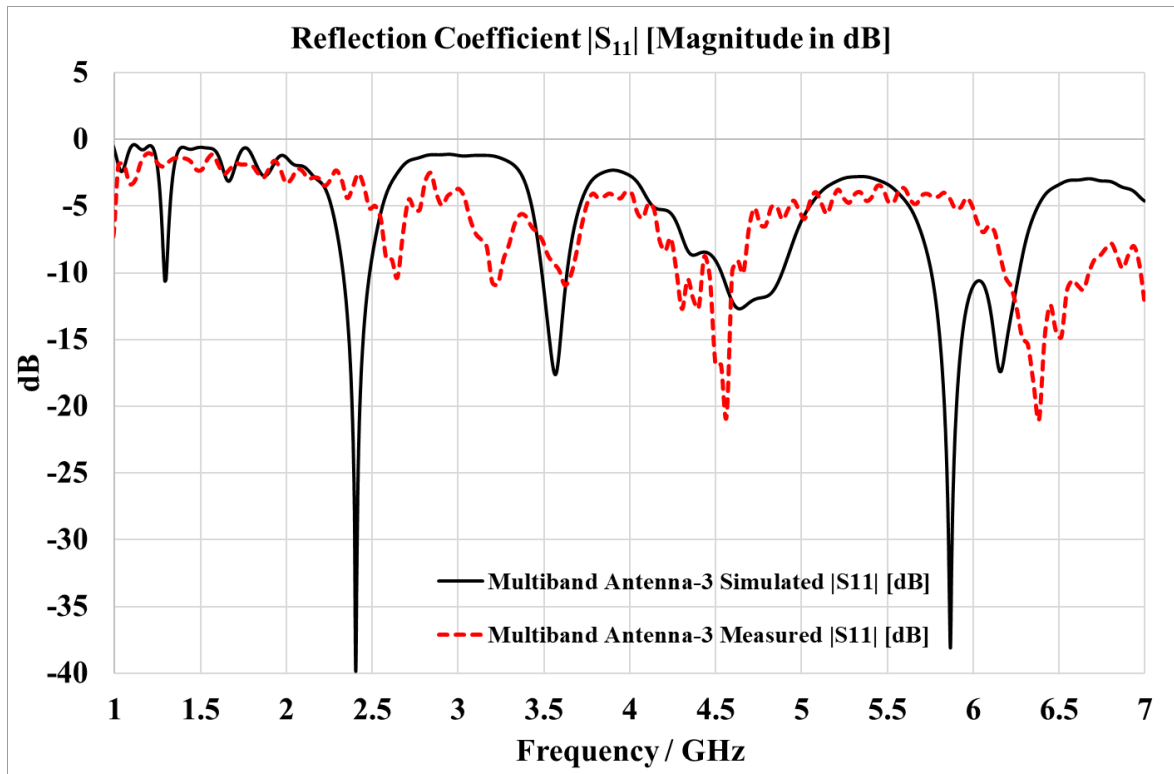


Figure 3.62 The reflection coefficient $|S_{11}|$ for both the simulated and the practical fabricated (Antenna-3).

The measurement results of the normalized 2D radiational pattern showed better matching with the simulated results for the frequency of 4.6 GHz compared to the frequency of 3.6 GHz as shown in Figure 3.63. The physical structure and the testing environment of the proposed (Antenna-3) are shown in Figure 3.64 and Figure 3.65 respectively.

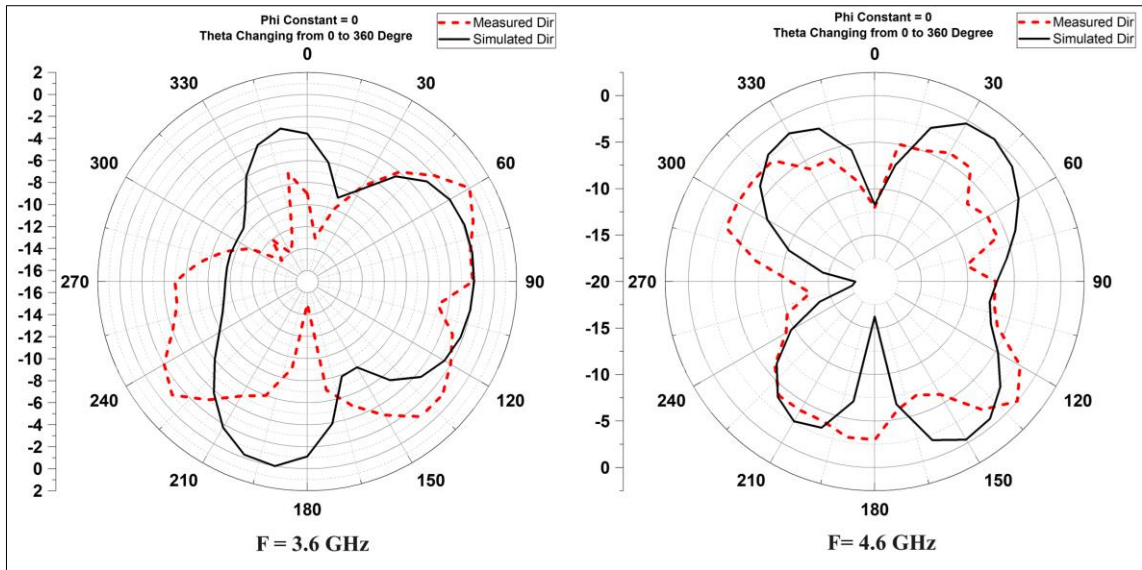


Figure 3.63 The normalized 2D radiational pattern of the directivity for the proposed (Antenna-3) showed the simulated and measured results.

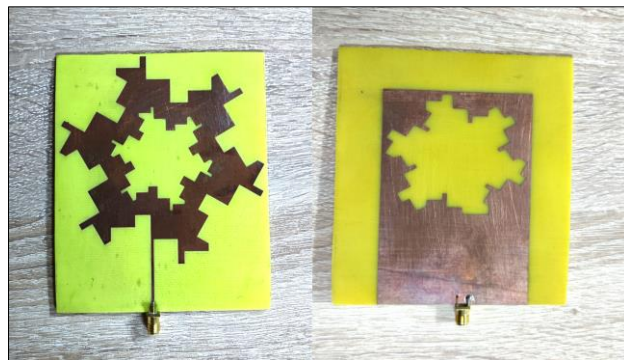


Figure 3.64 The physical structure of the proposed (Antenna-3).

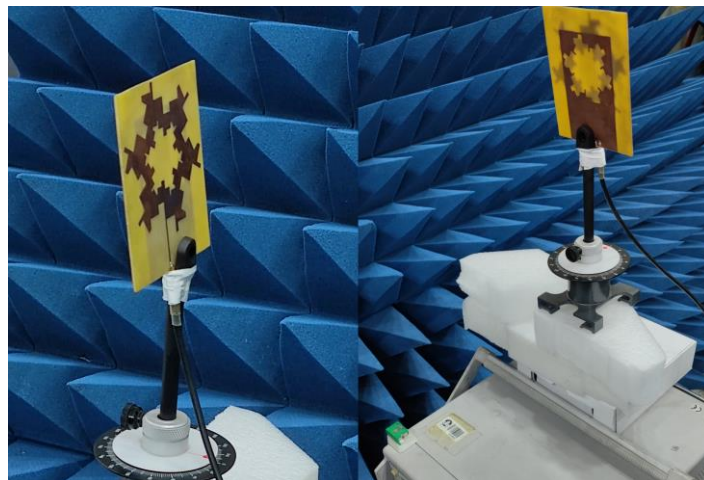


Figure 3.65 The testing environment used to measure the normalized 2D radiation pattern for the proposed (Antenna-3).

Chapter Four

Design, Simulation, and Implementation of Wideband Antennas for Radio Frequency Energy Harvesting Applications

4.1 Introduction

The variety of frequency band assignments for each wireless service in different countries makes wideband antennas suitable for RFEH systems since they support a wide range of frequencies and can be utilized in multiple nations [34]. Different wideband antennas for RFEH systems are introduced by the researchers [18], [57]-[59]. Three proposed wideband antennas are introduced in this chapter that support a lot of frequency bands that are required for RFEH systems, including WLAN-2.4G, WLAN-5G, WLAN-6G, Mobile LTE, Mobile 5G, and WIMAX services.

The first wideband antenna (Antenen-4) is a compact patch antenna with a modified ground structure constructed based on the concepts of the conventional Vivaldi antenna. The second wideband antenna (Antenen-5) is a modified square monopole patch antenna with a (CPW)-feeding technique. The third wideband antenna (Antenna-6) is a modified hexagonal monopole patch antenna with a (CPW)-feeding technique. All three proposed wideband antennas in this chapter are simulated using the (CST) Studio Suite software, then fabricated using PCB technology on FR-4 substrate due to its light weight, low cost, and low profile, with a dielectric constant $\epsilon_r = 4.3$, a thickness of 1.6 mm, and a loss tangent (δ) of 0.025.

4.2 (Antenna-4) a compact patch antenna with a modified structure

4.2.1 Design Fractal Shape 2

The design of the novel shape starts with an initiator line with a length of (L), as shown in Figure 4.1(a). The first iteration translates the initiator line into seven equal lines with a length of ($L/7$) for each of them to form the shape shown in Figure 4.1(b). The next step is to expand the shape of the first iteration by two operations. The first is to mirror the shape of the first iteration on the y -axis as shown in Figure 4.1(c), then mirror it on the x -axis to form the shape shown in Figure 4.1(d). The final shape is shown in Figure 4.1(e).

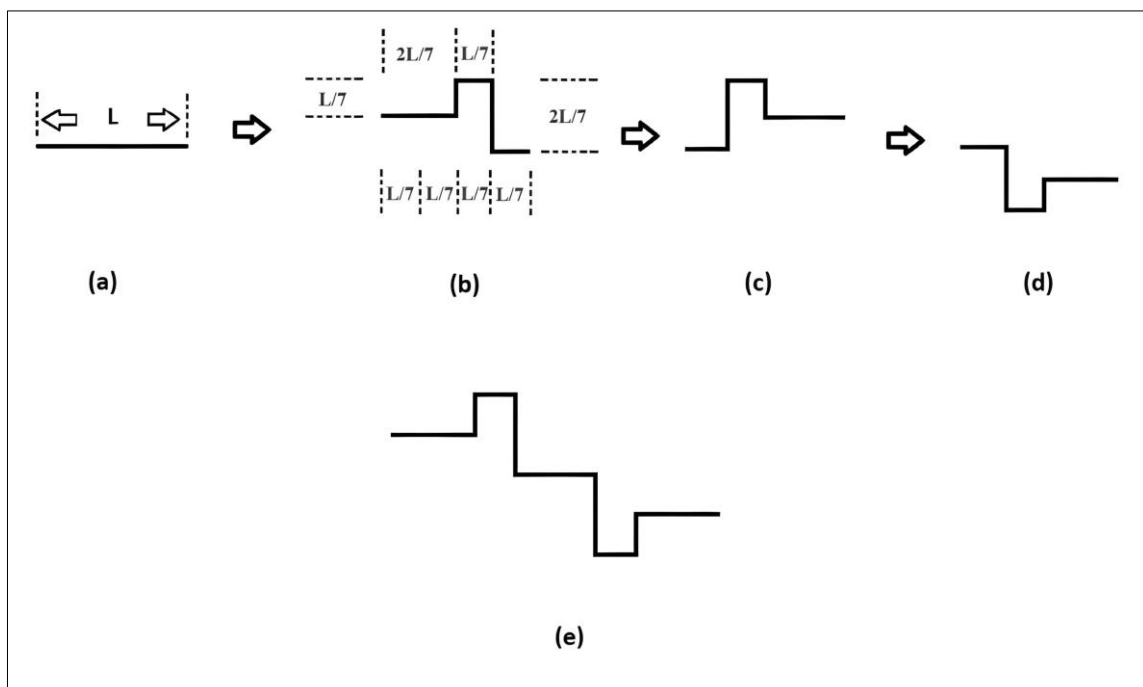


Figure 4.1 Fractal shape design 2: (a) initiator line; (b) first iteration; (c) mirror shape (b) on y -axis; (d) mirror shape (c) on x -axis; (e) final shape design.

4.2.2 Design and Construction

The first step of the design started by selecting (2.4 GHz) as the target operating frequency, since it's the most widely used frequency for WLAN services. The second step is to calculate the halfwave length ($\lambda/2$) of the target frequency using equation (4-1) and it is equal to (30.1 mm) [56]. The previous calculation was used to select a reasonable value for the distance between the two opposite modified radiation tapered structures for the proposed antenna (Antenna-4) since the distance between the two opposite exponential tapered curves of the conventional Vivaldi antenna should be greater than the halfwave length ($\lambda/2$) of the lowest operating frequency [60]-[62]. The next step is to create two modified radiation tapered structures that are opposite to each other's and act as a ground by gradually increasing the number of the modified shapes that were created previously in Figure 4.1(e) and attaching them to each other with a total length of initiator line $L = [4.9 \text{ mm}]$ to form the two modified opposite radiation tapered structures shown in Figure 4.2. The conventional Vivaldi patch antenna consists of two opposite ground radiators with flare shapes, which are formed by two exponential tapered slot curves on one side of the substrate and a microstrip feed line on the other side of the substrate.

$$\lambda = \frac{C}{\sqrt{\epsilon_r} F} \quad (4 - 1)$$

Where:

C = The speed of light. [meter / second]

λ = The maximum operating wavelength. [meter]

F = The operating frequency. [hertz]

ϵ_r = Dielectric constant

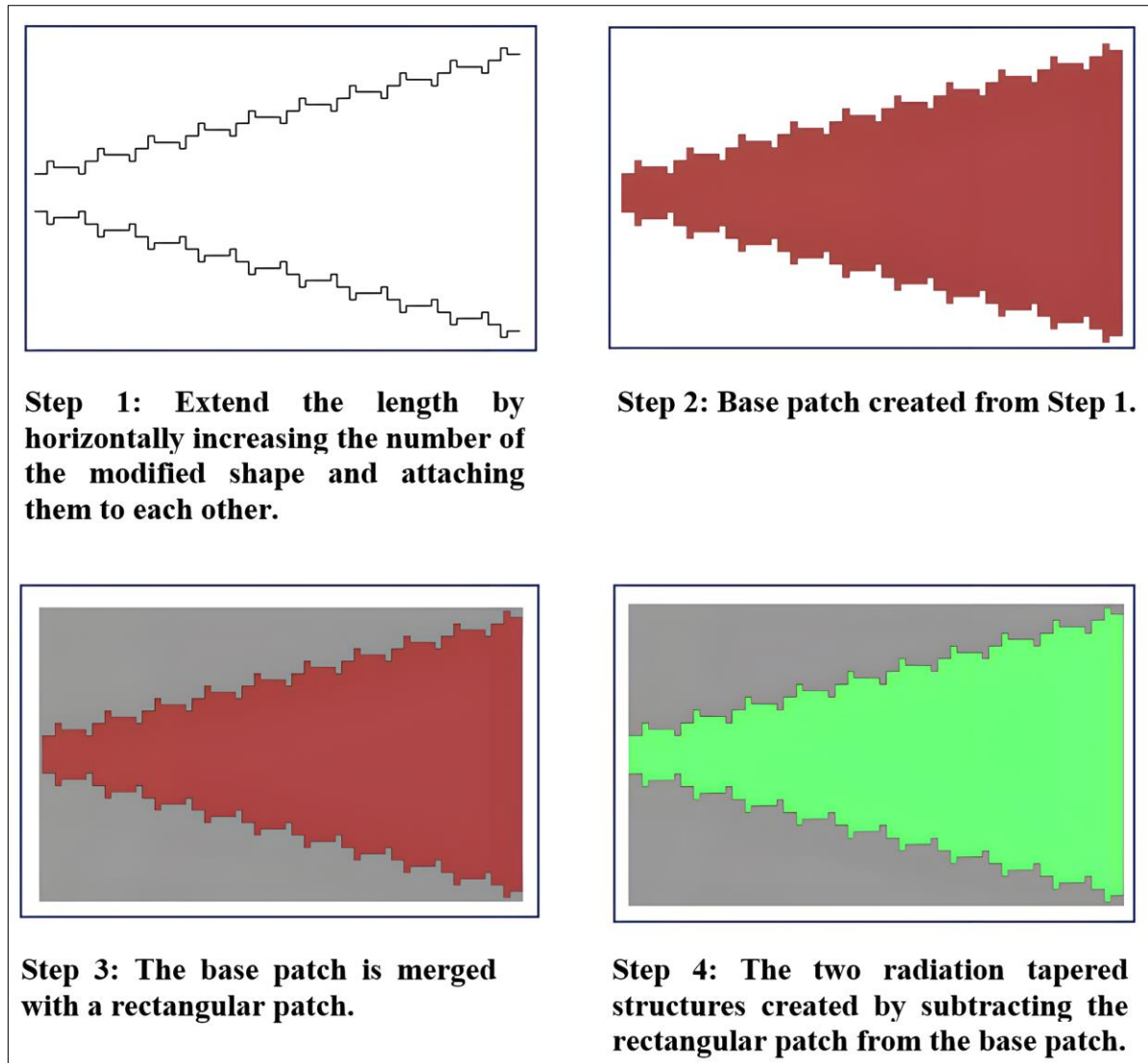


Figure 4.2 Construction steps for creating the two modified radiation tapered structures of the proposed (Antenna-4).

The substrate dimensions for the proposed (Antenna-4) are [58.87 mm] of width, [32.94 mm] of length, and [1.6 mm] of thickness, respectively. Also, the dimensions of the microstrip feed line are designed to be [6.05 mm] of width, [22.25 mm] of length, and [0.035 mm] of thickness, respectively. Furthermore, perfect electrical conductor (PEC) material is selected for creating the two modified radiation tapered structures and the microstrip feed line with [0.035 mm] of thickness during the simulation. The dimensions of the proposed (Antenna-4) are shown in Figure 4.3.

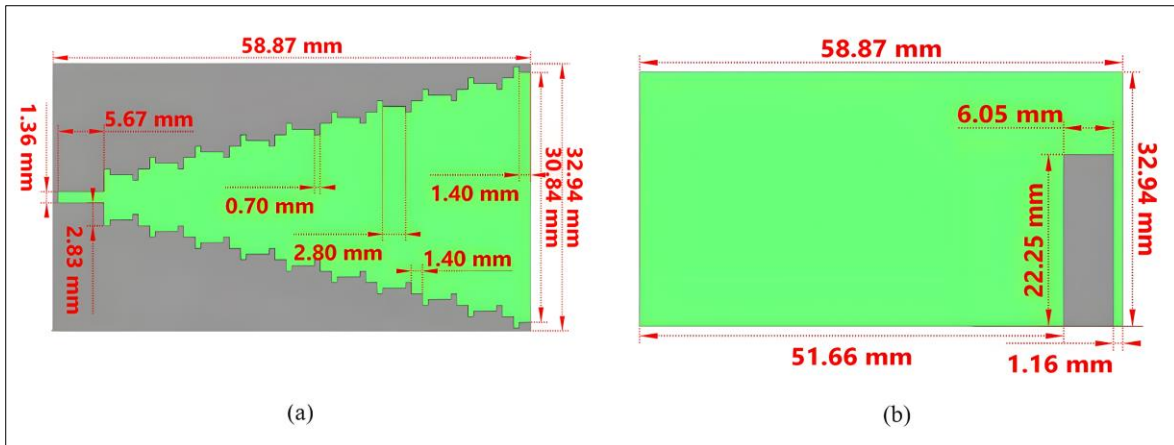


Figure 4.3 Dimensions of the proposed (Antenna-4): (a) the two opposite modified radiation tapered structures; (b) the microstrip feed line.

4.2.3 Simulated Results for the Proposed Antenna-4

The simulated results for the reflection coefficient $|S_{11}|$ show that the proposed antenna (Antenna-4) has a dual-band feature, as shown in Figure 4.4. The first frequency band (2.347 GHz - 3.4283 GHz) has a resonance frequency of 2.48 GHz. The second frequency band (4.9532 GHz - 5.57 GHz) has a resonance frequency of 5.232 GHz. All the frequency ranges that are supported by the (Antenna-4) are required for RFEH applications since it supports a wide range of RF wireless services, including WLAN, WIMAX, mobile LTE, and mobile 5G. Also, the simulated result agrees with the calculated result and confirms that the distance between the two opposite radiation tapered structures of the proposed (Antenna-4) approximately represents the half wave length ($\lambda/2$) of the lowest operating frequency (2.347 GHz) since the calculation using equation (4-1) results in half wave length ($\lambda/2$) equal to [30.1 mm] and the distance between the two opposite radiation tapered structures equal to [30.84 mm] as shown in Figure 4.3.

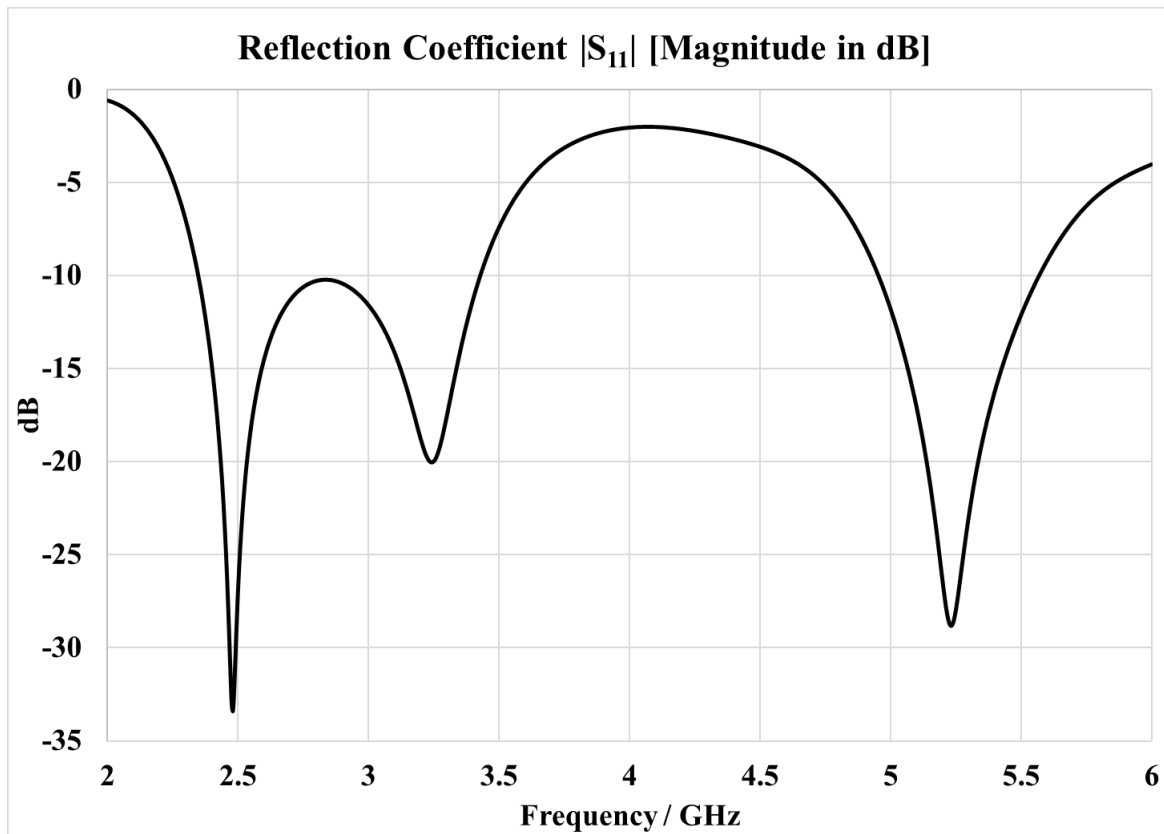


Figure 4.4 Simulated result of the reflection coefficient $|S_{11}|$ for the proposed (Antenna-4).

The simulated results showed that the proposed (Antenna-4) has high gain compared to its physical size since the antenna is designed with a compact substrate dimension of [58.87 mm] of width, [32.94 mm] of length, and [1.6 mm] of thickness, respectively. The antenna theory states that there is a trade-off between the antenna gain and its size [37]. In addition, the simulated results showed that the proposed antenna (Antenna-4) has a high gain of (3.2 dBi) at the frequency of 3.2 GHz, (4 dBi) at the frequency of 5.4 GHz, (2.865 dBi) at the frequency of 2.4 GHz, and (2.287 dBi) at the frequency of 2.8 GHz. Table 4-1 demonstrates more details about the simulated results of the proposed Antenna-4.

Table 4-1 Simulated results for the proposed (Antenna-4)

Resonating Frequency (GHz)	Return Loss $ S_{11} $ (dB)	Minimum Frequency (GHz)	Maximum Frequency (GHz)	Band Width (GHz)	Directivity (dBi)	Peak Gain (dBi)	Applications	Reference
2.48	-33.4	2.347	3.4283	1.0813	4.394	3.2 dBi @ 3.2 GHz	WLAN, WIMAX, Mobile LTE, Mobile 5G	[54], [55]
5.232	-28.2	4.9532	5.57	0.6168	5.309	4 dBi @ 5.4 GHz		

4.2.4 Parametric Analysis for the Proposed Antenna-4

A. Impact of Changing the Width of the Microstrip Feed Line

Figure 4.5 shows simulated results for the reflection coefficient $|S_{11}|$ magnitude in [dB] for different width values of the antenna feed line. The results showed the best feeding line width value was [6.05 mm].

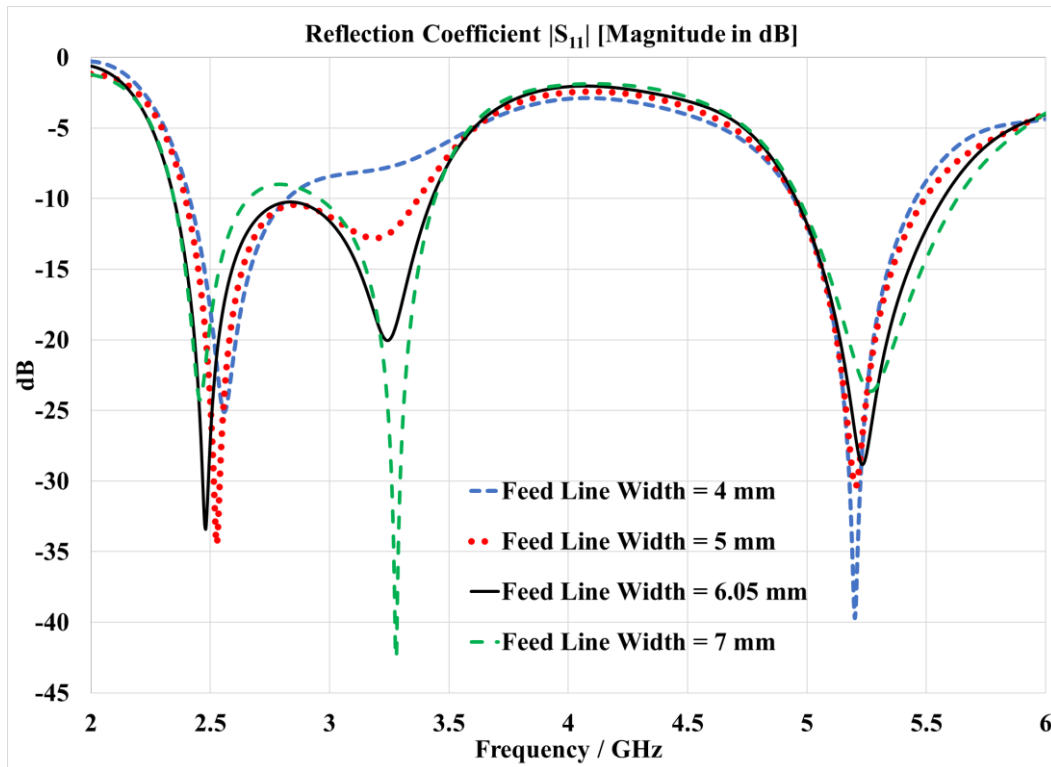


Figure 4.5 Simulated result of the reflection coefficient $|S_{11}|$ for the proposed (Antenna-4) for different width values of the antenna feed line.

B. Impact of Changing the Length of the Microstrip Feed Line

Figure 4.6 shows simulated results for the reflection coefficient $|S_{11}|$ magnitude in [dB] for different length values of the antenna feed line. The results showed the best feeding line length value was [22.25 mm].

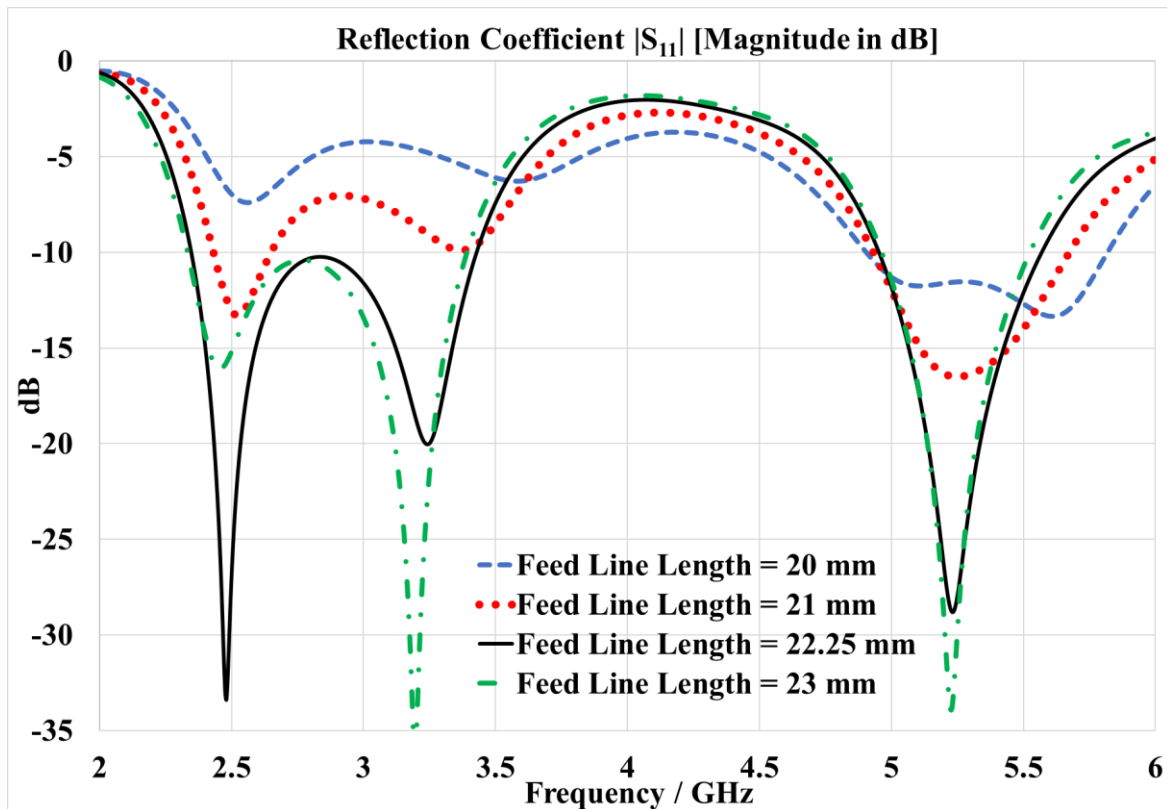


Figure 4.6 Simulated result of the reflection coefficient $|S_{11}|$ for the proposed (Antenna-4) for different length values of the antenna feed line.

C. Impact of Decreasing the Number of the Modified Shape

Figure 4.7 shows the simulated results for the reflection coefficient $|S_{11}|$ magnitude in [dB] when decreasing the number of the modified shapes that were used to create the two modified radiation tapered structures, which act as a ground for the proposed (Antenna-4). Decreasing the number of the modified shape will result in a decrease in the distance between the two modified radiation tapered structures, resulting to shifting all antenna resonating frequencies to the right of the frequency spectrum. since this distance represents the antenna maximum halfwave length ($\lambda/2$) that is inversely proportional to the lowest operating frequency.

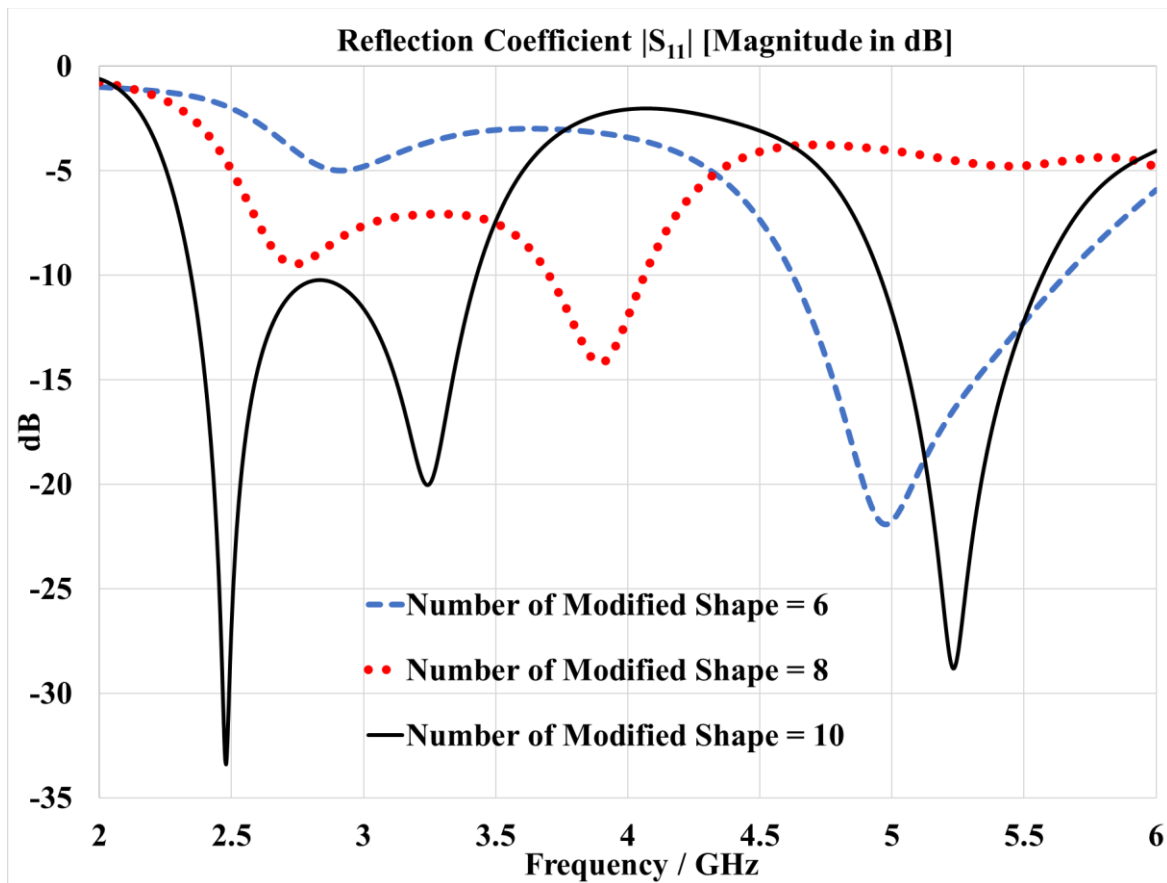


Figure 4.7 Simulated result of reflection coefficient $|S_{11}|$ for the proposed (Antenna-4) for different number of modified shapes.

D. Impact of Scaling-Up the Proposed (Antenna-4)

Figure 4.8 shows the simulated results for the reflection coefficient $|S_{11}|$ magnitude in [dB] for different scale-up factors (1), (1.1), and (1.2). It's clear from the simulation results that when increasing the scale of the proposed (Antenn-4), all the resonating frequency values will decrease and will be shifted to the left of the frequency spectrum. This will confirm that when the scale of the antenna increases, the electrical lengths of the antenna will increase, resulting in a decrease in the resonating frequency values since the frequency is inversely proportional to the wavelength of the signal (λ).

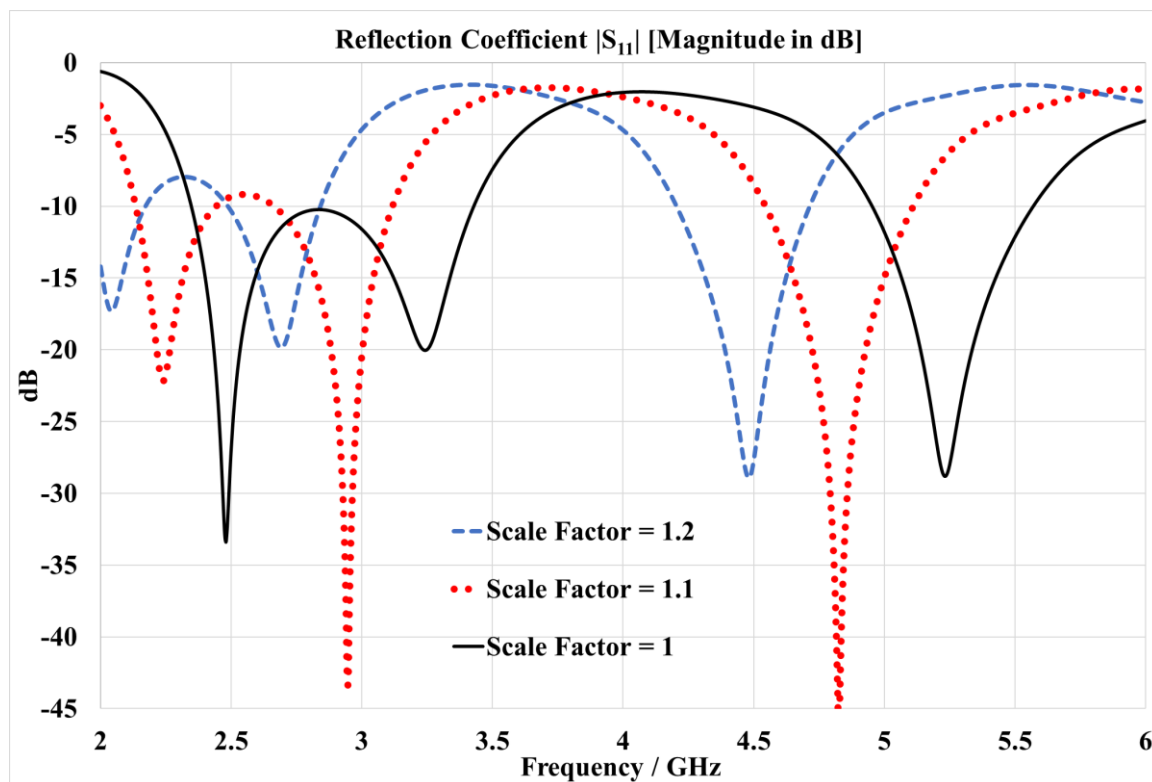


Figure 4.8 Simulated result of reflection coefficient $|S_{11}|$ for the proposed (Antenna-4) for different scale-up factors.

E. Impact of Scaling-Down the Proposed (Antenna-4)

Figure 4.9 shows the simulated results for the reflection coefficient $|S_{11}|$ magnitude in [dB] for different scale-down factors (1), (0.9), and (0.8). It's clear from the simulation results that when decreasing the scale of the proposed antenna (Antenn-4), all the resonating frequency values will increase and will be shifted to the right of the frequency spectrum. Also, the resonating frequency (5.232 GHz) disappeared since the frequency spectrum range studied was between 2 GHz and 6 GHz. This will confirm that when the scale of the antenna decreases, the electrical lengths of the antenna will decrease, resulting in an increase in the resonating frequency values since the frequency is inversely proportional to the wavelength of the signal (λ).

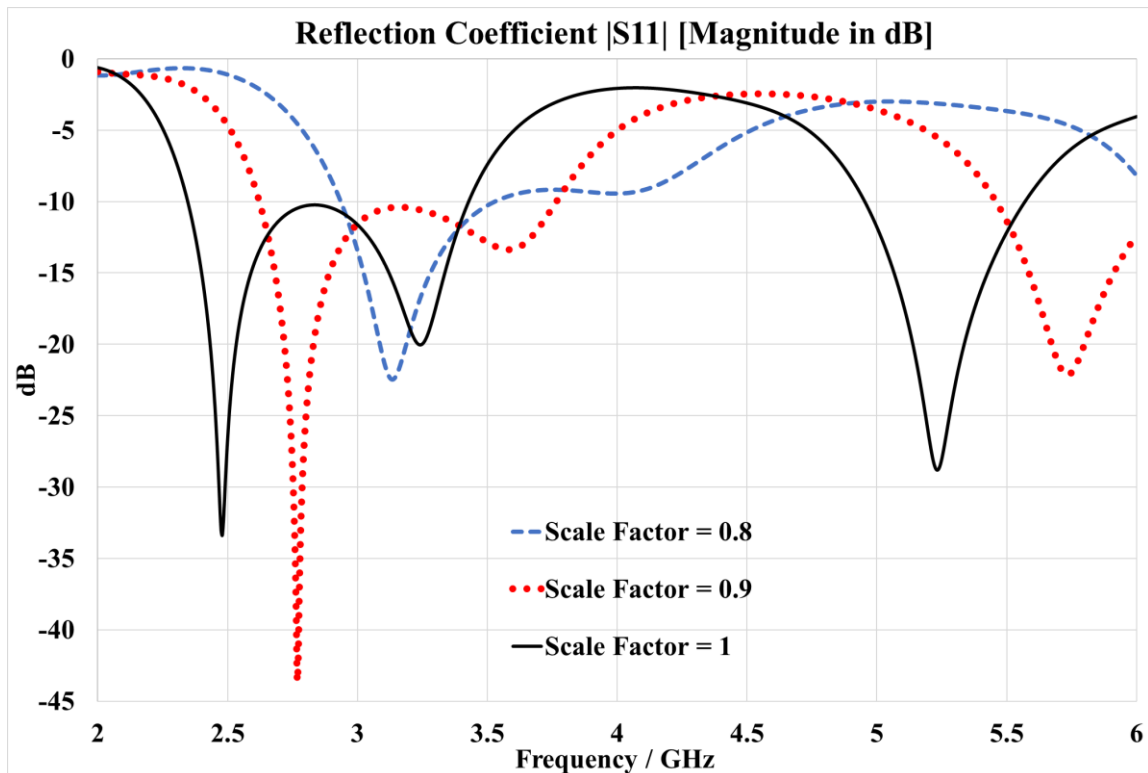


Figure 4.9 Simulated result of reflection coefficient $|S_{11}|$ for the proposed (Antenna-4) for different scale-down factors.

4.2.5 Simulated Radiation Pattern for the Proposed (Antenna-4)

Figure 4.10 demonstrates the simulated 3D radiation pattern of the directivity magnitude in [dBi] for some of the proposed (Antenna-4) supported frequencies. Also, Figure 4.11 demonstrates the simulated 2D radiation pattern.

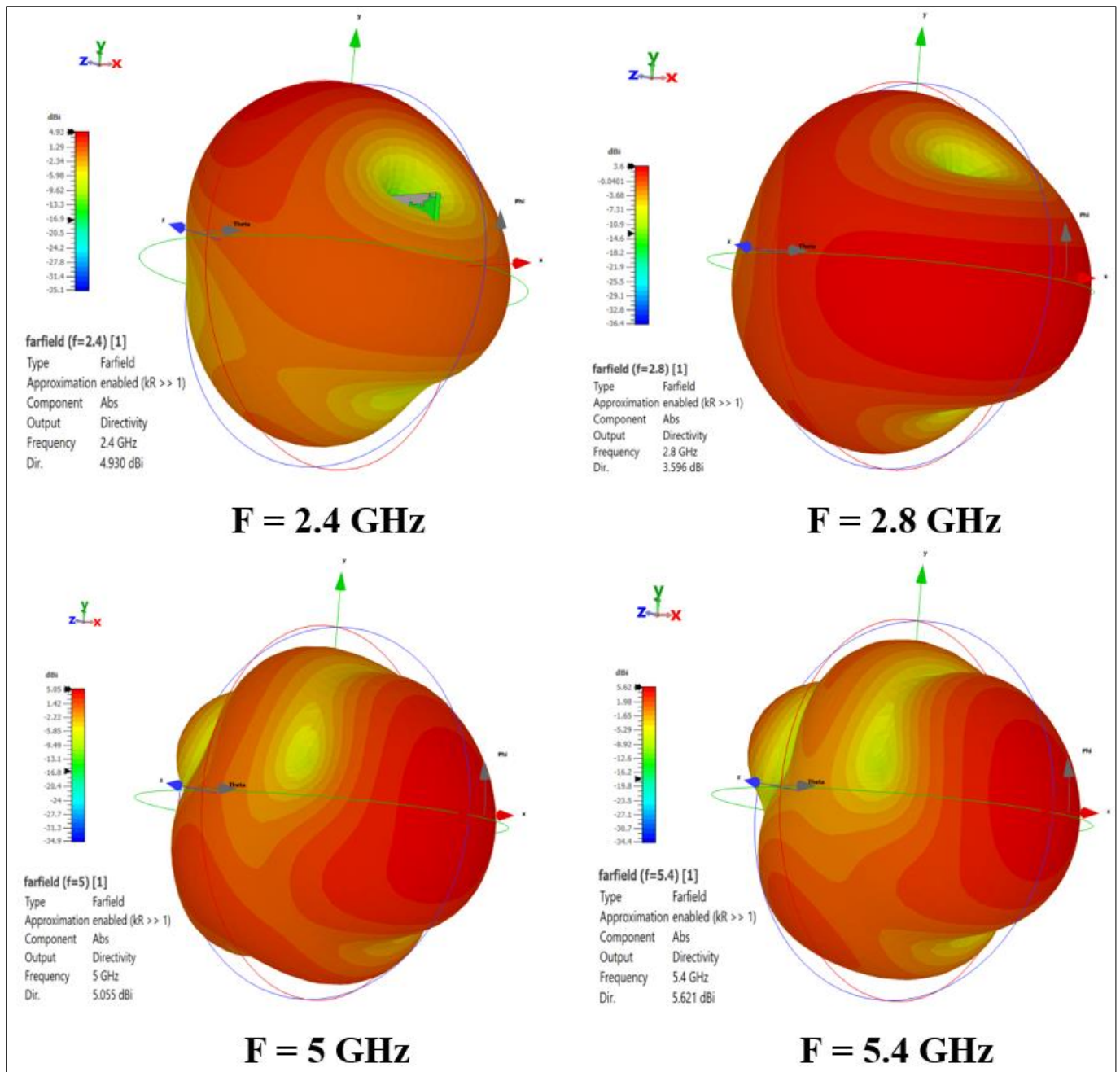


Figure 4.10 Simulated 3D radiation pattern of the directivity magnitude in [dBi] for the proposed (Antenna-4).

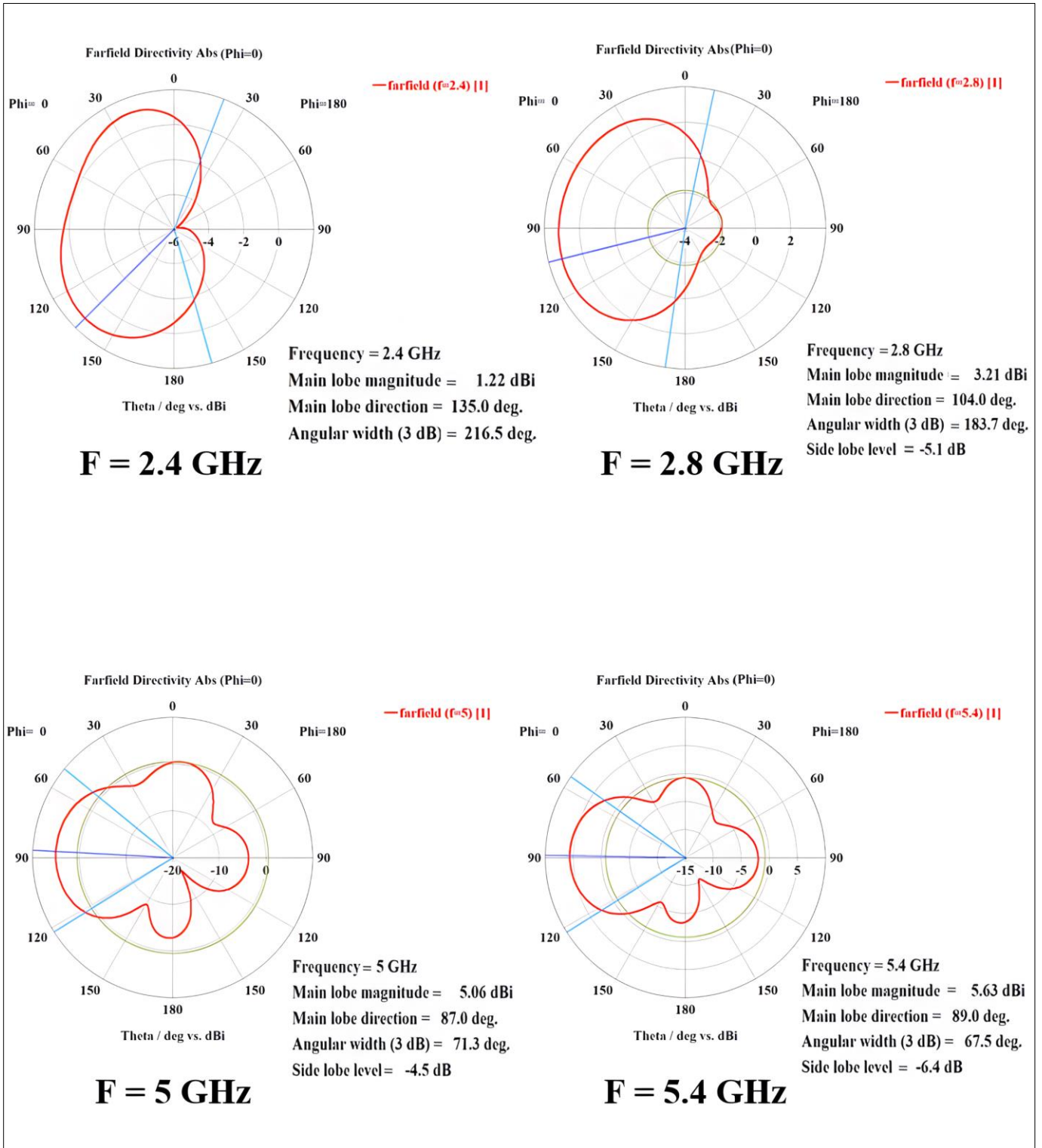


Figure 4.11 Simulated 2D radiation pattern of the directivity magnitude in [dBi] for the proposed (Antenna-4).

4.3 (Antenna-5) a Modified Square Monopole Patch Antenna with (CPW) Feeding Technique

4.3.1 Design and Construction

Wideband antennas can be constructed by combining a fractal shape with one of the different geometric shapes (triangle, square, pentagonal, hexagonal, nonagonal, etc.) [63]. Many antennas' structures could be created by combining the novel fractal shape 1 shown in Figure 3.1 in Chapter 3 with one of the geometrical shapes shown in Figure 3.2. The first step of designing the monopole patch of the proposed (Antenna-5) is implemented by using the modified square patch shown in Figure 3.2 (b), which is created by replacing the four standard square patch sides with the novel fractal shape 1 shown in Figure 3.1(e) to create the modified square patch shown in Figure 3.2(b). Additionally, a (CPW) feeding technique is implemented for antenna excitation [64]. The proposed (Antenna-5) has been designed and simulated with CST Studio Suite software. A standard FR-4 substrate with $\epsilon_r = 4.3$, a thickness of 1.6 mm, and a loss tangent (δ) of 0.025 was utilized. The proposed (Antenna-5) is implemented on a substrate with dimensions of [119.07 mm] of length, [92.61 mm] of width, and [1.6 mm] of thickness, respectively, with a microstrip feed line length of [48.96 mm] and width of [2.65 mm]. Also, two symmetrical rectangular ground planes with dimensions of [44.32 mm] of width and [11.91 mm] of length were implemented on the front side of the substrate adjacent to the microstrip feed line, as shown in Figure 4.12. The proposed (Antenna-5) is designed for RFEH applications and tuned to target the required frequencies for radio RFEH applications, including WLAN-2.4G, WLAN-5G, WLAN-6G, WIMAX, mobile LTE, and mobile 5G frequencies.

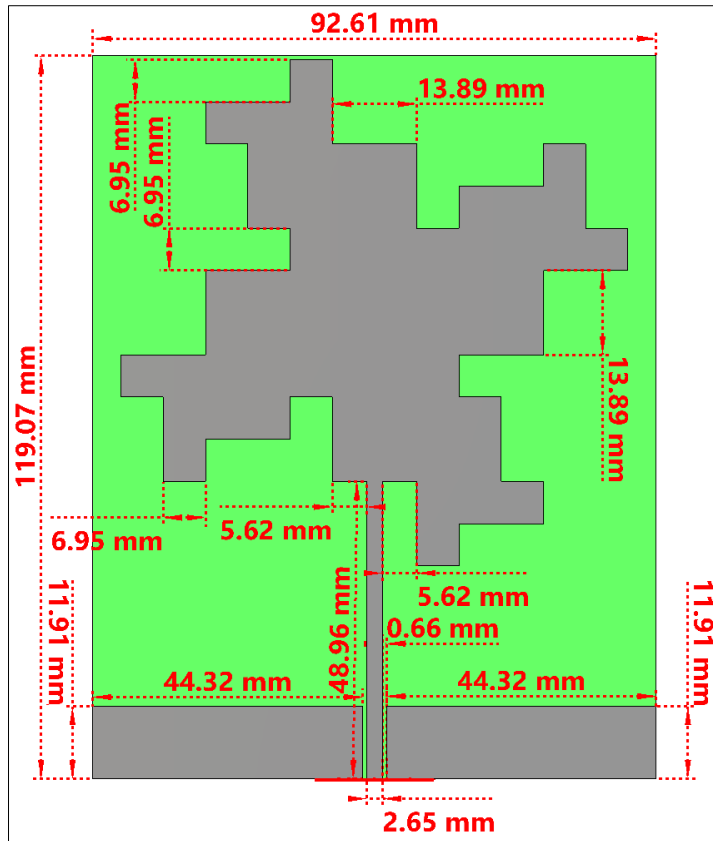


Figure 4.12 The dimensions for the proposed (Antenna-5).

4.3.2 Simulated Results for the Proposed (Antenna-5)

The simulated results for the reflection coefficient $|S_{11}|$ show that the proposed (Antenna-5) has dual-band characteristics, as shown in Figure 4.13. The first frequency band (2.4 GHz - 5.363 GHz) has a resonance frequency of 2.73 GHz. The second frequency band (6.542 GHz - 7.254 GHz) has a resonance frequency of 6.9 GHz. All the frequency ranges that are supported by the (Antenna-5) are required for RFEH applications since it supports a wide range of RF wireless services, including WLAN, WIMAX, mobile LTE, and mobile 5G. Furthermore, the simulated results of the proposed (Antenna-5) show that the antenna has a high gain of (4.31 dBi) at the frequency of 2.6 GHz, (3.176 dBi) at the frequency of 2.4 GHz, (2.592 dBi) at the frequency of 3.5 GHz, and (2.449 dBi) at the frequency of 4.2 GHz, which makes it a

suitable antenna for RFEH applications. Table 4-2 demonstrates more details about the simulated results of the proposed Antenna-5.

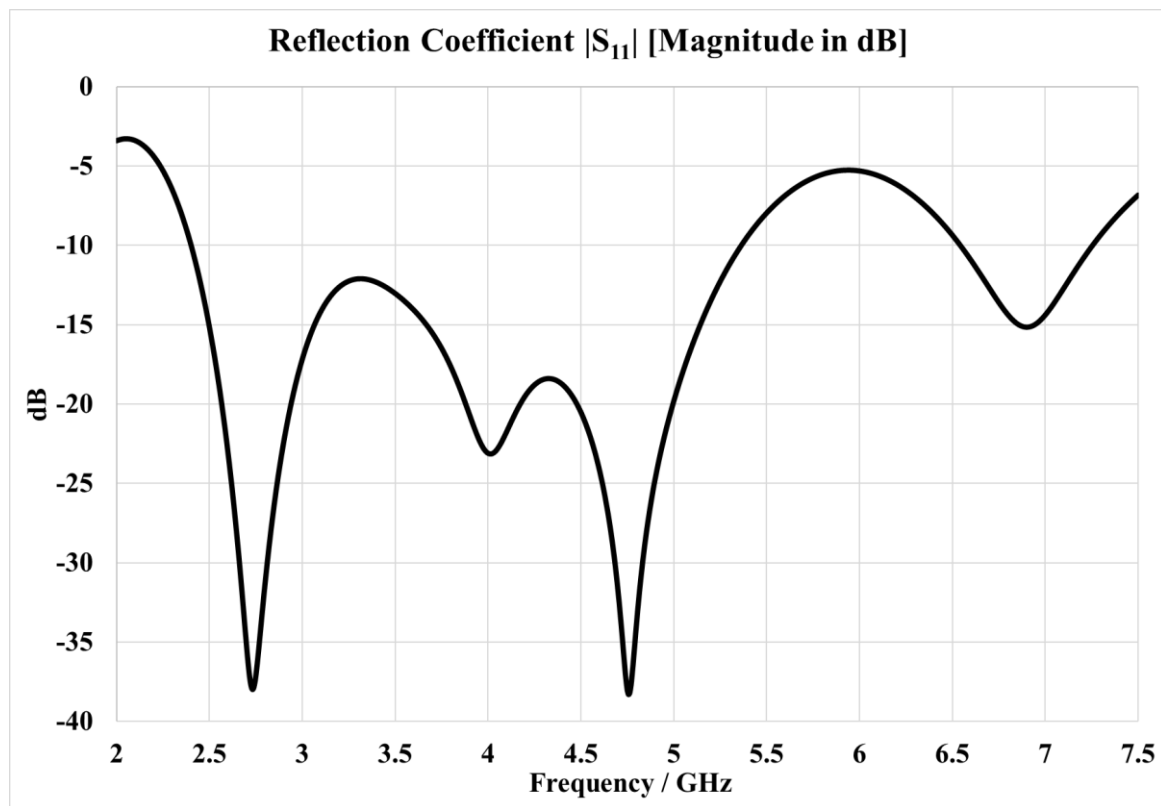


Figure 4.13 Simulated result of the reflection coefficient $|S_{11}|$ for the proposed (Antenna-5).

Table 4-2 Simulated results for the proposed (Antenna-5).

Resonating Frequency (GHz)	Return Loss (S_{11}) (dB)	Minimum Frequency (GHz)	Maximum Frequency (GHz)	Band Width (GHz)	Directivity (dBi)	Peak Gain (dBi)	Applications	Reference
2.73	-38	2.4	5.363	2.963	5.654	4.31 dBi @ 2.6 GHz	WLAN, WIMAX, Mobile LTE, Mobile 5G	[54], [55]
6.9	-15.16	6.542	7.254	0.712	4.481	2.18 dBi @ 6.543 GHz	WLAN, Mobile LTE, Mobile 5G	[54], [55]

4.3.3 Parametric Analysis for the Proposed (Antenna-5)

A. Impact of Changing the Width of the Microstrip Feed Line

Figure 4.14 shows the simulated results for the reflection coefficient $|S_{11}|$ magnitude in [dB] for different width values of the antenna feed line. The results showed the best feeding line width value was [2.65 mm].

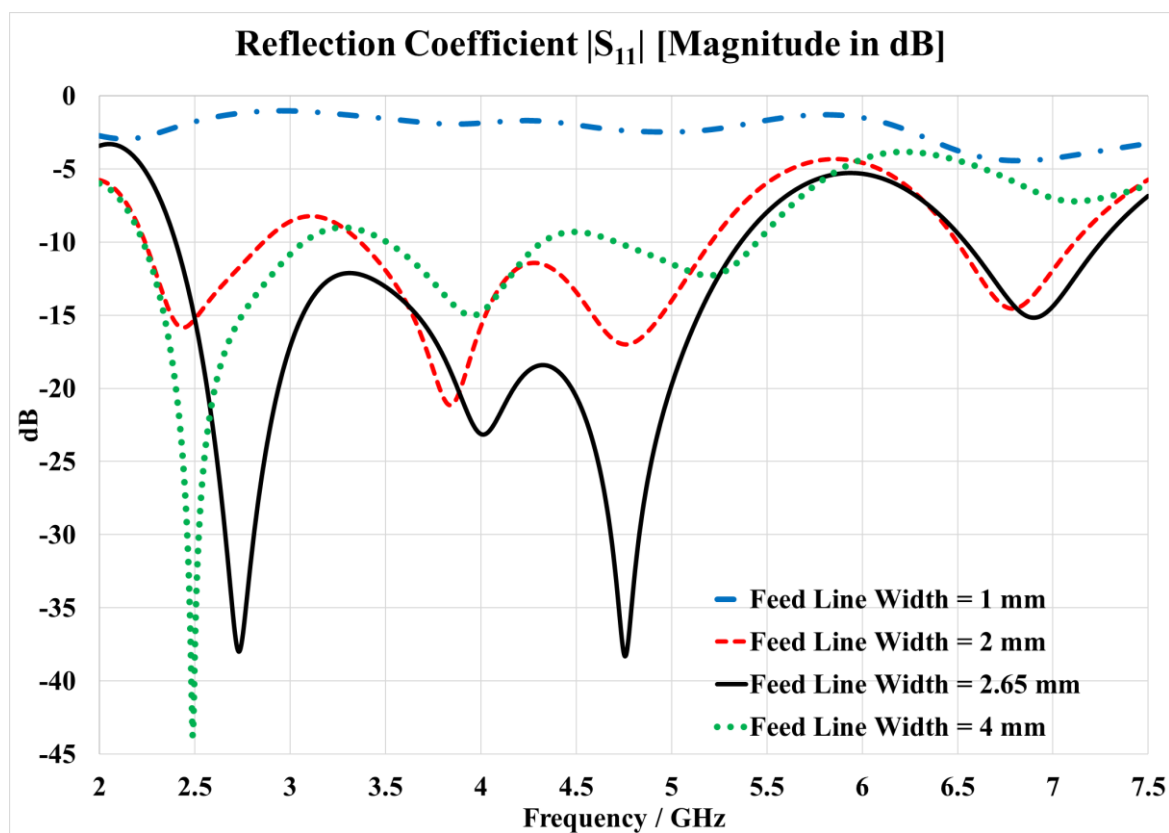


Figure 4.14 The simulated results of the reflection coefficient $|S_{11}|$ for different width values of the (Antenna-5) feed line.

B. Impact of Changing the Length of the Microstrip Feed Line

Figure 4.15 shows the simulated results of the reflection coefficient $|S_{11}|$ magnitude in [dB] for different length values of the (Antenna-5) feeding line. The simulated results showed that when reducing the feed line length of the antenna, resulting in decreased values of the resonating frequencies since the electrical length of the antenna monopole patch will decrease, shifting the frequencies to the right of the frequency spectrum since the frequency is inversely proportional to the wavelength (λ) of the signal, the best feeding line length value was [48.96 mm].

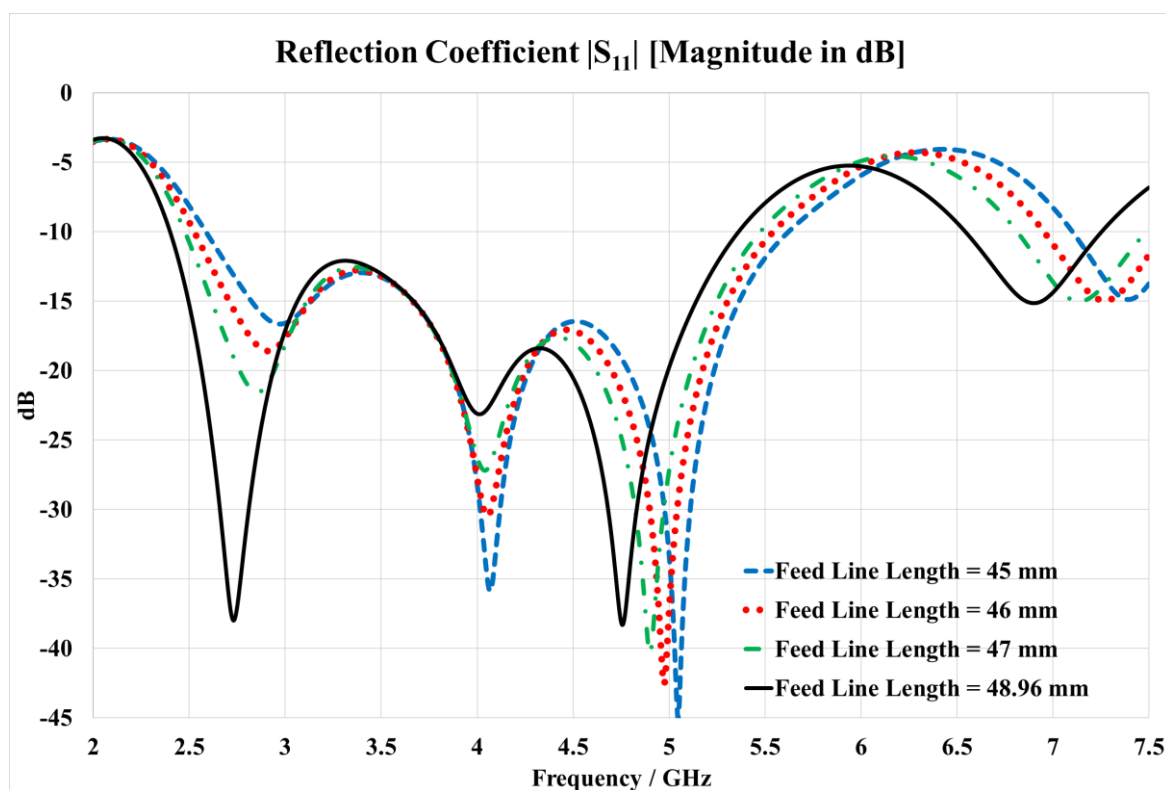


Figure 4.15 The simulated results of the reflection coefficient $|S_{11}|$ for different length values of the (Antenna-5) feed line.

C. Impact of Changing the Two Ground Planes Length

Figure 4.16 shows the simulated results of the reflection coefficient $|S_{11}|$ magnitude in [dB] for different ground plane lengths applied to the proposed (Antenna-5). The simulated results showed that increasing the two-ground plane lengths of the proposed (Antenna-5) will result in a decrease in the bandwidth of the resonating frequencies, while reducing the two-ground plane lengths of the antenna will result in splitting the first band into two separate bands. The best length value for the two-ground plane was [11.91 mm].

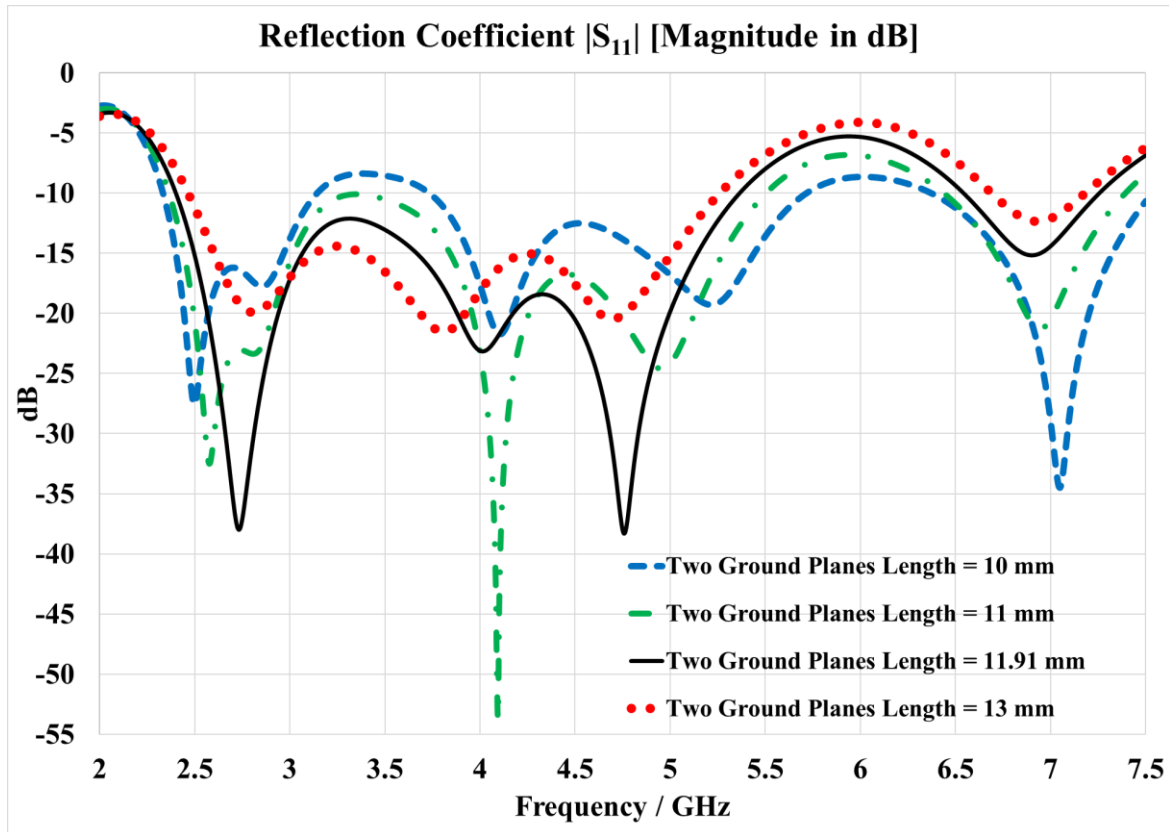


Figure 4.16 The simulated result of the reflection coefficient $|S_{11}|$ for different length values of the two-ground plane of the proposed (Antenna-5).

D. Impact of Changing the Two Ground Planes Width

Figure 4.17 shows the simulated results of the reflection coefficient $|S_{11}|$ magnitude in [dB] for different width values of the two-ground plane of the proposed (Antenna-5). The best width value for the two-ground plane was [44.32 mm].

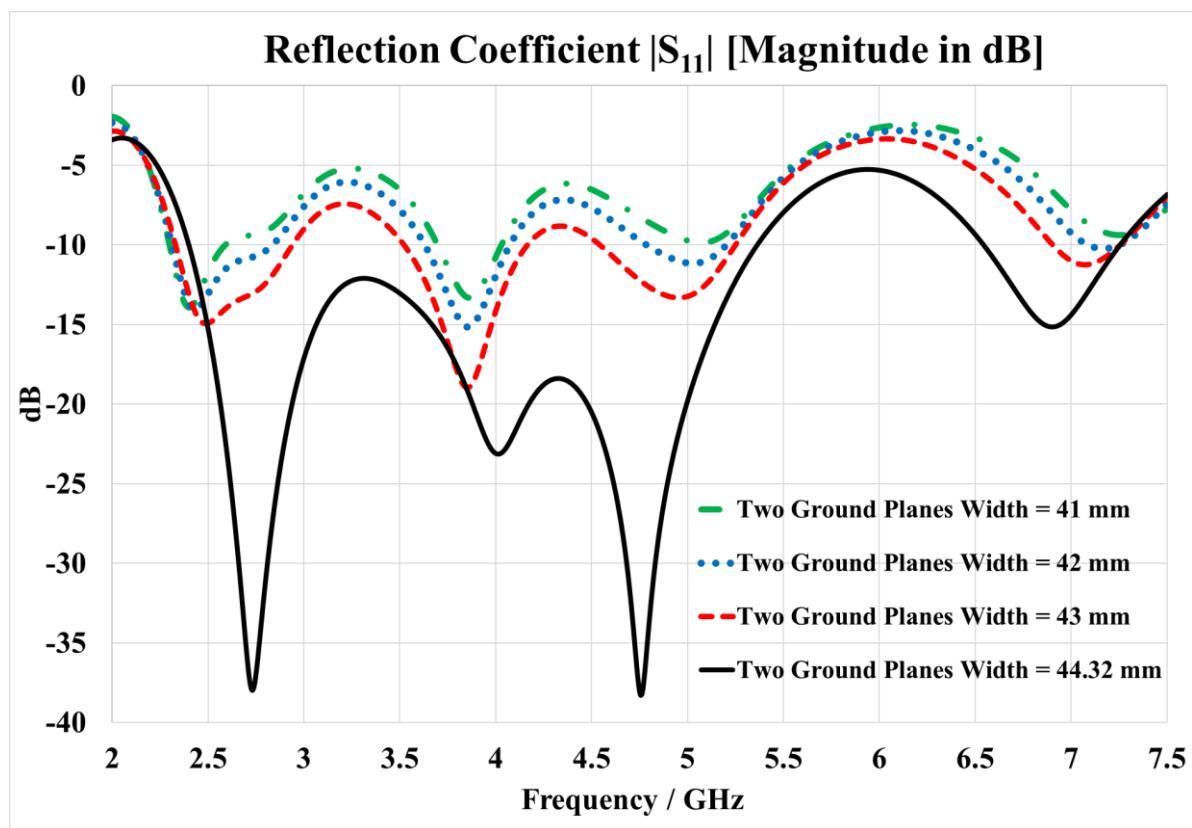


Figure 4.17 The simulated result of the reflection coefficient $|S_{11}|$ for different width values of the two-ground plane of the proposed (Antenna-5).

E. Impact of (Antenna-5) Scale-Up

Figure 4.18 shows the simulated results for the reflection coefficient $|S_{11}|$ magnitude in [dB] for different scale-up factors (1), (1.2), and (1.4). It's clear from the simulation results that when increasing the scale of the proposed (Antenn-5), all the resonating frequency values will decrease and will be shifted to the left of the frequency spectrum. This will confirm that when the scale of the antenna increases, the electrical lengths of the antenna will increase, resulting in a decrease in the resonating frequency values since the frequency is inversely proportional to the wavelength of the signal (λ).

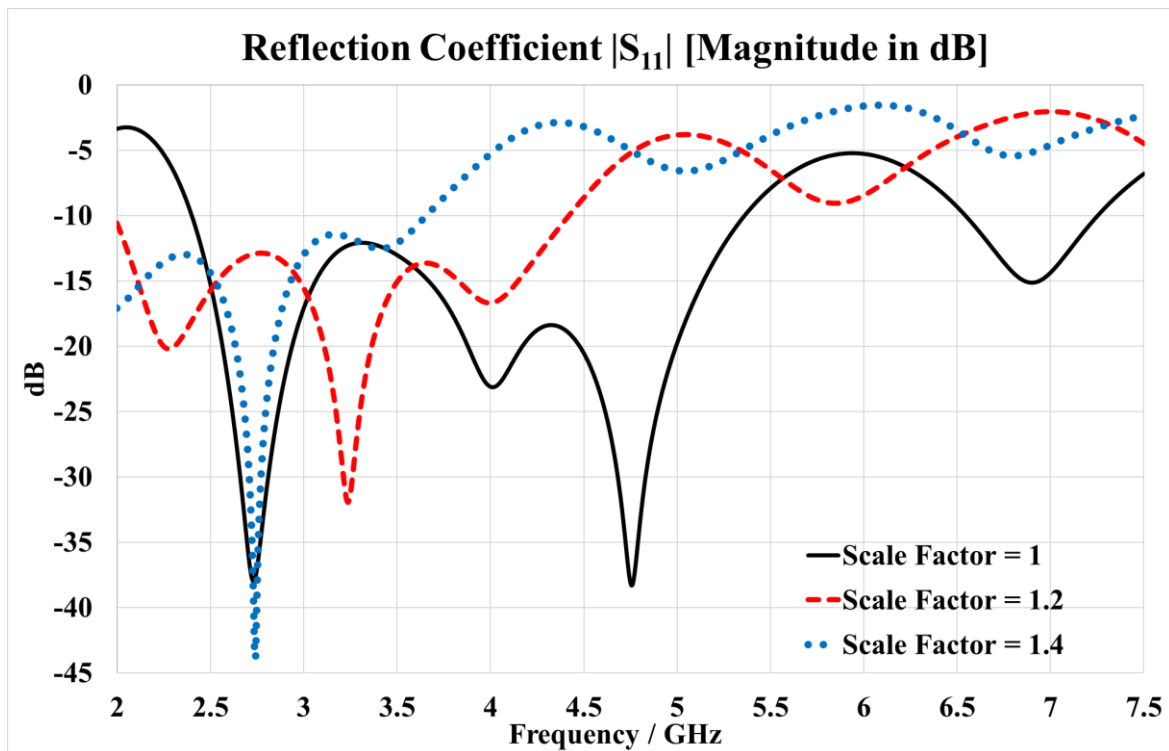


Figure 4.18 The simulated result of the reflection coefficient $|S_{11}|$ for different scale-up factors of the proposed (Antenna-5).

F. Impact of (Antenna-5) Scale-Down

Figure 4.19 shows the simulated results for the reflection coefficient $|S_{11}|$ magnitude in [dB] for different scale-down factors (1), (0.8), and (0.6). It's clear from the simulation results that when decreasing the scale of the proposed (Antenn-5), all the resonating frequency values will increase and will be shifted to the right of the frequency spectrum. Moreover, the resonating frequency (6.9 GHz) vanished since the frequency spectrum range studied was between 2 GHz and 7.5 GHz. This will confirm that when the scale of the antenna decreases, the electrical lengths of the antenna will decrease, resulting in an increase in the resonating frequency values since the frequency is inversely proportional to the wavelength of the signal (λ).

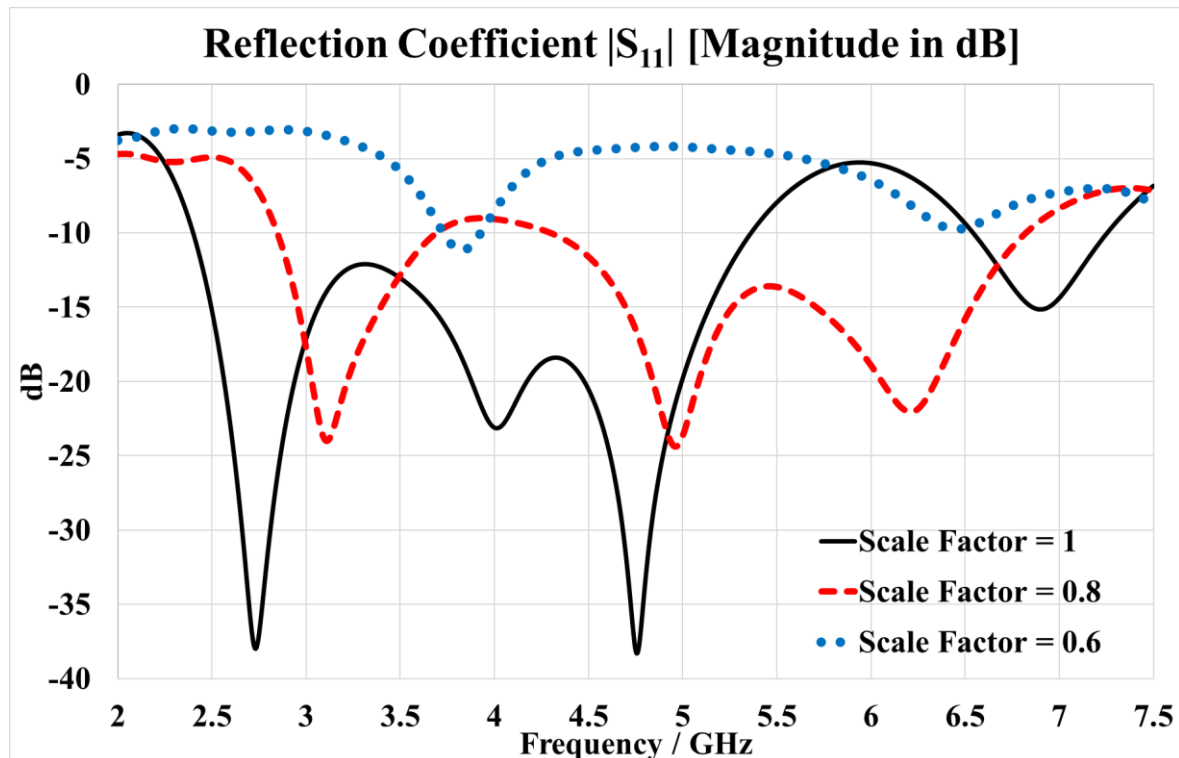


Figure 4.19 The simulated result of the reflection coefficient $|S_{11}|$ for different scale-down factors of the proposed (Antenna-5).

4.3.4 Simulated Radiation Pattern for the Proposed (Antenna-5)

Figure 4.20 demonstrates the simulated 3D radiation pattern of the directivity magnitude in [dBi] for some of the proposed (Antenna-5) supported frequencies. Also, Figure 4.21 demonstrates the simulated 2D radiation pattern.

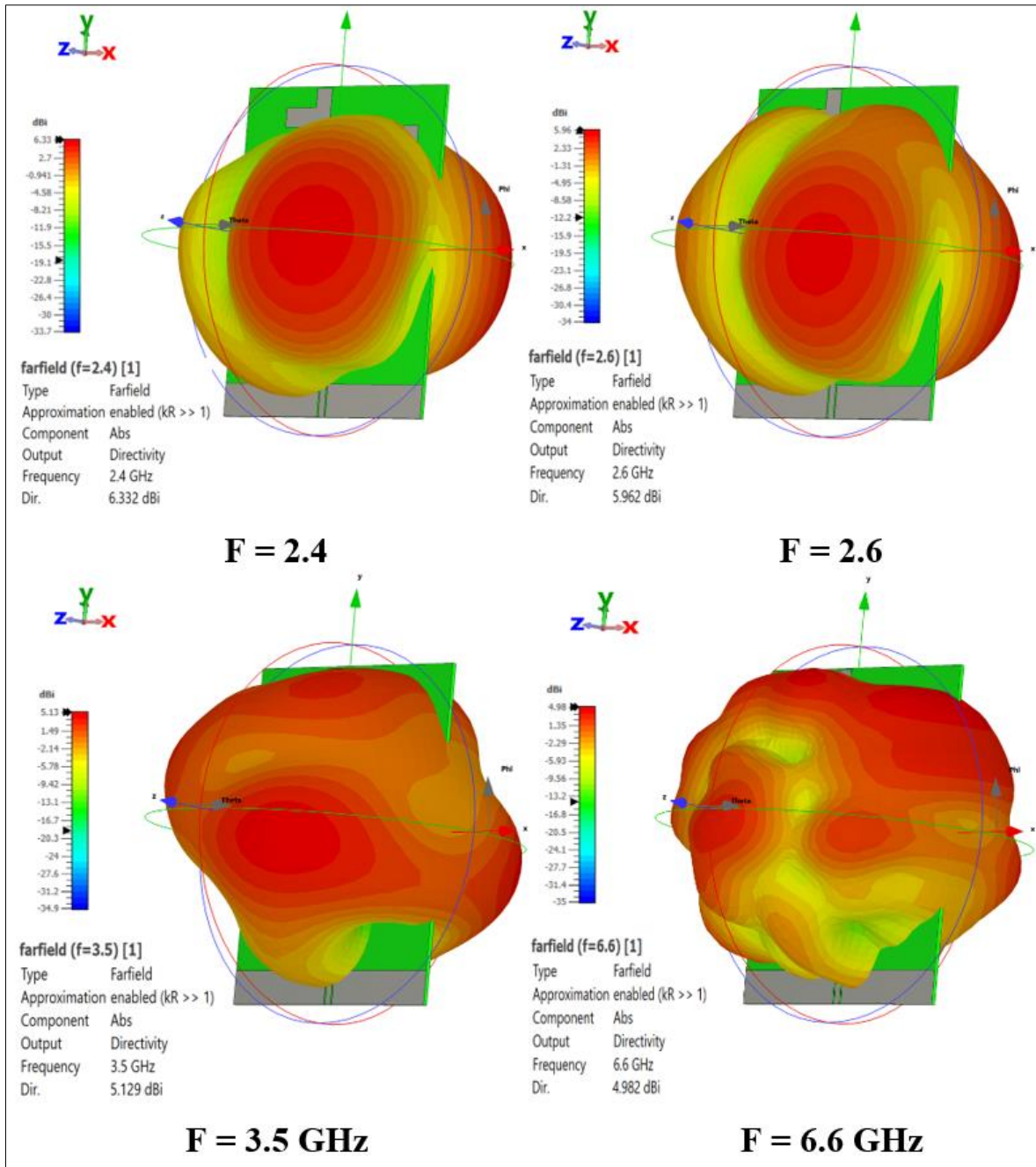


Figure 4.20 The simulated 3D radiation pattern of the directivity magnitude in [dBi] for the proposed (Antenna-5).

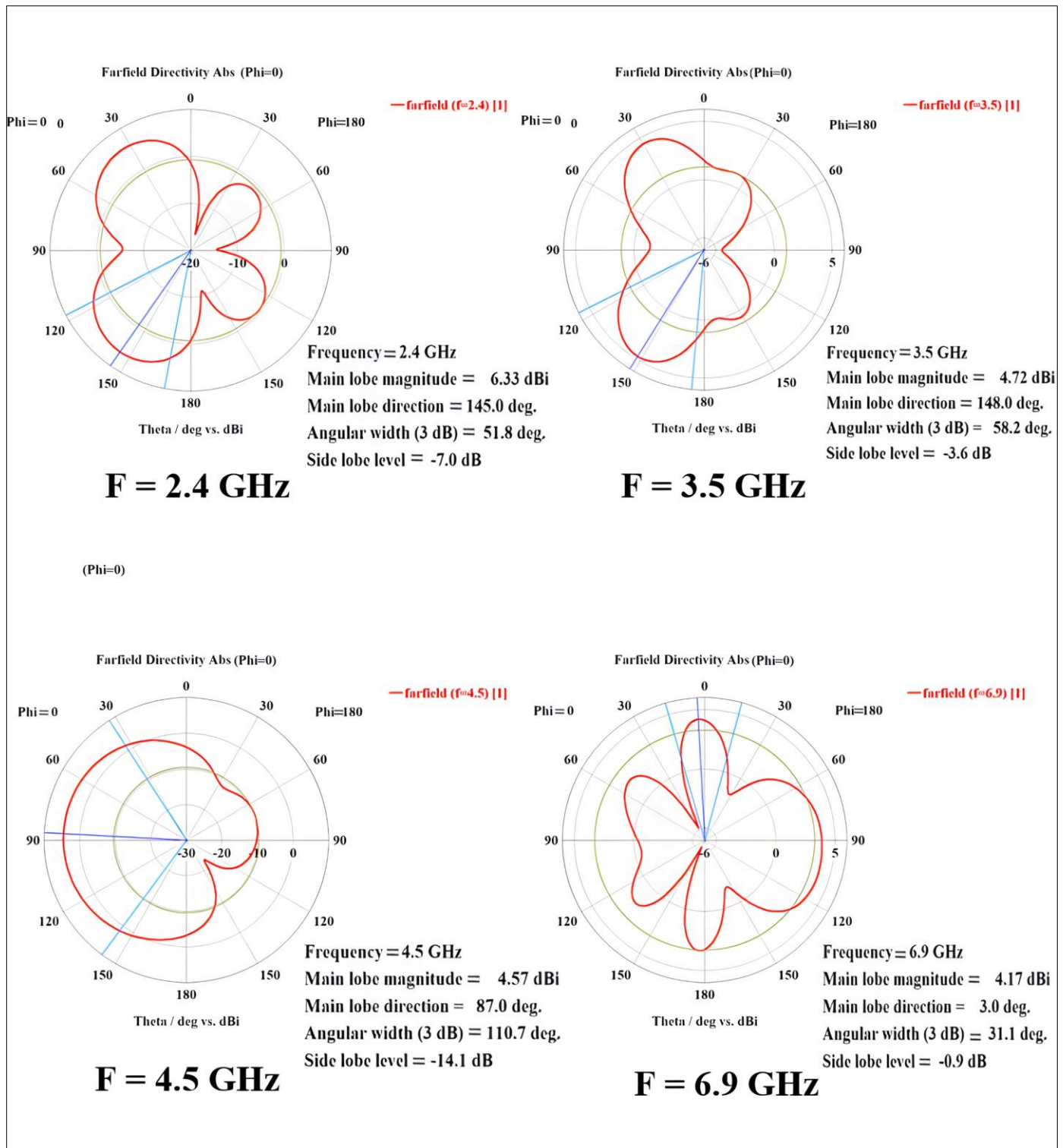


Figure 4.21 The simulated 2D radiation pattern of the directivity magnitude in [dBi] for the proposed (Antenna-5).

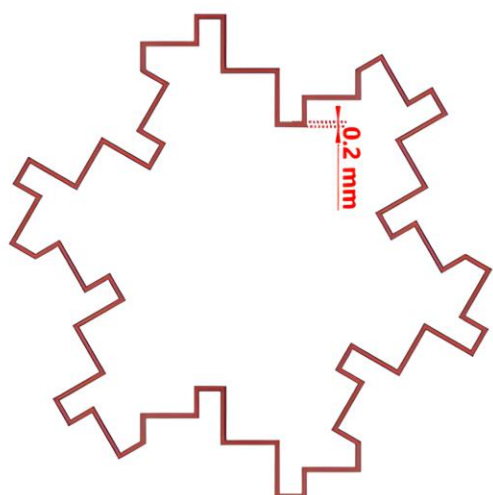
4.4 (Antenna-6) a Modified Hexagonal Monopole Patch Antenna with (CPW) Feeding Technique

4.4.1 Design and Construction

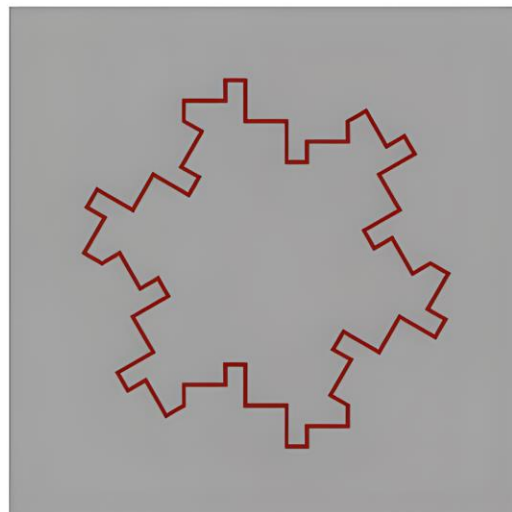
The construction procedures of the proposed wideband antenna (Antenna-6) are similar to those of the wideband antenna (Antenna-5). The first step of constructing the monopole patch of the proposed (Antenna-6) is implemented by using the modified hexagonal patch shown in Figure 3.2(d), which is created by replacing the six standard hexagonal patch sides with the novel fractal shape 1 shown in Figure 3.1(e) to create the modified hexagonal patch shown in Figure 3.2(d). The construction steps for creating the modified hexagonal monopole patch are shown in Figure 4.22. Furthermore, a (CPW) feeding technique is implemented for antenna excitation [64]. The proposed (Antenna-6) has been designed and simulated with CST Studio Suite software. A standard FR-4 substrate with $\epsilon_r = 4.3$, a thickness of 1.6 mm, and a loss tangent (δ) of 0.025 was utilized.

The proposed (Antenna-6) is implemented on a substrate with dimensions of [121.72 mm] of length, [81.14 mm] of width, and [1.6 mm] of thickness, respectively, with a microstrip feed line length of [49.48 mm] and width of [2.60 mm]. Also, two symmetrical rectangular ground planes with dimensions of [38.75 mm] of width and [12.48 mm] of length were implemented on the front side of the substrate adjacent to the microstrip feed line, as shown in Figure 4.23.

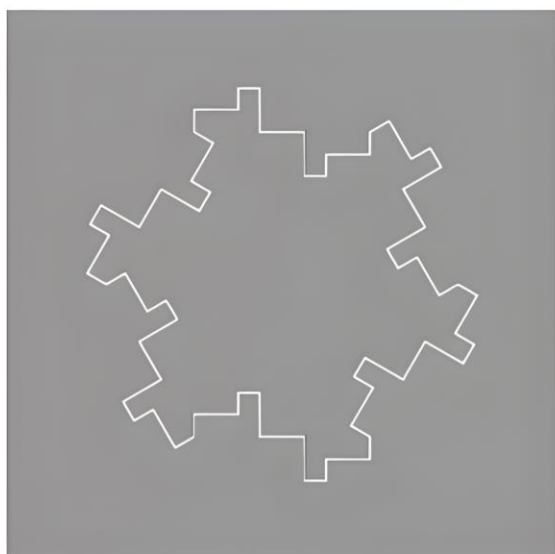
The proposed (Antenna-6) is designed for RFEH applications and tuned to target the required frequencies for RFEH applications, including WLAN-2.4G, WLAN-5G, WLAN-6G, WIMAX, mobile LTE, and mobile 5G frequencies.



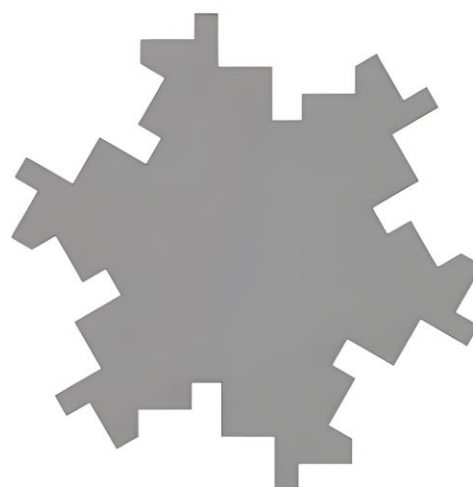
Step 1: Create a modified hexagonal polygon with a line width of 0.2 mm.



Step 2: The modified hexagonal polygon is merged with a square patch.



Step 3: Subtracting the square patch from the modified hexagonal polygon



Step 4: deleting the square patch and keeping the inner modified hexagonal polygon

Figure 4.22 Construction steps for creating the modified hexagonal monopole patch of the proposed (Antenna-6).

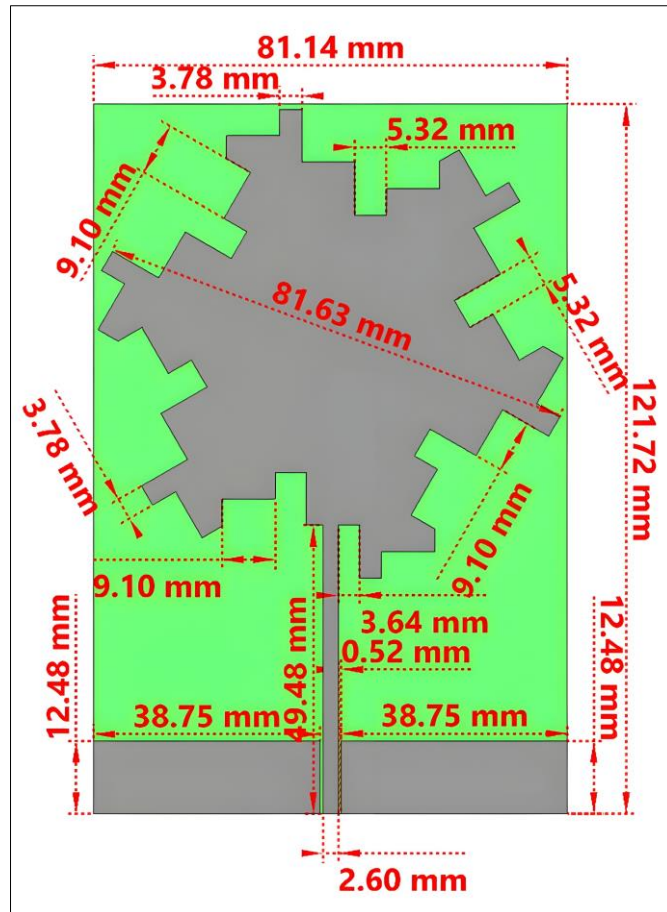


Figure 4.23 The dimensions for the proposed (Antenna-6).

4.4.2 Simulated Results for the Proposed (Antenna-6)

The simulated results for the reflection coefficient $|S_{11}|$ show that the proposed (Antenna-6) has a resonance frequency of 3.215 GHz and a wide frequency band of (2.3917 GHz to 6.364 GHz), as shown in Figure 4.24 and Table 4-3. Furthermore, the simulated results of the proposed (Antenna-6) show that the antenna has a high overall gain with a peak of (4.481 dBi) at the frequency of 3 GHz, (3.127 dBi) at the frequency of 2.4 GHz, (2.471 dBi) at the frequency of 3.5 GHz, and (2.078 dBi) at the frequency of 5 GHz, which makes it a suitable antenna for RFEH applications.

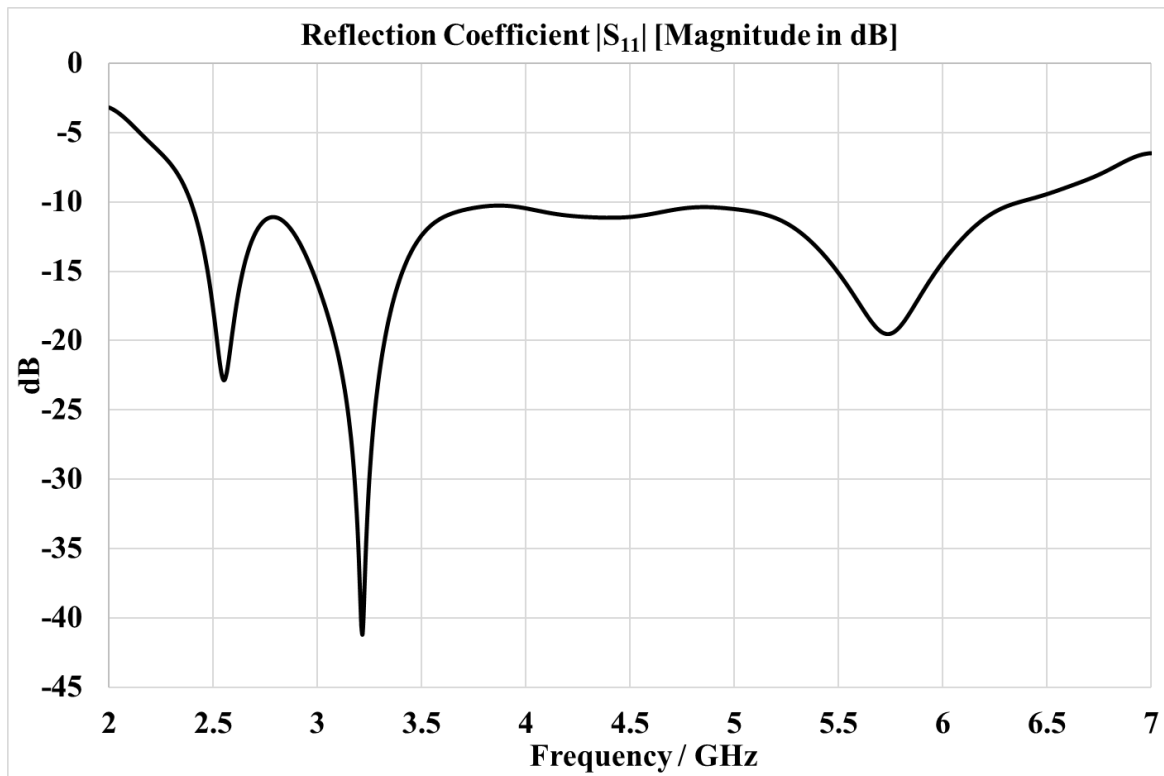


Figure 4.24 The simulated result of the reflection coefficient $|S_{11}|$ for the proposed (Antenna-6).

Table 4-3 Simulated results for the proposed (Antenna-6).

Resonating Frequency (GHz)	Return Loss (S11) (dB)	Minimum Frequency (GHz)	Maximum Frequency (GHz)	Band Width (GHz)	Directivity (dBi)	Peak Gain (dBi)	Applications	Reference
3.215	-41.22	2.3917	6.364	3.9723	5.348	4.481 dBi @ 3 GHz	WLAN, WIMAX, Mobile LTE, Mobile 5G	[54], [55]

All the frequencies that are supported by the proposed (Antenna-6) are required for RFEH applications since it supports a wide range of RF wireless services, including WLAN, WIMAX, mobile LTE, and mobile 5G.

4.4.3 Parametric Analysis for the Proposed (Antenna-6)

A. Impact of Changing the Width of the Microstrip Feed Line

Figure 4.25 shows the simulated results for the reflection coefficient $|S_{11}|$ magnitude in [dB] for different width values of the antenna feed line. The simulated results showed that the single wideband band is split into multiple bands when changing the width of the antenna feed line from [2.6 mm] to [3 mm and 2 mm]. The best feeding line width value was [2.6 mm].

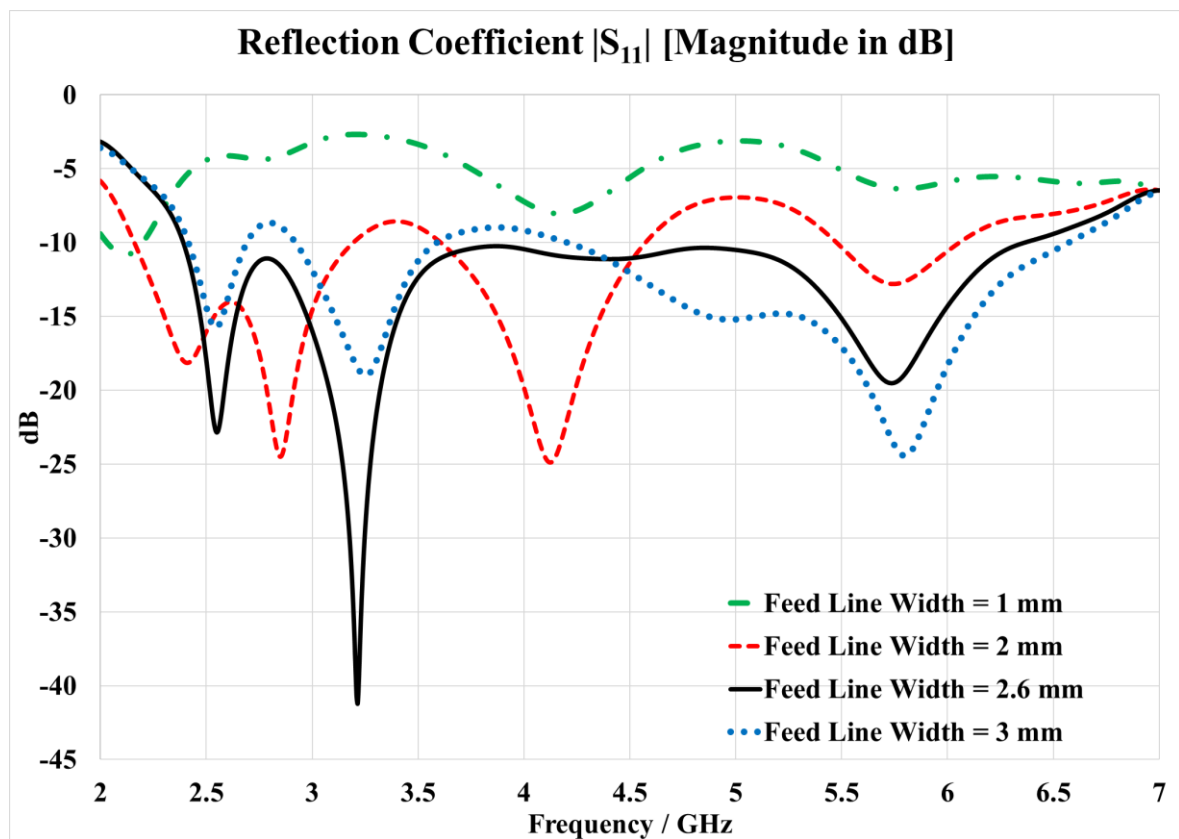


Figure 4.25 The simulated results of the reflection coefficient $|S_{11}|$ for different width values of the (Antenna-6) feed line

B. Impact of Changing the Length of the Microstrip Feed Line

Figure 4.26 shows the simulated results of the reflection coefficient $|S_{11}|$ magnitude in [dB] for different length values of the (Antenna-6) feeding line. The simulated results showed that when reducing the feed line length of the antenna, resulting in a decreased value of the resonating frequency since the electrical length of the antenna monopole patch will decrease, shifting the frequencies to the right of the frequency spectrum since the frequency is inversely proportional to the wavelength (λ) of the signal, the best feeding line length value was [49.48 mm].

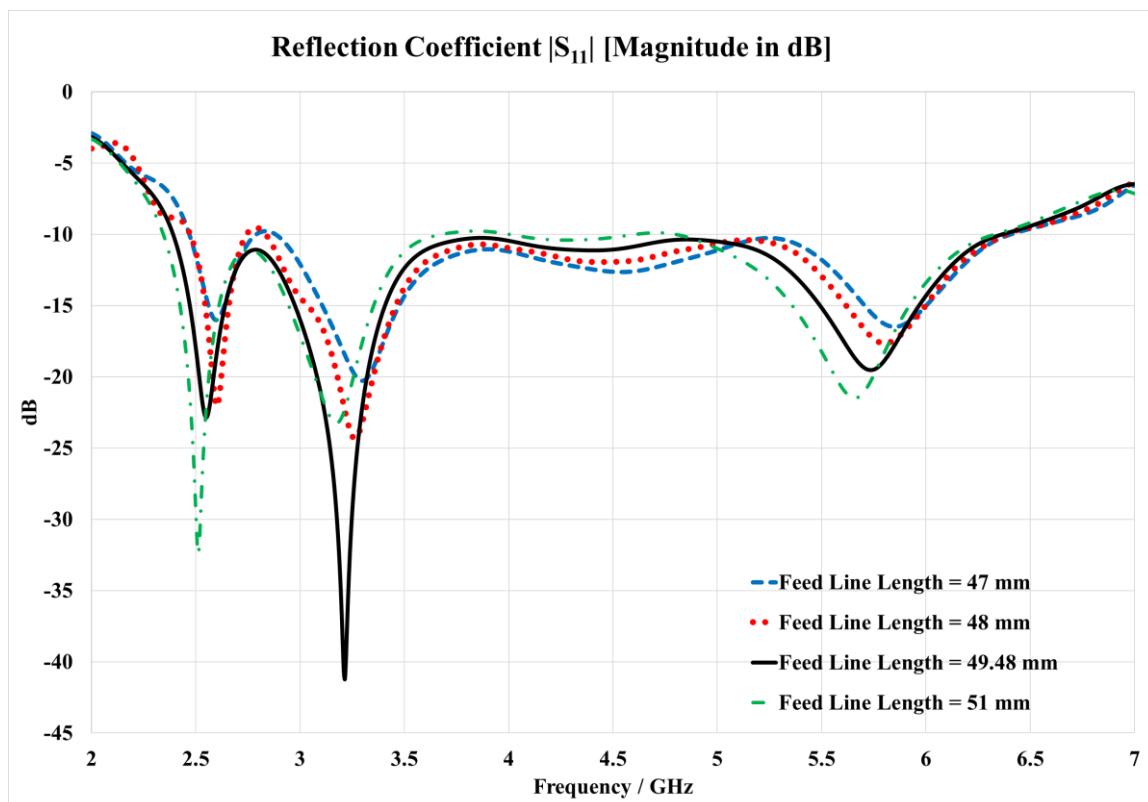


Figure 4.26 The simulated results of the reflection coefficient $|S_{11}|$ for different length values of the (Antenna-6) feed line.

C. Impact of Changing the Two Ground Planes Length

Figure 4.27 shows the simulated results of the reflection coefficient $|S_{11}|$ magnitude in [dB] for different two-ground plane lengths applied to the proposed antenna. The simulated results showed that increasing the two-ground plane length of the proposed antenna (Antenna-6) will result in a decrease in the frequency bandwidth and split the single wideband into two separate bands, while reducing the ground plane length of the antenna will result in splitting the single wideband into three separate bands. The best length value for the two-ground plane was [12.48 mm].

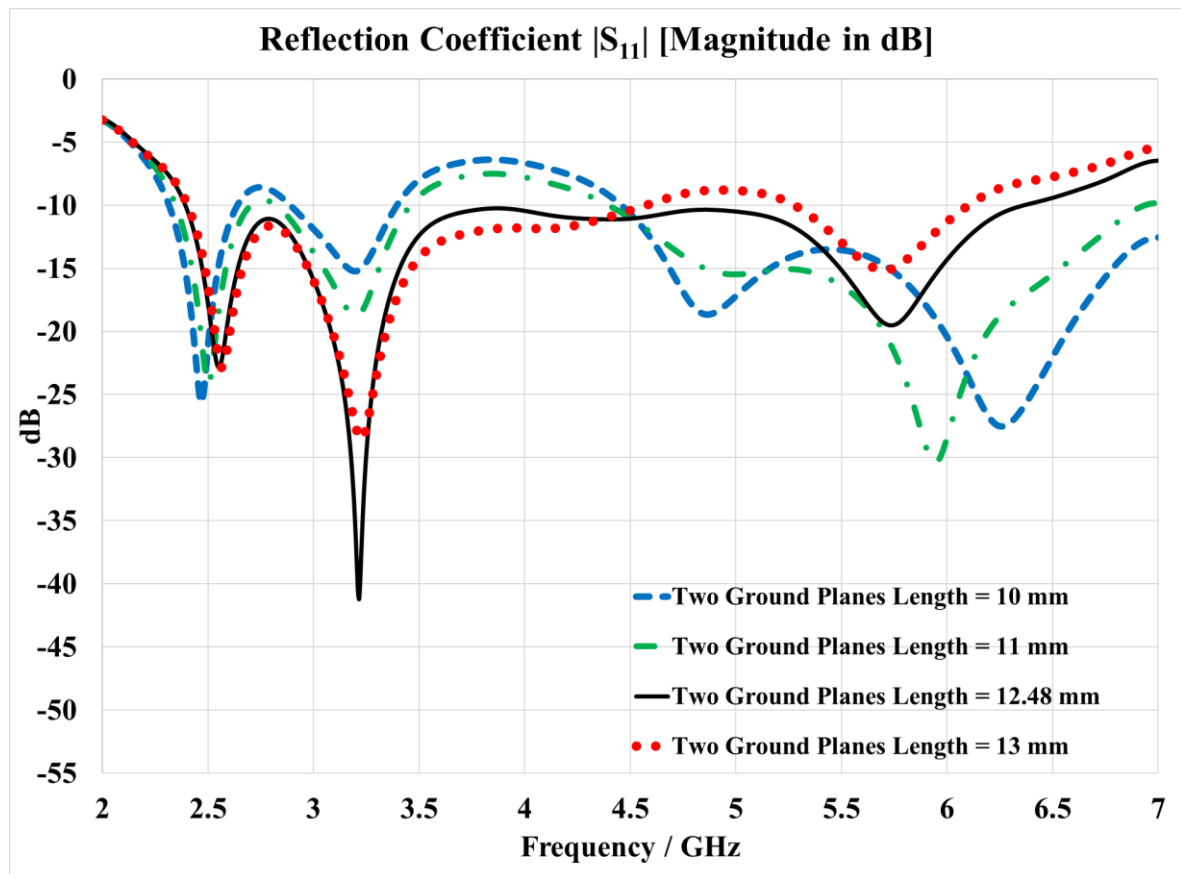


Figure 4.27 The simulated result of the reflection coefficient $|S_{11}|$ for different length values of the two-ground plane of the proposed (Antenna-6).

D. Impact of Changing the Two Ground Planes Width

Figure 4.28 shows the simulated results of the reflection coefficient $|S_{11}|$ magnitude in [dB] for different width values of the two-ground plane of the proposed (Antenna-6). The simulated results showed that decreasing the two-ground plane width of the proposed antenna (Antenna-6) will result in splitting the single wideband into three separate bands. The best width value for the two-ground plane was [38.75 mm].

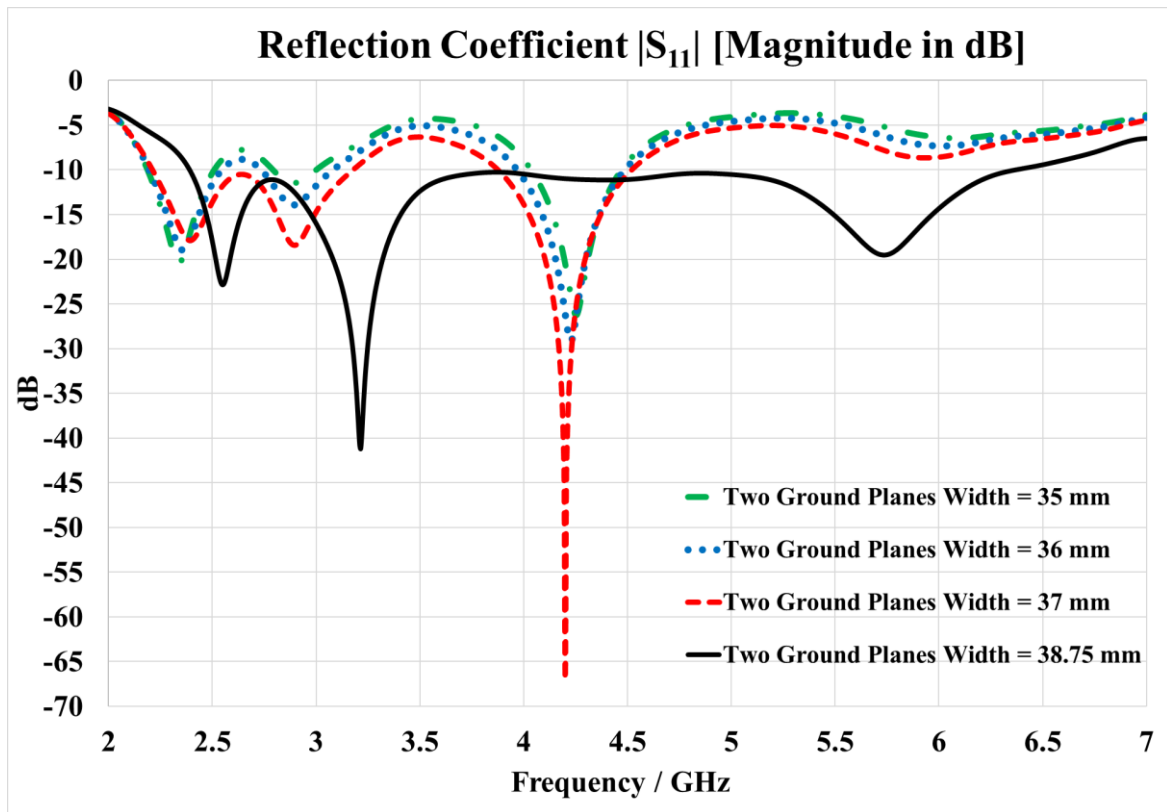


Figure 4.28 The simulated result of the reflection coefficient $|S_{11}|$ for different width values of the two-ground plane of the proposed (Antenna-6).

E. Impact of (Antenna-6) Scale-Up

Figure 4.29 shows the simulated results for the reflection coefficient $|S_{11}|$ magnitude in [dB] for different scale-up factors (1), (1.2), and (1.4). It's clear from the simulation results that when increasing the scale of the proposed (Antenn-6), the resonating frequency value will decrease and will be shifted to the left of the frequency spectrum. This will confirm that when the scale of the antenna increases, the electrical lengths of the antenna will increase, resulting in a decrease in the resonating frequency value since the frequency is inversely proportional to the wavelength of the signal (λ).

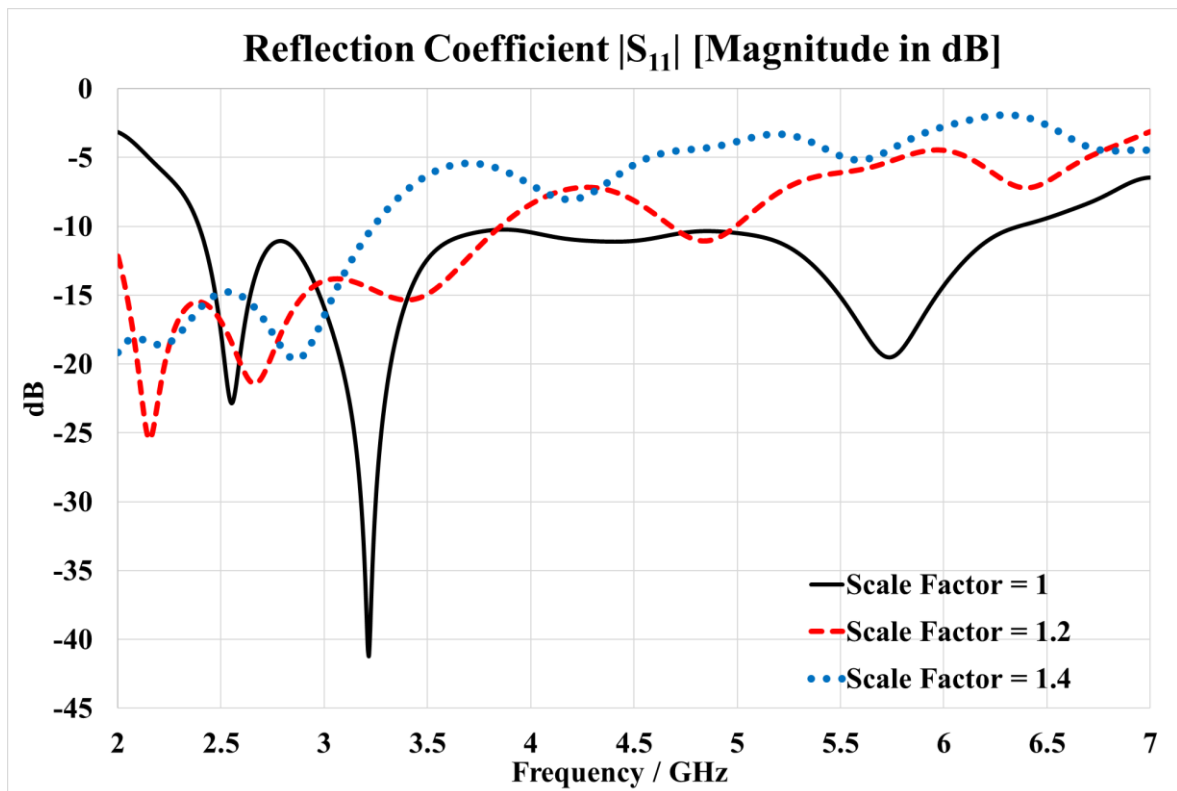


Figure 4.29 The simulated result of the reflection coefficient $|S_{11}|$ for different scale-up factors of the proposed (Antenna-6).

F. Impact of (Antenna-6) Scale-Down

Figure 4.30 shows the simulated results for the reflection coefficient $|S_{11}|$ magnitude in [dB] for different scale-down factors (1), (0.8), and (0.6). It's clear from the simulated results that when decreasing the scale of the proposed (Antenn-6), the resonating frequency value will increase and will be shifted to the right of the frequency spectrum. This will confirm that when the scale of the antenna decreases, the electrical lengths of the antenna will decrease, resulting in an increase in the resonating frequency values since the frequency is inversely proportional to the wavelength of the signal (λ).

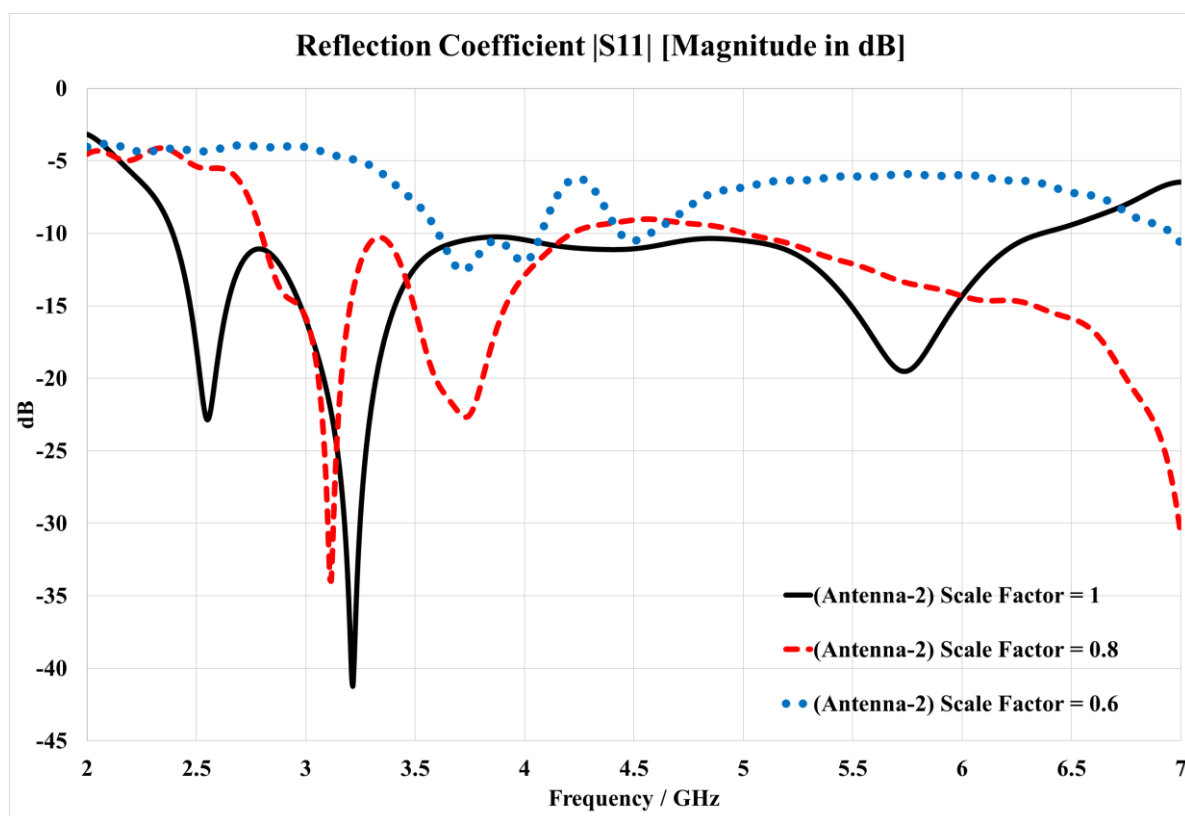


Figure 4.30 The simulated result of the reflection coefficient $|S_{11}|$ for different scale-down factors of the proposed (Antenna-6).

4.4.4 Simulated Radiation Pattern for the Proposed (Antenna-6)

Figure 4.31 demonstrates the simulated 3D radiation pattern of the directivity magnitude in [dBi] for some of the proposed (Antenna-6) supported frequencies. Also, Figure 4.32 demonstrates the simulated 2D radiation pattern.

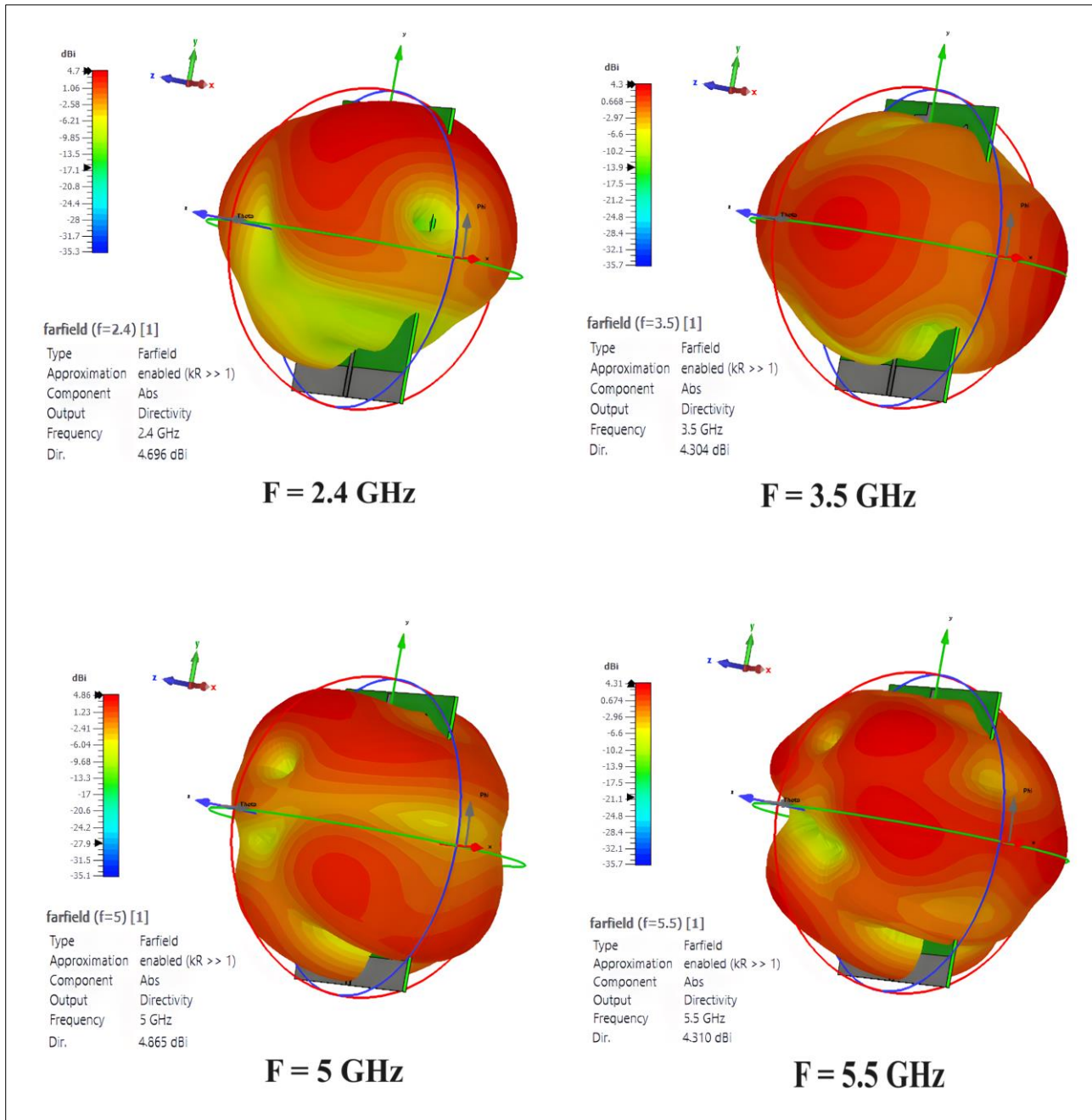
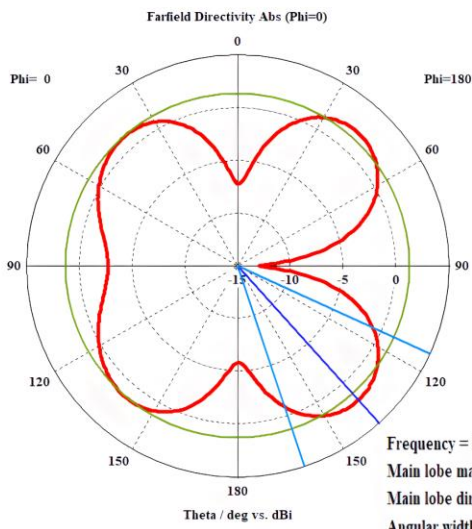
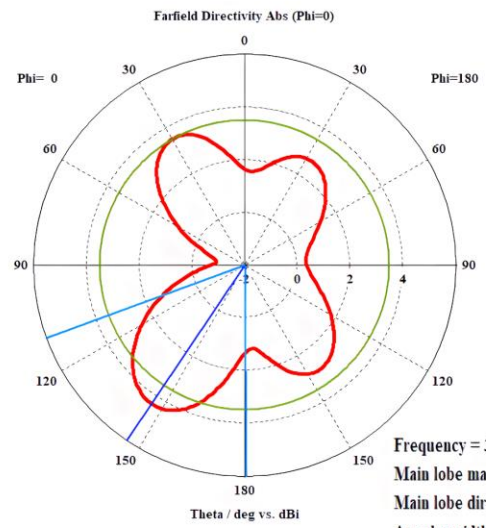


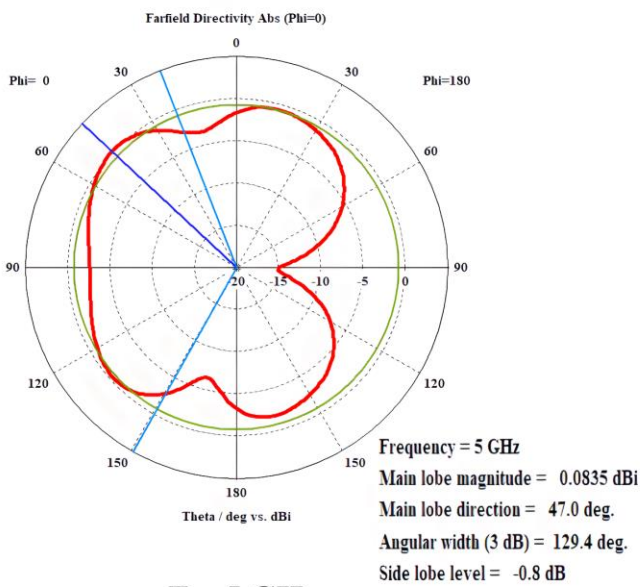
Figure 4.31 The simulated 3D radiation pattern of the directivity magnitude in [dBi] for the proposed (Antenna-6).



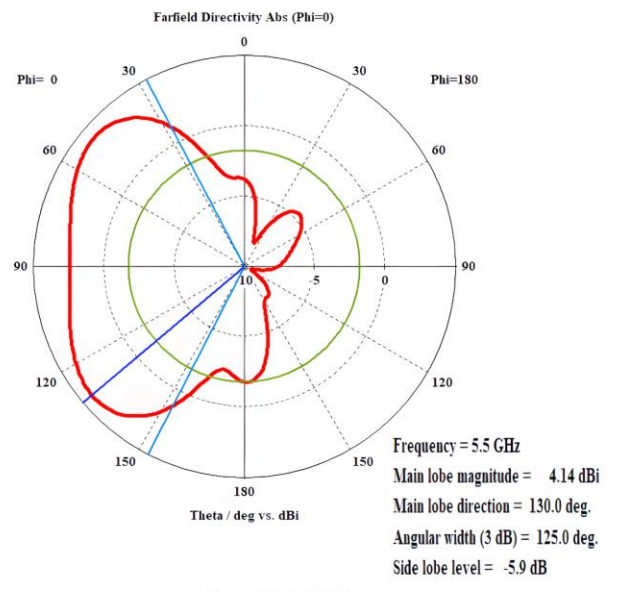
F = 2.4 GHz



F = 3.5 GHz



F = 5 GHz



F = 5.5 GHz

Figure 4.32 The simulated 2D radiation pattern of the directivity magnitude in [dBi] for the proposed (Antenna-6).

4.5 Fabrication and Experimental Results

This section provides a comparison between the simulated results and the experimentally measured results for the three proposed wideband antennas that were introduced in this chapter. The measurement results of the reflection coefficient $|S_{11}|$ and the normalized 2D radiation pattern showed reasonable tolerance errors, with the simulated results taking into consideration the difficulties in fabricating the proposed antenna due to its intricate geometries, soldering effects, and an inadequate testing environment due to the absence of a fully anechoic chamber at the university where the measurement was taken. The same experimental testing environments and procedures used to measure the proposed fabricated multiband antennas in Chapter 3 have been applied here in this section to measure the proposed fabricated wideband antennas by using the same measurement devices.

4.5.1 The experimental results for the proposed wideband Antenna-4

The measurement results of the reflection coefficient $|S_{11}|$ showed perfect matching with the simulated results for the resonating frequency of 5.232 GHz, whereas there was a shifting for the resonating frequency of 2.48 GHz by 60 MHz to the right of the frequency spectrum as shown in Figure 4.33.

Furthermore, the measurement results of the normalized 2D radiational pattern showed better matching with the simulated results for the frequency of 5.3 GHz compared to the frequency of 2.6 GHz as shown in Figure 4.34.

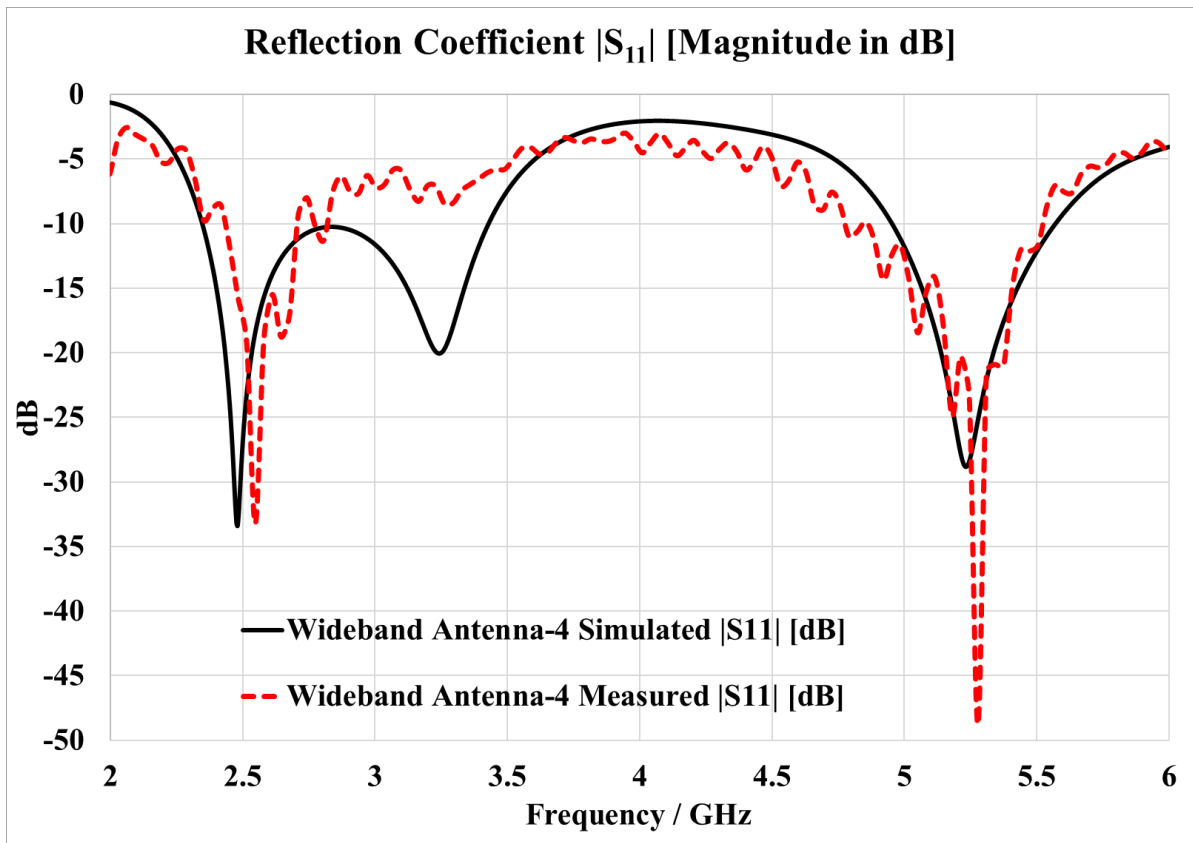


Figure 4.33 The reflection coefficient $|S_{11}|$ for both the simulated and the practical fabricated (Antenna-4).

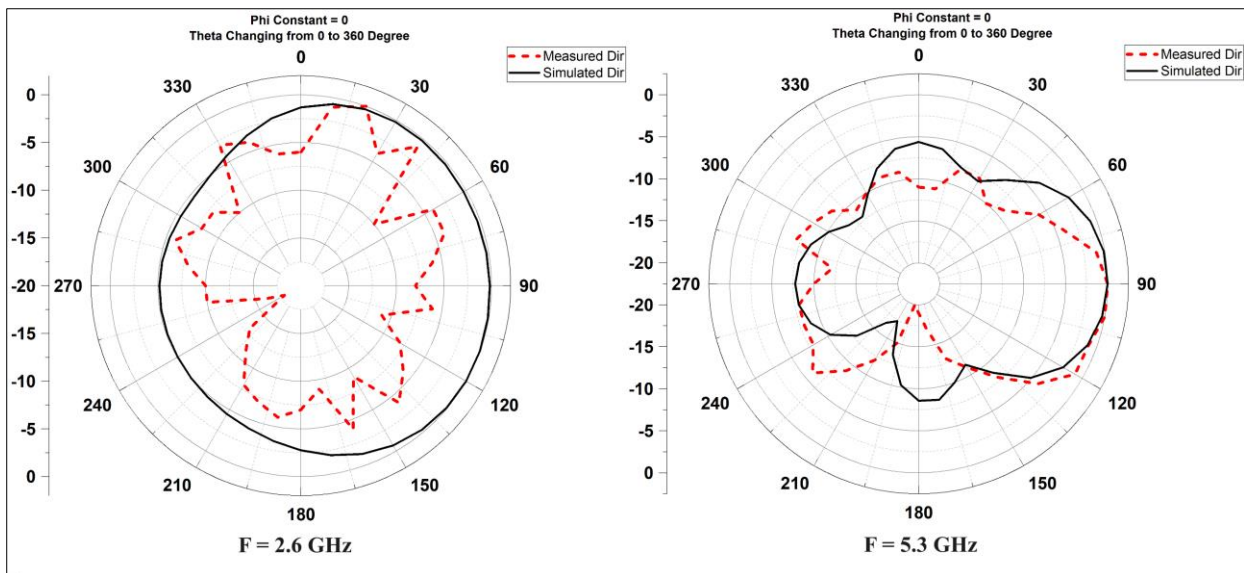


Figure 4.34 The normalized 2D radiational pattern of the directivity for the proposed (Antenna-4) showed the simulated and measured results.

The physical structure and the testing environment of the proposed (Antenna-4) are shown in Figure 4.35 and Figure 4.36 respectively.

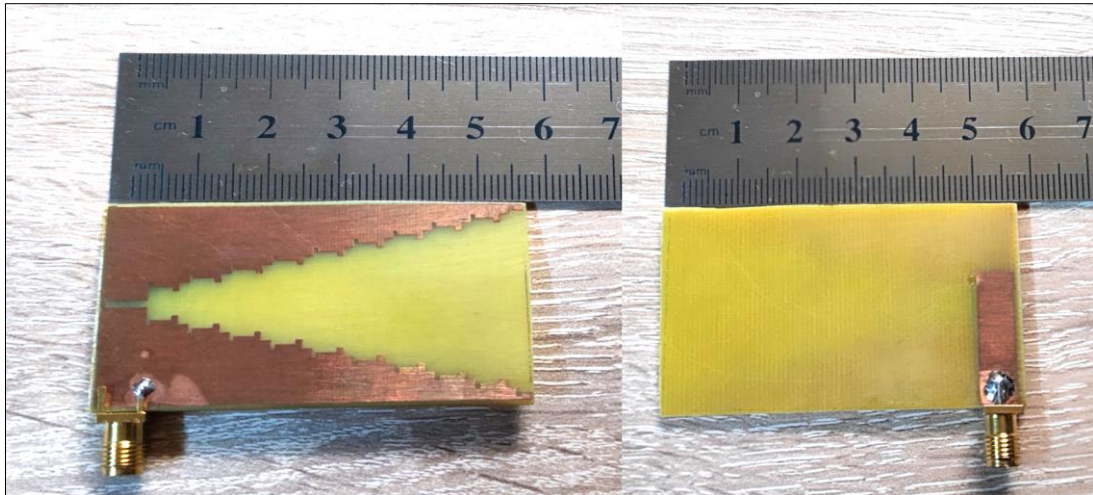


Figure 4.35 The physical structure of the proposed (Antenna-4).

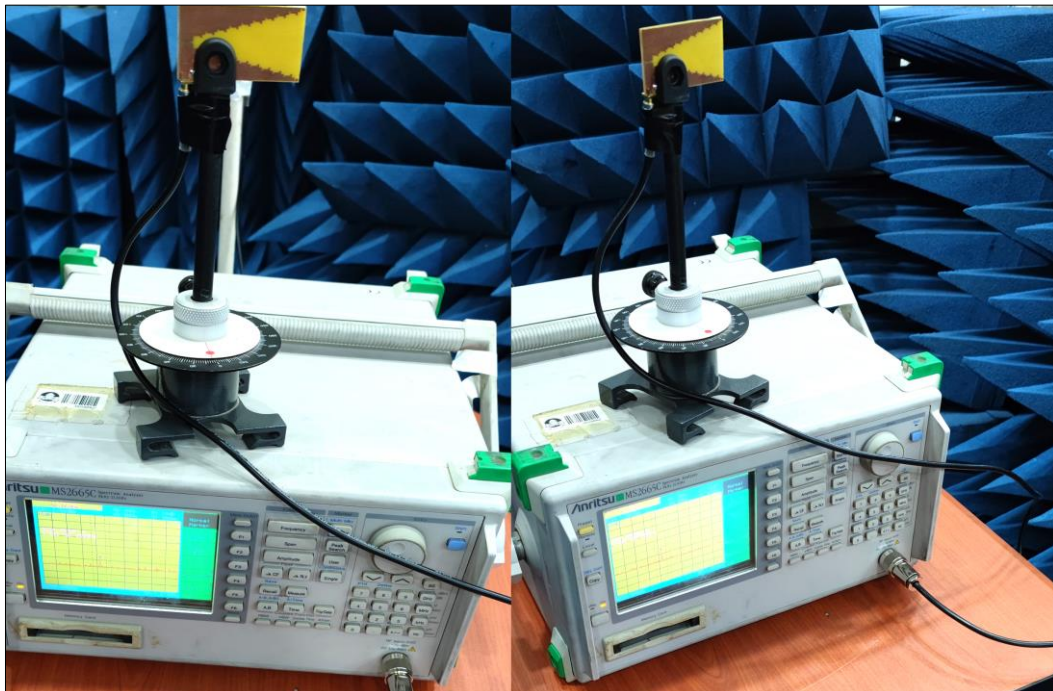


Figure 4.36 The testing environment for the proposed (Antenna-4).

4.5.2 The experimental results for the proposed wideband antenna-5

The measurement results of the reflection coefficient $|S_{11}|$ showed reasonable matching with the simulated results for the resonating frequency of 2.73 GHz, whereas there was a shifting for the resonating frequency of 6.9 GHz by 390 MHz to the left of the frequency spectrum as shown in Figure 4.37.

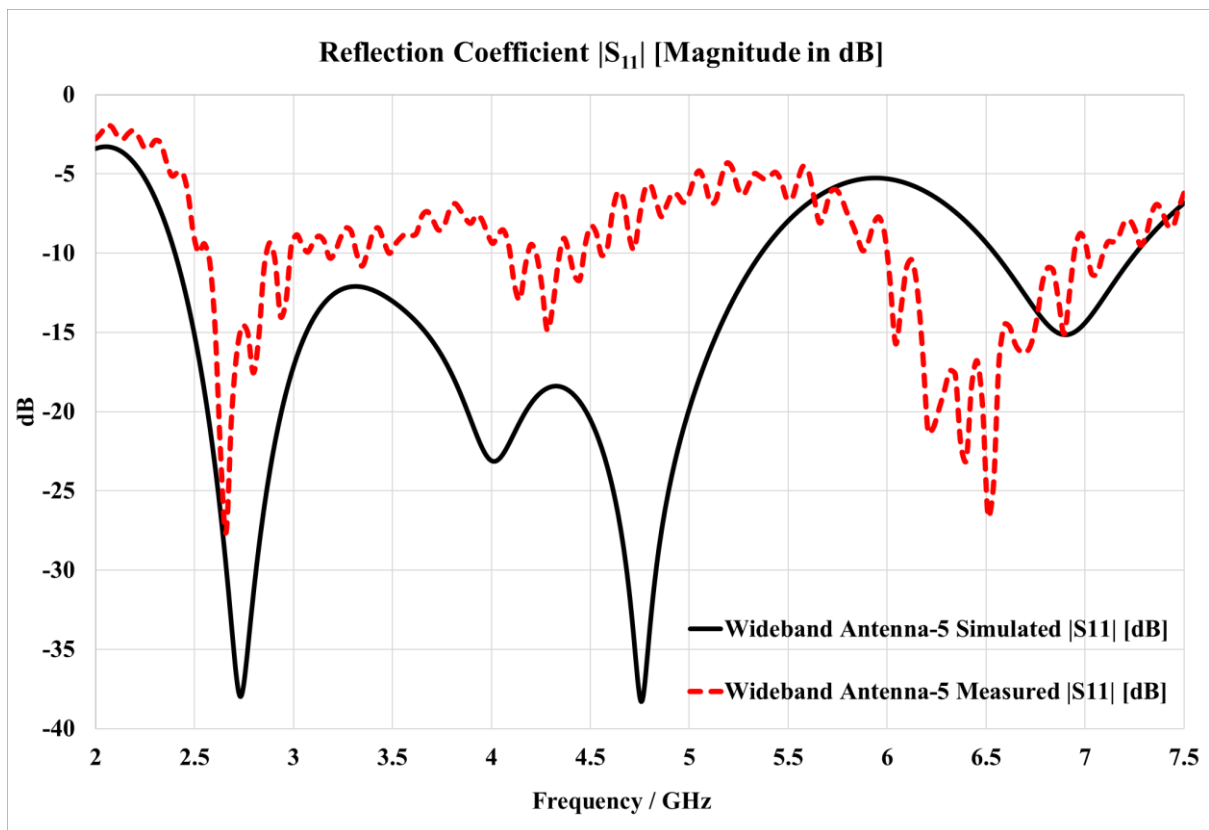


Figure 4.37 The reflection coefficient $|S_{11}|$ for both the simulated and the practical fabricated (Antenna-5).

Furthermore, the measurement results of the normalized 2D radiational pattern showed better matching with the simulated results for the frequency of 5.36 GHz compared to the frequency of 2.6 GHz as shown in Figure 4.38.

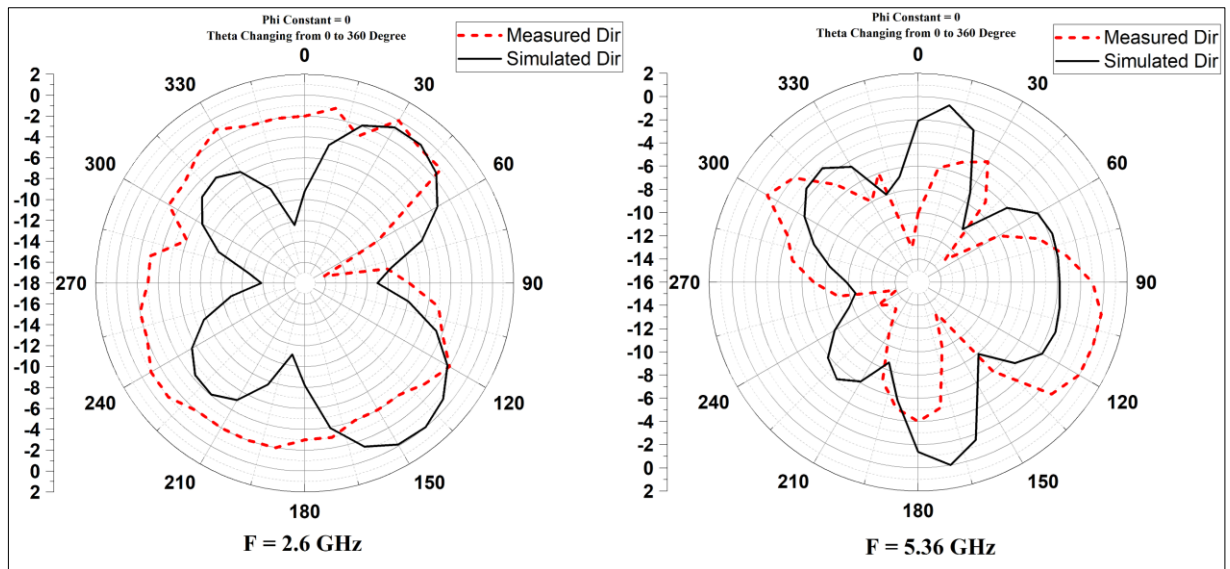


Figure 4.38 The normalized 2D radiational pattern of the directivity for the proposed (Antenna-5) showed the simulated and measured results.

Furthermore, the physical structure and the testing environment of the proposed (Antenna-5) are shown in Figure 4.39 and Figure 4.40 respectively.



Figure 4.39 The physical structure of the proposed (Antenna-5).



Figure 4.40 The testing environment used to measure the normalized 2D radiation pattern for the proposed (Antenna-5).

4.5.3 The experimental results for the proposed wideband antenna-6

The measurement results of the reflection coefficient $|S_{11}|$ showed shifting the frequency of 2.58 GHz by 45 MHz to the right of the frequency spectrum, whereas shifting the frequencies of 3.25 GHz by 175 MHz and 5.8 GHz by 500 MHz to the left of the frequency spectrum as shown in Figure 4.41.

Furthermore, the measurement results of the normalized 2D radiational pattern showed a shift of 45-degree clockwise compared with the simulated results for the frequency of 5.3 GHz. The measurement results of the normalized 2D radiational pattern showed better matching with the simulated results for the frequency of 5.3 GHz compared to the frequency of 2.6 GHz as shown in Figure 4.42

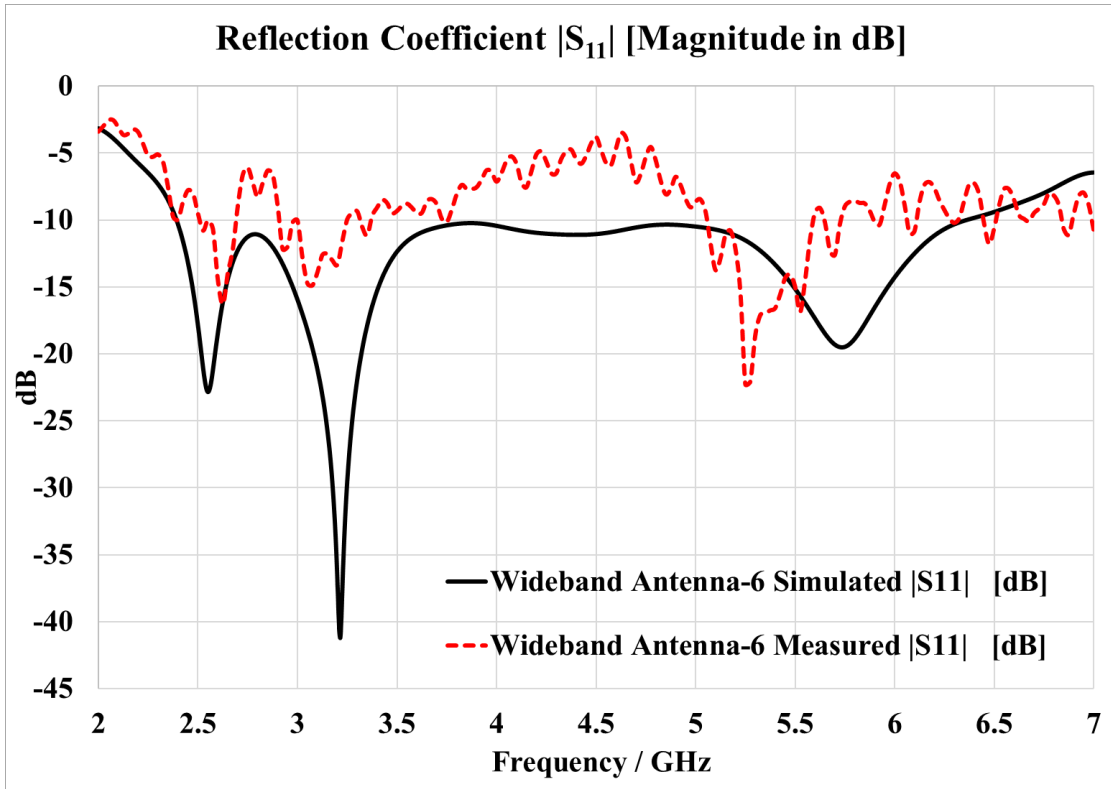


Figure 4.41 The reflection coefficient $|S_{11}|$ for both the simulated and the practical fabricated (Antenna-6).

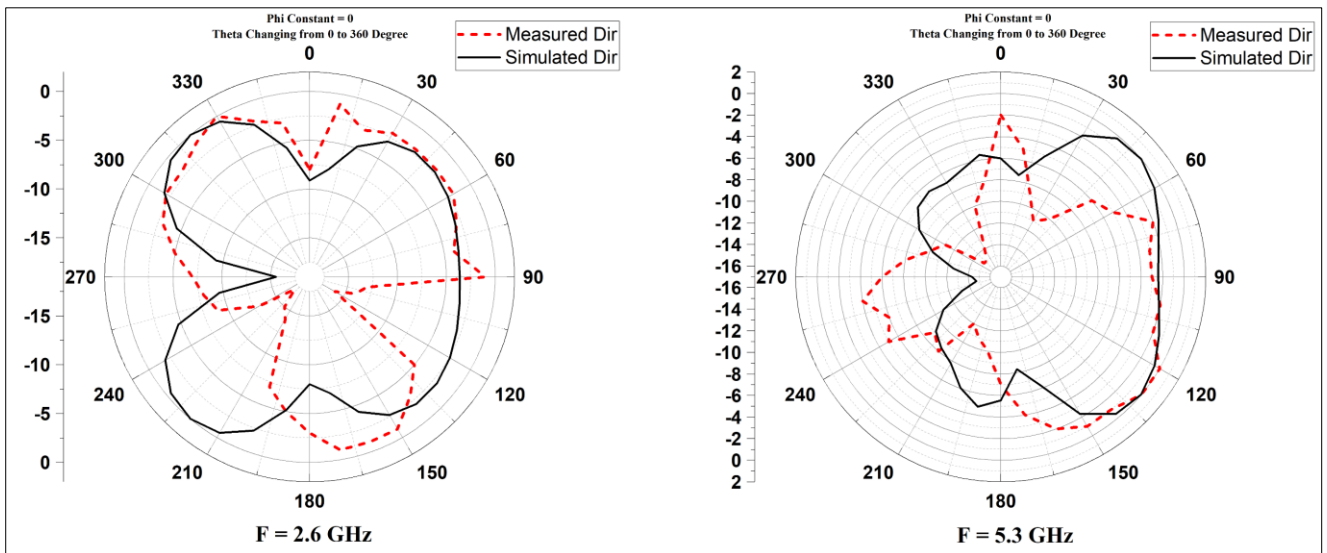


Figure 4.42 The normalized 2D radiational pattern of the directivity for the proposed (Antenna-6) showed the simulated and measured results.

Furthermore, the physical structure and the testing environment of the proposed (Antenna-6) are shown in Figure 4.43 and Figure 4.44 respectively.



Figure 4.43 The physical structure of the proposed (Antenna-6).



Figure 4.44 The testing environment used to measure the normalized 2D radiation pattern for the proposed (Antenna-6).

Chapter Five

CONCLUSIONS AND FUTURE WORKS

5.1 Conclusions

In this work, six proposed patch antennas (three multiband and three wideband) were designed, simulated, and fabricated using PCB technology on the FR-4 substrate due to its light weight, low cost, and low profile. Each of the proposed antennas is carefully studied and optimized to target the most required frequencies for radio frequency energy harvesting applications, including WLAN-2.4G, WLAN-5G, WLAN-6G, Mobile LTE, Mobile 5G, and WIMAX services. Several techniques, including combining fractal geometry, applying defected ground structure (DGS), and making slot cuts, are implemented during the design process in order to improve the performance of the reflection coefficient $|S_{11}|$, increase the bandwidth and gain, and generate more required frequencies for RFEH applications. Furthermore, the (CPW) feeding technique has been used in order to get wideband antenna characteristics. In general, the results showed that the proposed multiband antennas in this thesis have better overall performance than the proposed wideband antennas since they support more resonating frequencies utilized by different wireless services. Furthermore, the results of the reflection coefficient $|S_{11}|$ for the proposed multiband antennas showed better performance compared to the proposed wideband antennas, which means less reflected power and maximum power transfer could be achieved by using the multiband antenna instead of the wideband antenna. Also, the best proposed antenna in this thesis is the second multiband antenna (Antenna-2) since it showed outstanding performance by supporting a high number of total (11) eleven resonating frequencies required for RFEH application and achieved high performance in terms of the reflection coefficient $|S_{11}|$, bandwidth, and gain. Furthermore, the measurement results of

the reflection coefficient $|S_{11}|$ and the normalized 2D radiation pattern showed acceptable tolerance errors compared with the simulated results for all of the proposed antennas, taking into account the fabrication difficulties due to the fine detail of the fractal geometries that were implemented on the proposed antennas, the soldering effects, and the imperfect testing environment since no fully anechoic chamber was available in the university where the measurements were recorded. The following points demonstrate the achieved results from each of the proposed antennas that were introduced in this thesis:

- The first proposed antenna (Antenna-1) supports six resonate frequencies (1.7155 GHz, 2.424 GHz, 3.36 GHz, 3.789 GHz, 5.843 GHz, and 6.886 GHz) and has a peak gain of (2.83 dBi) at the frequency of 2.45 GHz and a maximum bandwidth of (0.4281 GHz) at the resonate frequency of 5.8 GHz.
- The second proposed antenna (Antenna-2) supports eleven resonate frequencies (0.776 GHz, 1.4108 GHz, 1.5971GHz, 1.8455 GHz, 2.4527 GHz, 2.8736 GHz, 3.191 GHz, 4.06 GHz, 5.2058 GHz, 5.7164 GHz, and 6.9584 GHz) and has a peak gain of (6.349 dBi) at the frequency of 3.95 GHz and a maximum bandwidth of (0.6996 GHz) at the resonate frequency of 6.9584 GHz.
- The third proposed antenna (Antenna-3) supports four resonate frequencies (2.4045 GHz, 3.568 GHz, 4.6405 GHz, and 5.869 GHz) and has a peak gain of (3.203 dBi) at the frequency of 2.4045 GHz and a maximum bandwidth of (0.5101 GHz) at the resonate frequency of 5.869 GHz.
- The fourth proposed antenna (Antenna-4) has dual wideband frequency characteristics and has two resonance frequencies of 2.48 GHz and 5.232 GHz. The proposed wideband antenna achieved a peak gain of (4 dBi) at

the frequency (5.4 GHz) and a maximum bandwidth of (1.0813 GHz) at the frequency of 2.48 GHz.

- The fifth proposed antenna (Antenna-5) has dual wideband frequency characteristics and has two resonance frequencies of 2.73 GHz and 6.9 GHz. The proposed wideband antenna achieved a peak gain of (4.31 dBi) at the frequency (2.6 GHz) and a maximum bandwidth of (2.963 GHz) at the resonance frequency of 2.73 GHz.
- The sixth proposed antenna (Antenna-6) has a single wideband frequency of (3.9723 GHz) at a resonance frequency of 3.215 GHz. The proposed wideband antenna achieved a peak gain of (4.481 dBi) at the frequency (3 GHz).
- All of the previously mentioned antennas support a variety of RF wireless services, including WLAN and mobile cellular services.

5.2 Future Works

The performance of the receiving antenna is important for any radio frequency energy-harvesting system and has a lot of potential for future research and development. The following are some possible future works:

- Interface the proposed multiband and wideband antennas with the appropriate rectifying circuits in order to see the overall system performance of the rectenna.
- Explore new materials, like metasurface, and fabrication methods for implementing multiband and wideband antennas that may lead to more performance improvements and/or smaller sizes. such as using another type of antenna substrate.
- Examining the performance of the proposed multiband and wideband antennas in various environmental situations, including temperature, humidity, and air pressure.
- Investigates a new design technique that may improve the performance of multiband and wideband antennas.

5.3 Publications Arising from This Research

- 1- Mohammed Muataz Hasan, and Ahmed M. A. Sabaawi, "Microstrip Patch Antenna with Multi-Fins for Radio Frequency Energy Harvesting Applications," Progress In Electromagnetics Research C, Vol. 142, 61-73, 2024. doi:10.2528/PIERC24012803.

- 2- Mohammed Muataz Hasan, and Ahmed M. A. Sabaawi, "A Modified Fractal Hexagonal Slot Antenna with a Defected Ground Structure for RF Energy Harvesting Applications" INTERNATIONAL JOURNAL OF MICROWAVE AND OPTICAL TECHNOLOGY, Vol. 19, No. 2, 2024.

- 3- Mohammed Muataz Hasan, and Ahmed M. A. Sabaawi, "Drone Shaped Fractal Antenna with Defected Ground Structure for RF Energy Harvesting Applications" Submitted to the journal of Periodica Polytechnica Electrical Engineering and Computer Science. (Accepted and it's in copyediting stage).

References

- [1] L. S. Vailshery, “Global IoT and non-IoT connections 2010-2025 | Statista.” Accessed: Jan. 21, 2024. [Online]. Available: <https://www.statista.com/statistics/1101442/iot-number-of-connected-devices-worldwide/>
- [2] A. Mouapi, “Radiofrequency Energy Harvesting Systems for Internet of Things Applications: A Comprehensive Overview of Design Issues,” *Sensors*, vol. 22, no. 21. MDPI, Nov. 01, 2022. doi: 10.3390/s22218088.
- [3] M. A. Ullah, R. Keshavarz, M. Abolhasan, J. Lipman, K. P. Esselle, and N. Shariati, “A Review on Antenna Technologies for Ambient RF Energy Harvesting and Wireless Power Transfer: Designs, Challenges and Applications,” *IEEE Access*, vol. 10. Institute of Electrical and Electronics Engineers Inc., pp. 17231–17267, 2022. doi: 10.1109/ACCESS.2022.3149276.
- [4] L. G. Tran, H. K. Cha, and W. T. Park, “RF power harvesting: a review on designing methodologies and applications,” *Micro and Nano Systems Letters*, vol. 5, no. 1. Society of Micro and Nano Systems, Dec. 01, 2017. doi: 10.1186/s40486-017-0051-0.
- [5] A. Georgiadis, G. Andia, and A. Collado, “Rectenna design and optimization using reciprocity theory and harmonic balance analysis for electromagnetic (EM) energy harvesting,” *IEEE Antennas Wirel Propag Lett*, vol. 9, pp. 444–446, 2010, doi: 10.1109/LAWP.2010.2050131.

- [6] A. Nimo, D. Grgić, and L. M. Reindl, “Ambient electromagnetic wireless energy harvesting using multiband planar antenna,” in *International Multi-Conference on Systems, Signals and Devices, SSD 2012 - Summary Proceedings*, 2012. doi: 10.1109/SSD.2012.6198036.
- [7] G. Monti, F. Congedo, D. De Donno, and L. Tarricone, “Monopole-based rectenna for microwave energy harvesting of UHF RFID systems,” *Prog. Electromagn. Res. C*, vol. 31, pp. 109–121, 2012.
- [8] K. Niotaki, S. Kim, S. Jeong, A. Collado, A. Georgiadis, and M. M. Tentzeris, “A compact dual-band rectenna using slot-loaded dual band folded dipole antenna,” *IEEE Antennas Wirel Propag Lett*, vol. 12, pp. 1634–1637, 2013, doi: 10.1109/LAWP.2013.2294200.
- [9] S. Ladan, N. Ghassemi, A. Ghiotto, and K. Wu, “Highly efficient compact rectenna for wireless energy harvesting application,” *IEEE Microw Mag*, vol. 14, no. 1, pp. 117–122, 2013, doi: 10.1109/MMM.2012.2226629.
- [10] M. K. Hosain, A. Z. Kouzani, M. F. Samad, and S. J. Tye, “A miniature energy harvesting rectenna for operating a head-mountable deep brain stimulation device,” *IEEE Access*, vol. 3, pp. 223–234, 2015, doi: 10.1109/ACCESS.2015.2414411.
- [11] S. T. Khang, J. W. Yu, and W. S. Lee, “Compact folded dipole rectenna with RF-based energy harvesting for IoT smart sensors,” *Electron Lett*, vol. 51, no. 12, pp. 926–928, Jun. 2015, doi: 10.1049/el.2015.0138.
- [12] C. Song et al., “A Novel Six-Band Dual CP Rectenna Using Improved Impedance Matching Technique for Ambient RF Energy Harvesting,” *IEEE Trans Antennas Propag*, vol. 64, no. 7, pp. 3160–3171, Jul. 2016, doi: 10.1109/TAP.2016.2565697.

- [13] C. Song et al., “Matching network elimination in broadband rectennas for high-efficiency wireless power transfer and energy harvesting,” *IEEE Transactions on Industrial Electronics*, vol. 64, no. 5, pp. 3950–3961, May 2017, doi: 10.1109/TIE.2016.2645505.
- [14] S. Shen, C. Y. Chiu, and R. D. Murch, “A dual-port triple-band L-probe microstrip patch rectenna for ambient RF energy harvesting,” *IEEE Antennas Wirel Propag Lett*, vol. 16, pp. 3071–3074, Oct. 2017, doi: 10.1109/LAWP.2017.2761397.
- [15] A. Jie, N. Nasimuddin, M. Karim, and K. Chandrasekaran, “A dual-band efficient circularly polarized rectenna for RF energy harvesting systems,” *International Journal of RF and Microwave Computer-Aided Engineering*, vol. 29, p. e21665, Dec. 2018, doi: 10.1002/mmce.21665.
- [16] S. Chandravanshi, S. Sen Sarma, and M. J. Akhtar, “Design of Triple Band Differential Rectenna for RF Energy Harvesting,” *IEEE Trans Antennas Propag*, vol. 66, no. 6, pp. 2716–2726, Jun. 2018, doi: 10.1109/TAP.2018.2819699.
- [17] Y. Shi, J. Jing, Y. Fan, L. Yang, and M. Wang, “Design of a novel compact and efficient rectenna for WiFi energy harvesting,” *Prog. Electromagn. Res.*, vol. 83, pp. 57–70, 2018.
- [18] A. Khemar, A. Kacha, H. Takhedmit, and G. Abib, “Design and experiments of a dual-band rectenna for ambient RF energy harvesting in urban environments,” *IET Microwaves, Antennas and Propagation*, vol. 12, no. 1, pp. 49–55, Jan. 2018, doi: 10.1049/iet-map.2016.1040.
- [19] L. Yang, Y. J. Zhou, C. Zhang, X. M. Yang, X. X. Yang, and C. Tan, “Compact Multiband Wireless Energy Harvesting Based Battery-Free Body Area Networks Sensor for Mobile Healthcare,” *IEEE J Electromagn RF Microw Med Biol*, vol. 2, no. 2, pp. 109–115, Jun. 2018, doi: 10.1109/JERM.2018.2817364.

- [20] V. Palazzi et al., “A Novel Ultra-Lightweight Multiband Rectenna on Paper for RF Energy Harvesting in the Next Generation LTE Bands,” *IEEE Trans Microw Theory Tech*, vol. 66, no. 1, pp. 366–379, Jan. 2018, doi: 10.1109/TMTT.2017.2721399.
- [21] M. Zeng, Z. Li, A. S. Andrenko, Y. Zeng, and H. Z. Tan, “A Compact Dual-Band Rectenna for GSM900 and GSM1800 Energy Harvesting,” *Int J Antennas Propag*, vol. 2018, 2018, doi: 10.1155/2018/4781465.
- [22] M. A. M. Said, Z. Zakaria, M. N. Husain, M. H. Misran, and F. S. M. Noor, “2.45 GHz rectenna with high gain for RF energy harvesting,” *Telkomnika (Telecommunication Computing Electronics and Control)*, vol. 17, no. 1, pp. 384–391, Feb. 2019, doi: 10.12928/TELKOMNIKA.v17i1.11592.
- [23] G. Shukla, S. Verma, A. Sao, S. Srivastava, S. Tripathi, and S. Prasad Mukherjee, “RF Energy Harvesting for GSM and Wi-Fi Band,” 2020, doi:10.23919/URSIRCRS49211.2020.9113646.
- [24] S. Roy, J. J. Tiang, M. Bin Roslee, M. T. Ahmed, A. Z. Kouzani, and M. A. Parvez Mahmud, “Quad-band rectenna for ambient radio frequency (Rf) energy harvesting,” *Sensors*, vol. 21, no. 23, Dec. 2021, doi: 10.3390/s21237838.
- [25] S. Roy, J. J. Tiang, M. Bin Roslee, M. T. Ahmed, A. Z. Kouzani, and M. A. P. Mahmud, “Design of a Highly Efficient Wideband Multi-Frequency Ambient RF Energy Harvester,” *Sensors*, vol. 22, no. 2, Jan. 2022, doi: 10.3390/s22020424.
- [26] S. Muhammad et al., “Design of Wideband Circular-Slot Antenna for Harvesting RF Energy,” *Int J Antennas Propag*, vol. 2022, 2022, doi: 10.1155/2022/5964753.

- [27] L. Xie, Y. Shi, Y. Hou, and A. Lou, “Wireless power transfer and applications to sensor networks,” *Wireless Communications, IEEE*, vol. 20, pp. 140–145, Aug. 2013, doi: 10.1109/MWC.2013.6590061.
- [28] K. Wu, D. Choudhury, and H. Matsumoto, “Wireless power transmission, technology, and applications [scanning the issue],” *Proceedings of the IEEE*, vol. 101, no. 6, pp. 1271–1275, 2013, doi: 10.1109/JPROC.2013.2257590.
- [29] M. Ettorre, W. Alomar, and A. Grbic, “Radiative Wireless Power-Transfer System Using Wideband, Wide-Angle Slot Arrays,” *IEEE Trans Antennas Propag*, vol. PP, p. 1, Mar. 2017, doi: 10.1109/TAP.2017.2688930.
- [30] H. Shoki, “Issues and Initiatives for Practical Deployment of Wireless Power Transfer Technologies in Japan,” *Proceedings of the IEEE*, vol. 101, pp. 1312–1320, Jun. 2013, doi: 10.1109/JPROC.2013.2248051.
- [31] D. M. Pozar, *Microwave Engineering*. Hoboken, NJ, USA: Wiley, 2011.
- [32] S. Divakaran, D. Das Krishna, and N. Nasimuddin, “RF energy harvesting systems: An overview and design issues,” *International Journal of RF and Microwave Computer-Aided Engineering*, vol. 29, p. e21633, Dec. 2018, doi: 10.1002/mmce.21633.
- [33] A. Costanzo, F. Donzelli, D. Masotti, and V. Rizzoli, “Integration of numerical and field-theoretical techniques in the design of single- and multi-band rectennas for micro-power generation,” *Int J Microw Wirel Technol*, vol. 2, no. 3–4, pp. 293–303, 2010, doi: DOI: 10.1017/S1759078710000553.
- [34] M. M. Fakharian, “A Wideband Rectenna Using High Gain Fractal Planar Monopole Antenna Array for RF Energy Scavenging,” *Int J Antennas Propag*, vol. 2020, 2020, doi: 10.1155/2020/3489323.

- [35] A. T. Abed et al., “Challenges and limits of fractal and slot antennas for WLAN, LTE, ISM, and 5G communication: a review paper,” *Annales des Telecommunications/Annals of Telecommunications*, vol. 76, no. 9–10, pp. 547–557, Oct. 2021, doi: 10.1007/s12243-020-00828-6.
- [36] S. Shen, Y. Zhang, C.-Y. Chiu, and R. Murch, “An ambient RF energy harvesting system where the number of antenna ports is dependent on frequency,” *IEEE Trans. Microw. Theory Techn.*, vol. 67, no. 9, pp. 3821–3832, Sep. 2019.
- [37] C. Balanis, “Antenna theory: analysis and design 4th edition / Constantine A. Balanis,” Jan. 2016.
- [38] S. D. Assimonis, V. Fusco, A. Georgiadis, and T. Samaras, “Efficient and Sensitive Electrically Small Rectenna for Ultra-Low Power RF Energy Harvesting,” *Sci Rep*, vol. 8, no. 1, Dec. 2018, doi: 10.1038/s41598-018-33388-w.
- [39] Y. Shi, J. Jing, Y. Fan, L. Yang, Y. Li, and M. Wang, “A novel compact broadband rectenna for ambient RF energy harvesting,” *AEU - International Journal of Electronics and Communications*, vol. 95, pp. 264–270, 2018, doi: <https://doi.org/10.1016/j.aeue.2018.08.035>.
- [40] U. Olgun, C.-C. Chen, and J. Volakis, “Design of an efficient ambient WiFi energy harvesting system,” *Microwaves, Antennas & Propagation, IET*, vol. 6, pp. 1200–1206, Aug. 2012, doi: 10.1049/iet-map.2012.0129.
- [41] N. Singh et al., “Low Profile Multiband Rectenna for Efficient Energy Harvesting at Microwave Frequencies,” *International Journal of Electronics*, vol. 106, Jun. 2019, doi: 10.1080/00207217.2019.1636302.

- [42] U. Olgun, C.-C. Chen, and J. Volakis, Low-profile planar rectenna for batteryless RFID sensors. 2010. doi: 10.1109/APS.2010.5562220.
- [43] A. H. Majeed and K. H. Sayidmarie, “Fractal Sectoral Monopole Antenna for UWB Band Applications,” *The Applied Computational Electromagnetics Society Journal (ACES)*, Jan. 2023, doi: 10.13052/2022.aces.j.370810.
- [44] F. Zhang et al., “Design of a compact planar rectenna for wireless power transfer in the ISM band,” *Int J Antennas Propag*, vol. 2014, 2014, doi: 10.1155/2014/298127.
- [45] M. Fallahpour and R. Zoughi, “Antenna Miniaturization Techniques: A Review of Topology- and Material-Based Methods,” *IEEE Antennas Propag Mag*, vol. 60, no. 1, pp. 38–50, Feb. 2018, doi: 10.1109/MAP.2017.2774138.
- [46] M. A. Ullah, T. Alam, and M. T. Islam, “A UHF CPW-fed patch antenna for nanosatellite store and forward mission,” *Microsystem Technologies: micro and nanosystems information storage and processing systems*, vol. 26, pp. 2399–2405, Aug. 2020, doi: 10.1007/s00542-020-04780-2.
- [47] M. Ramya and R. Boopathi Rani, “A Compendious Review on Fractal Antenna Geometries in Wireless Communication,” in *Proceedings of the 5th International Conference on Inventive Computation Technologies, ICICT 2020*, Institute of Electrical and Electronics Engineers Inc., Feb. 2020, pp. 888–893. doi: 10.1109/ICICT48043.2020.9112580.
- [48] A. Q. Khan, M. Riaz, A. Bilal, and A. Qadir Khan, “Various Types of Antenna with Respect to their Applications: A Review,” *INTERNATIONAL JOURNAL OF MULTIDISCIPLINARY SCIENCES AND ENGINEERING*, vol. 7, no. 3, 2016, [Online]. Available: www.ijmse.org

- [49] “Microstrip Width Calculator.” Accessed: Jan. 23, 2024. [Online]. Available: <https://www.everythingrf.com/rf-calculators/microstrip-width-calculator>
- [50] R. E. Musril, H. A. Rahim, M. Abdulmalek, M. Jusoh, and M. E. M. Salleh, “An Enhanced Gain of Yagi-Uda Antenna with Folded Dipole for Amateur Radio VHF Band Application,” in *Journal of Physics: Conference Series*, Institute of Physics Publishing, Jun. 2019. doi: 10.1088/1742-6596/1175/1/012064.
- [51] W. D. Prather, D. V. Giri, and R. L. Gardner, “Dr. Carl Baum: One Remarkable Career.” *The Radio Science Bulletin* No 312 (March, 2005).
- [52] A. M. A. Sabaawi, Q. H. Sultan, and T. A. Najm, “Design and Implementation of Multi-Band Fractal Slot Antennas for Energy Harvesting Applications,” *Periodica polytechnica Electrical engineering and computer science*, vol. 66, no. 3, pp. 253–264, 2022, doi: 10.3311/PPee.20301.
- [53] M. K. Khandelwal, B. K. Kanaujia, and S. Kumar, “Defected ground structure: Fundamentals, analysis, and applications in modern wireless trends,” *International Journal of Antennas and Propagation*, vol. 2017. Hindawi Limited, 2017. doi: 10.1155/2017/2018527.
- [54] “Frequency Allocation Chart for LTE, WiMAX and WLAN systems / bands.” Accessed: Jan. 13, 2024. [Online]. Available: <https://wireless-instruments.com/lte-wimax-bands/>
- [55] “The European table of frequency allocations and applications in the frequency range 8.3 khz to 3000 ghz (eca table)” Report25 Approved October 2021, Editorial update 7 July 2023.
- [56] Fawwaz T. Ulaby and U. Ravaioli, “Fundamentals of applied electromagnetics”, Pearson Education Inc, Jan. 2015.

- [57] C. Song, Y. Huang, J. Zhou, J. Zhang, S. Yuan, and P. Carter, "A high-efficiency broadband rectenna for ambient wireless energy harvesting," *IEEE Trans Antennas Propag*, vol. 63, no. 8, pp. 3486–3495, Aug. 2015, doi: 10.1109/TAP.2015.2431719.
- [58] G. Srinivasu, T. Gayatri, M. K. Meshram, and V. K. Sharma, "Design Analysis of an Ultra-Wideband Antenna for RF Energy Harvesting in 1.71-12GHz," 2020.
- [59] Q. Awais, Y. Jin, H. T. Chattha, M. Jamil, H. Qiang, and B. A. Khawaja, "A compact rectenna system with high conversion efficiency for wireless energy harvesting," *IEEE Access*, vol. 6, pp. 35857–35866, Jun. 2018, doi: 10.1109/ACCESS.2018.2848907.
- [60] A. Bhattacharjee, D. Bhattacharya, A. Bhawal, A. Karmakar, and A. Saha, "Vivaldi antennas: a historical review and current state of art," *Int J Microw Wirel Technol*, vol. 13, no. 8, pp. 833–850, 2021, doi: DOI: 10.1017/S1759078720001415.
- [61] P. Gibson, "The Vivaldi aerial," in *Proc. 9th Eur. Microw. Conf.*, vol. 1, 1979, pp. 101–105.
- [62] A. S. Dixit and S. Kumar, "A Survey of Performance Enhancement Techniques of Antipodal Vivaldi Antenna," *IEEE Access*, vol. 8. Institute of Electrical and Electronics Engineers Inc., pp. 45774–45796, 2020. doi: 10.1109/ACCESS.2020.2977167.
- [63] Y. K. Choukiker and S. K. Behera, "Wideband frequency reconfigurable Koch snowflake fractal antenna," *IET Microwaves, Antennas and Propagation*, vol. 11, no. 2, pp. 203–208, Jan. 2017, doi: 10.1049/iet-map.2016.0238.
- [64] C. P. Wen, "Coplanar Waveguide, a Surface Strip Transmission Line Suitable for Nonreciprocal Gyromagnetic Device Applications," 1969 *G-MTT International Microwave Symposium*, Dallas, TX, USA, 1969, pp. 110-115, doi: 10.1109/GMTT.1969.1122668.

المخلص

يعد هوائي الاستقبال أحد المكونات الرئيسية لنظام حصاد طاقة الترددات الراديوية (RFEH) ونظام نقل الطاقة اللاسلكي (WPT)، لأنه مسؤول عن التقاط الموجات الكهرومغناطيسية من الفضاء الحر. توضح الأطروحة مواصفات التصميم المثالي لهوائيات الاستقبال المستخدمة من قبل أنظمة حصاد طاقة الترددات الراديوية وكيف يتم تفضيل الهوائيات متعددة النطاقات والعريضة النطاق لأنظمة حصاد طاقة الترددات الراديوية. تقدم هذه الأطروحة مجموعة متنوعة من ثلاثة هوائيات جديدة متعددة النطاق بالإضافة إلى ثلاثة هوائيات جديدة واسعة النطاق مصممة ومحسنة لأنظمة حصاد طاقة الترددات الراديوية. تم تصنيع جميع الهوائيات المقدمة باستخدام تقنية لوحة الدوائر المطبوعة (PCB) من نوع (FR-4)، وتم اختبار أدائها في المختبر حيث أظهرت نتائج القياس تقارب جيد مقارنة بنتائج المحاكاة. تم استخدام العديد من التقنيات أثناء تنفيذ الهوائيات المقدمة من أجل زيادة عرض النطاق الترددي وتحسين الأداء، بما في ذلك الجمع بين الهندسة الكسورية واستخدام البنية الأرضية المعيبة (DGS). يدعم الهوائي المقترح الأول (drone-shaped fractal antenna) ستة ترددات رنين وحقق كسباً قدره (2.83 ديسيبل) عند تردد 2.45 جيجا هرتز. الهوائي المقترح الثاني (microstrip patch antenna based on a half-wave dipole modified hexagonal) يدعم أحد عشر تردداً رنينياً وحقق كسباً قدره (6.349 ديسيبل) عند تردد 3.95 جيجا هرتز. أما الهوائي الثالث المقترح (slot antenna a compact patch antenna with a modified structure) فهو يدعم أربعة ترددات رنانة وحقق كسباً قدره (3.203 ديسيبل) عند التردد 2.4045 جيجا هرتز. أما الهوائي الرابع المقترح (modified square modified structure) فلديه عرض نطاق قدره (1.0813 جيجا هرتز) وحقق كسباً أقصى قدره (4 ديسيبل) عند التردد (5.4 جيجا هرتز). أما الهوائي الخامس المقترح (monopole patch antenna with coplanar waveguide (CPW)-Feeding technique) فلديه عرض نطاق قدره (2.963 جيجا هرتز) وحقق كسباً قدره (4.31 ديسيبل) عند التردد (2.6 جيجا هرتز). الهوائي السادس المقترح (a modified hexagonal monopole patch antenna with coplanar waveguide (CPW) feeding technique) لديه عرض نطاق قدره (3.9723 جيجا هرتز) وحقق كسباً قدره (4.481 ديسيبل) عند التردد (3 جيجا هرتز).

إقرار المشرف

أشهد بأن هذه الرسالة الموسومة (تصميم هوائي متقدم لأنظمة حصاد الطاقة المعتمدة على الترددات اللاسلكية) تم إعدادها من قبل الطالب (محمد معتز حسن) تحت إشرافي في قسم هندسة الإلكترونيك / كلية هندسة الإلكترونيات / جامعة نينوى، وهي جزء من متطلبات نيل شهادة الماجستير/علوم في اختصاص هندسة الإلكترونيك.

التوقيع:

الاسم: أ.م.د. احمد محمد احمد

التاريخ: / / 2024

إقرار المقوم اللغوي

أشهد بأنه قد تمت مراجعة هذه الرسالة من الناحية اللغوية وتصحيح ما ورد فيها من أخطاء لغوية وتعبيرية وبذلك أصبحت الرسالة مؤهلة للمناقشة بقدر تعلق الأمر بسلامة الأسلوب أو صحة التعبير.

التوقيع:

الاسم: م. د. لطيف احمد محمد

التاريخ: / / 2024

إقرار رئيس لجنة الدراسات العليا

بناءً على التوصيات المقدمة من قبل المشرف والمقوم اللغوي أشرح هذه الرسالة للمناقشة.

التوقيع:

الاسم: أ.م.د. حارث أحمد محمد

التاريخ: / / 2024

إقرار رئيس القسم

بناءً على التوصيات المقدمة من قبل المشرف والمقوم اللغوي ورئيس لجنة الدراسات العليا أشرح هذه الرسالة للمناقشة.

التوقيع:

الاسم: أ.م.د. حارث أحمد محمد

التاريخ: / / 2024

إقرار لجنة المناقشة

نشهد بأننا أعضاء لجنة التقويم والمناقشة قد اطلعنا على هذه الرسالة الموسومة (تصميم هوائي متقدم لأنظمة حصاد الطاقة المعتمدة على الترددات اللاسلكية) وناقشنا الطالب (محمد معتز حسن) في محتوياتها وفيما له علاقة بها بتاريخ 2024/5/19 وقد وجدناه جدير بنيل شهادة الماجستير/علوم في اختصاص هندسة الالكترونك.

التوقيع:

التوقيع:

عضو اللجنة: أ.م.د. محمد عبدالرحمن احمد

رئيس اللجنة: أ.د. جعفر رمضان محمد

التاريخ: 2024/ /

التاريخ: 2024/ /

التوقيع:

التوقيع:

عضو اللجنة (المشرف): أ.م.د. احمد محمد احمد

عضو اللجنة: أ.م.د. سعد وسمي عصمان

التاريخ: 2024/ /

التاريخ: 2024/ /

قرار مجلس الكلية

اجتمع مجلس كلية هندسة الالكترونيات بجلسته المنعقدة بتاريخ: 2024 / /
وقرر المجلس منح الطالبة شهادة الماجستير علوم في اختصاص هندسة الالكترونك

رئيس مجلس الكلية: أ.د. خالد خليل محمد

مقرر المجلس: أ.م.د. بلال علاءالدين جبر

التاريخ: 2024/ /

التاريخ: 2024 / /

تصميم هوائي متقدم لأنظمة حصاد الطاقة المعتمدة على الترددات اللاسلكية

رسالة تقدم بها

محمد معنز حسن

إلى

مجلس كلية هندسة الإلكترونيات-جامعة نينوى

وهي جزء من متطلبات نيل شهادة الماجستير علوم في

هندسة الإلكترونيك

بإشراف

الاستاذ المساعد الدكتور

احمد محمد احمد سلامة السبعاعي



جامعة نينوى
كلية هندسة الإلكترونيات
قسم هندسة الإلكترونيك

تصميم هوائي متقدم لأنظمة حصاد الطاقة المعتمدة على الترددات اللاسلكية

محمد معتز حسن

رسالة في هندسة الإلكترونيك

بإشراف

الاستاذ المساعد الدكتور

احمد محمد احمد سلامة السبعاعي